THE UNIVERSITY *of* EDINBURGH

High Resolution Simulations of Synoptic Scale "Paleometeorology" During the Last Glacial Maximum

By

Matthew B. Unterman

Thesis submitted for the degree of

Doctor of Philosophy

University of Edinburgh

2011

Declaration

I certify that the work described in this thesis is my own, except where otherwise stated, and has not been previously submitted for any other degree at this, or any other university.

Matthew B. Unterman

30/05/2012

Acknowledgements and Dedication

This work would not be possible without the help of my supervisors Tom Crowley and Simon Tett, and my co-authors David Erickson, Kevin Hodges and Seong-Joong Kim. Thank you also to my committee members, Dick Kroon and Bob Harwood, and to my examiners Mary Elliot and Alan Haywood. I would also like to thank my friends and peers who made this effort and 4-year journey a memorable one.

I sincerely dedicate this effort to my mother, Gail; my father, Lee; my sister, Caitlin, and the rest of my family who have supported and motivated me throughout the duration of my research. I also dedicate this effort to Jayne and Lou Concra for their constant praise and motivation. And to my dearest Liz who has practically earned this Ph.D. with me.

I further dedicate this effort in loving memory of my grandfather, William "Gaga" Trimmer; my grandmother, Irene "Reenee" Trimmer; my grandfather, Israel Unterman; my grandmother, Ruth Unterman; and to my uncle, Robert "Uncle Bob" Unterman, who have always thought I could save the world.

Abstract

Hourly winter weather conditions of the Last Glacial Maximum (LGM) are simulated using the Community Climate Model version 3 (CCM3) on a globally resolved T170 (~75 km) grid. This simulation has been run in-tandem with a lower temporally resolved six-year climatological run. The purpose of the study is to determine: (1) whether examination of higher-resolution simulations, on both spatial and temporal scales, can enhance paleometeorological inferences based previously on monthly statistics of model output and (2) whether certain synoptic-scale events, which may have only a modest impact on seasonal statistics, might exert a disproportionate impact on geological climate records. Analysis is focused on changes in wind flow, no analogue climate "states", synoptic scale events including Northern Hemisphere cyclogenesis, and gust events over glacial dust source regions. Results show a decrease in North Atlantic and increase in North Pacific cyclogenesis during the LGM. Storm trajectories react to the mechanical forcing of the Laurentide Ice Sheet, with Pacific storms tracking over middle Alaska and northern Canada and terminate in the Labrador Sea. The latter result supports observations and other model runs showing a significant reduction in Greenland winter precipitation. The modified Pacific track results in increased precipitation and the delivery of warmer air along the west coast of North America. This could explain "early" glacial warming inferred in this region from proxy climate records, potentially representing instead a natural regional response to ice age boundary conditions. Results also indicate a low variability, "no analogue" region just south of the Laurentide Ice Sheet margin which has appropriate conditions to harbour temperature-sensitive trees west of the Appalachian Mountains. Combined with pollen data, this lends valuable insight into the known disagreement between modern seed dispersal experiments and calculated migration rates. Finally, hourly-scale gust events over dust source regions during the LGM are two to five times greater than the modern, providing a mechanism to help explain the increased glacial dust load seen in the ice cores. Backwards air-parcel trajectories from Antarctic ice core locations show air sources

over Patagonia and the Altiplano with some inputs from South Africa agreeing with recent isotopic tracer analyses. Results demonstrate that high temporal and spatial resolution simulations can provide valuable insight to add to the cornucopia of information already available from lower-resolution runs. They can also enhance our interpretation of geological records, which have been previously assumed to record longer time-scale climatological mean-states and thus ignoring any extreme synoptic events which may actually have had a disproportionate impact on their preservation.

Table of Contents

List of Figures

List of Tables

Chapter 1

Aim and Motivation

Previous global climate simulations of the Last Glacial Maximum (LGM) have lent considerable insight into the dynamics of the ice age atmosphere. However, many questions still remain with varying degrees of uncertainty, which may benefit from the increase in model resolution, and the ability to describe features on or below the synoptic scale. The persistence of such discrepancies is due to several reasons, of which include: (1) the ever changing incorporation of new or re-examined geological data into simulations as boundary conditions and (2) the recognition of the impact of specific synoptic scale events on proxy data, such as regional precipitation from cyclones, dust emissions (McGee et al., 2010), wind driven sea ice transport (Geibert et al., 2010) and others. Consequently, by increasing both spatial and temporal resolution in an effort to simulate "paleometeorological" events, computer simulations may give better understanding to geological data by lending insight into the mechanisms which impact their regional preservation. In one example, the Laurentide Ice Sheet over North America has been known to have perturbed northern hemisphere westerly flow for decades, but the positioning of LGM mid-latitude storm tracks, lifetimes, and intensity of cyclones given ice age physics is continually under investigation. Understanding the trajectories of such storms inherently lends insight into many geological records, such as those along the west coast of North America and the ice cores on Greenland which have been traditionally used in many paleoclimatological studies.

The work herein analyses a series of high spatial and temporal resolution global climate simulations of the Last Glacial Maximum (LGM) in an attempt to first analyze and explore the benefits of what may be considered to be a

"paleometeorological" simulation. The simulations presented here are the highest spatial and temporal resolution global simulations of the LGM at this time.

This work may be considered a non-traditional pilot study into "paleometeorology" as the original motivation was exploration into LGM weather and to determine the benefits of saving data at such a scale. Here the results are used to determine the differences in northern hemisphere mid-latitude flow and cyclogenesis between the modern and the ice age Earth and make comparisons to the geological record. Specifically, the aim is to determine: (1) whether examination of higher-resolution simulations, on both spatial and temporal scales, can enhance meteorological inferences based previously on monthly statistics of model output; and (2) whether certain synoptic-scale events (such as storms), which may have only a modest impact on seasonal statistics, might exert a disproportionate impact on geological climate records. It is hypothesized here, that they do exert such an impact, and that forcing of the continental ice sheets on storm tracks creates conditions appropriate to explain regional warming along the west coast of North America and a large reduction in Greenland wintertime precipitation during the LGM. It is also hypothesized that with increased resolution, such a simulation can describe individual synoptic events that may account for the majority of the wintertime precipitation on Greenland during this time. Furthermore, it is suspected that a large increase in high velocity surface wind events may provide a mechanism appropriate to explain the large increase in dust emissions seen in the ice cores, and that a model at this scale will find source air locations over ice age dust source areas comparable to more recent geological interpretations (cf. Chapter 2). Such results will provide valuable insight into how proxy records are interpreted and integrated into future paleoclimatological and paleometeorological studies. It is only until now, that there been any effort in doing high resolution paleo-modelling on the order of a weather forecast model, in which the effects of topography on atmospheric flow can be better described.

Here, hourly resolved weather conditions of one LGM northern hemisphere winter are simulated using the National Center for Atmospheric Research Community Climate Model (CCM) version 3.6.6 (cf. Duffy et al., 1993) on a high spatial

resolution global grid (~75 km). Due to the intrinsic shortness of this synoptic scale simulation, and its strain on computing, it has been run in-tandem with a lower temporally resolved climatological simulation first reported in Kim et al. (2008), the data of which will be further explored in the work presented here.

From a climatological viewpoint, this exploration would seem limited given the short duration of both the synoptic-scale and climatological integrations. However, from the meteorological perspective, the duration of the "record" is comparable to those obtained from large-scale field experiments (such as GATE or TOGA-CORE) which have been of considerable value not only to the meteorological but also the climate communities (e.g. Shin et al., 1990; Webster and Lucas, 1992; cf. McGee et al., 2010). It is also on the order of, or longer than, experiments concerned with analyzing features responsible for aerosol dust emissions (cf. Sow et al., 2009; McGee et al., 2010; Maher et al., 2010; and others), the results of which are highly important to the paleoclimate community.

***

The quality of any climate simulation is only as good as the boundary conditions that it incorporates. These include, but are not limited to sea surface temperatures (SSTs), atmospheric concentration of carbon dioxide (CO_2), topography, ice sheet orography and location, orbital parameters, and vegetation. For paleo-simulations, these values are not included based on observations, but on geological data. For the most part, robust boundary conditions can be expected to produce more robust modelling results.

The simulations presented here use many documented boundary conditions to simulate the atmospheric conditions of the ice age earth. Chapter 2 is the formal introduction to this work and it will discuss specific reconstructions and the errors associated with those reconstructions, as well as general background on the LGM.

Chapter 3 is methods based and will discuss the specific model, model settings and boundary conditions in more detail as well as a preface to the validation of the CCM.

***

Just as boundary conditions affect a simulations outcome, so does the model and computing resources available. As the computing power available to the modelling community increases, so does the capability to model the Earth's climate at higher degrees of detail. In regards to cyclogenesis, it has been shown that at higher resolutions, there is a more accurate representation of storm tracks and storm processes within a full storm lifecycle (Kageyama et al., 1999; Bengtsson et al., 2009; Blender and Schubert, 2009; and others). However, a much larger percentage of paleoclimate modelling studies are analyzed on the daily, monthly, seasonal, or annual timescale, as compared to those on the sub-daily level. In terms of spatial scales, global general circulation models (GCMs) used in paleoclimatological integrations are generally on the order of one to a few hundred kilometres. Yet, in order to describe meteorological phenomena and its effect on the regional scale, higher resolution and higher frequency outputs are desirable. One problem with this however, is that as you increase the level of detail you also increase the necessary number of calculations that need to be made and therefore further strain the available computing. Increasing the output frequency of a simulation also requires more resources such as disk space. Consequently, the model methodology chosen in any given study is mainly determined by the aim and scope of the research and the available computing resources. Chapter 2 will also discuss the importance of earlier modelling in relation to the research discussed here. Afterwards, methodology will be further discussed in Chapter 3, and discussion of the northern hemisphere mid-latitude flow, and it's comparison to geological data sets will be discussed in Chapter 4. A quantitative analysis of Northern Hemisphere ice age storms and storm tracks will be presented in Chapter 5 and a first-look at LGM gust events and air parcel trajectories within the Northern and Southern Hemisphere mid to high-latitudes will be discussed in Chapter 6. Chapter 7 will wrap up the work, drawing conclusions and outlining the importance of this work.

Chapter 2

Introduction

Foreword:

The work presented here, describes a series of high resolution simulations which comprise the first attempt at a paleometeorological analysis of the last glacial maximum on the global scale. By increasing both model spatial and temporal resolution, it is the first attempt to study individual synoptic scale events during the LGM which may exert a disproportionate impact on the geological record. The nature of this work spans numerous different scientific fields, including but not limited to paleoclimatology, paleoceanography, sedimentology, geomorphology, numerous aspects of paleoecology, paleontology and meteorology. As such, it would be impossible to review the entirety of historical and contemporary literature which impacts such work. Consequently, this introductory chapter will focus on a general background of the surface of the ice age earth, as well as several specific studies which have either lead to our ability to enter into the field of paleometeorology, or comprise investigations of the geological interpretations incorporated as boundary conditions into the simulations presented here.

It is important to mention early the documented boundary conditions used here to simulate the atmospheric conditions of the ice age earth. Atmospheric CO_2 was reduced to 200 ppm to be consistent with the Vostok ice core (Petit et al., 1999). Sea level was dropped globally by 120 m, and the North Atlantic sea ice was extended to 42°N based on sedimentological data (cf. Chapter 3). Sea surface temperatures were taken from a comprehensive assessment of the surface of the ice age earth known as CLIMAP (a detailed discussion of which can be found later in this chapter) and were

uniformly lowered by another 1°C to be more consistent with recent estimates (e.g. Ballantyne et al, 2005). Ice sheet topography, to account for the massive continental ice sheets, was taken from the ICE-4G reconstruction of Peltier (Peltier, 1994; Peltier 2004). All boundary conditions inherently have some error associated with them, depending on the specific reconstruction, and require further discussion and context. The rest of this chapter will focus on providing such context, detailing a general picture of the surface of the ice age earth, background into geological reconstructions, an introduction into climate modelling, and a review of some of the literature which make a study of this kind possible. Further discussion on the specific boundary conditions used here, although will be discussed in a comparative nature to other reconstructions in this chapter, is reserved for Chapter 3.

2.0 The Last Ice Age:

Mankind has long been fascinated by climate extremes. This includes the warmer Eocene (50-60 Ma) when crocodiles roamed the Arctic and the concern over future warming given the findings of the Intergovernmental Panel on Climate Change (IPCC). Yet it is has been the ice ages that have tantalized both scientific curiosity and childhood wonder probably since the 18th and 19th century when erratic boulders were attributed to the movements of massive glaciers (cf. Agassiz, 1840). The most recent peak of the last ice age, which occurred roughly 21,000 years ago, known as the Last Glacial Maximum (LGM), is certainly no exception.

Paleothermometers show that for the past ~900 thousand years after the mid-Pleistocene transition, glacial cycles have had a primary ~100 thousand year oscillation (cf. Petit et al., 1999). Before this, glacial-interglacial cycles were, in terms of temperature, smaller in amplitude and occurred more frequently at every ~41 thousand years. The LGM was the peak of the last glacial cycle, when tremendous continental ice sheets draped across our planet and drastically modified the climate system for several thousand years before eventually signalling in the warmer Holocene around 10ka. Historically, the glaciation has been called the Wisconsin, Weichselian, or Wurm depending on whether America, Western Europe

or the Alps is referred to (cf. Crowley and North, 1991). The Wurm for instance, is derived from a river in the foreland of the Alps, roughly marking the maximum of glacial extent in the region – as well as region for the initial scientific research by Louis Agassiz in the early 19th century.

Although, at the peak of the ice age, there was the Patagonia Ice Sheet in the southern hemisphere covering the southern edges of Argentina and Chile, it was the northern hemisphere ice sheets that predominately affected the Earth system. Submerged and exposed terraces, and preserved shallow water corals, show that global sea level dropped roughly 120 metres (cf. section 2.1) in developing of the ice sheets, exposing large areas of continental shelves and creating vast exposed land bridges in the Bearing Straight, north-west Europe, the English Channel, Indonesia and a region off the coast of northern Australia in the Arafura Sea (cf. Peltier, 1994). North-western Europe was dominated by the Fennoscandian Ice Sheet, which reached heights of ~3 km above sea level (CLIMAP, 1976; Gates, 1976; Peltier, 1994; Peltier, 2004). It completely covered Norway, Sweden, Finland, the Baltic Sea, the Gulf of Finland and the Republic of Estonia. Northward, it extended over the exposed continental shelf and Siberia. In the United Kingdom, all but the southernmost points were covered by ice.

The Laurentide Ice Sheet (LIS) over North America covered all of Canada, and extended over the Great Lakes and as far south as 40°N near modern Ohio in the continental United States. In parts, the Laurentide Ice Sheet was several kilometres thick. Its massive dome, the area of maximum thickness named the "Keewatin Dome", was arguably over 4 kilometres thick just west of Hudson Bay, Canada (CLIMAP, 1976; Gates, 1985; Peltier, 1994; Peltier, 2002; Peltier, 2004). It was so massive that it depressed into the Earth's crust, reacting to the viscoelastic structure of the mantle, modified the Earth's rotation, and as a consequence, changed the length of an Earth day (cf. Wu and Peltier, 1984; Peltier, 1994; Peltier, 2004).

In terms of the atmosphere, the height of the LIS split the mid-level jet, modifying northern hemispheric westerly flow, sending a southern branch of the jet stream

towards Mexico (Kim et al., 2008) and a northerly branch over middle Alaska and over Canada (Manabe and Broccoli, 1985; Kim et al., 2008). This affected overall moisture sources to large areas of North America and Greenland and, in conjunction with lowered sea surface temperatures (SSTs, cf. below), modified northern hemispheric storm tracks (cf. Charles et al., 1994; Fawcett et al., 1997; Langen and Vinther, 2009). The Atlantic storm track shifted eastward over the extended sea ice margin (potentially as far south as 42°N) in the North Atlantic (McIntyre et al., 1976; Kim et al., 2008). In the Pacific, storms were diverted northward over middle Alaska, bringing relatively warmer air and precipitation to the region.

Numerous geological indicators of past land temperature, such as pollen, glacial sediments, borehole temperatures and noble gas concentrations in ground water, show that surface temperatures were on average roughly 4-8°C below present over the entire globe (Stute et al., 1992; Stute et al., 1997; Crowley and Baum, 1997; Unterman, 2007; Kim et al., 2008). Northern hemisphere high latitude surface air temperatures were much cooler with areas around Greenland, Iceland, northeast Atlantic, and the Barents Sea ranging from 15-30°C cooler than today (CLIMAP, 1976; Crowley and Baum, 1997; Kim et al., 2008). This is in part due to the increased elevation of the Greenland Ice Sheet and extensive North Atlantic sea ice. The same can be said for the southern hemisphere and the Antarctic ice sheet, cooling surface air temperatures around the Weddell and Ross Seas to temperatures to perhaps around 22°C below their average today (Kim et al., 2008). However, discrepancies between geological land data, sea surface temperatures, and model results continue to be present.

Sea surface temperatures (SSTs) and polar fronts were also highly modified. Excluding regions covered by ice, the global ocean cooled ~3.3-4.3°C below present. SSTs in the northern hemisphere Atlantic cooled on average ~4.8°C below present, as opposed to ~2.7°C in the southern hemisphere Atlantic. In the Pacific, this relationship was ~3.3°C and ~3.6°C respectively (modified from CLIMAP, 1971; cf. Ballantyne et al., 2005; Kim et al., 2008). In the North Atlantic, the Gulf Stream was forced southward off the Carolina coast and eastward. Sedimentological criteria

show that the resulting strong thermal gradient to its north marked the southern most extent of the North Atlantic polar front at 42°N, also providing a potential geological limit of LGM wintertime sea ice (McIntyre et al., 1976). Lower sea level blocked waters from entering the Sea of Japan and Bearing Sea in the North Pacific. This in part contributed to the large negative SST anomalies in the region. Large cooling in the North Pacific occurred between the southward shifted Kuroshio and Oyashio currents in the eastern North Pacific around ~6°C below present (CLIMAP, 1971). However, at high latitudes the cooling in the North Pacific is small compared to similar latitudes in the North Atlantic.

Cooler surface temperatures in the northern hemisphere, as well as a reduction in atmospheric CO_2 to ~200 ppm (as of August, 2010, atmospheric CO_2 was 388.15 ppm as measured from the Mauna Loa Observatory in Hawaii) drastically changed global vegetation. As much as ~1160Gt of carbon was removed from land during the LGM (Adams et al., 1990; Crowley, 1995). Cold-temperature sensitive trees were forced equatorward to warmer refugia and allowed conifer forests to dominate at mid to high latitudes (cf. Jackson et al., 2000; McLachlan and Clark, 2005). Pollen and plant macrofossils show that over North America, robust open *Picea* (Spruce) forests grew along the edge of the Laurentide ice sheet, with tundra to the northwest edge in North America. Pine (*Pinus*), including some now extinct species (*P. critchfieldii*), and Spruce forests extended towards 34°N implying relatively modest cooling towards the interior (Jackson et al., 2000). Florida and the southern states were occupied by more open vegetation with warmer variants of Pine. Extensive areas of Florida and within the continental interior west of the Appalachian Mountains, had vegetation unmatched by any modern pollen samples creating a no-analogue vegetation condition in the region. Some evidence suggests that a relatively warm and low sea level pressure variability area, just south of the ice sheet in the region, extending from 40°N in Ohio, could have harboured more temperature sensitive trees (McLachlan and Clark, 2005; and here, Chapter 4). This is in agreement with cool-temperate hardwood and cool-temperate conifer macrofossils found as far north as 35°N and 34°N respectively (Jackson et al., 2000) suggesting that at least in this region, conditions were not as severe as the pollen data alone implies. In the tropics,

rainforests greatly diminished. Savannah encroached into the Amazon Basin leaving approximately 30% of the current range of the rainforest (cf. Crowley, 1995; Crowley and Baum, 1997). Over Africa, grasslands dominated the south and arid desert regions intruded from the north, reducing tropical rainforests around the Congo area (cf. Crowley and Baum, 1997).

2.1 Reconstructing the Surface of the Ice Age Earth

Although the picture of the ice age outlined in the previous section is certainly realistic given the literature, uncertainties and the existence of other paleoreconstructions make it necessary to examine other possibilities. This is primarily due to the fact that past climate model experiments, which have provided meaningful results but are at variance with other findings, do not always use identical initial (or boundary) conditions due to the availability of geological data of the time. It actually may not have been until the first Paleoclimate Modelling Intercomparison Project (PMIP) that rigid guidelines were formed in an attempt to resolve this issue (cf. Joussaume and Taylor, 1995). Consequently, it is necessary to discuss other ice age reconstructions as the accuracy of a simulation is only as good as the quality of its boundary conditions. Comparisons to previous studies will be made in later sections, so it is also important to describe mechanisms that may result in such discrepancies.

The Geologic Record and Early Sea Surface Temperature Estimates of the LGM:

Geological evidence of the LGM surface has been observed for centuries. Glacial striations on bedrock, ice cut valleys, ice transported boulders, sediments and even subsequent glacial uplift have all been noted by geologists as early as the 19th century. During the LGM, the weight of the ice sheet over North America for instance, depressed the crust so deeply that the subsequent uplift is still visibly detectible today, such as areas in Canada around Hudson Bay.

Early geological studies in North America and Europe suggested four historical glaciations based on sequences of glacial till interbedded with highly weathered soils which take long periods of interglacial time to properly form. However the chronology of the earlier events was hard to pinpoint given the range of ^{14}C dating (around 50,000 years). It is extremely fortunate then, that from the viewpoint of the paleoclimate community, that the LGM lies right within the range of such ^{14}C dating (Flint 1971; Crowley 1983; cf. Peltier, 1994).

Early estimates of Pleistocene SSTs relied on transfer functions to determine the response of plankton populations to certain marine parameters. Imbrie and Kipp (1971) for instance, did a factor analysis of core-top samples (simply put, this is the top most portion of a marine sediment section which has been recovered in a cylindrical hollow core which was pressed into marine sediments) to determine how species react to ecological parameters such as sea surface temperature. In this, species from 61 core-tops were mapped into geographic assemblages varying in response to an ecological gradient – the maximum complexity of which will result in each individual species to be mapped to its own monospecific assemblage. Species that react dependently to another species (to the same ecological gradient) would ideally be marked within an "assemblage" (cf. Imbrie and Kipp, 1971 Fig. 3). Consequently assemblages could have different degrees of complexity, resulting in one or more species of plankton at each locality. Using this analysis on modern samples, and assuming that plankton biological behaviour has remained relatively unchanged within the Pleistocene (i.e. a species would react to marine forcing today, just as it did in the past), the analysis was directed onto a marine core in the Caribbean for a quantitative paleoclimatological analysis for the first time, in respect to changes in SST over time (cf. McIntyre, 1971; Imbrie and Kipp, 1971 Fig. 32). Results suggested that the extreme fluctuation of average temperatures of the Caribbean surface waters was on the order of 5°C over the Pleistocene.

The Climate: Long Range Investigation, Mapping, and Prediction Project:

It is generally understood that the accuracy of the SST field within a climate model is directly related to the quality of the simulation itself (cf. Crowley, 1997; Toracinta et al., 2004). A vast amount of data and knowledge on the LGM already existed before a comprehensive assessment of ice age SSTs was even possible, let alone integrated into complicated climate models. Yet, it probably wasn't until the "Climate: Long Range Investigation, Mapping, and Prediction" (CLIMAP) project that a comprehensive assessment of the LGM surface was completed (CLIMAP, 1976; 1981). Using a large array of geological criteria, a picture of the ice age earth emerged that was vastly different than today. Pollen, snow line and glacial sediment records showed that vegetation shifted towards more desert regions, grasslands, steppes and outwash plains, in part due to a large decrease in eustatic sea level as water became locked in terrestrial ice sheets, exposing more of the continents. This expanse was synchronous with a decrease of overall forest cover and slightly increased global albedo, or reflectivity, over regions not already covered by ice (cf. Crowley and Baum, 1997).

However, it is the CLIMAP sea surface temperature (SST) reconstruction which has served both as a fundamental component to boundary conditions of general circulation models (GCMs) even to this day, and as a basis for considerable debate for over three decades. In this, CLIMAP estimated that the global ocean on average varied from modern SSTs by about -2.3°C (CLIMAP, 1976, 1981). Yet, it is their suggestion that tropical, low latitude SSTs varied only by about -1.5°C, with some cases less than -1°C (e.g. the northern hemisphere Indian Ocean only varied by about -0.8°C in this reconstruction) that has been argued to be underestimated (cf. Fig. 2).

The idea that CLIMAP's LGM cooling estimate may have been underestimated may have started with Emiliani (1971) when he observed faunal variations, and a morphological shift in a species of foraminifera (*Globigerinoides ruber*) at the Pleistocene boundary. Such shifts are generally associated with large changes in a species environment. In addition, oxygen isotope compositions of the shell walls of the foraminifera were used to estimate the magnitude of cooling of the Pleistocene.

During the glacial, he suggested that 5°C for the tropical Atlantic and 4°C for the equatorial Pacific should have occurred (Emiliani, 1971).

Rind and Peteet (1985) ran a simple GCM simulation using the boundary conditions outlined in CLIMAP. After obtaining six model years worth of data, the GCM was unable to produce as much cooling as geological data suggested. By lowering the original CLIMAP estimates by a further 2°C, they were able to get a better proxy agreement, and an overall LGM cooling of 5°-6°C, in line with Emiliani's approximation. Further evidence arose in the early 1990's with Stute et al., (1992; 1995) and their analysis of noble gas concentrations in tropical ^{14}C dated ground water sites. These gases are exchanged with soil air and the concentrations of which are primarily associated with temperature right at the water table. Analysis of numerous tropical and mid-latitude localities (cf. Stute et al., 1995) suggests an LGM cooling of around 5°C with a 5.4°C in the 40°N to 40°S Americas sector. This is argued to require cooler SSTs than the original CLIMAP estimate, and implies greater mid-latitude CO_2 climate sensitivity – something of serious importance given the current predictions for future emissions. Other studies have also indicated that the CLIMAP SSTs should be reconsidered (Anderson et al., 1989; Guilderson et al., 1994; Beck et al., 1992, 1997; Broecker, 1997; Lee and Slowey, 1999; Crowley, 2000; Toracinta et al., 2004; cf. Ballantyne et al., 2005; cf. Langen and Vinther, 2009).

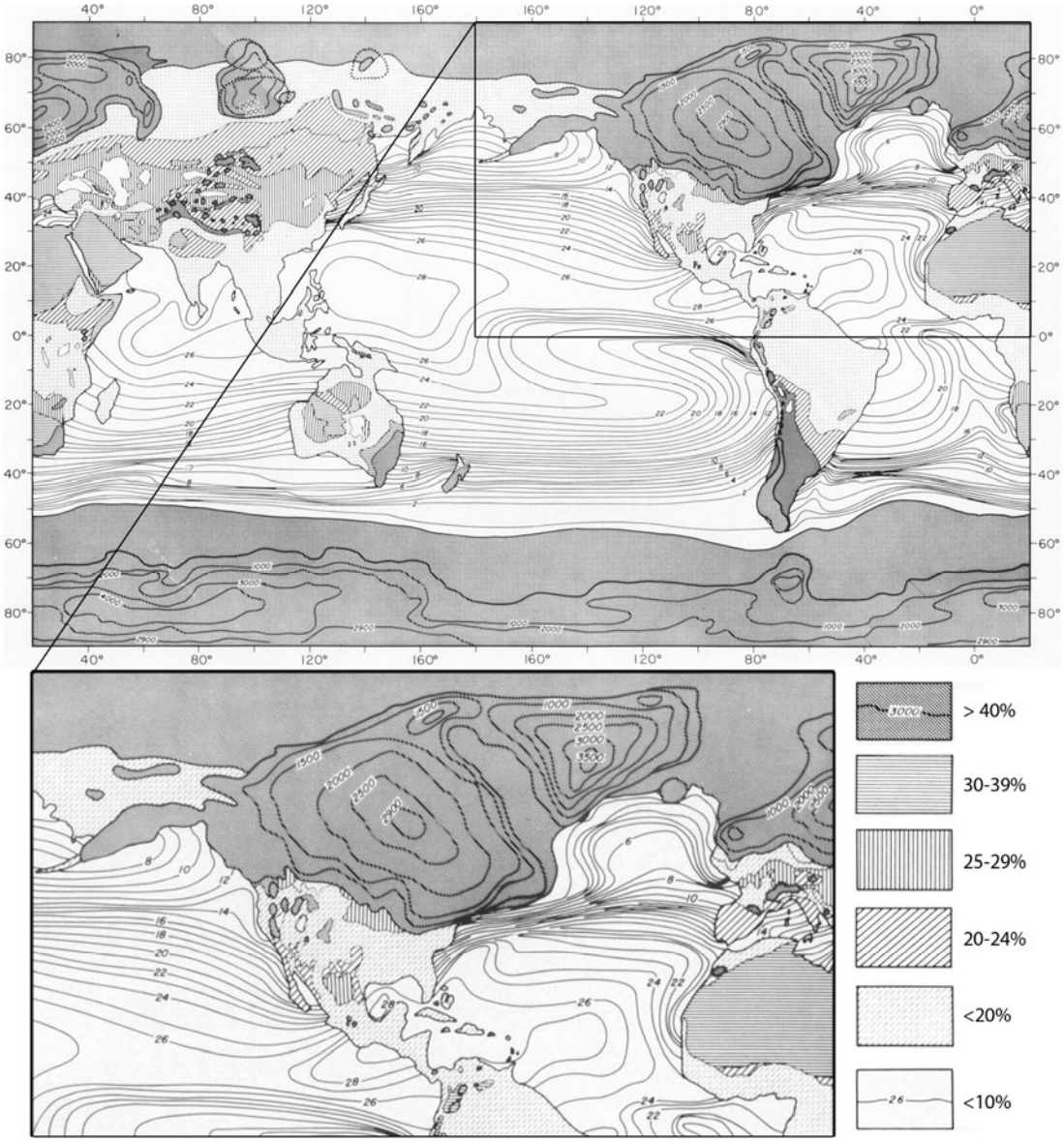

Figure 2.1: The original CLIMAP surface of the ice age earth reconstruction with sea surface temperatures, ice extent, ice sheet elevation, and continental albedo for the Northern Hemisphere summer (modified from CLIMAP, 1976). Magnified region is taken from 0°N-90°N to 40°E-180°W and shows the Laurentide and western edge of the Fennoscandian ice sheets as well as the North and equatorial Atlantic. Percentages represent albedo. Albedo over 40% represents snow and ice with contours representing elevation above sea level in metres.

Reconciling the CLIMAP SST Reconstruction with Recent Estimates:

There are numerous reasons why reconciling the magnitude of LGM SST cooling is important, especially in regards to the CLIMAP reconstruction. These include, but

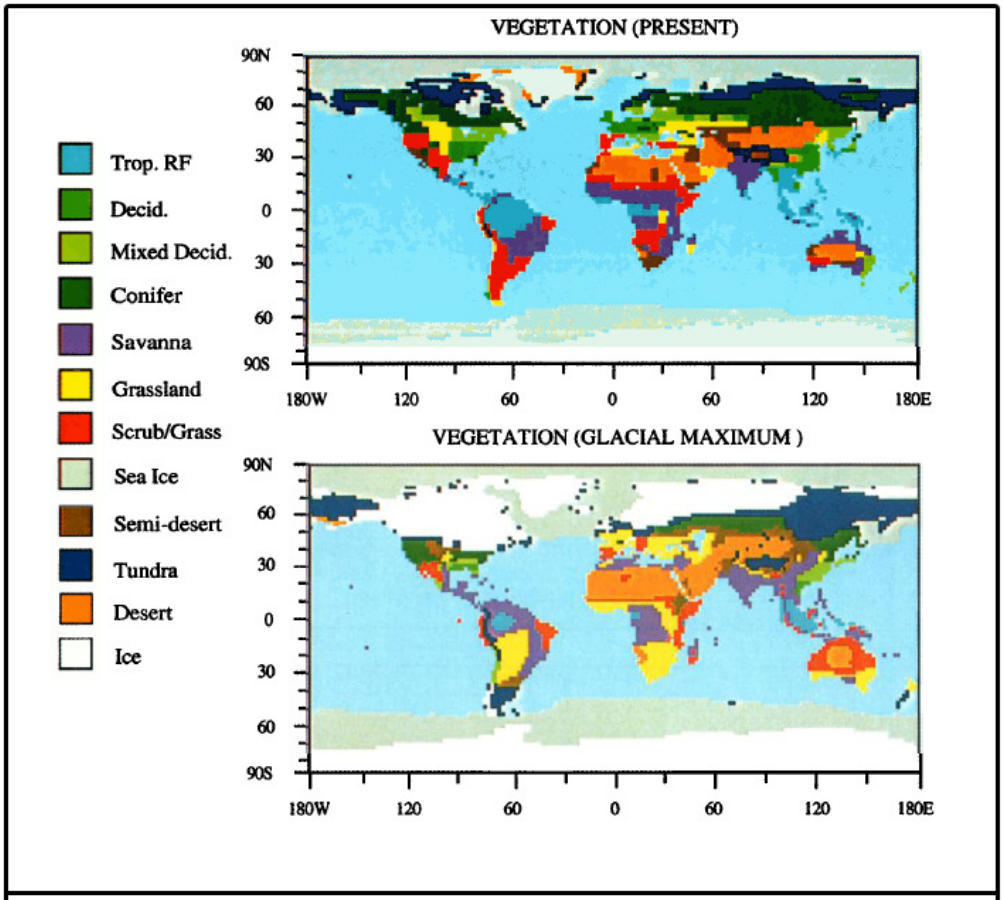
VEGETATION (PRESENT)
Trop. RF
Decid.
Mixed Decid.
Conifer
Savanna
Grassland
Scrub/Grass
Sea Ice
Semi-desert
Tundra
Desert
Ice
90N
60
30
0
30
60
90S
180W
120
60
0
60
120
180E
VEGETATION (GLACIAL MAXIMUM)

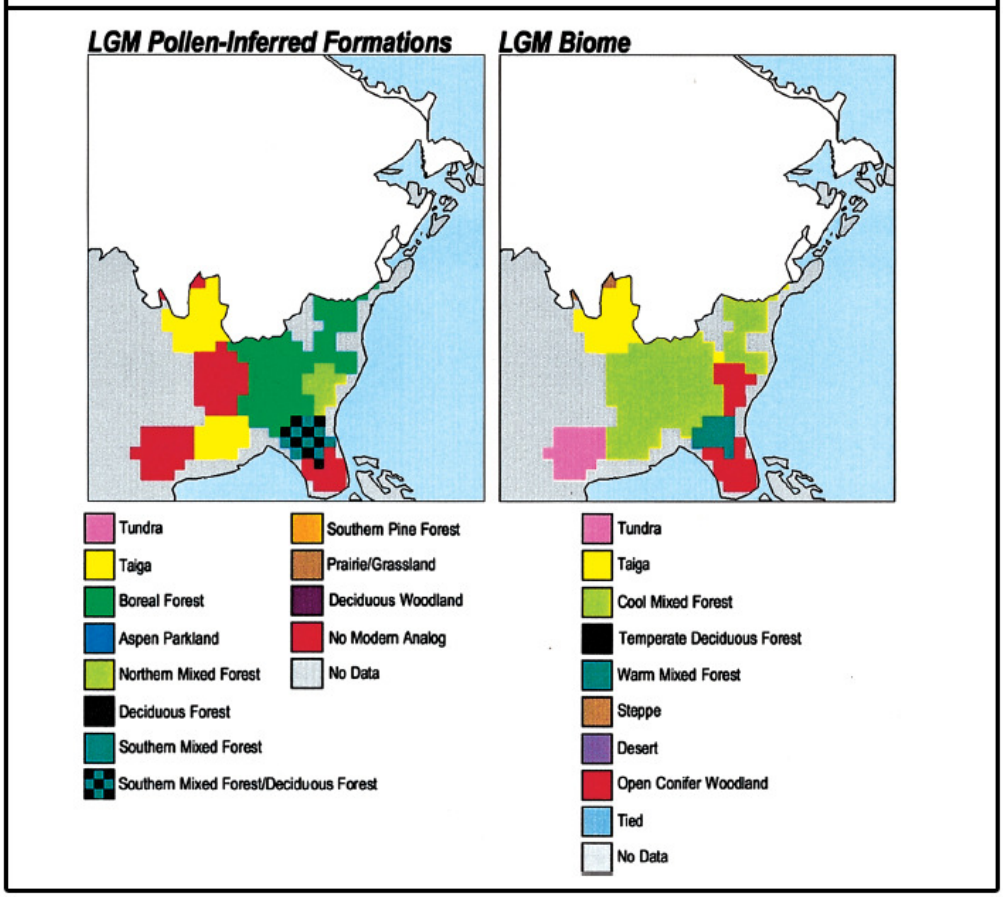
LGM Pollen-Inferred Formations
LGM Biome
Tundra
Taiga
Boreal Forest
Aspen Parkland
Northern Mixed Forest
Deciduous Forest
Southern Mixed Forest
Southern Mixed Forest/Deciduous Forest
Southern Pine Forest
Prairie/Grassland
Deciduous Woodland
No Modern Analog
No Data
Tundra
Taiga
Cool Mixed Forest
Temperate Deciduous Forest
Warm Mixed Forest
Steppe
Desert
Open Conifer Woodland
Tied
No Data

Figure 2.2: A global LGM vegetation reconstruction and comparison to present (from Crowley and Baum, 1997) and the analogue reconstruction from Jackson et al. (2000) for eastern North America below the ice sheet margin (from Jackson et al., 2000).

are not limited to: (1) The CLIMAP reconstruction, both the original values and slight modifications of such, have been used as SST paleoclimate GCM boundary conditions for over 30 years – and are still used today. It is important therefore to understand the results of such simulations, given the knowledge that the SST boundary condition effects integration results as the temperature of the sea surface will effect ocean-atmosphere interactions and subsequently temperatures over land; (2) Resolving the level of cooling during the LGM has serious implications for understanding the sensitivity of the climate system to reduced (and increased) greenhouse gasses, such as CO_2. A larger degree of cooling, one not originally supplied by CLIMAP, implies greater sensitivity to fluctuations in CO_2. If estimates of ~5°C were to be correct, climate sensitivity would be rather high, on the order of 4.5°C to a doubling of CO_2. This is twice that of the original CLIMAP estimate (Crowley, 1994, 2000).

Crowley (2000) revisited the CLIMAP reconstruction in order to resolve the potential LGM SST underestimation. Each line of evidence for a 5°C tropical cooling was re-examined for validity, including the positives and negatives of using specific proxy data. In one instance, the argument for a tropical cooling on the order of 5°C doesn't seem logical given the physical stability of tropical plankton populations. Although changes do occur in certain tropical species (cf. Emiliani, 1971), as well as within characteristics of tropical populations, large scale populations are relatively stable during the peak of the ice age, which one wouldn't expect if a 5°C cooling occurred. The same is true for tropical corals with about only 5% of corals adapted well enough to sustain a population given such a drop in surface temperature (cf. Crowley, 2000, Fig. 5). Additionally, caution is needed when drawing conclusions with terrestrial pollen data (as well as upper tree line records). Pollen data can be used to estimate temperatures over land, as was done with foraminifera over the ocean in CLIMAP. Although there were wide scale changes in terrestrial plant populations, including those within the tropics, these

changes may not necessarily reflect a 5°C surface cooling. This is because terrestrial plants may be just as susceptible to glacial CO_2 changes as they are to shifts in surface temperatures. In fact, large scale changes in plant populations could have occurred solely due to the large decrease in atmospheric CO_2 and not necessarily at all related to temperature (cf. Hostetler and Clark, 2000). For instance, a move to higher populations of C4 plants (cf. Crowley, 1995) which have a different carbon isotopic signature than C3 plants. C4 plants are better affiliated for ice age conditions than their C3 counterparts and could have proliferated during the LGM and were then subsequently deposited back into the marine record during the interglacial. Consequently, changes in low elevation plant populations may not be directly and exclusively attributed to a massive decrease in tropical surface temperatures.

Even though the momentum to reconsider the CLIMAP SST reconstruction in the tropics had been mounting since the 70's, the meta-analysis of Ballantyne et al., (2005) was the first comprehensive assessment of different proxy measurements and their relation to the CLIMAP reconstruction. Different proxies understandably have different errors associated with them, such as alkenone measurements and their unsaturation index, or pollen data and the relation to CO_2 as mentioned previously. Consequently, a better representation of the true mean would be acquired if the errors associated with each measurement are weighed. Taking this into account, the meta-analysis estimated an LGM mean tropical sea surface temperature cooling of -2.7 ± 0.5°C and a terrestrial surface air temperature (SAT) cooling of -5.4 ± 0.3°C (Ballantyne et al., 2005). Although the meta-analysis estimate for the Atlantic is within the (relatively large) uncertainty of CLIMAP (-2.6 ± 1.9°C), the Pacific is cooler than the original estimate. Nonetheless, as the Pacific only decreased further on the order of a degree, lends credence to the equatorial Atlantic being colder than the equatorial Pacific during the LGM. Furthermore, the fact that terrestrial proxies (such as pollen) persistently arrive at cooler temperatures continues to suggest that the LGM land environment was indeed colder. Several proxies from the Andes for instance continually arrive at a cooling of 6°-7°C (cf. Crowley, 2000; Ballantyne et al., 2005). However, the Ballantyne et al. (2005) estimate of a tropical cooling of -2.7 ± 0.5°C is a more intermediate conclusion of the proposed -5°C that has been

continually argued (cf. Emiliani, 1971). Consequently, a uniform lowering of CLIMAP temperatures of about 1°C would better agree with more recent estimates (cf. Chapter 3).

***

The Multiproxy Approach for the Reconstruction of the Glacial Ocean Surface project (MARGO) was an attempt to do a rigorous re-synthesis of sea surface temperatures during the LGM (MARGO, 2009; which began with Kucera et al., 2005). The primary objective was to compile and analyze en-mass, estimates of LGM sea surface temperature based on microfossil and geochemical paleothermometers – in an attempt to correct the apparent shortcomings of the CLIMAP project. Using multiple proxies, the MARGO approach argued that no single proxy method is objectively better than any other and thus a multiproxy method reduces bias in the interpretation of LGM SSTs (see also Ballantyne et al., 2005). By setting a defined chronological window for the LGM (19-23 kya) several records used historically were discarded. A total of 696 different SST reconstructions were integrated into the MARGO analysis. Due to the differences in record density in individual ocean basins (cf. MARGO, 2009 Fig. 1), the data was projected onto a regular 5°x5° with each grid box being assigned a separate SST estimate based on the proxies contained within that grid. Results suggest 90°S-90°N mean temperature anomalies of -2.4°C +- 2.2°C (annual) and -2.7°C +-2.4°C (January-February-March) for the Atlantic, -1.5°C +- 1.8°C (annual) and -1.5°C +- 2.1°C (JFM) for the Pacific. For the tropical band, 15°S-15°N, mean temperature anomalies were reconstructed to -2.9°C +-1.3°C (annual) and -2.5°C +- 1.7°C (JFM) for the Atlantic and -1.2°C +- 1.1°C (annual) and -1.2°C +- 1.7°C (JFM) for the Pacific. The colder Atlantic compared to the Pacific was also suggested by CLIMAP. The large uncertainties associated with the basin-wide averages are presumably caused by the density of regions not covered by some proxies which, as MARGO (2009) point out, highlights the problem of extrapolating single LGM SST reconstructions to global estimates. The best convergence in regards to the smallest range of estimates for a single latitude-band occurs in the 30°S-30°N strip. The higher latitudes, going into

the Nordic Seas, experience the largest uncertainties partially due to the interpretation of microfossil evidence (cf. MARGO, 2009 Fig. 3). Like CLIMAP, the strongest annual mean cooling (in some areas above -10°C) occurred in the mid-latitude North Atlantic reaching towards the western Mediterranean (cf. MARGO, 2009 Fig. 2). The cooling in MARGO however was more pronounced in the eastern than the western portion of the basin. Noticeably however, in regards to the mean estimates and errors associated with each latitude-band (cf. MARGO, 2009 Table 1), the MARGO tropical SST estimates are not *that* different than those proposed by the original CLIMAP reconstruction (see CLIMAP discussion above). CLIMAP even suggested that the northern and southern subtropical gyres may have been slightly warmer (~1-2°C) than today, which is also supported by a few points in the MARGO estimates. Given the MARGO findings, the suggested remedy of the CLIMAP SSTs by Ballantyne et al., (2005; see also Crowley, 2000) is quite reasonable in regards to integrating into model experiments.

The Northern Hemisphere Continental Ice Sheets:

The majority of GCM's used to simulate conditions from the LGM to the present have used CLIMAP or modified CLIMAP boundary conditions. Although the extent of surface cooling and the CLIMAP SST reconstruction have all been mostly reconciled (see above), it is the paleotopography and ice sheet reconstruction which is recognized to be by far, the most poorly constrained (cf. Denton and Hughes, 1981; Peltier, 1994; Peltier, 2004). Margins of the ice sheets have been for the most part, geologically documented, however it is the thickness, elevation, and subsequent mass load which is still under consideration. Geological results show that the sheer size of the ice sheets would have been a considerable obstacle for northern hemispheric westerly flow, and would have greatly perturbed atmospheric dynamics through simple mechanical forcing, similar to large scale mountain ranges today. Consequently, as the quality of a simulation is primarily determined by the accuracy of its boundary conditions, it is necessary to explore the various ice sheet reconstructions for the LGM.

CLIMAP reconstructed ice cover over land which was supplemented by geological field work and is shown in Fig. 2.1 for the Northern Hemisphere summer. In this reconstruction, the massive Laurentide Ice Sheet, situated over North America, extended down towards 40°N, covering parts of New England, Maine, and the Great Lakes. Its dome was ~ 3km metres in elevation near Hudson Bay, Canada (58°N, 90°W). Interestingly, Canada was completely covered by the ice sheet, but parts of Alaska remained ice free – a fascinating result given the northerly latitudes of Alaska, and a result that will be discussed in detail in later sections. Additionally, CLIMAP estimated that ice over the Greenland dome reached elevations of around ~3.5 km above sea level (74°N, 40°W), while the Fennoscandian Ice Sheet covered Europe with an estimated ~3 km metres of ice, and a pocket over Northern Siberia had another ~2.5-3 km of elevation (cf. Fig. 2.2; CLIMAP, 1976; Gates, 1976).

Before CLIMAP, ~130 metres of eustatic sea level was presumably thought to have been transferred from the oceans to the continental ice sheets (Curray et al., 1965). CLIMAP however, estimated sea level to have dropped only ~85 m based on terraces and undated wave-cut notches located in the Caribbean Sea. Although this is at variance with more recent reconstructions of ~120 m (Peltier, 1994; Peltier, 2004), it would have little effect on GCMs in the 1970's and 1980's with global resolutions on the order of 250-500 km.

Other early estimates suggested two alternative reconstructions to the CLIMAP data (Denton and Hughes, 1981). These two reconstructions attempted to provide minimum and maximum bounds to the LGM continental ice sheets based on ice volumes, in association with a change in eustatic sea level. The maximum reconstruction was based on 163 metres of global sea level change, while the minimum was attributed to 127 metres of sea level. Both of these, as suggested by Peltier (1994, 2004), are still overestimated, with the maximum reconstruction being too excessive by ~55%. This is primarily based on the fact that the ice volume peak in the LGM only occupied that state for about 5,000 years which wouldn't be the case in a more steady-state system as suggested by Denton and Hughes (1981) and the CLIMAP reconstruction. The change in this reconstruction, and consequently the

ice sheet boundary condition of GCMs, would drastically affect climate results such as storm tracks (cf. Peltier, 1994) simply due to the differences in mechanical forcing of the modified ice sheets on atmospheric flow.

The ICE-4G reconstruction of Peltier (1994) is a ice sheet reconstruction that estimates the magnitude of LGM ice sheets based on 400 geological relative sea level history points (RSL), such as exposed or submerged terraces or shore line indicators, and terrestrial areas where land is still responding from ice sheet mass loading (Peltier, 1994). These terraces are one of the best geological records of the distribution of the LGM ice sheets (and subsequently the redistribution of mass on the Earth's surface) as they can be accurately dated within the range of ^{14}C, and with U-Th on preserved shallow water corals. Although many of the RSL data points are confined to the postglacial period and within the Holocene, some go further back in time. Taking into account postglacial rebound rates, mantle viscosity, and an ocean function based on eustatic sea level, the ICE-4G theory shows that enough ocean water is redistributed onto land masses such that three large land bridges became exposed at 21 ka: (1) the Bearing Sea between Alaska and East Asia; (2) the eastern English Channel between Britain and France; (3) the Arafura Sea region between Australia and New Guinea. Large areas of continental margin are also exposed around eastern North, Central and South America, Eastern Asia, and Indonesia. The maximum thickness of the Laurentide and Fennoscandian ice sheets is reconstructed to be 3 km and is approximately 1.5 km shorter than the maximum CLIMAP estimate (Peltier, 1994). The area of maximum thickness on the Laurentide is The Keewatin Dome just west of Hudson Bay, Canada. This thickness however, does not necessarily infer elevation above sea level, as isostatic depression of the Earth's crust needs to be taken into account.

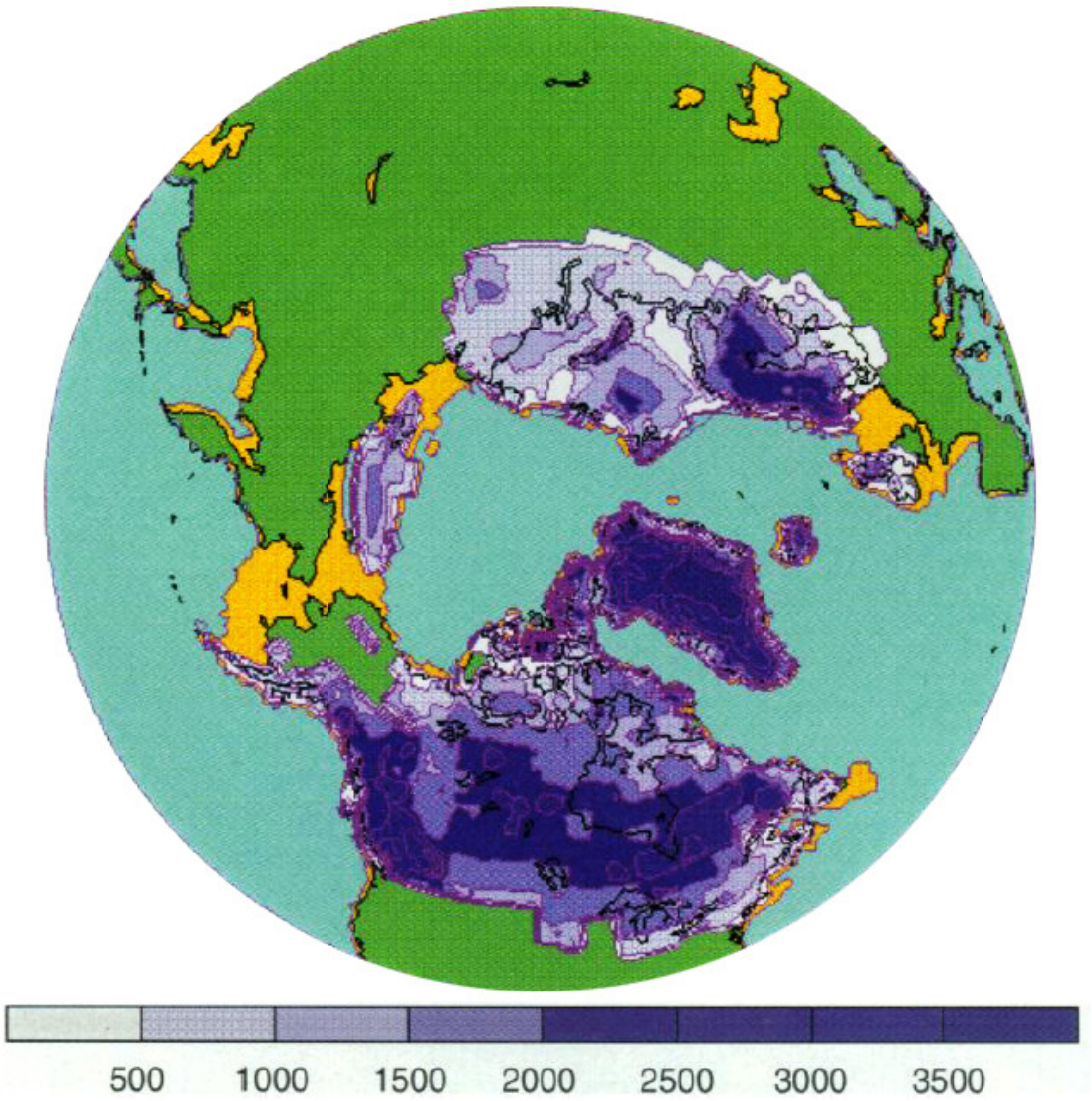

Figure 2.3: Reconstructed northern hemisphere ice topography (purple gradient in metres) and exposed land areas (orange) showing the Laurentide Ice Sheet over Canada and North America, and the Fennoscandian Ice Sheet over Northern Europe (taken from Peltier, 1994).

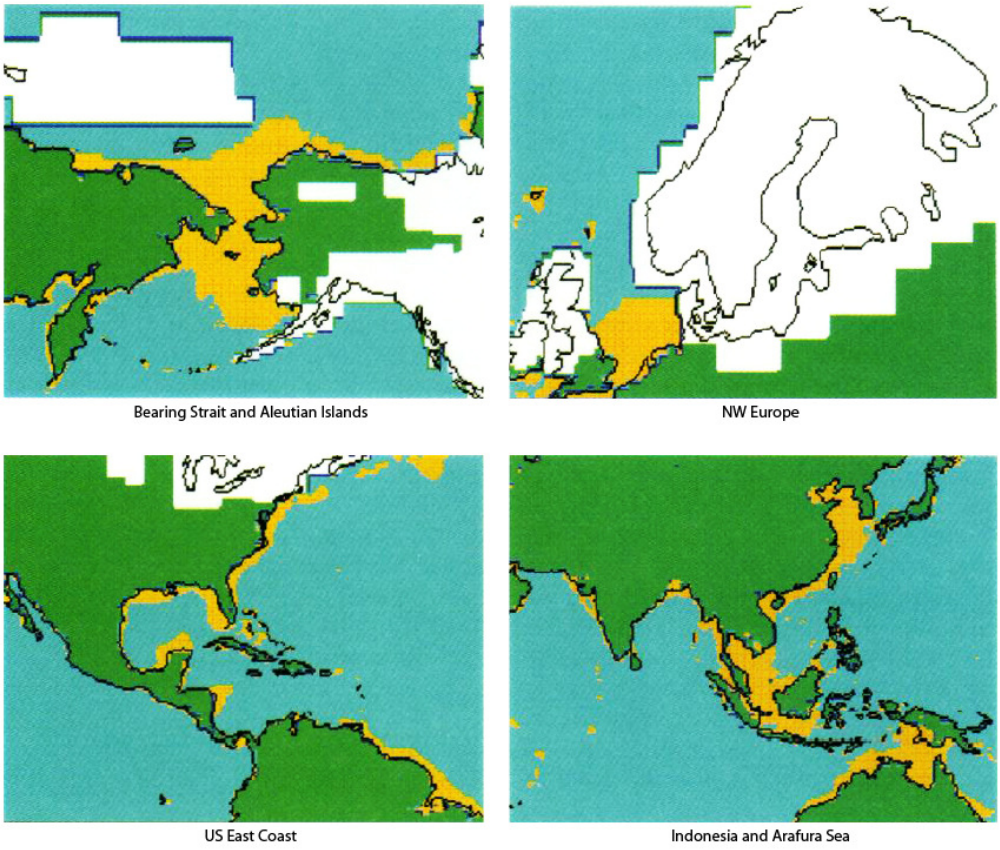

Figure 2.4: Magnified ICE-4G exposed land areas (orange) and nearby ice sheets (white) from the original ICE-4G theory (modified from Peltier, 1994)

Although there are several differences between the newer ICE-5G (Peltier, 2004) reconstruction and the earlier iterations of the theory, most involve the deglacial history of the ice sheets. The differences in the paleotopography of the LGM however, are critical given their common usage in paleo-GCM studies and deviations away from the CLIMAP estimate. One of the main differences between the ICE-4G and ICE-5G reconstructions results from a "flaw" based on the net amount of water added to the oceans during the marine isotope stage 2 (MOIS 2, LGM) to MOIS 1 (the Holocene) transition (glacial-interglacial melting). During the construction of ICE-4G the sole record for this transition involved a U-Th dated coral-based site from Barbados in the Caribbean Sea off the northeast coast of South America by Fairbanks (1989). The original ICE-4G reconstruction calculated a 105.3 metres in total eustatic sea level drop with later ICE-4G realizations dropping it even further (cf. Peltier, 2002). With data now available from the Sunda Shelf of Indonesia and

the J. Bonaparte Gulf of northern Australia (cf. Hanebuth et al., 2000; Yokoyama et al., 2000) this was dropped even further in ICE-5G to approximately 126 metres with an increased contribution from the Laurentide Ice Sheet over Canada, and a more extensive Keewatin Dome west of Hudson Bay. This is more similar to the 120 metres that is usually assumed (cf. Peltier, 2004). Further discussion on ICE-4G versus ICE-5G can be found in Chapter 3.

2.2 Climate Models:

General Circulation Models:

Climate models attempt to simulate the climate system based on a series of mathematical calculations on a "gridded interval". Models can be very simple ranging from basic one dimensional energy balance models (EBMs) concerned with radiative interactions at the Earth's surface and within the atmosphere, to three dimensional, time based general circulation models (GCMs) concerned with past or future climate change scenarios. They can focus over the entire globe in a global climate model, or over a specific region in a regional climate model. GCMs are an integral component to very sophisticated global climate models. Traditionally, they calculate a series of basic equations involving the conservation of momentum, mass, energy, and the ideal gas law. From there, a suite of variables are calculated from diagnostic equations including temperature, surface pressure and humidity. The number of calculations will be related to the dimensionality of the model itself, as well as the fineness of the "grid domain", or resolution (Fig. 2.5). However, it is important to remember that all models, both running past and future simulations, simplify natural dynamics regardless of boundary conditions or resolution. It is interesting to think then, that a "real" paleo-scenario potentially sits somewhere between what a model suggests and what the geology tells us.

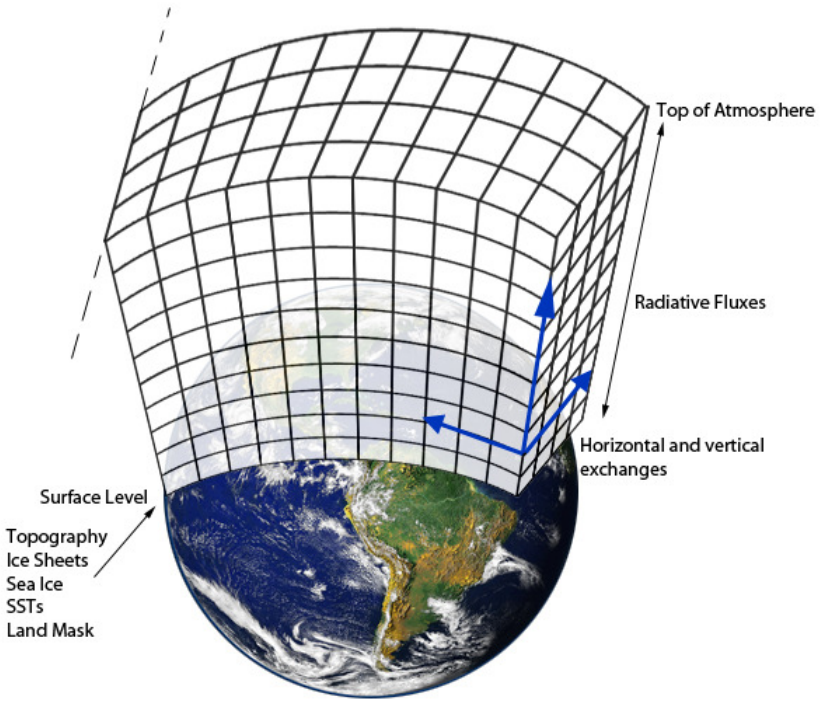

Figure 2.5: A simple graphical representation of a global GCM partial grid domain in three-dimensional space. Topography, ice sheets, sea ice, and SSTs are included along the surface as boundary conditions (see text). Grid boxes are, for visual purposes, increased to a scale much larger than current high resolution GCM capabilities. Earth image is a modified portion of the NASA Earth Observatory Blue Marble Project.

Natural processes range from centimetres in scale to the entire length of the planet, and consequently do not necessarily fit within a model domain. Some features in the natural system, such as the condensation of clouds and cloud microphysics, turbulence in the atmospheric boundary layers, interaction of flow on microtopography, or even small scale thunderstorms, are too fine for GCM grids to pick up. These features are subsequently simplified through parameterisation and generally can only be useful for first order effects and consequently insert a level of uncertainty in all models. Even extraordinarily high resolution models, with very fine grid spacing, should still be considered as a simplification of the natural system as each grid box is still representative of a mean over that defined area. The more grid boxes a model contains, the more calculations need to be done, the higher the detail of surface orography, and the higher the resolution it is said to have. The downside to

this however, is that as resolution increases, so does the necessary computing time. Consequently, the resolution chosen in any given study is mainly determined by the aim and scope of the research and the available computing resources. The impacts of resolution on results will be discussed in the next section.

For global models, the simplest way to overlap the latitude-longitude grid is through a basic finite difference method where a fixed grid interval is spread over the entire globe. Issues arise with this method as you converge towards the poles. Gaussian grid spaces can also be used which solves this issue by fixing distances along a dimension. A reduced Gaussian grid permits an increase in the longitudinal direction as poles are approached to allow for a more constant longitudinal spacing between grid points. It is interesting to point out that this works because the Earth's atmosphere is naturally almost spherical. Other variants of "gridding" methods are also available including using different grid spacing for the different areas of coupled models (e.g. the ocean) and modified spaces using spherical harmonics.

All atmospheric GCMs (AGCMs) require input data to form their boundary conditions. Commonly, these are observations or measurements of the climate system such as sea surface temperature. For past climates, geological data, rather than observations, are used to construct boundary conditions for the desired time period. Quite often, global GCM output is used as the boundary conditions, or starting conditions, for higher spatial resolution regional climate models to better understand regional dynamics. GCMs generally require users to designate features such as orbital and solar parameters, surface topography, and some properties of exposed land masses. Sophisticated AGCMs require inputs from everything not already stated in the model itself. This ranges from the topography of continental ice sheets, sea ice boundaries, atmospheric CO_2 concentration, and other land and vegetation parameters. Some models use an atmospheric component, coupled to another model such as a land or ocean model. These would require further boundary conditions such as ocean bathymetry.

Spatial Resolution Effects in Climate Models:

A first pass assessment of the effect model resolution on surface results was done in Unterman (2007) and was continued in Kim et al., (2008). This used a global GCM known as the Community Climate Model (defined further in Chapter 3). LGM-Modern mean annual surface temperature was compared at both T170 and T42 resolution to four sites of noble gas concentrations in glacial groundwater (cf. Crowley and Baum, 1997; Unterman et al., 2007; Kim et al., 2008). The geological data compares in detail to that of the T170 simulation while the T42 run differs by up to 3°C especially in the northeast United States around Maryland (39.0°N, 76.0°W) and in Georgia (33.0°N, 83.0°W). This is caused by different levels of surface accuracy around the Appalachian Mountains. Isotherms in the T42 integration run orthogonal to the axis of the mountains while the T170 isotherms curve northward along the axis resulting in better proxy agreement. The same is true for precipitation in the Indian monsoon region around the Ganges Plain in summer. The area of maximum rainfall in the T170 simulation is south of the Tibetan plateau margin along the plain, while results in the T42 integration again runs orthogonal to the mountain range, the highest on the planet. A smaller mountain range, along the eastern side of India, known as the Eastern Ghats, is visible in the T170 simulation, in terms of reflection in the precipitation field, while it is fully absent in the T42 run – an important regional result considering the known importance of a slightly cooler climate and higher precipitation to vital crops in the east (cf. Unterman et al., 2007; Kim et al., 2008).

The same four noble gas points from Unterman (2007) were integrated into a more detailed, 51 point, geological comparison in Kim et al. (2008) outlining the differences in T170 surface temperature, T42 surface temperature, and their comparisons to several geological observations (cf. Chapter 3). The T170 compares to all noble gas concentrations alone, by only disagreeing up to 0.77°C on average, while the average difference is 1.28°C when compared to the T42 integration. Taking into account all proxies, including pollen measurements with large degrees of variance, the T170 simulation is on average 1.97°C different than the geological data

and the T42 is 2.40°C different. Although each point should be considered on its own, it is clear that the T170 more resembles the geological observations due to its better representation of orography at the regional scale.

Although the effect of resolution on surface temperature and regional rainfall (cf. Jost et al., 2005) is understandable given the forcing of topography on these fields, the sensitivity of spatial resolution on cyclogenesis and storm life cycles may not be as clear. The impact of spatial resolution on storm track results was first comprehensively analysed in a multi model ensemble run of Kageyama et al. (1999). This compared modern model results to the ERA40 reanalysis data set and to LGM simulations using the CLIMAP SST reconstruction as well as simulations with computed SSTs. In all cases LGM storm tracks were forced eastward by the LGM boundary conditions. Yet the intensity and spatial distributions varied in all models. In all models, storm tracks and their amplitude and eastward extensions are better represented in the higher resolution runs (Kageyama et al., 1999). The lower resolution runs often have much shorter tracks. For example, in some of the lower resolution integrations, the magnitude of the Pacific storm track maximum is much smaller and situated nearly 20° too far west (from around 180° to 160°E in the present day run). Furthermore, the lower resolution runs fail to produce any transient eddy activity in the modern eastern Pacific or over the American continent. The intensity of the cyclones is also generally weaker. Consequently, a different conclusion may be drawn simply from changing the spatial resolution. That is, that the weaker eddies in the lower resolution runs only have a weak impact on the mean flow (Kageyama et al., 1999). One might infer the same for the LGM storm track integrations. It is interesting to note that although Kageyama et al. (1999) recognize stronger baroclinicity off the east coast of the continents, they make it clear that this does not necessarily imply stronger eddies.

Similar to the Kageyama (1999) experiment, the Bengtsson et al. (2009) study analyzed the ECHAM5/OM results of Bengtsson et al., (2006) at T63 resolution, and compared them with both the ERA40 T159 data and a newer T213 (63 km on a grid box side) ECHAM5 atmospheric simulation. This was to determine the effect of

resolution on storm track results for future climate projections using the IPCC AIB emission scenario (the middle of the road scenario where there is a globally technologically advanced world with mixed energy sources from both fossil fuel and non-fossil fuel based resources). Although this simulation is for the future, understanding the impact of resolution on storm track results and their associated levels of precipitation and wind speed, is vital to synoptic scale simulations of past climate extremes, such as the one presented here. This is especially for the case over Greenland where the positions of the North Atlantic and North Pacific storm tracks determine flow and moisture sources to the Greenland Ice Sheet, which impact the $\delta^{18}O$ isotope record (and its validation) preserved in the ice (cf. Charles et al., 1994; Fawcett et al., 1997; Langen and Vinther, 2009).

The Bengtsson et al., (2006) T63 ECHAM simulation described in the 2009 project was integrated for a 30 year period from 2070-2099 following the AIB scenario, and used a control from 1960-1989. The higher resolution T213 simulation was integrated for 2069-2100 and used a control run from 1959-1990. Extremes of pressure, vorticity, wind and precipitation associated with simulated cyclones are investigated for both the higher and lower resolution runs for the northern hemisphere winter (DJF) with a 6-hourly output.

It has been suggested that during a warming climate, increased SSTs in the mid to high latitudes may intensify extra-tropical cyclones. Yet this has been of recent debate as increased warming in higher latitudes, and therefore a reduction in meridional SST gradients, may inhibit cyclogenesis. During the LGM however, temperature gradients are stronger and narrower than today as mid to high latitude SSTs are cooler, with the NH dominated by a southward migration of the North Atlantic sea ice, and massive NH ice sheets. Consequently, it is also important to understand cyclogenic changes given shifts in SST gradients, and its relation to model resolution.

The number of storms in the T63 compared to the T213 resolution simulation is approximately the same. However, the lower resolution simulation was unable to

accurately represent extremes of precipitation and wind. The mean intensity of cyclones in the higher resolution is much different than that in the lower resolution run. The minimum mean sea level pressure (MSLP) anomaly in the T213 is lower and the distribution of intensity in vorticity is much more broad with a peak intensity almost twice that of T63. This is attributed to the fact that the T213 resolution integration can accurately simulate cyclones within a whole range of intensities. This is also the case in the North Atlantic where the steep orography over Greenland and its impact on synoptic scale systems is more defined in the higher resolution case (cf. Moore and Renfrew, 2005; Bengtsson et al., 2009). Therefore, although both simulations calculate a similar number of cyclones, the range of intensities is quite different and more defined in the higher resolution run. This is further demonstrated in the fact that the ERA-40 T159 data set is an intermediate between the two simulations, while the higher resolution ERA-Interim data has a greater intensity distribution than that of the ERA40 (cf. Kageyama et al., 1999).

Another test of resolution on storm track characteristics was done in 2000 by Blender and Schubert. Similar to that of Kim et al., (2008) and Bengtsson et al., (2009), Blender and Schubert used a high resolution (T106 2-hourly) data set and compared it to lower resolution variants. Specifically, they mapped the T106 data to a variety of spatial resolutions including T86, T64, T42, and T21, to determine what tracks are missing (or present) in the integrations compared to the T106 reference set.

Using a 2-hour time interval, the number of mapped tracks increased with increased spatial resolution. At T21 an average 13.1 tracks are identified after each time step, while at T106 (the reference set) an average of 28.0 tracks are identified. The probability of any track in the T21 case being present in the higher resolution reference set (P_a) is 75%, at T42 it is 83% and increases to 91% in a T84 scenario. In terms of the ratio of missing tracks (r_m), the T84 case has a 0.30 ratio of tracks missing in the test set, but present in the reference data. This dramatically increases to 0.48 in the T42 case, and up to 0.95 in the T21 scenario (cf. Blender and Schubert, 2000). This is because at smaller spatial resolutions, fewer cyclones are tracked and consequently would also have a shorter range of intensities. However, the ones that

are tracked are generally correct (high P_a). The discrepancy between the increased storms with increased resolution between Blender and Schubert (2000) and Bengtsson et al., (2009) is that there is a dependence on the method of identification. Depending on the automatic tracking algorithm, smaller scale storms can be identified at increased resolution, and absent at lower ones. Further caveats regarding automated tracking methods can be found in Blender and Schubert (2000).

Effects of Spatial Resolution Summary:

Firstly, although spatial resolution may only affect cyclone counts when using specific identification methods, the effect on storm intensity and extremes in precipitation and wind speed is large. The simulated intensities in Bengtsson et al., (2009) were almost twice as large as those at T63. At higher resolutions, storms are simply simulated with greater realism including their structure and lifecycle, such as at the beginning and end of their lifetime when they are weaker and smaller.

Secondly, extra-tropical cyclones are heavily dependent on meridional temperature and SST gradients, and the southward migration of wintertime sea ice, at least in the North Atlantic. This is of considerable importance during climate extremes such as foreseeable changes in the future, or even the LGM, when temperature gradients were much more narrow and steeper than today, with the higher latitudes dominated by the massive Laurentide and Fennoscandian ice sheets, and a sea ice edge that was forced much further south (potentially up to 42°N). Consequently, understanding and describing the intricate details throughout the full lifetime of a cyclone (from genesis to terminus, or lysis region), and capturing the full range of intensities and extremes is necessary for a synoptic scale LGM study, and requires high spatial resolution outputs (cf. Kageyama et al., 1999; Blender and Schubert 2000; Kim et al., 2008; Bengtsson et al., 2009).

Temporal Resolution Effects:

As computing resources become more readily available, a question arises on what potential positive and negative effects increased temporal resolution has on climate results, if any. Blender and Schubert (2000) also compared the effects of changing temporal resolution on the accuracy of storm tracks and individual cyclones. Here, a T42 simulation at a 2-hourly interval was used as the reference set to compare to 4-hourly, 6-hourly, 12-hourly, 18-hourly, and 24-hourly data sets. The probability of correct tracks only decreases by 6% at 4-hourly to 0.94 but to 0.73 at 12-hourly, 0.54 at 18-hourly and even to 0.45 at 24-hourly (Blender and Schubert, 2000). Although this can be partially attributed to ones choice of identification algorithms through a cyclones 'minimum' lifetime parameter, the decrease in correct tracks is large as you approach lower resolutions such as daily time scales – a temporal threshold common in many modern GCM studies.

Another aspect of increased temporal resolution that needs to be considered is the effect it has on extreme events, and responses that react to rapid shifts in fields such as wind speed (event driven responses). An example of this is wind driven sea ice and its impact on ocean-atmosphere CO_2 exchange, and biological productivity.

Past fluctuations in CO_2 and hence surface temperature have been primarily attributed to ocean processes such as the ventilation of CO_2 from the deep ocean to the atmosphere (Skinner et al., 2010; Geibert et al., 2010). The Weddell Gyre in the Southern Ocean (SO) is the world's largest deep ocean-atmospheric boundary where such an exchange takes place. Modifications of this region therefore, both physical and biological, could drastically effect global carbon sequestration (both in the past and present), and the way it is preserved in the climate proxy record.

Both physical and biological processes in the Weddell are intimately linked to surface flow including the extremes and rapid shifts of wind speed. Sea ice is wind driven in the southern ocean (Giebert et al., 2010). As a result, ice bergs that have become embedded in a sea ice drift are also wind driven, both of which are enriched in iron, the major biological limiting nutrient in the region. As sea ice is forced into the Weddell by surface wind it melts as it hits the warmer Antarctic Circumpolar

Current (ACC) on the eastern boundary, creating a melting hot spot for iron deposition and salinity stratification. This in turn results in a massive bloom of phytoplankton which is not accurately resolved in satellite measurements (cf. Geibert et al., 2010). All of these processes in the southern ocean link CO_2 sequestration on the global scale to rapid wind events around Antarctica (Anderson et al., 2009), including massive katabatic flows off Queen Maud Land. Simulations that suffer from a coarse time resolution are unable to pick up features such as this, including the rapid shifts in wind, nor accurately identify the full range of extreme events which would influence such a system (cf. Bengtsson et al., 2009).

Similar to the effect in the Southern Ocean, analysis of LGM dust source locations may also benefit, or require, higher frequency outputs. During the last glacial, dust inputs were many times larger than what is observed in the modern. Mineral aerosols interact with the climate and biogeochemistry in several important ways including the modification of the energy balance of the atmosphere, acting as cloud condensation nuclei, deposition of iron into the ocean and consequently modify the oceanic uptake of CO_2, among others (cf. Mahowald et al., 1999; 2006; Chadwick et al., 1999). Although dust source locations were larger than today (cf. Mahowald et al., 1999) the changes in sub-daily wind speed ("gustiness") has been suggested to be a major, if not *the* mechanism responsible for the increase of the LGM atmospheric dust burden (McGee et al., 2010). The top 0.1% of gust events in a dust source region may supply up to 50% of dust emissions. Consequently, synoptic scale simulations may be used to analyse the gustiness over dust source areas on a level that is similar to a field experiment (see also McGee et al., 2010 Figure 3).

Effects of Temporal Resolution Summary:

Determining the temporal resolution of a simulation is still determined by the aim and scope of the integration as well as the available computing resources as mentioned above. However, as computing resources become more readily available, and research projects continue to focus on climate extremes and their effects (such as perhaps near future warming due to global carbon emissions or storm effects of

massive northern hemispheric ice sheets) moving to higher and higher temporal resolutions seems unavoidable. The positive or negative effects however are still debated simply due to the fact that as you increase the frequency of saved outputs, the more computing space a simulation would need, increasing the necessary funding for such a project.

However, since atmospheric mechanisms have been suggested to contribute to fluctuations in past climate on the order of a human lifetime rather than on much longer orbital timescales (cf. Charles et al., 1994; Fawcett et al., 1997; Langen and Vinther 2007) or on timescales primarily thought to be driven by slower ocean processes (cf. Broecker et al., 1985), higher temporal resolution models have become more of interest to the scientific community. This is especially for the case of the Greenland Ice Sheet where storm tracks, and subsequently the moisture sources to the ice sheet itself, modify the $\delta^{18}O$ preserved in the ice through isotopic fractionation. The longer distance travelled by the precipitation or perhaps even seasonal null deposition, could have modified the oxygen isotope ratio. Accurately resolving the LGM storm tracks would therefore give better understanding to the Greenland proxy record and the magnitude of cooling of past climate events. The same can be said for future emissions scenarios where North Atlantic storms will be affected by a change in equator to pole temperature gradients (Bengtsson et al, 2009). Increasing the accuracy of storm track characteristics requires higher temporal resolution outputs (Blender and Schubert, 2000; Bengtsson et al, 2009).

Further to this, current research suggests that more recent studies assessing the impact of a future warmer climate on extra-tropical storms, given the findings of the IPCC, may need to be re-assessed due to suffering from relatively low temporal resolutions which are unable to accurately resolve the full range of eddie intensities and rapid shifts in wind speed (cf. Bengtsson et al., 2009). Furthermore, certain processes such as the occlusion process happen on the order of a few hours which can only be fully described in more rapid model outputs. The same logic should be applied to similarly aimed synoptic scale studies of past climate simulations such as the one presented here.

2.3 Previous LGM Results in General Circulation Models:

In order to better appreciate the high resolution results presented in later chapters, it is important to be aware of known ice age atmospheric results that one may expect given LGM boundary conditions such as those described in the previous sections.

It is widely accepted that the large northern hemispheric ice sheets, roughly equivalent to 120 metres of global sea level, drastically affected westerly flow, similar to that of the modern day Himalayas. The first numerical experiments to assess the effect of continental ice on the ice age troposphere, and maintaining an ice age climate using CLIMAP data, was done by Manabe and Broccoli (1985). In this, the Laurentide Ice Sheet heavily influenced tropospheric westerly flow exiting the Pacific by splitting it in two. The southern branch brings strong flow over North America while the northerly branch extends up over Canada and brings extremely cold air into the North Atlantic, presumably sustaining the southern margin of the sea ice in the GCM. This therefore may also help to explain the difference in the magnitude of LGM cooling between the Pacific and Atlantic in the CLIMAP dataset as SSTs in the Atlantic would be much more susceptible to the northerly cold air branch (cf. CLIMAP 1976, 1981). This would also have been reflected towards the surface by forcing the spatial distribution of storm tracks.

It is important to determine regional changes in LGM storm tracks as they provide a key source of precipitation which would help maintain the continental ice sheets. The spatial displacement of ice age storm tracks was analyzed in model-model comparison study of Kageyama et al. (1999) using several different models at different spatial resolutions under the PMIP framework (cf. section 2.1). In all cases the positions of the Pacific and Atlantic storm tracks are heavily modified by the continental ice sheets which altered the mid-latitude stationary waves (Manabe and Broccoli, 1985). Both sets of tracks are forced eastward as compared to the modern using prescribed and computed SST (boundary condition) fields. The Atlantic track is pulled eastward, associated with the increased baroclinicity along the extended

(southward) sea ice edge, positioning it further away from its Pacific counterpart. In the computed SST case however, the eastward migration is slightly less. It should be noted that the difference between the modern and the LGM tracks is greater in all prescribed SST cases than integrations using computed SSTs.

There are several repercussions caused by the mechanical forcing and subsequent displacement of the North Pacific and North Atlantic storm tracks by the Laurentide Ice Sheet. These depend on the magnitude of the forcing and the interaction between the Pacific track exit and the area of high baroclinicity in the Atlantic. One of these involves the modified Pacific storm track and its delivery of moisture to both the northern edge of the LIS and the Greenland Ice Sheet.

The connection between storm track position and moisture source regions is vital to our understanding climate regimes, as fluctuations of past surface temperature are preserved in the $\delta^{18}O$ isotope record in ice cores such as those on Greenland. The extent of surface cooling during the LGM, and the sources of past Greenland precipitation which influence the ratio of ^{18}O have also been a topic of debate for decades (Broecker et al., 1985; Charles et al., 1994; Fawcett et al., 1997; Langen and Vinther, 2009). Rapid fluctuations in $\delta^{18}O$ in some cases reflect surface temperature changes of several degrees °C on the order of a human lifetime or shorter. Although the Ocean has been identified as a major culprit in this problem (Broecker et al., 1985), the atmosphere and changes in mid-latitude flow, such as the process described above, have also been suggested to cause such changes. For instance, Charles et al. (1994) used CLIMAP boundary conditions to simulate potential moisture sources to Greenland given the modified westerlies from the high elevation ice sheets. In the modern, moisture is delivered to Greenland from a variety of sources. These include a local North Atlantic source, a local Norwegian Sea/Greenland source, a North American source which includes common features such as Alberta Clippers off the Canadian Rockies, and a North Pacific source where storms exit the modern Pacific track. A variety of smaller sources include the tropical Atlantic and Eurasia (Charles et al., 1994). During the LGM however, these change dramatically with the presence of the northern hemispheric ice sheets, cooler SSTs,

and tighter equator-to-pole temperature gradients. The Manabe and Broccoli (1985) type split-jet is reflected at the surface with the North Pacific jet displaced northward towards the west-north Greenland coast. Northern Greenland is consequently dominated by a North Pacific moisture source, while the very southern part still contains a North Atlantic signal in the Charles et al. (1994) experiment. The longer distance travelled from the North Pacific would clearly have an effect on the nature of the $\delta^{18}O$ deposited in the ice core through mechanisms relating to the Dole Effect - heavier ^{18}O tends to precipitate sooner and closer to source regions than the lighter O^{16}. Consequently, rapid shifts in $\delta^{18}O$ should be considered to be also modified through atmospheric mechanisms rather than just surface temperature fluctuations (cf. Charles et al., 1994; Fawcett et al., 1997; Langen and Vinther, 2009).

Langen and Vinther (2009) revisited the problem of LGM Greenland moisture sources by varying both the SST and topography boundary condition independently to assess the impact of each. In this, the high elevation LGM ice sheets modify the winter stationary wave pattern similar to Manabe and Broccoli (1985) and Charles et al., (1994). However, when comparing a -4°C further SST cooling (Toracinta et al., 2004) to CLIMAP, it is clear that the SST field does impact the moisture source locations; only the CLIMAP SST boundary condition, and not the modified one, produces a greater Pacific LGM moisture source to northern Greenland. When using modern SSTs with LGM topography, moisture sources are still mainly from the Atlantic, though there is a small increased Pacific effect not seen in the modern. It is not to be said that the LGM topography field doesn't influence the moisture source shift in the Langen and Vinther (2009) simulations, it does, however the difference from LGM CLIMAP SSTs to a -4°C cooling from CLIMAP between 30°S and 30°N (with a linear transition from 30° to 40°) are more dominant in a precipitation response. However, this is not necessarily unexpected given a massive decrease in evaporation and holding capacity associated with such a large temperature deviation from the CLIMAP comparison. This result may be less dominant given a more intermediate SST boundary condition such as the one presented here (discussed later), or in Crowley (2000) or Ballantyne et al. (2005). It is also important to note for future reference, that Langen and Vinther (2009) study utilized the community

climate model version 3 (CCM3) at a T42 resolution (roughly 2.5° x 2.5 ° grid boxes) which is an earlier version of the model that will be used here.

Although during the LGM the meridional temperature gradient in the North Atlantic was greater than today, recent studies have suggested that there is actually less North Atlantic mid-latitude storm activity during the glacial when compared to the modern (Unterman 2007; Li and Battisti, 2008; Donohue and Battisti, 2009). Although a definite reason for such a reduction is still under investigation, and will be discussed in this work, Donohue and Battisti (2009), have suggested that a reduction in Atlantic cyclogenic seeding during the LGM to be the cause. The Laurentide Ice Sheet disrupts North American and North Pacific communication to the North Atlantic baroclinic zone especially given a Manabe and Broccoli (1985) type ridge along the northern edge of the ice sheet. In the low resolution CAM3 integration of Donohue and Battisti (2009) there is a reduction in Alberta Clippers (large cyclones that form off the lee side of the Canadian Rockies and generally track over North America and into the North Atlantic) and the North Pacific track exit is forced far northward of its modern day position. Consequently, disturbances from the debris of storms exiting the Pacific track are repressed by the LIS and are unable to enter the North Atlantic track (cf. Hoskins and Hodges, 2002). LGM storm track intensity, cyclogenesis, and its comparison to modern results are further discussed in detail in later chapters.

Chapter 3

Methodology

3.0 The Community Climate Model:

In the early 1980's, the National Center for Atmospheric Research (NCAR) created a comprehensive three-dimensional global atmospheric model that would appeal to both university and research scientists. Due to its intended widespread use, it was given the name the Community Climate Model (CCM). The first version of the model is described in Williamson (1983). The CCM0 was heavily documented with a user guide, technical notes including detailed access to the code, algorithms, and a series of circulation statistics (cf. Sato et al., 1983; Williamson et al., 1983).

The second generation and first major revision of the CCM came in 1987 with the CCM1. Significant modifications were made including the addition of a seasonal mode where surface conditions could vary with time. Changes to parameterisation of radiation and diffusion processes were also made (Williamson, 1987; Hack, 1988; cf. Hack, 1998). However, it was the complete restructuring to the third generation CCM2 that sparked a major effort to improve a whole suite of climate processes including smaller scale systems which were parameterised, as well as its ease of use (cf. section 2.2 and 2.3). Improvements included radiative cooling in the model stratosphere, more sophisticated cloud optical properties and the addition of a diurnal cycle to better represent the diurnal cycle's effect on surface fluxes. Other improvements made in the CCM2 can be found in Bath et al. (1992) and Hack (1994).

In terms of nomenclature, the CCM3 was the fourth and final generation of what falls under the name Community Climate Model. It was introduced in 1996 (Kiehl et al., 1996) and although formulation and implementation remained identical to the CCM2, it included some changes to the parameterised physics to remove biases found in the previous version. Modifications were made to correct errors in a weak stationary wave structure in the northern hemisphere winter, an overly vigorous hydrological cycle, and problems with biases of land temperature during summer (cf. Hack et al., 1998). The original build is a T42 global spectral model with 18 vertical levels and a top of atmosphere at 2.9 mb. It has the same vertical and horizontal resolution as the previous CCM2 version and still contains the diurnal cycle. The CCM3 also uses a detailed model to deal with land surface dynamics called the Land Surface Model (LSM), which is described in detail by Bonan (1998). With the CCM3, an optional slab ocean model (SOM) was introduced for climate change forecast studies (cf. Kiehl et al., 1996; Hack et al., 1998; Bonan, 1998).

3.1 Model Settings

The Community Climate Model version 3.6 (CCM 3.6) physics, coupled with a Land Surface Model (LSM) version 1.1, housed at the Department of Energy's (DOE) Center for Computational Science (CCS) at Oak Ridge National Labs (ORNL) is used here. This utilizes the same physics as the CCM3.6.6 but the computational aspects of the model have been rewritten to be more efficient on massively parallel computers. Model outputs were saved at every hour for both an LGM and short control run, the former being referred to herein as the "synoptic run". The simulation incorporated the CCM 3.6's T170 resolution, where a ~75 km grid interval was spread over a global domain. A total of 68 variables on 18 sigma levels were saved at hourly steps. The simulations have been run in-tandem with a courser temporal resolution, climatological, LGM and control run due to the intrinsic shortness of the much higher frequency output synoptic run (cf. Kim et al., 2008 – this will sometimes be referred to herein as the 'climatological' simulation). Both the synoptic simulation and climatological simulation use the CCM3.6.6 high resolution T170 grid and the same initial boundary conditions, compiler, and supercomputer.

The LGM climatological simulation was integrated for 6 model years with the first two being thrown out for spin-up. The synoptic integrations achieved 2000 hours with the first 500 regarded as spin-up. The combined output and processed data of the two sets of simulations used the total allotted computing resources detailed in the ORNL INCITE awards presented to Unterman (2006-2012), and resulted in approximately 4.4 terabytes of data. A complete list of variables available on the CCM3.6.6 can also be found in Unterman (2007).

3.2 CCM 3.6.6 Boundary Conditions and Model Validation Preface:

The research presented here analyses four separate high-resolution simulations in varying detail: (1) a climatological ice age run, (2) a climatological control run, (3) a synoptic scale LGM simulation, and (4) a synoptic scale control simulation. The climatological initial results were first presented in Kim et al. (2008) but the data will be examined further in this work.

Although the beginning versions of the community climate model had been documented against the current climate since the early 80's, the first series of validations of the CCM version 3 came within a series of reports including Hurrel (1998), Hack et al., (1998), and Kiehl et al., (1998). Modifications to the CCM3 (mentioned in the beginning of this chapter) resulted in a clear improvement over the CCM2 in the overall simulated climate of the model (cf. Kiehl et al., 1998). The sea level pressure field was reproduced well compared to the NCEP reanalysis data (cf. Hurrell, 1998), including the major interseasonal changes in the subtropical high pressure centres and the high-latitude low pressure systems. SLP in the subtropics of both hemispheres tends to be slightly higher than the reanalysis data, while the subpolar regions tend to be slightly lower (Hurrel, 1998). This is also true for the areas around the Azores High which is slightly higher (1-3 mb) in the CCM3 and shifted eastward over Africa – an important finding, as this is also a discrepancy found in the validation of Kim et al. (2008), and here. The biggest model to observational differences in the T42 version of the CCM3 occurs south of New

Zealand. However, even the largest regional differences compared to the NCEP reanalysis data are a factor of two lower than the CCM2.

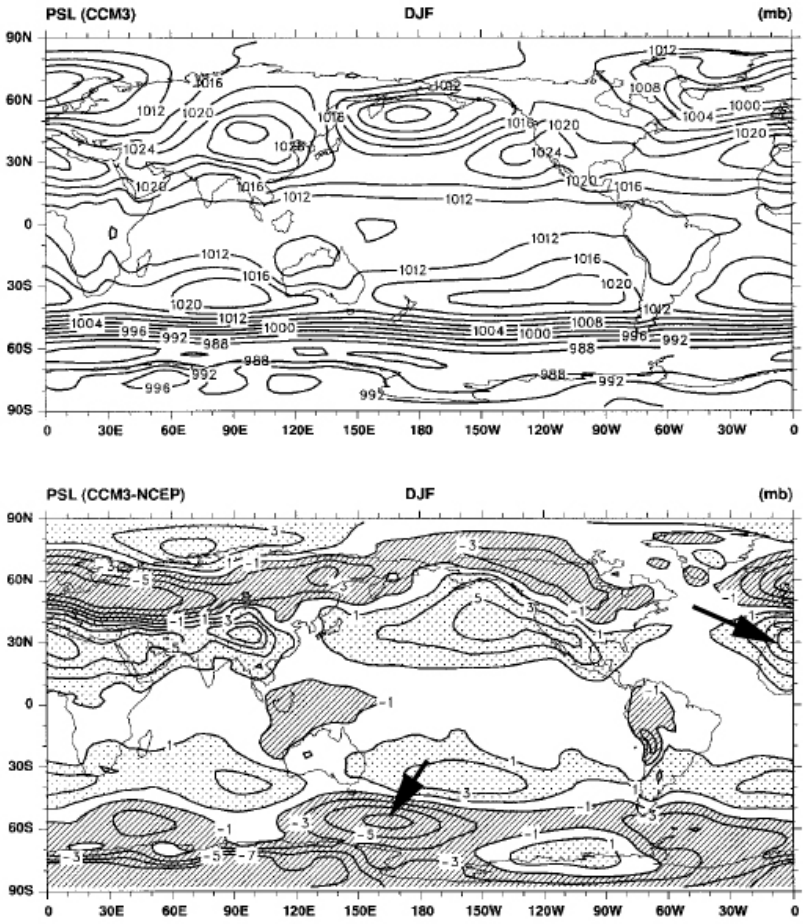

Figure 3.1: Sea level pressure in the T42 CCM3 (top panel) compared to the NCEP reanalysis data (bottom panel). Note the differences over Northern Africa. The area south of New Zealand is the largest model to observational discrepancy present in the model, although all differences are a factor of two better than the previous CCM2 (cf. Hurrel, 1998; figure modified from Hurrel, 1998).

With the creation of a higher resolution build of the CCM3, further validation was done to compare how well a finer grid-mesh simulated the modern climate compared to that at the original T42 scale (Duffy et al., 2003). Duffy et al., (2003), evaluated the standard resolution build (T42) and two higher resolution builds of the CCM3 (T170 and T239 – approx. 75 km and 55 km respectively). The standard T42 model configuration was tuned at NCAR to optimize results of the build. Duffy et al., (2003) performed initial simulations of the higher resolution configurations without

retuning the model paramterizations (only time steps and diffusion coefficients were changed). Then, a first-order retuning of the T170 configuration was done to bring global variables as close as possible to the observed values (cf. Hurrel, 1998; Duffy et al., 2003). The retuned coefficients were used in a second series of higher resoution integrations. Results were then compared between the simulations, interpolated to the original T42 grid, to assess the effect of including finer scales on the ability to simulate large-scale features. Duffy et al. (2003), did this for both tuned and untuned higher resolution integrations. In nearly all quantities examined, "there was a better agreement between the spatio-temporal pattern of model results and observations in the higher resolution simulations" (Duffy et al., 2003). With the reception of a multi-year INCITE award from Oak Ridge National Labs and the access to pro-bono computing time, the higher resolution build of the CCM3 was adopted here, and forced to output hourly, for the analysis of paleometeorological features. Further validation of the standard configuration of the CCM3, as well as the higher resolution versions, can be found in Kim et al. (2008), and below

***.

The control boundary conditions used in the simulations presented here, include climatologically averaged sea surface temperatures and sea ice distributions from the NCAR data repository and are derived from Shea et al. (1990). CO_2 concentration was set to 335 ppm, and a contemporary land mask and topography was also used (cf. Kim et al., 2008).

Certain conditions of the LGM can be ascertained from numerous geological proxies such as ice cores, deep sea sediments, pollen, macrofossils, coral, and borehole data. These then can be used to reconstruct certain aspects of the ice age surface such as the concentration of carbon dioxide, sea surface temperatures, vegetation cover, ice volume and surface temperatures. However, due to many factors such as the availability of data and proxy error, different reconstructions are available for many of these features, many of which were discussed in Chapter 2. Since the accuracy of a simulations boundary conditions determines the accuracy of its results, it is

important to discuss the initial conditions used in the CCM3.6.6 simulation presented here. The following are the boundary conditions for the T170 hourly simulation for the Last Glacial Maximum:

1. Ice cores provide a unique paleoclimate record with 'fossilized' air bubbles which become trapped in the ice during compression. These give a direct measurement of past changes in atmospheric trace-gas composition. Atmospheric CO_2 for the LGM simulation has been reduced to 200 ppm to be consistent with such measurements from the Vostok ice core (Petit et al., 1999).
2. Prescribed sea surface temperatures (SST) are derived from CLIMAP (1981), except that temperatures have been uniformly lowered by 1°C to be more consistent with recent analyses (e.g., Crowley, 2000; Ballantyne et al., 2005; cf. MARGO, 2009) and to maintain continuity with the Kim et al. (2008) study. This adjustment is of course simplistic, but any other approach seemed so complicated as to quickly become *ad hoc* (cf. Ballantyne et al., 2005). As a check on the adjustment, a comparison between the simulated mean annual surface temperatures in the climatological run over North America with borehole temperatures was completed (e.g. Fig. 3.1). These are generally considered the most reliable indicator of temperature changes on land. Results indicate very good agreement, with the four groundwater sites differing by only 0.4°C with the climatological run using the modified CLIMAP SSTs. A more in-depth validation in Table 3.1 shows the borehole temperatures mentioned above with additional proxy and observational comparisons (cf. Kim et al, 2008).
3. LGM sea level has been uniformly lowered by 120 metres (cf. Fairbanks 1989; Clark and Mix., 2002) to take into account the major redistribution of water from the oceans onto land to form the continental ice sheets. The model land mask is modified such that large areas of continental shelf are exposed around the western margin of the Pacific and Atlantic. Large areas of the Caribbean Sea, Arafura Straight, North East United States, eastern margins of

China and northeast Siberia become exposed. The Bearing Straight also becomes completely closed.

4. 21,000 BP orbital parameters (cf. Berger et al., 1978).
5. LGM Topography follows the ICE-4G reconstruction from Pelitier (1994) with a maximum height of the Laurentide Ice Sheet around 3,000 metres. Although the newer ICE-5G reconstruction was available at the start of the synoptic scale simulation presented here, it was not for climatological simulation (cf. Kim et al., 2008). Consequently, the ICE-4G reconstruction was chosen for the synoptic run to primarily (a) keep the two simulations as in-tandem integrations to allow further comparisons of the two simulations and (b) provide a means to validate atmospheric responses to that of ICE-4G features. It should be noted however, that the ICE-5G reconstruction is different than the ICE-4G used here, including the representation of LGM topography and deglacial history, the later of which is outside the scope of this study. A detailed description of some of the differences between the reconstructions can be found in section 2.1, but it is important to re-mention a certain change in the topographic field. ICE-5G has a much larger dome (Keewatin Dome) west of Hudson Bay, Canada approaching another 1 km in elevation compared to the older ICE-4G version. This suggests that the mechanical forcing due to the elevation of the Laurentide Ice Sheet, may be more pronounced in an ICE-5G boundary condition scenario. This possibility will be re-visited in Chapter 4.
6. Although ice age vegetation reconstructions have been used for some simulations (Crowley and Baum, 1997), vegetation has been kept unchanged except for areas that have become exposed due to lower sea level, or covered by ice. In these instances a default median CCM parameter was used.
7. Sea ice patterns were also modified from the original CLIMAP estimate. The maximum extent of wintertime sea ice during the LGM has been disputed. Instead of integrating recent estimates of wintertime glacial ice extent, used here is the faunal assemblage counts and sedimentological criteria outlined by McIntyre et al. (1976) to position a maximum southward margin in the North Atlantic sea ice at 42°N. This represents the limit of ice rafted debris and the

presence of polar foraminiferal assemblages, as well as the absence of coccoliths – the carbonate plates created by coccolithophores. Although this limit can be debated as it represents an extreme value, it is useful to test the model response to this condition.

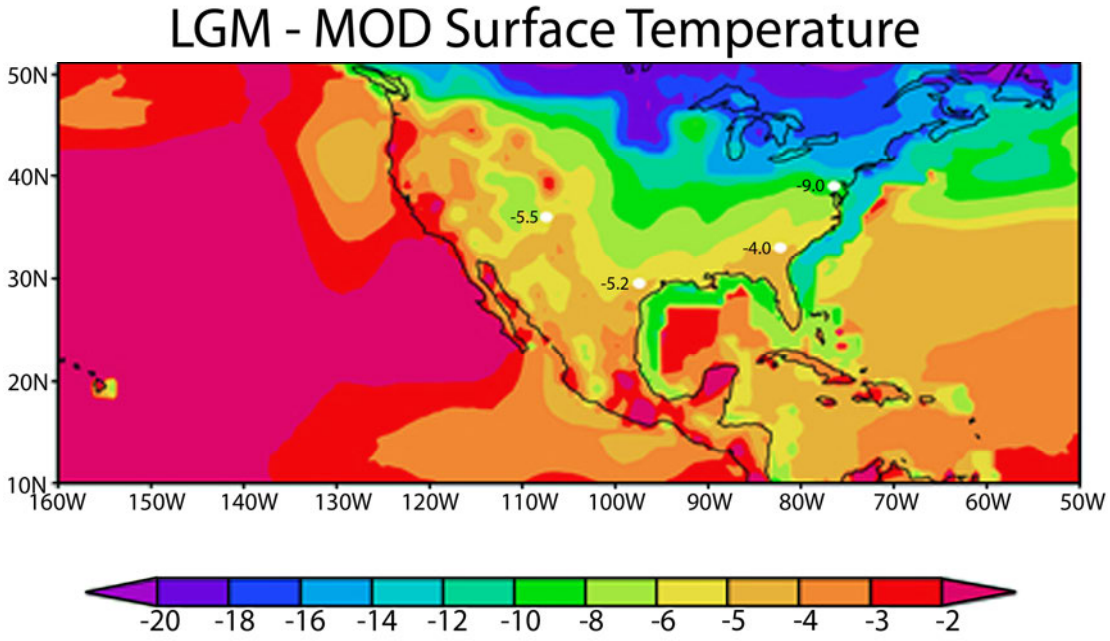

Figure 3.2: LGM-MOD mean surface temperatures from the climatological runs compared to four high-quality proxy locations over North America. There is a high level of agreement between the two data sets at this resolution. Comparison to an experimental T42 can be further found in Kim et al., 2008. A more detailed analysis can be found in Table 3.1 (below).

Latitude	Longitude	ΔOBS	ΔT170	OBS-T170	ΔT42	OBS-T42	|OBS-T170|	|OBS-T42|	Proxy Notes
72.6 N	38.5 W	21	23	-2	16	4	2	4	Borehole
72.6 N	37.6 W	21	23	-2	17	3	2	3	Borehole
78.3 S	106.5 E	15	13	2	9.5	5.5	2	5.5	Borehole
28.5 S	137 E	9	5.3	3.7	4.6	4.4	3.7	4.4	Emu Eggshell
29.1 N	98.8 W	5.2	5	0.2	6.9	-1.7	0.2	1.7	Noble Gas/Borehole
36.5 N	108 W	5.5	6.1	-0.6	4.3	1.2	0.6	1.2	Noble Gas/Borehole
7 S	41.5 W	5.4	3.6	1.8	4.2	1.2	1.8	1.2	Noble Gas/Borehole
10 N	106 E	5	4.1	0.9	5.8	-0.8	0.9	0.8	Noble Gas/Borehole
11 N	13 E	6.4	4.9	1.5	6.6	-0.2	1.5	0.2	Noble Gas/Borehole
33 N	83 W	4.3	5.3	1	6.9	-2.6	1	2.6	Noble Gas/Borehole
39 N	76 W	9	9	0	9.9	-0.9	0	0.9	Noble Gas/Borehole
23.5 N	58 E	6.5	5.4	1.1	7.9	-1.4	1.1	1.4	Noble Gas/Borehole
43.5 N	1.5 W	5.7	5.8	-0.1	6.5	-0.8	0.1	0.8	Noble Gas/Borehole
48 N	21 E	8.7	9.2	-0.5	10.7	-2	0.5	2	Noble Gas/Borehole
0.27 N	66.7 W	5–6	2.4	3.1	3.1	2.4	3.1	2.4	Pollen
4.9 N	74.33 W	3–4	2.8	0.7	1.1	2.4	0.7	2.4	Pollen
16 S	69 W	5–7	5.8	0.2	0.8	5.2	0.2	5.2	Pollen
3.5 S	29.57 E	5–6	4.1	1.4	4.2	1.3	1.4	1.3	Pollen
24.43 S	28.75 E	5–6	2.2	3.3	4.3	1.2	3.3	1.2	Pollen
0.03 N	37.47 E	5.1–8.8	5.9	1.1	4.7	2.3	1.1	2.3	Pollen
20.08 S	43.37 W	5–7	4	2	3.2	2.3	2	2.3	Pollen
22 N	100.5 W	1.5–3	3.7	-1.45	1.7	0.55	1.45	0.55	Pollen
27.68 N	85.4 E	6–8	4.8	2.2	5.2	1.8	2.2	1.8	Pollen
47 N	38.5 E	20	7.6	12.4	7.5	12.5	12.4	12.5	Pollen
47 N	6 E	9	8.1	0.9	8.6	0.4	0.9	0.4	Pollen

Table 3.1: Comparison of temperature anomaly estimates at numerous locations around the globe to the climatological data set.

Latitude	Longitude	ΔOBS	ΔT170	OBS-T170	ΔT42	OBS-T42	|OBS-T170|	|OBS-T42|	Proxy Notes
55 N	83 E	10	9.8	0.2	9.8	0.2	0.2	0.2	Pollen
55.17 N	57.58 E	8	8.1	-0.1	7.9	0.1	0.1	0.1	Pollen
47.52 N	111.27 E	10	5.3	4.7	7.5	-2.5	4.7	2.5	Pollen
51.21 N	99.45 E	5	5.9	-0.9	7.9	-2.9	0.9	2.9	Pollen
3.2 N	50.4 E	1.5	1.8	-0.3	1.9	-0.4	0.3	0.4	Alkenone
1 N	139 W	0.5	2.4	-1.9	2.4	-1.9	1.9	1.9	Alkenone
0	23 W	1.8	3.9	-2.1	4.3	-2.5	2.1	2.5	Alkenone
25.02 N	16.65 W	4.5	9.1	-4.6	7.7	-3.2	4.6	3.2	Alkenone
21.48 N	17.95 W	2–2.5	9.8	-7.55	10.3	-8.05	7.55	8.05	Alkenone
13.2 N	59.3 W	5	3	2	3	2	2	2	Coral
14.52 S	117.1 E	0.4	5.4	-5	5.8	-5.4	5	5.4	Faunal
33.38 S	161.61 E	4.2	3.4	0.8	3.4	0.8	0.8	0.8	Faunal
44.26 S	150 E	3.3	3.6	-0.3	3.8	-3.5	0.3	3.5	Faunal

Table 3.1: (Continued) Comparison of temperature anomaly estimates at numerous locations around the globe to the climatological data set.

Latitude	Longitude	ΔOBS	ΔT170	OBS-T170	ΔT42	OBS-T42	|OBS-T170|	|OBS-T42|	Proxy Notes
16.01 S	76.33 W	6–9	1.5	6	0.8	6.7	6	6.7	Faunal
0	15 W	5	3.8	1.2	3.7	1.3	1.2	1.3	Faunal
10 N	40 W	2–3	2.6	-0.1	2.8	-0.3	0.1	0.3	Faunal
3 S	82 W	4–5	2	2.5	0.1	4.4	2.5	4.4	Faunal
1 S	110 W	2–3	1.2	1.3	1.3	1.2	1.3	1.2	Faunal
42 N	130.01 W	3.5	4.7	-1.2	4.9	-1.4	1.2	1.4	Faunal
21.36 N	158.19 W	2	0	2	0.3	1.7	2	1.7	Faunal
0.3 N	159.4 E	2.8	3.3	-0.5	3.2	-0.4	0.5	0.4	Mg/Ca
2.3 N	91 W	2.6	2	0.6	2.3	0.3	0.6	0.3	Mg/Ca
43.22 S	11.74 E	4–5	3.8	0.7	5.2	-0.7	0.7	0.7	Radiolaria
49 S	12.7 W	3–4	7.8	-4.3	8.8	-5.3	4.3	5.3	Radiolaria
3.2 N	101.43 W	3.2	1.2	2	1.3	1.9	2	1.9	Radiolaria
16.45 S	77.57 W	3.7	2	1.7	2.2	1.5	1.7	1.5	Radiolaria
					Total Difference		100.7	122.6	Total
					Average Difference		1.97	2.40	Total

Table 3.1: (Continued) Comparison of temperature anomaly estimates at numerous locations around the globe to the climatological data set. Simulated temperature differences on land compare well to the interpretations of proxy records. Furthermore, there is better agreement with the T170 integrations compared to T42. Further discussion can be found in Chapter 2. Data was re-plotted from the Kim et al., (2008) data set for further analysis. The noble gas/borehole proxies differ from observations in the T170 case by 0.77° and 1.28° at T42. The pollen proxies differ from observations in the T170 case by 2.31° and 2.54° at T42. This is reduced to 1.59° at T170 and 1.83° at T42 if the 47°N 38.5°E point is removed (the largest measured difference among all locations in both cases).

High Resolution Animations:

High-resolution animations of the ice age can be utilized to analyze and "observe" the "paleometeorological" circulation in the hourly integration. Animations comprised of frames from hourly saves were rendered using the NCAR Command Language (NCL), IDL, and from a Matlab software package built to handle the large data sets and to accurately compile high resolution, 256 colour images from the high resolution outputs. Pre-built packages, such as the Grid Analysis and Display System (GrADS), would not accurately portray certain climatological parameters and surface features at the T170 level as they are generally limited in their options and colour profile. The initial animations portray surface flow, surface temperature and convective precipitation for the northern hemisphere bound at 10°N-70°N, 100°E-30°E. This region was chosen to capture flow in the North Pacific, North Atlantic and over North America and the Laurentide Ice Sheet. Frames of upper level wind for the mid-latitude jet, and geopotential height were also developed using the same process.

Storm Tracking – Cyclones and Lysis regions:

Storm tracking diagnostics were performed on the synoptic scale data set. Tracking methods were similar to Hoskins and Hodges (2002). Specific regions of the North Atlantic and North Pacific were chosen for storm count, lifetime, and intensity analysis. The regions were bound at 10°N-60°N, 10°W-70°W in the North Atlantic and 0°N-60°N, 160°E-130°W in the North Pacific. These were chosen to coincide with the majority of transient eddies seen in the animations, which for the North Atlantic resides along the southward extent of the sea ice margin. Lysis regions, location points where storm death occurs, were also calculated for a filtered (storms lasting longer than one day and minimum distant coefficient) and unfiltered scenario (no time duration limit, and no minimum distant coefficient). Due to the shortness of the synoptic integration, this was kept as point regions as opposed to point density regions mentioned in Hoskins and Hodges (2002). Further information regarding temporal resolution and storm track accuracy can be found in Chapter 2.

Tracking was done on the raw data files for both mean sea level pressure (MSLP), and vorticity fields (VORT). The MSLP method tends to focus on the larger scales, while vorticity picks up more "noise", on smaller spatial scales, which sometimes results in tracking of high values of vorticity along frontal regions. MSLP Intensities are also calculated with the large scale background removed (cf. Hoskins and Hodges, 2002). This is different from the typical analysis of analyzing pressure minima from the full field, and was done in order to remove biases that may occur given changes in the large scale field – especially at this level of detail.

Parcel Trajectory Software:

Three-dimensional parcel trajectory diagnostics were performed to analyze the source of air over geologically important locations in order to investigate the recognized increased dust emissions during the glacial. The main functionality of the trajectory software is derived from the two-dimensional algorithm by Law (1993) and later applied in Perrin and Simmonds (1995). The newer version (which was modified here), introduces three-dimensional capabilities not included in the former iterations of the software with the basic non-modified method described in Noone and Simmonds (1999) and Barras and Simmonds (2009). This version is capable of running both the 2D and 3D pathways. Modifications were necessary in order to work with the paleo-dataset as the original software was only created to work on contemporary data from the European Centre for Medium-Range Weather Forecasts (ECMWF) which has different data structures and a different file output. Although the desire was to change the software to be capable of handling all of the hourly-outputs it would require a complete top-down restructuring of the software. Consequently, 6-hourly blocks from the hourly data set were instead used as inputs. Binaries were also separately compiled using GFORTRAN to work on the University of Edinburgh's EDDIE computing cluster. During the modifications, an error was found in the original code where a latitude variable was instead listed as longitude. This is now fixed. It is unclear how, or if, it would have impacted previous studies given it's location in the source code.

***

It should be noted here that this work has benefited from *pro bono* computing time at Oak Ridge National Labs and series of consecutive INCITE awards (2006-2012) from ORNL. This primarily came about given the immediate desire for exploration into LGM weather by Thomas Crowley and David Erickson at the Center for Computational Sciences at ORNL. The nature of this however (see above) did bring about the primary reasons for the shortness of the hourly-scale and climatological simulations: (a) the computing time necessary on the Cheetah Supercomputer and (b) the decommissioning of her systems. Continuing the simulation on another machine would have greatly modified the results and as a consequence, it was determined that the analysis of the already acquired several terabytes of high-resolution data was to be the most important as the first investigation into weather processes during the LGM.

Chapter 4

Results: Paleometeorology - Northern Hemisphere Flow and Variability during the LGM

4.0 Introduction and Background:

This chapter focuses on sea level pressure, pressure variability, and regional wind flow in the synoptic scale simulation for the northern hemisphere during the LGM. These results are also manifested in terms of changes in LGM cyclogenesis and storm tracks, a detailed analysis of which is reserved for the next chapter. The results presented in Chapter 4 (general flow) and Chapter 5 (synoptic scale eddies) are intimately linked, but are separated due to their differences in scope. Comparisons will be made between the two throughout both chapters.

Since the synoptic scale hourly simulation is within the 2σ of the sea-level pressure variability (discussed shortly) of the "climatological" simulation (cf. Kim et al., 2008) and many of the general results of both simulations agree with other recent findings which have lent considerable insight into our understanding of the LGM (e.g. Charles et al., 1994; Bromwich et al., 2004; Langen and Vinther, 2008; Donohue and Battisti, 2009; and several others) comparisons will also be made between the geological record and the interpretation of such records for a first-pass test of robustness – and a means to further validate proxies (cf. Chapter 2 and Chapter 5). Although many will be made here, a separate section dedicated to highlighting the key comparisons between the synoptic scale simulation and the

climatological run, GCMs and geological data sets will be presented later in Chapter 5. This discussion does not imply that the high-resolution hourly simulation represents *every* winter during the LGM, but rather it represents a wintertime possibility given ice age boundary conditions.

***

Ice age conditions have been known to have greatly perturbed northern hemisphere westerly flow for decades both from the geological stand point, and within the modelling community (cf. Manabe and Broccoli, 1985). In terms of changes in general surface flow, evidence within the geological record is preserved for instance in sand dune orientation and other eolian features which demonstrate that over North America, surface winds were more north-westerly, especially in the mid-western states, bringing relatively cooler air from the north (cf. Crowley, 1991, after Wells, 1983). Interestingly, advection of this cold air from the northwest might have greatly affected the evaporation rates of the Gulf Stream, whose heat transfer to the atmosphere is heavily impacted by synoptic scale cold air outbreaks – a three decade old observational result that might benefit from future synoptic scale case studies (SethuRamen et al., 1986). Also, as briefly mentioned in Chapter 2, upwelling indices and windblown material in ocean cores further suggest glacial wind velocity increases of about 30% for the North Pacific trade winds (20% for North Pacific westerlies) and 50% in the North Atlantic trades.

Other geological evidence showing changes in surface flow is preserved as chloride in ice cores. This comes from the deposit of sea salt from the atmosphere, the concentration of which is determined by surface wind velocities and the height at which it is lofted - analogous to the proposed mechanisms responsible for terrestrial mineral dust emissions (McGee et al., 2010). Consequently, changes in ice age aerosols can be used to infer changes in wind velocities of about +5-8 m/s (~50%) for the North Atlantic and Southern Ocean (SO). This represents an increase in LGM wind velocities of 20-50%, which may strongly affect surface dynamics of the ocean

including heat loss and circulation, as well as sea ice transport and ocean productivity (Crowley, 1991; Geibert et al., 2010).

Terrestrial dust emissions from dust source locations (e.g. Eastern Asia, African Sahel region and the Arabian Peninsula) also increased by a factor of 2-5 (or more) times higher during glacial intervals (cf. Hovan et al., 1994; Rea et al., 1994; McGee et al., 2010; and others). Studies however continue to disagree on the dominant mechanism responsible for glacial-interglacial dust emission changes, with the causative agents ranging from source area aridity (e.g. Rea, 1994), fine-grained sediment supply from glacial erosion (e.g. Sugden et al., 2009), changes in regional vegetation, exposure of "virgin" sediments on continental shelves due to decreased eustatic sea level, and changes in synoptic-scale wind strength (McGee et al., 2010). Several of these mechanisms, such as wind gustiness, can be explored with a synoptic scale simulation such as the one presented here and will be discussed as a first-look in Chapter 6.

From the modelling perspective, ice age boundary conditions have been known to greatly perturb general northern hemispheric westerly flow since the mid-1980's when Manabe and Broccoli (1985) demonstrated that given a large Laurentide Ice Sheet (LIS), westerly-flow becomes 'split' with a northern branch arching over Canada, and a southern branch forced southward. Although some paleo-GCM studies have presented variations of this split (Kageyama et al., 1999; Toracinta et al., 2004; Kim et al., 2008 and others), the mechanical forcing of the massive LIS is apparent, and is similar to the manner at which the Himalayas perturb the westerlies today. Further discussion on past modelling experiments and their results can be found in Chapter 2, section 2.2 and section 2.3.

4.1 Model Comparisons and LGM Surface Flow:

Here, comparisons are made between the synoptic scale simulation, the climatological simulation and ERA reanalysis data to document similarities and differences between the simulations. Differences between the climatological run and

hourly integration should arise given their time-scale - although the general features should be comparable within the range of the climatological variability.

The four years of December, January, and February (DJF) sea level pressure (SLP) in the climatological control run were first compared to the ERA40 re-analysis to determine if the modern climatology was comparable to observations in Fig. 4.1. Given the offset in baseline years for the two runs (and the admitted shortness of the later; see figure), the positions of the Aleutian and Icelandic lows and subtropical highs are realistic. The eastward displacement of the Azores high towards Africa is expected for this version of the CCM (Hurrell et al. 1998). The much higher SLP in the LGM (Fig. 4.1, panel c and d) over Canada and Greenland result from the continental ice sheets. The intricate and tightly bound contours around mountain ranges such as the Rocky Mountains in western North America, are indicative of the high degree of regional detail in this version of the CCM3 (Duffy et al., 2003). Consequently, both the climatological and synoptic-scale regional results, on such a fine grid-space, may help better validate regional proxy records in areas impacted by orography, such as borehole temperature reconstructions (Stutte et al., 1992; Stutte et al., 1995; Appendix), in-situ pollen records (e.g. Jackson et al., 2000), analysis of dust source regions (McGee et al., 2010) and many others.

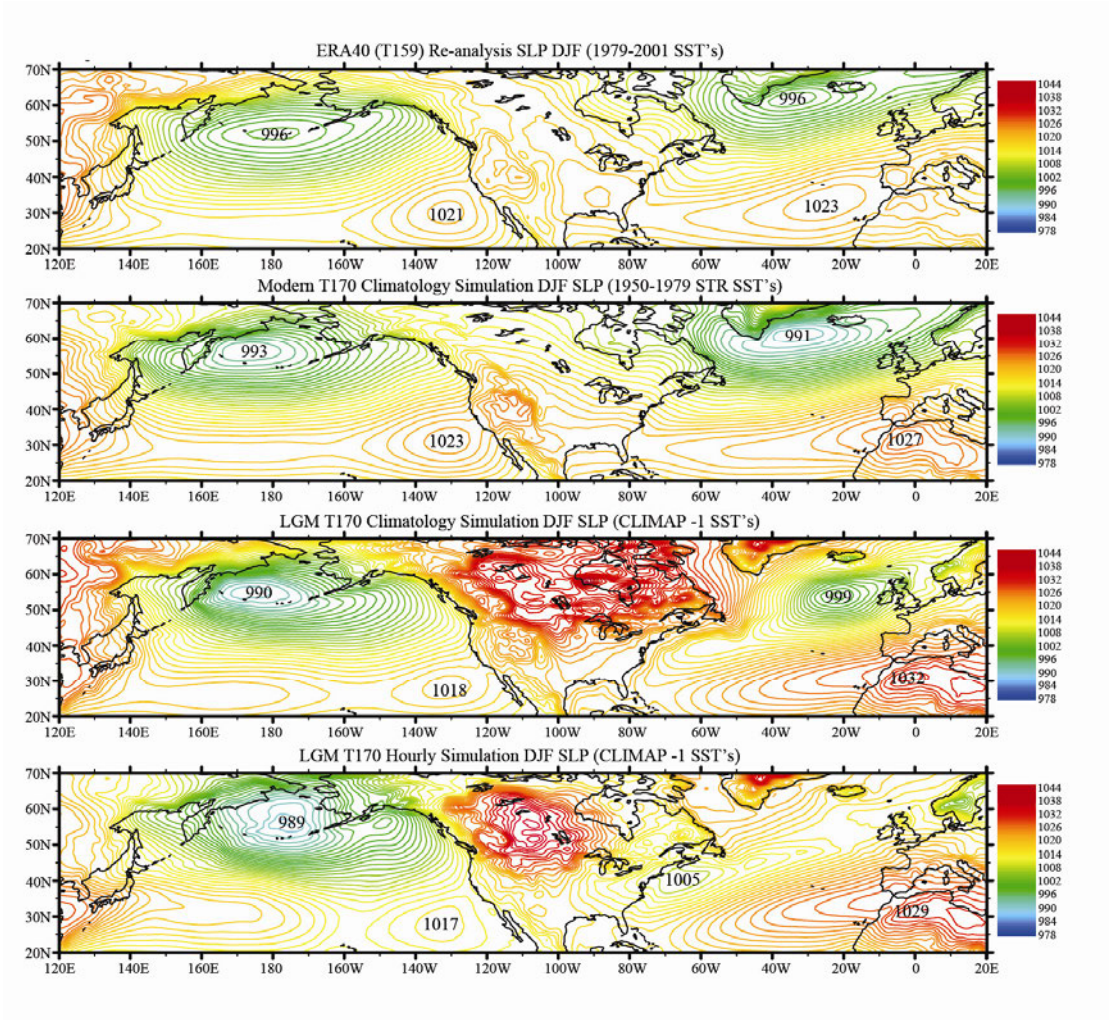

Figure 4.1: ERA40 SLP data obtained from the British Atmospheric Data Centre (top panel) is compared to the multi-year climatological simulation of Kim et al. (2008) and the two different temporal resolution simulations of the LGM. To aid in comparison with the present, LGM SLP has been decreased by 12 mb to be roughly consistent with a lowering of 120 m in sea level (Betts and Ridgway, 1992). Contours changed to 1 mb to show regional spatial detail.

Although model SLP in the Atlantic and Pacific lows are equivalent in the modern, in the LGM Pacific-Atlantic differences are ~10 hPa. Mean LGM sea level pressure in the North Pacific low is only 3 hPa deeper than the modern, but the North Atlantic low in the LGM is ~8 hPa shallower (cf. Fig. 4.1, 4.2; Table 4.1). Though the number of winter realizations is small, there are indications of moderate interannual variability (Table 1) in the climatological run, with Atlantic-Pacific swings similar to a see-saw between the two regions during the January months (cf. Appendix).

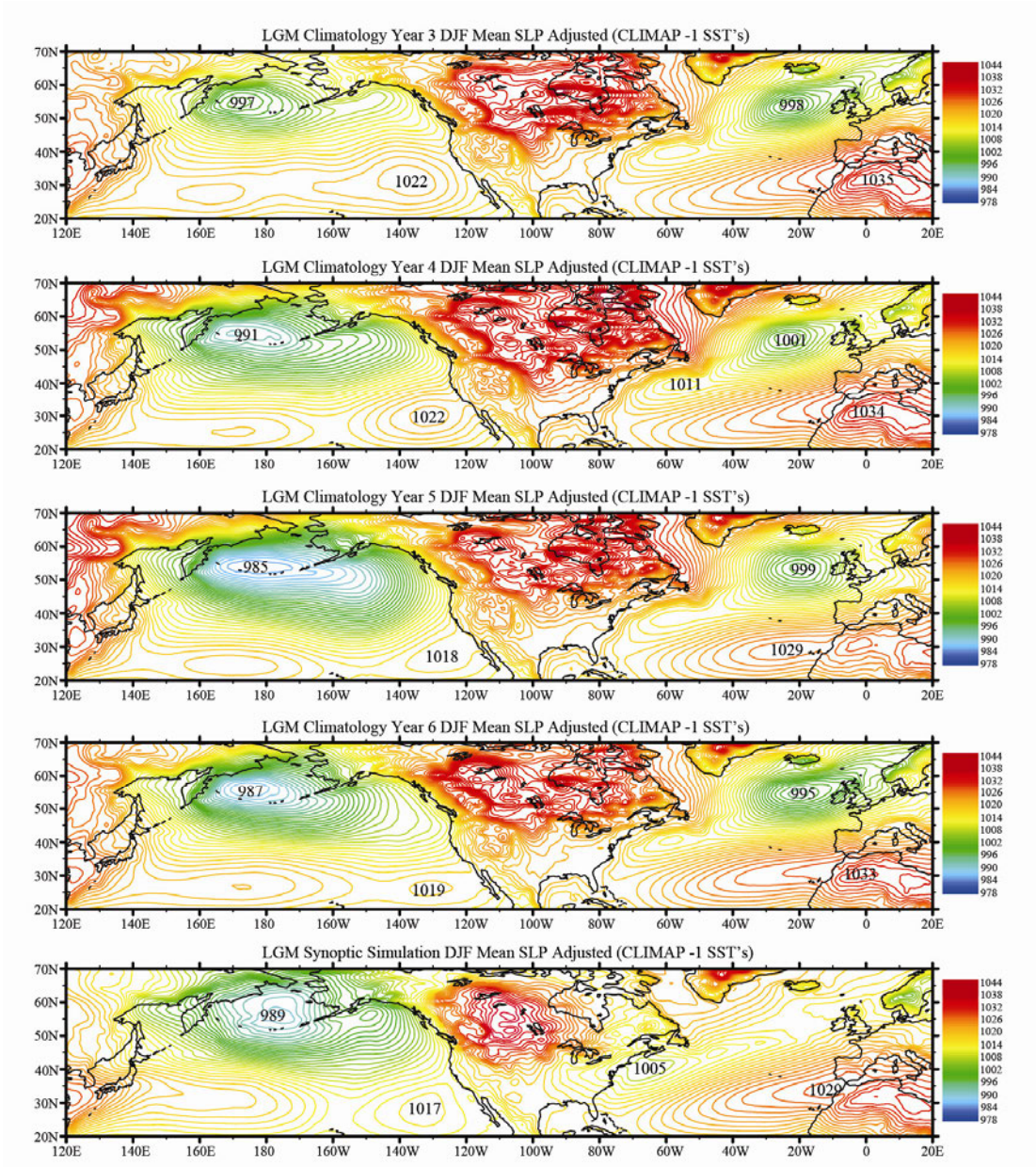

Figure 4.2: LGM DJF mean SLP between the four consecutive years after spin up in the LGM climatological simulation and the hourly simulation. To aid in comparison with the present, LGM SLP has been decreased by 12 mb to be roughly consistant with a lowering of 120 m in sea level (Betts and Ridgway, 1992). Contours changed to 1 mb to show regional spatial detail.

MOD DJF Sector (4 Year)	Mean:	2σ:
Aleutian Low Region	992.1	5.0
Icelandic Low Region	989.4	4.8
Subtropical Pacific	1026.3	4.5
Azores High Region	1028.0	3.3

ERA40 DJF Sector (1979-2000):	Mean:	2σ:
Aleutian Low Region	995.8	8.7 (8.1)
Icelandic Low Region	994.4	8.1 (6.5)
Subtropical Pacific	1022.7	3.6 (3.3)
Azores High Region	1024.8	5.4 (5.4)

LGM DJF Sector	Mean:	2σ:
Aleutian Low Region	990.1	10.9
Icelandic Low Region	999.1	5.0
Subtropical Pacific	1020.2	3.3
Azores High Region	1032.3	5.2

LGM Jan. Sector	Mean:	2σ:
Aleutian Low Region	988.3	24.8
Icelandic Low Region	995.3	13.4
Subtropical Pacific	1019.5	3.4
Azores High Region	1028.8	4.6

Table 4.1: LGM Mean sea level pressure mean and two-sigma variability for the Aleutian Low, Icelandic Low, Subtropical North Pacific and the Azores High regions. Also shown is the average ERA40 4 year running two-sigma values in parentheses.

MSLP variability within the climatological simulations and observations is shown in Table 4.1 (above). Wintertime variability over the Aleutian sector is 990.1 hPa ± 10.9 hPa and over the Icelandic low it is 999.1 hPa ± 5.0 hPa. In the Subtropical pacific and Azores high region it is 1020.2 ± 3.3 hPa and 1032.3 ± 5.2 hPa respectively. For the January month, the mean and two sigma range of variability for the Aleutian and Icelandic Low regions are 988.2 hPa ± 24.9 hPa and 995.2 hPa ± 13.4 hPa respectively. The mean and 2σ variability in the subtropical Pacific and Azores high regions is 1019.5 hPa ± 3.4 hPa and 1028.7 hPa ± 4.6 hPa respectively. In the climatological run the northeast Atlantic contains a well defined low pressure core that is absent in the shorter simulation (or displaced far to the west). This result reflects significant Arctic outflow, such as through the Siberian “Lena River Gap”

(cf. Fig. 4.6) between two Siberian ice sheets during the winter (see figure). Considering the westward displacement, the synoptic run is within the range of variability during the LGM climatological run (Kim et al., 2008). The Icelandic low is ~35% less variable in the LGM compared to the re-analysis data (2σ of 5.0 hPa during the LGM and 8.1 hPa in the ERA40), while the Aleutian low is ~25% more variable (2σ of 10.9 hPa during the LGM and 8.7 hPa in the ERA40).

4.2 LGM Surface Flow:

It is important to describe the flow patterns seen in the synoptic scale *and* climatological integrations as many features can then be compared between other models and to specific regional geological data sets if the synoptic results can be shown to be manifested further (and therefore considered typical) in the climatology. In the North Pacific for instance, the changes in SLP described in the previous section are further manifested in terms of changes in climatological winds (Fig. 4.3). Over a large region of the central North Pacific (30°N-50°N, 170°E-150°W) winds are 4-8 m/s stronger in the LGM compared to the climatological modern simulation, with differences rising to 8-16 m/s along the coastal strip of the Gulf of Alaska and ~10°N in the eastern equatorial Pacific. The latter increase should have had a significant effect on the primarily wind-driven transport of the eastern North Pacific Equatorial Current system. The large positive anomaly in the Aleutian region is coincident with the driving of mass trans-Pacific cyclones originating off the coast of Japan and eastern Siberia as is evident in the hourly simulation – and increased precipitation along the coast (Fig. 4.4, 4.5, and 4.6; Chapter 5).

The subsequent large increase in Ekman pumping in the central North Pacific should have also increased percentages of upwelling plankton in this region, and possibly sub-surface mode-water formation (e.g. Mikolajewicz et al., 1997; Sugimoto and Hanawa, 2010). However, it would be difficult to test this prediction because the very deep water and corrosive bottom chemistry usually results in poor/nil preservation of surface plankton in sediments from this region.

The surface flow pattern in the synoptic run is also presented in Figures 4.5 and 4.6. In the Pacific, strong winds are coincident with the climatological velocity anomalies in the same region. The strand of high velocity winds off the southwest coast of Panama, towards the Galapagos around 120°W is also coincident with the ~+4 m/s anomaly seen in (Fig. 4.3) the climatological run. Also within the synoptic integration, within the Indian Ocean, a strong surface current follows the axis of the Euphrates River, all the way from the Mediterranean region, until it descends off the coast of Oman, turning southward and merging with flow from the Indian Ocean. This region represents the highest wind velocity positive anomaly compared to the modern in the climatological run, with values approaching +8-16 m/s. This should have significantly affected coastal upwelling and consequently productivity of the region – if Indian Ocean productivity during climate extremes such as the ice age is heavily dependent on these offshore wind vectors, any modifications of velocity or direction in the region should result in large changes in overall productivity, which would be subsequently recorded in Indian Ocean cores.

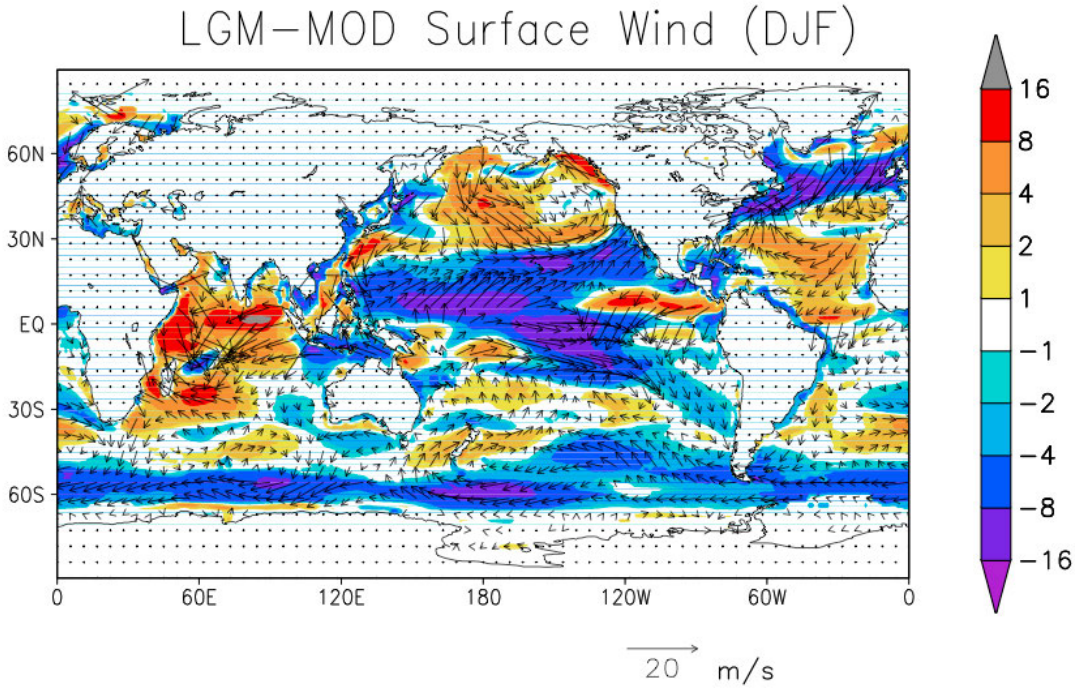

Figure 4.3: LGM –MOD global surface wind velocities over ocean basins at T170 resolution taken from the dataset of Kim et al. (2008). Note the region of large positive velocities in the North Pacific whereas the North Atlantic, south of Greenland, is largely negative. There is also a clear focusing of winds along the Northern American coast and Canada.

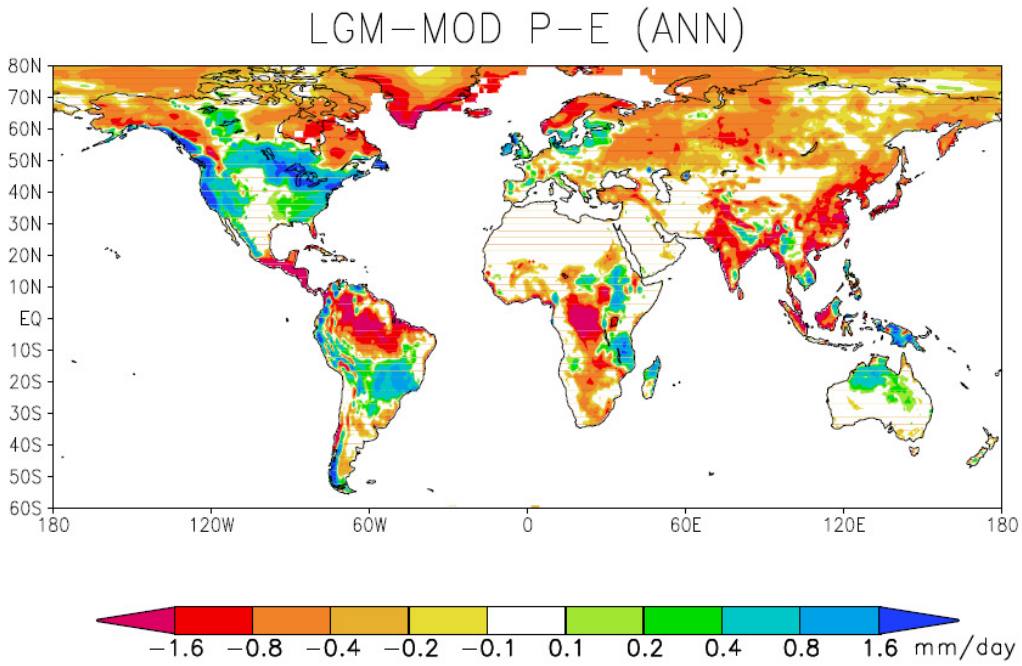

Figure 4.4: LGM-MOD annual global P-E in the climatological run (unpublished figure from Kim et al., 2008). Positive anomalies exist over North America including the west coast and along the Canadian coastline. This area is coincident with Pacific storm focusing (see next chapter on cyclogenesis) and the recorded rise of Great Basin lakes during this time period (Benson et al., 1990).

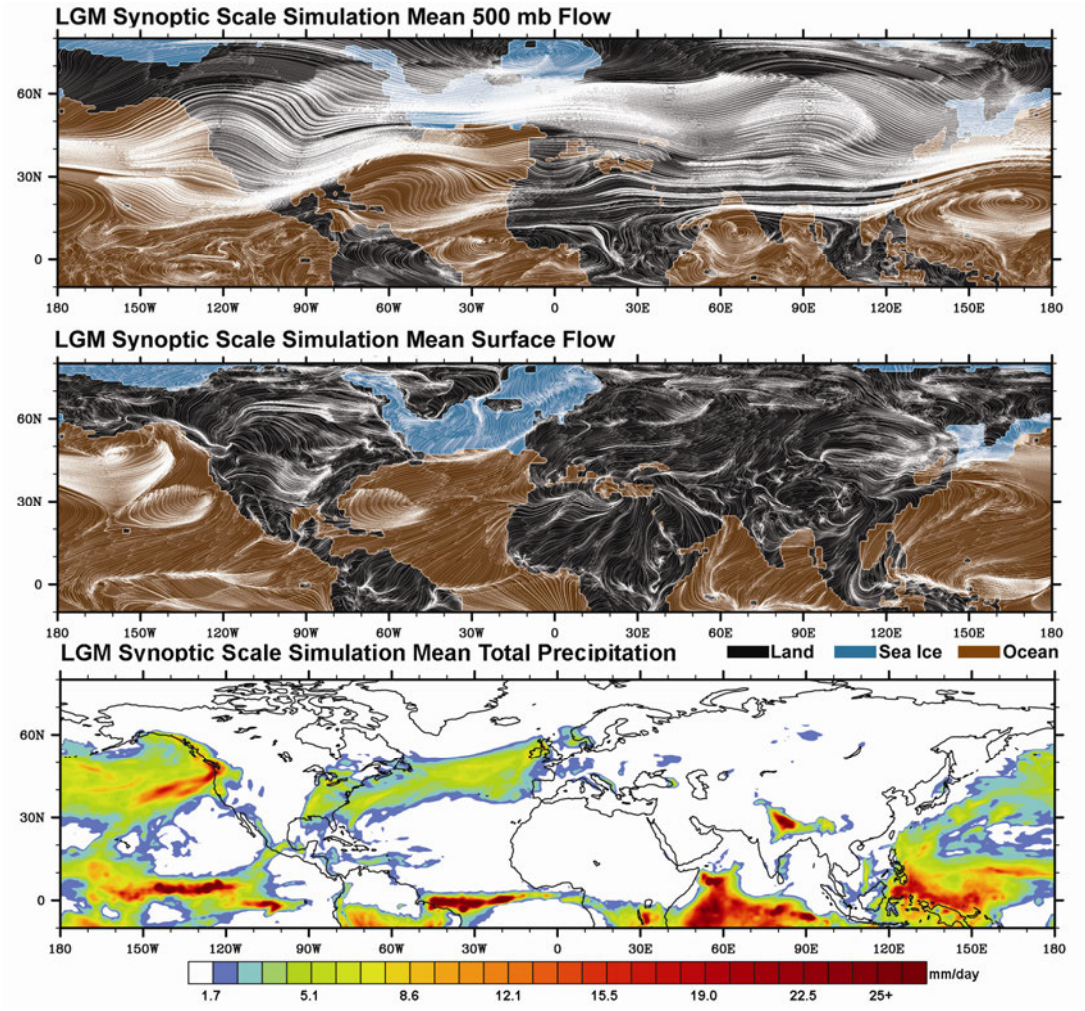

Figure 4.5: Synoptic scale simulation mean upper (top panel) and surface level (middle panel) flow field and total precipitation (bottom panel) produced in NCL showing the land mask. Note an "atmospheric boundary current" along the north eastern edge of the Laurentide Ice Sheet, and another along the east side of the Greenland Ice Sheet. Specific regional velocities and precipitation further clarified in the polar projection of Figure 6.

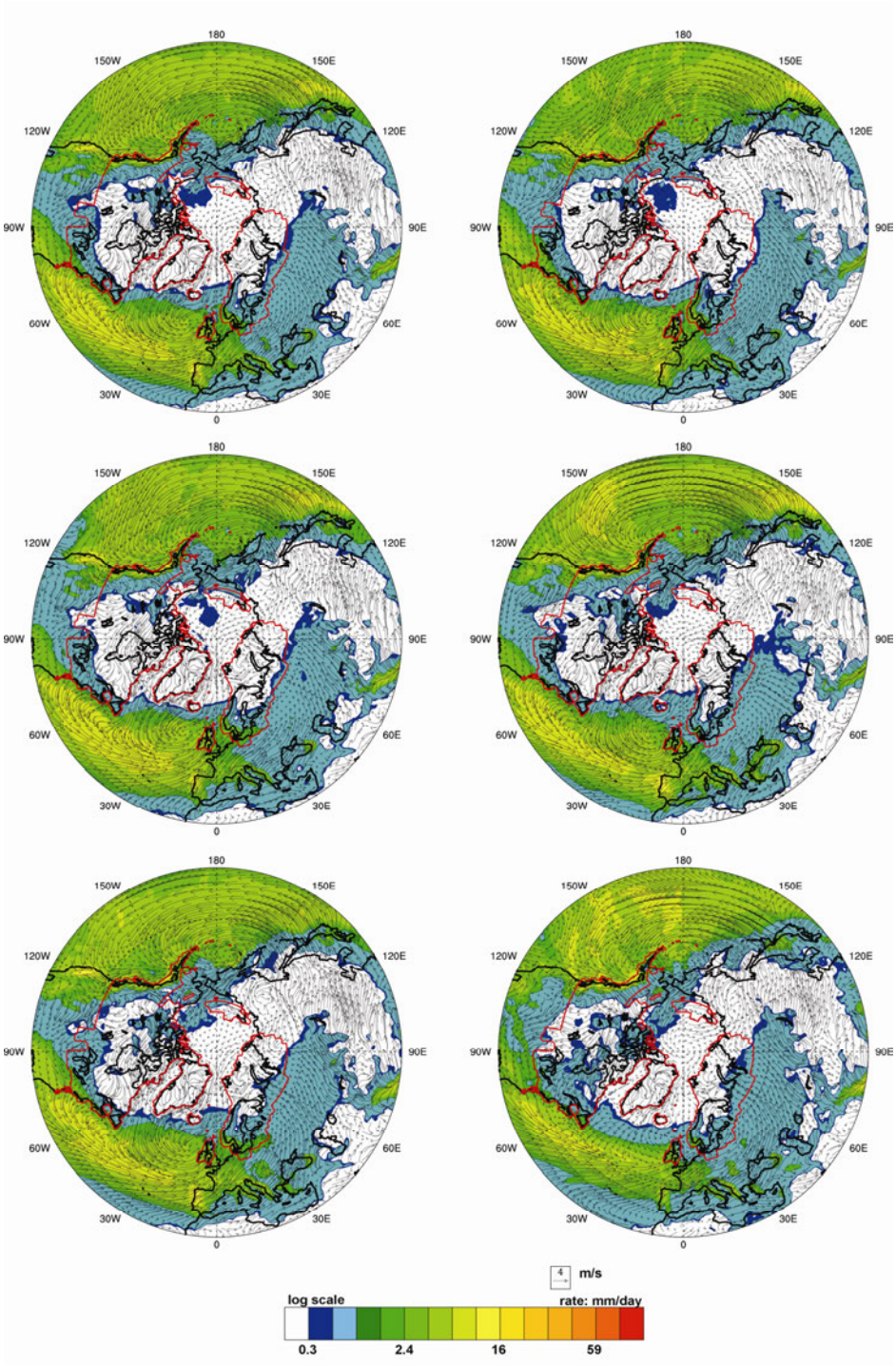

Figure 4.6a: Total precipitation and surface wind flow for the mean of the four year climatological run (top-left), year 3 of the climatological simulation (top-right), year 4 (middle-left), year 5 (middle-right), year 6 (bottom-left), and the synoptic scale simulation. Red boundaries denote ice sheet margins. High resolution close-ups of each panel can be found in the Appendix.

The synoptic scale enlargement (Fig. 4.5, 4.6b; cf. Appendix) illustrates some additional features of the circulation. The surface high on Greenland is situated almost exactly over the site of the Summit ice cores (GISP2 and GRIP). There is a clear atmospheric boundary current on the eastern margin of the Laurentide Ice Sheet, immediately west of the Labrador Sea. A thin strand of this flow connects to the main North Atlantic storm track (see also Chapter 5). There is similar katabatic/boundary flow on the east side of the Greenland Ice Sheet, but this flow then merges with N/NE flow over the sea ice then bifurcates around Iceland. After merging, the surface jet heads almost directly south in a coherent narrow band extending over 1000 km south of Greenland. This flow pattern could conceivably have caused divergence of sea ice, and possibly partial open water in this area (cf. the analysis of McIntyre et al., 1976).

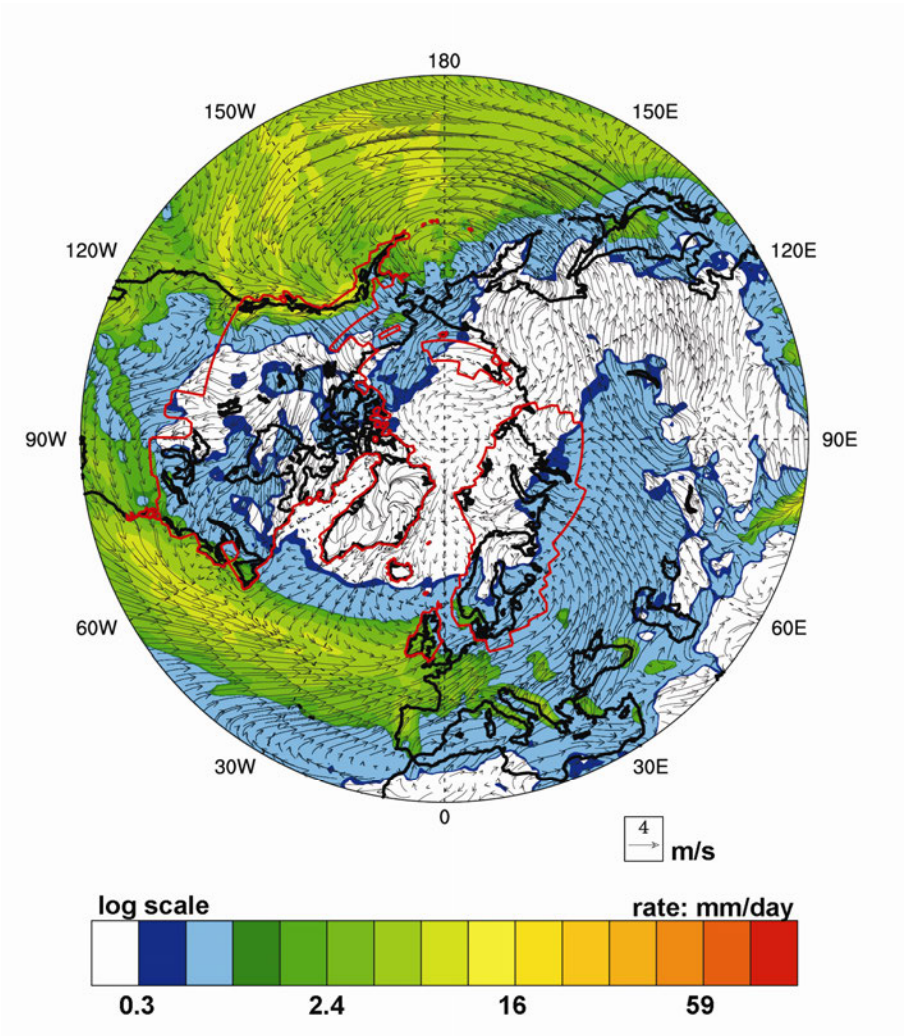

Figure 4.6b: Synoptic scale mean total precipitation and surface wind flow for the LGM winter (DJF).

Further circulation features involve a high pressure system situated over the eastern Mediterranean, a turn to southerly flow (from the Gulf of Mexico) east of 90°W (i.e. the Mississippi River), and a centering of the subtropical high along 30°N in the central North Atlantic. This latter region is almost *exactly* where plankton distributions suggest the location of the LGM subtropical convergence zone (Crowley and Matthews, 1983, Fig. 1).

Total precipitation within the Pacific-Atlantic sector (Fig. 4.5, 4.6) summarizes many of the effects seen in the circulation analysis. Results of particular interest involve the focusing of Aleutian cyclogenesis on the Alaskan coastal mountains (cf. Fig. 4.4). There is also a tongue of moisture extending eastward into the Great Basin of western North America at about 40°N; this was one of the few regions that had large, rising lakes during the LGM (Benson et al., 1990) and which the increased storm tracking in the area found in the synoptic simulation may lend credence to (an important result discussed in detail in Chapter 5). A second tongue of high moisture occurs in the southern United States, east of the Mississippi, west of the Appalachians, and south of the southernmost extension of the Laurentide Ice Sheet on North America. It occurs in the region where the synoptic wind composite (Fig. 4.5; 4.6) illustrates a turn to southerly flow. This moisture source could conceivably have been partially responsible for the expansion (and/or trajectory) of this lobe of the LIS.

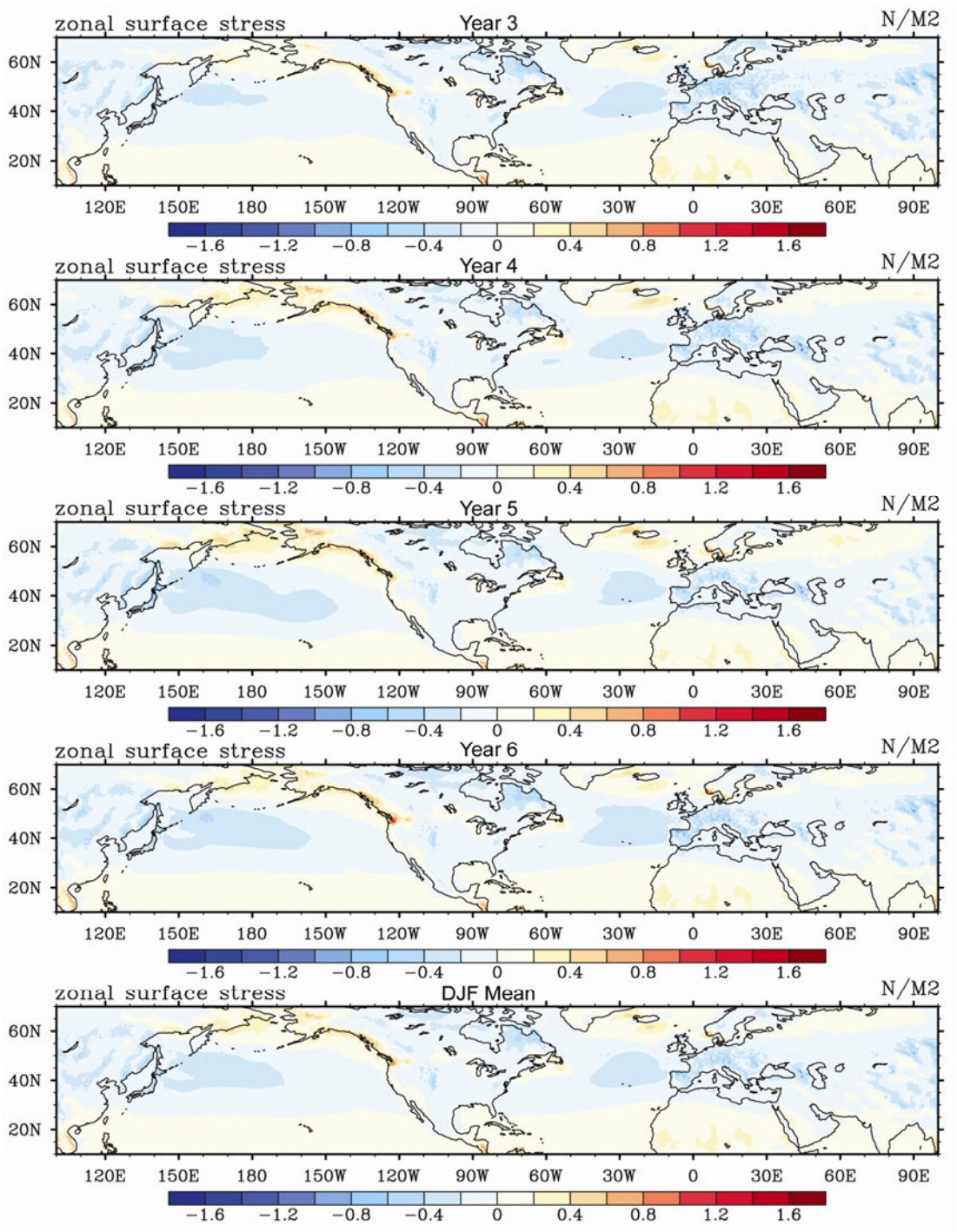

Figure 4.7: DJF wintertime mean zonal surface stress in the climatological simulation. High values extend across eastern Asia and into the North Pacific, the northern most edge of the Laurentide Ice Sheet and in the eastern North Atlantic along Northern Europe, the United Kingdom, and the Fennoscandian Ice Sheet sector due to the focusing of storms out of the Atlantic storm track as seen in the hourly integration.

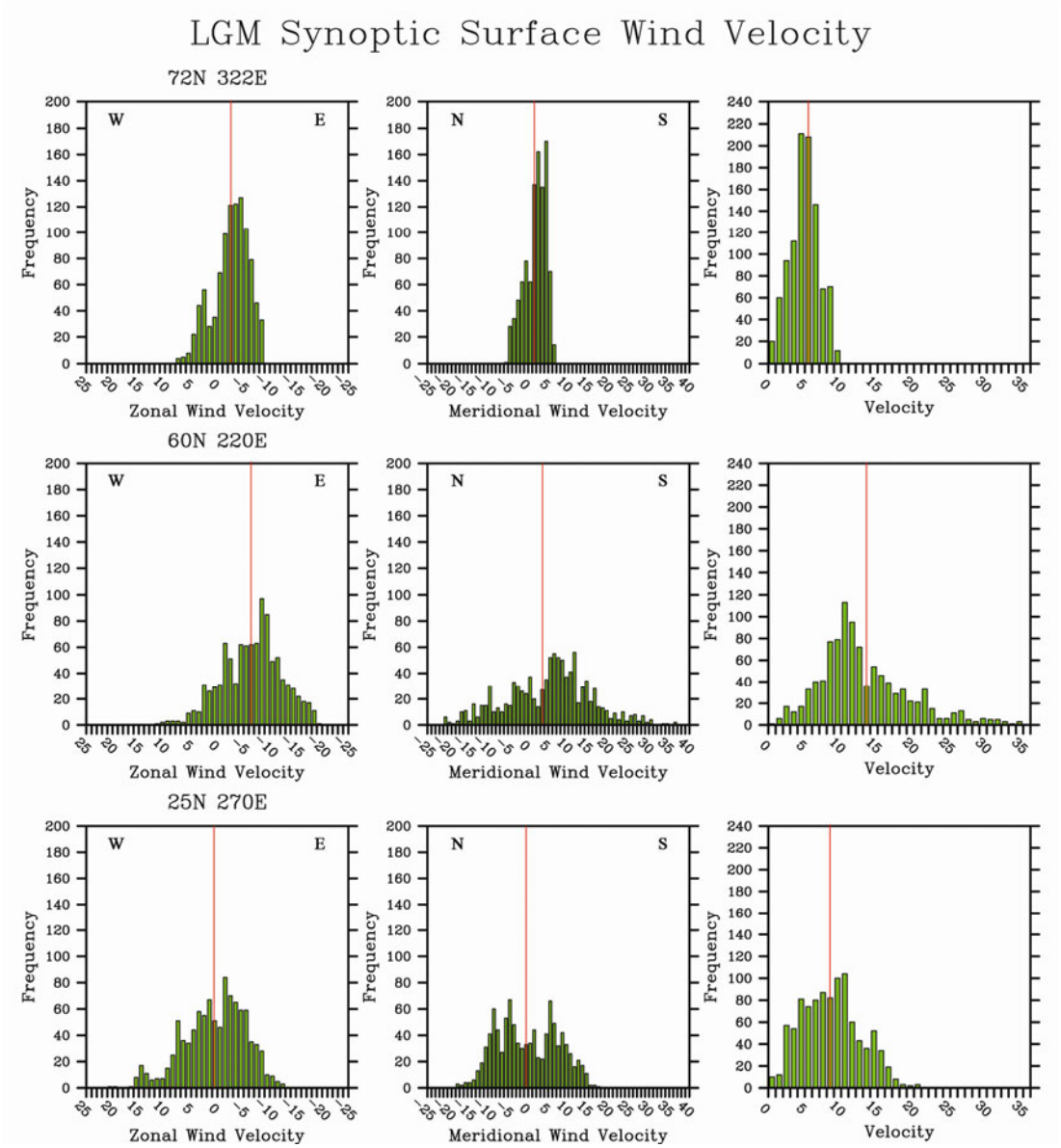

Figure 4.8: Surface wind velocity component frequencies on the hourly scale for three grid point locations including the region around Summit, Greenland (top), the coast of Alaska (middle), and the Gulf of Mexico (bottom).

Unusual tropical precipitation patterns (Appendix and also Fig. 4.5; 4.6) include a band in the Indonesian/New Guinea sector associated with the equatorward NW/NE wind streams emanating from the mid-latitudes (which is also visible in the climatological wind anomalies). The strong surface current in the Indian Ocean descends down the NW-SE axis of Tigris-Euphrates Rivers and then directed southward toward the zone of maximum precipitation, now located about 10°S. The

plume of high precipitation around 10°N in this band appears to be associated with convergence of wind streams. It isn't possible to conclude that all of these streams may actually have occurred in the ice age but the simulation demonstrates that their occurrence on the synoptic scale is possible given ice age physics. It is therefore conceivable that some geological data may eventually be able to further test such detailed responses. For this reason these responses have been described without necessarily claiming at this stage that they may actually have been a permanent feature of the ice age circulation.

Figure 4.8 and 4.11 shows the hourly frequency of total and component wind velocities over three locations significant to the cyclogenesis analysis (next chapter), but are important to mention here within the surface flow results. The frequency analysis demonstrates that the component wind velocities are not necessarily normally distributed around the mean; Although the mean upper air velocity is near zero over central Greenland, the distribution in this region is not normal, showing a distinct secondary mode of higher velocities from the west that can be linked to some of the extreme Pacific storms documented in the synoptic run, including after their terminus (e.g. Chapter 5; Appendix; e.g. two large Pacific storms at hours 737-822, and 816-901). This is also true for the surface level analysis (Fig. 4.8; cf. 4.6) over the Gulf of Alaska where instances of extreme wind gusts are present in the region. This, combined with the precipitation results is intriguing not only because of its relation to the cyclogenesis results but also because of the suggested ice-free section in the Alaska region (Chapter 2) - and other findings such as the potential arctic dust source found in the BIOME3 simulation of Mahowald et al. (1999 Fig. 1) in this area. The synoptic scale hourly analysis of LGM gustiness is presented in Chapter 6.

4.3 The LGM 300 hPa Mid-Latitude Jet:

Figure 4.9 illustrates the upper level flow for the synoptic scale simulation. Here, there is a modified split of the westerly jet over North America, with a large ridge over Alaska and Canada and a southerly branch extending down towards the southern States and Mexico (see top panel). The northern branch drops southwards

towards the Atlantic, south of Greenland along the northern edge of Canada. Over large areas of Northern Asia and Siberia there is strong north-westerly flow into the Pacific near the Sea of Japan. This area is coincident with the region of strong cyclogenesis of the trans-Pacific storms seen in the tracking results presented in Chapter 5. The modified split is in agreement with numerous other GCM experiments that suggest a jet of varying form (Manabe and Broccoli, 1985; Kageyama et al., 1999; Toracinta et al., 2004; Bromwich et al., 2004; 2007; and many others).

The upper level winds were also compiled into high resolution hourly animations to investigate the synoptic properties of the mid-level jet and its reflection at the surface via convective precipitation (cf. dynamic material in Appendix). Results from the climatological run, and the mean of the synoptic integration, correspond to the modified split jet with the northern branch extending up over the LIS and the southern branch dipping towards Mexico. Synoptically however, the mid-level jet fluctuates between various wave-forms including a modified and fully split jet with two distinct branches similar to that of the mean state (Fig. 4.10). This modification is an important observation as there are rare upper-level events (on the order of a few hours) during which the mid-level jet strongly dips southward towards the intertropical

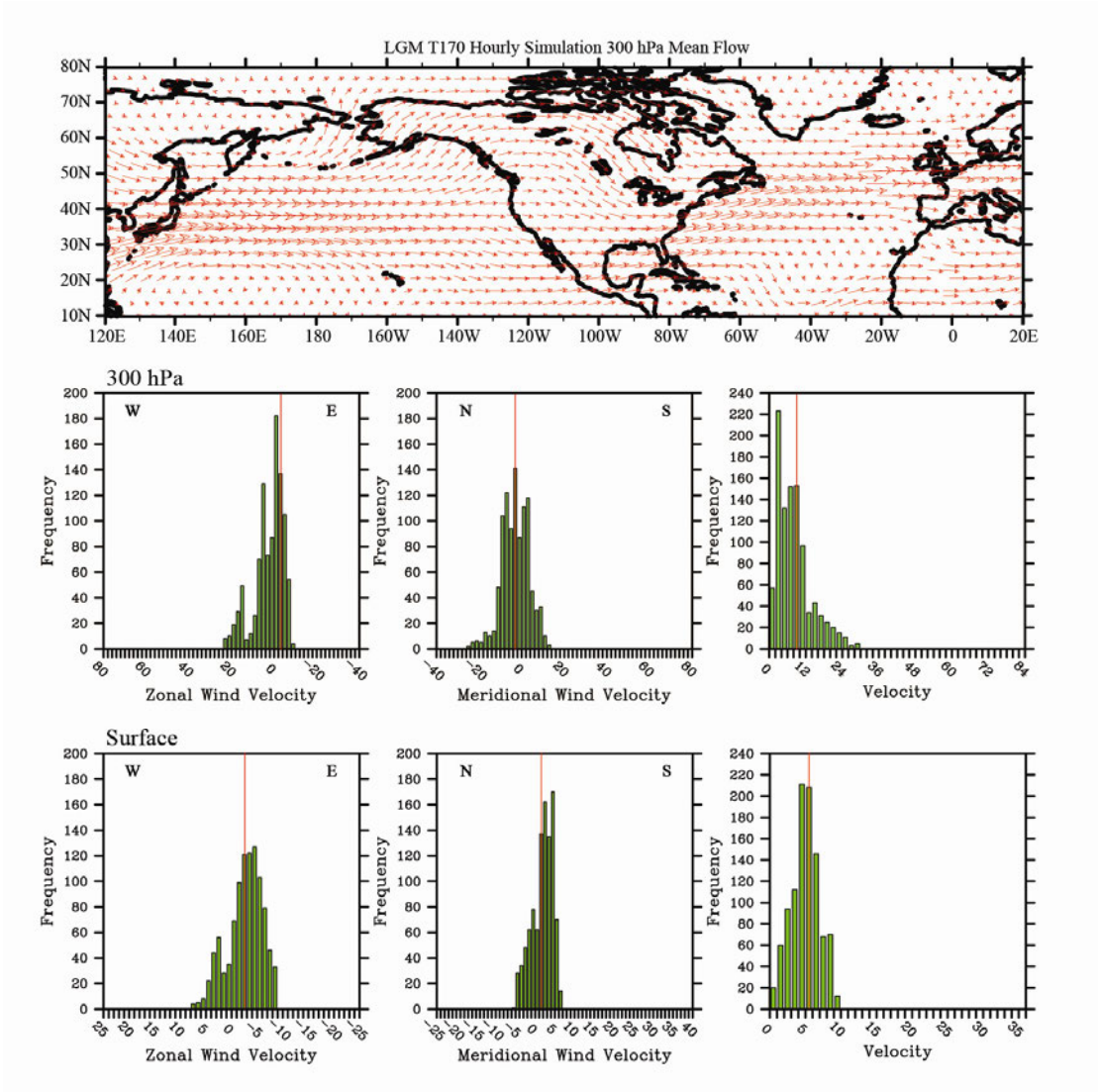

Figure 4.9: Upper level flow (300 hPa) mean (top) and the wind component frequencies for Summit, Greenland at 300 hPa (middle) and the surface (bottom).

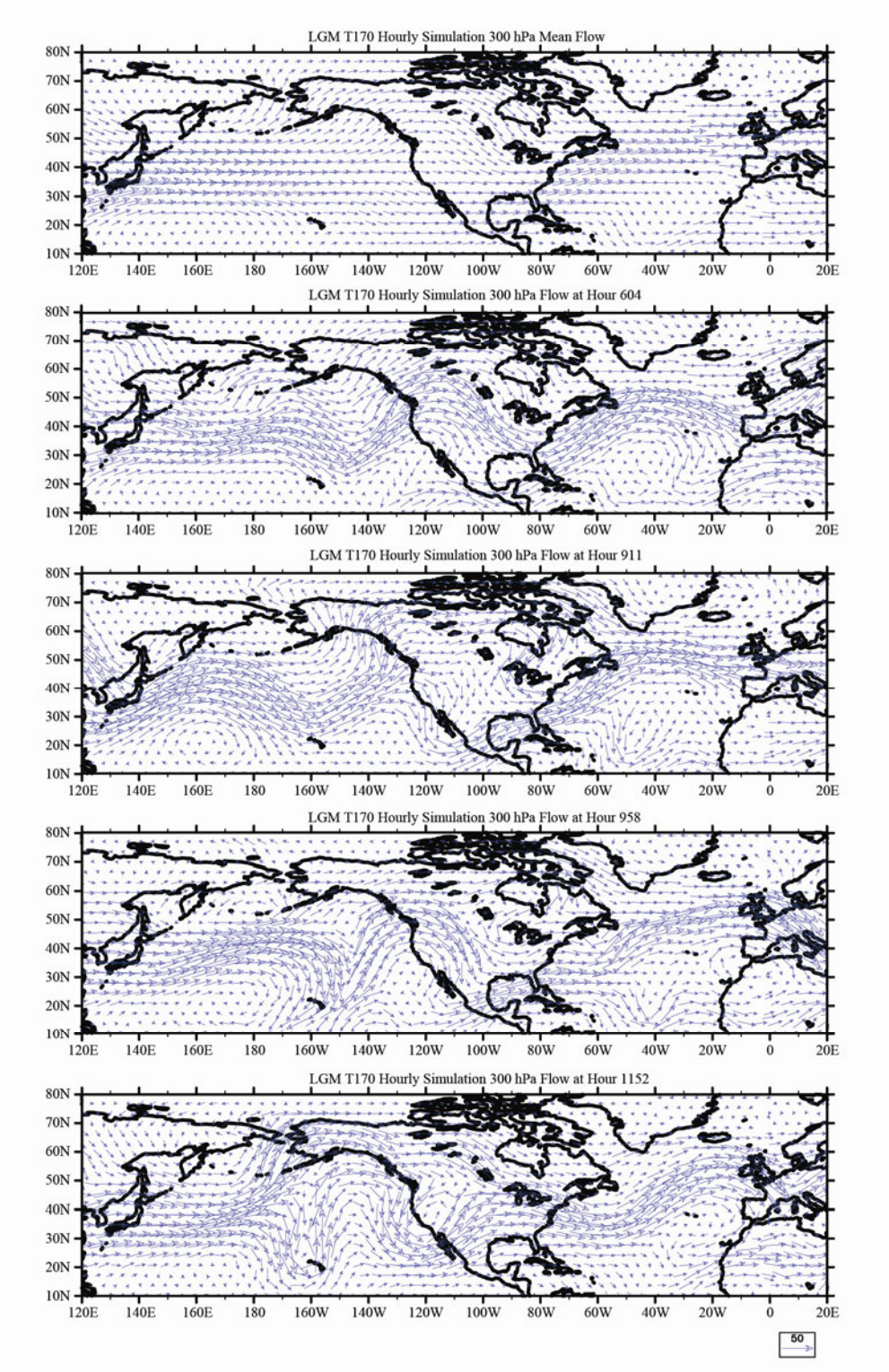

Figure 4.10: 300 hPa wind flow for the synoptic scale mean (top) and specified hourly snapshots demonstrating the transient wave-forms of the jet. Kona Low development occurs after the imbrication seen in the panels listed as hours 958 and 1152.

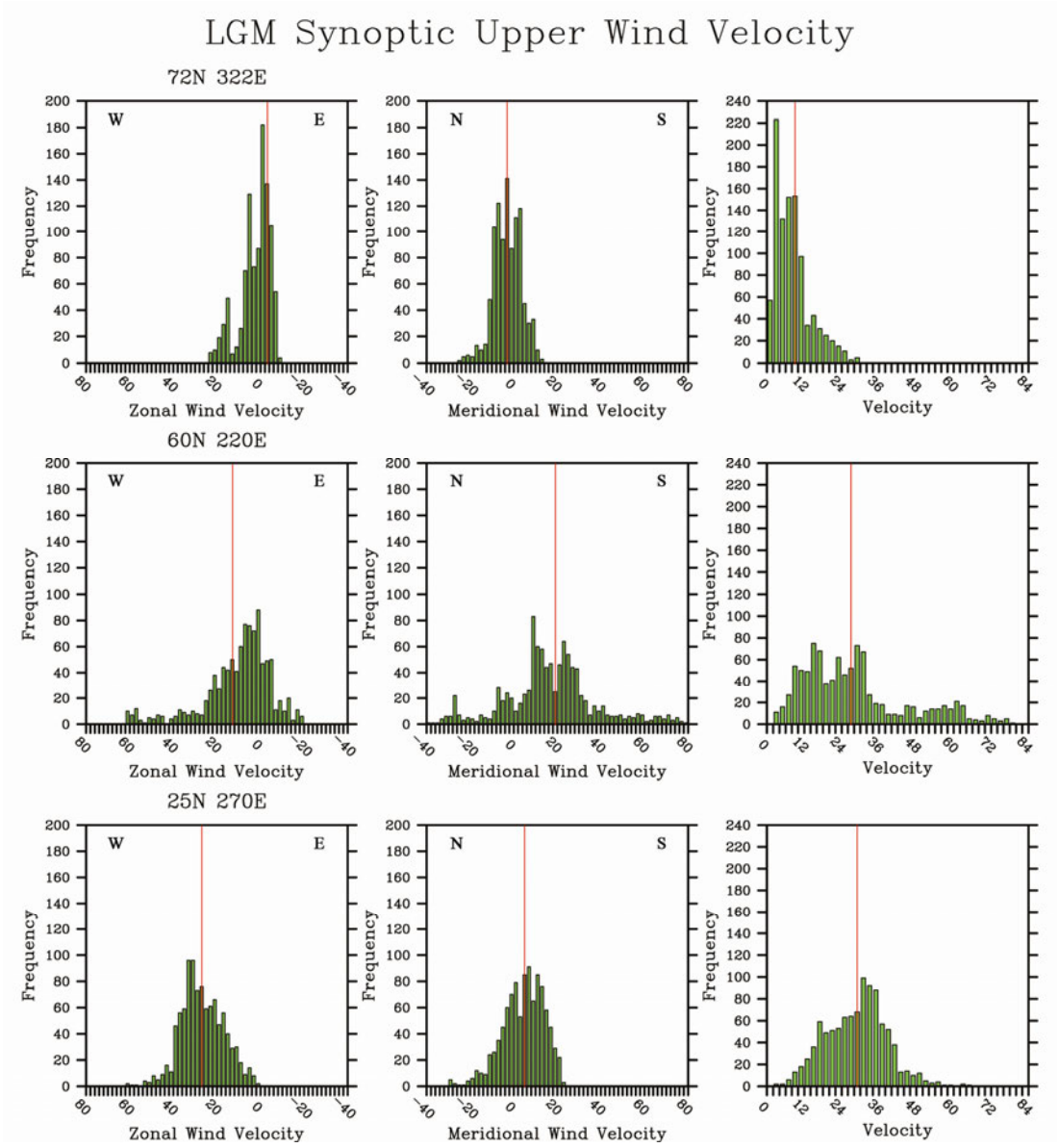

Figure 4.11: 300 hPa wind velocity component frequencies on the hourly scale for three grid point locations including the region around Summit, Greenland (top), the coast of Alaska (middle), and the Gulf of Mexico (bottom).

convergence zone. During these times, convective precipitation at the surface is pulled from the tropics into the mid-latitudes towards the Pacific storm track.

Instances of this extreme dip also produce a recognized meteorological event known as a Kona Low (model hour 1109 and 1168). This occurs when the mid-level jet dips extremely southward below 20°N but imbricates creating a detached eddy (Kona Lows are further described in Moore et al., 2008). Figure 4.10 shows some of these mid-level jet wave patterns as seen in the synoptic scale simulation. Panel (a) is a wave pattern similar to the mean state, with a distinct northern and southern branch splitting apart off the coast of California in the Pacific. Panel (b) and (c) contain a single branch state with panel (b) producing a large ridge-trough pattern with the ridge extending up over the Laurentide Ice Sheet beginning with the southerly flow in the Aleutians. The subplots (d) and (e) represent wave-pattern moments when the jet extends equatorward as described above. Panel (d) also shows the beginning of the formation of a Kona Low, near the 160°W line.

It is conceivable that precipitation derived from the low latitudes could bias the oxygen isotope ratios preserved in ice cores on Greenland if it were to become incorporated into the Pacific track. LGM wintertime precipitation on Greenland is significantly reduced compared to the modern and precipitation derived from sources further into the Pacific (or even tropical Pacific) would have a much lighter oxygen signature. This will be further explored in Chapter 5.

4.4 Variability below the LIS & Comparisons to Paleoecology:

Paleoecological studies continually try to reconstruct the vegetation of the glacial world (Crowley and Baum, 1987; Jackson et al., 2000; Mclachlan and Clark, 2004; and others). One of the primary assumptions in regards to changes in vegetation is that during the deglaciation, temperature sensitive trees rapidly migrated from southern refugia towards their modern day ranges. This notion relies on the consensus of global, highly variable, pollen reconstructions and macrofossil evidence, and the assumption that northern latitudes were simply too cold to maintain a steady population of cold-temperature sensitive (thermophilous) tree species during the LGM. According to these reconstructions, tree migrations rates range on the order of 10^2 – 10^3 metres per year (Mclachlan and Clark, 2004). Although these

calculations have been challenged before, these rates have been incorporated into models that are used to assess both climatic and ecological consequences given the predicted climate change of this century. However it has been hard to reconcile modern measurements of seed dispersal and the estimated paleo-rates derived from the LGM. One problem in reconciling measurements and reconstructions is simply the fact that LGM samples are so few, as well as the nature of pollen as a proxy. It can easily be blown long distances by synoptic-scale surface winds (e.g. gustiness) and estimates are highly variable depending on species. Trace amounts of pollen can therefore overestimate the range of a species (Mclachlan and Clark, 2004).

Here, the atmospheric hourly-scale findings are used to approach this discrepancy by comparing the high resolution results to regional vegetation reconstructions as a first-pass determination of what sorts of species could populate the region just below the ice margin - given simply the hourly scale variability and the potential for cold air outbreaks or large katabatic flows from the LIS to the north. It also provides the opportunity to compare (and maybe validate) an intriguing spatial result from the CCM3.6 against specific geological data sets.

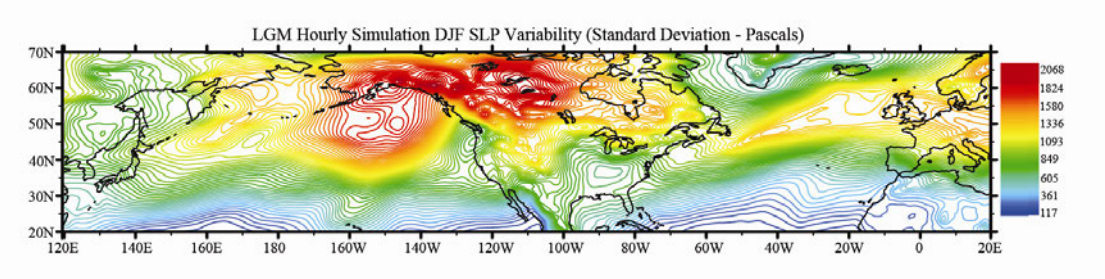

Figure 4.12a: Mercator projection of the synoptic scale (hourly) variability (standard deviation) around the Laurentide Ice Sheet region. The Atlantic storm track is clearly visible in the North Atlantic (yellow), as well as the area of injection of trans-Pacific storms into middle Alaska between 40°-70°N, 160°-140°W, (red).

Previous comparisons of pollen-inferred paleoclimates with GCM results have indicated large data to model differences especially for the Last Glacial Maximum in the eastern North American sector (COHMAP, 1988; Webb et al., 1993; Webb et al., 1998; Kutzbach et al., 1993; Kutzbach et al., 1998). Many data compilations indicate

substantially cooler temperatures in the eastern United States than those simulated in paleo GCM integrations with the CCM0 and CCM1 (cf. Chapter 2). Bartlein et al., (1998) suggested that this discrepancy is in part due to the spatial resolution of the model, and model specific processes that impact circulation. However, the geological data sets are also hard to reconcile due to the limited number of locations dated for the LGM as well as the tendency for pollen and small-scale macrofossils (e.g. small needles) to be distributed far distances via surface winds. Furthermore, the large decrease in the LGM concentration of atmospheric CO_2 (the boundary conditions used here for instance assume an atmospheric concentration of 200 ppm; cf. Chapter 3) may have had a direct physiological effect on plants, such as a change in water use efficiency, and may have altered the way certain species react to the modified climate. Most reconstructions do not take this into account (cf. Jackson et al., 2000). The magnitude of this effect however is debatable (cf. Crowley, 1995; Crowley and Baum, 1997). Further problems arise with the geological distribution of relevant LGM sites, geological distributions of preserved macrofossils, the dominance of extinct or no-analogue populations within a site and the assumptions used to create full biome or analogue maps.

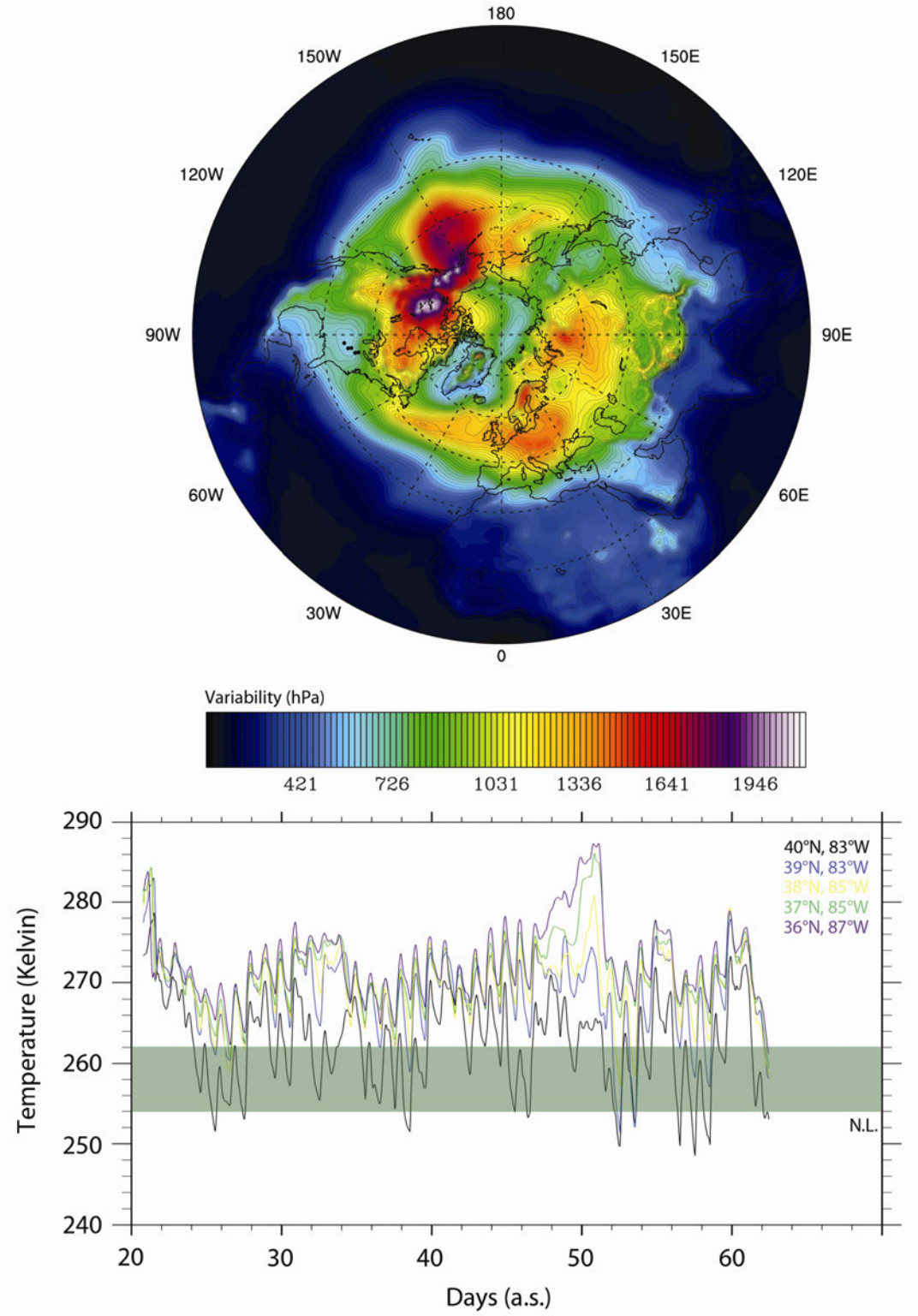

Figure 4.12b: Polar projection of the Northern Hemisphere sea level pressure variability (standard deviation) with the latitude and longitude data points of the temperature time series transect over the days after spin-up (bottom). Green window represents the modern northern limit of thermophilous tree species such as the Red Maple and American Beech (cf. Mclachlan and Clark, 2004).

Variability of sea level pressure and temperature has a large impact on regional biomes including below the ice sheet margin. The North American sector sea level pressure variability plot (Fig. 4.12a) and the Northern Hemisphere expansion (Fig. 4.12b) show areas of expected higher SLP variability around locations described later (Chapter 5) to be the North Atlantic storm track and the area of large cyclogenic "injection" of trans-Pacific storms in the North Pacific, towards middle Alaska. The Northern Canada and Aleutian sector contain the highest level of variability seen in the synoptic scale record for this sector. A tongue of high variability is also noticeable further south, along the eastern edge of the Rocky Mountains, south of the margin of the Laurentide Ice Sheet. Just east of this area is coincident with eolian sediments that suggest a shift to north-westerly flow during the glacial in this area (cf. Wells, 1983; Crowley, 1991). There are also regions of high variability near the Fennoscandian Ice Sheet in Western Europe, Norway and Sweden. Northern Siberia also has a peak of higher variability, approaching the modern Lena River. The switch from a low variability region, to higher levels in Northern Siberia and the Sea of Japan coincides with cyclogenesis in the North Pacific (also Chapter 5).

A low variability area is also seen around Greenland. Although this will be discussed in more detail later, it is important to first mention it here as it links the Pacific and Atlantic variability sectors (note also the tongue of higher variability to the W/NW). It is bound around 0°W-60°W and wraps around on the eastward side of the continent. The high variability just to the west represents the exit of the Pacific storm track north of the Laurentide Ice Sheet.

The primary area of concern in regards to comparison of the synoptic-scale results with paleo-ecological data sets is the pan-handle of low variability within the continental United States just west of the Appalachian Mountains. The northern most edge of the low variability resides near Columbus, Ohio at 40°N, 83°W, just along the ice sheet margin. This area encompasses ~8250 km^2 east of the Mississippi River extending southward (along "strike" of the Appalachian Mountains) and is specifically within the area of significant data to (lower resolution) model

discrepancies in other analyses (see above). Within the LGM simulations, this area may represent a no-analogue condition, where it is bound by topography on three sides during the LGM: the Appalachian Mountain Range to the east, the Laurentide Ice Sheet to the north and the Rocky Mountains and Colorado Plateau to the west. This condition therefore, may be reflected in regional paleo-vegetation reconstructions if it represents a real feature of the ice age wintertime.

The modern northern limit of two thermophilous tree species is also plotted in the time series in Figure 4.12b (bottom). The green window is the northern limit of Red Maple (*Acer rubrum*) and American Beech (*Fagus grandifolia*). Events which cause the reduction of temperature below this level may result in tree loss if the physiological reactions to temperature were the same during the LGM as they are today. The majority of the time-series is dominated by the beat of the diurnal cycle. The excursions away from this beat represent moments of synoptically interesting events that would affect the surface air temperature. Yet, over most of the time series, the areas just south of 40°N, 83°W rarely break the modern northern limit of these species, relating to the low variability nature seen in Fig. 4.12a and 4.12b and the aforementioned surface flow characteristics (e.g. in section 4.2).

The low variability area is first compared to Jackson et al. (2000) who reconstructed LGM vegetation using pollen and microfossil data from 21 and 17 well-dated locations. Each site was chosen with assemblages within the LGM time span of 21,000 ± 1,500 calendar yr BP (cf. Jackson et al., 2000 Fig. 1 and table 1). Pollen percentages were interpolated simultaneously along spatial and temporal coordinates to a 100x100 km grid in a region east of the Mississippi River below the ice sheet margin. Both an analogue and biome technique was implemented to determine the extent of vegetation types. Analogue results indicate vast areas that lack modern floristic analogues during the LGM in the region. Overall, the reconstructions suggest a cool North American interior in the region (more so than Webb et al., 1998 for instance). However, macrofossil evidence suggests that the degree of cooling may be overestimated (cf. Jackson et al., 2000). One of the main reasons for this is the

presence of a large amount of material from a now extinct species of Pine (*Pinus critchfeldii*) that is associated with temperate deciduous trees, and warmer

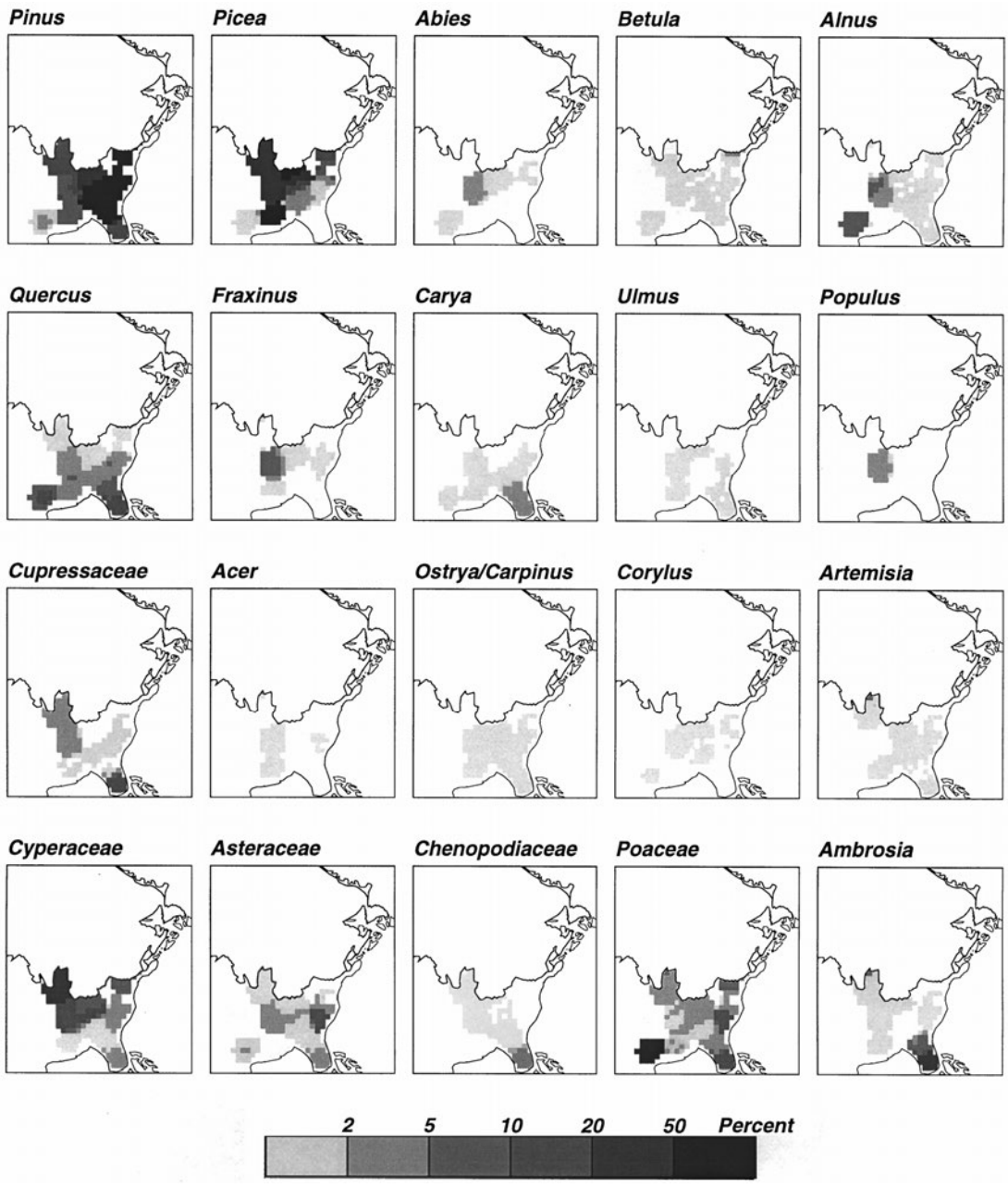

Figure 4.13: Isopoll maps from Jackson et al. (2000). Pockets of *Fraxinus* (Ash), *Acer* (Maple), *Populus* (Poplar), *Ulmus* (Elm), *Ambrosia* (Ragweed), *Asteraceae* (Aster or Daisy Flower), and certain sedges (*Cyperaceae)* are found in the area of low variability seen in the synoptic scale integration. Many of the pollen inferred formations of Jackson et al. (2000) are no-analogue in this region, and pollen suggests relatively cooler LGM temperatures here, in respect to other

reconstructions such as Webb et al. (1998). However, the northern progression of warmer species of *Pinus*, and macrofossils suggests the cooling of the LGM interior is overestimate here.

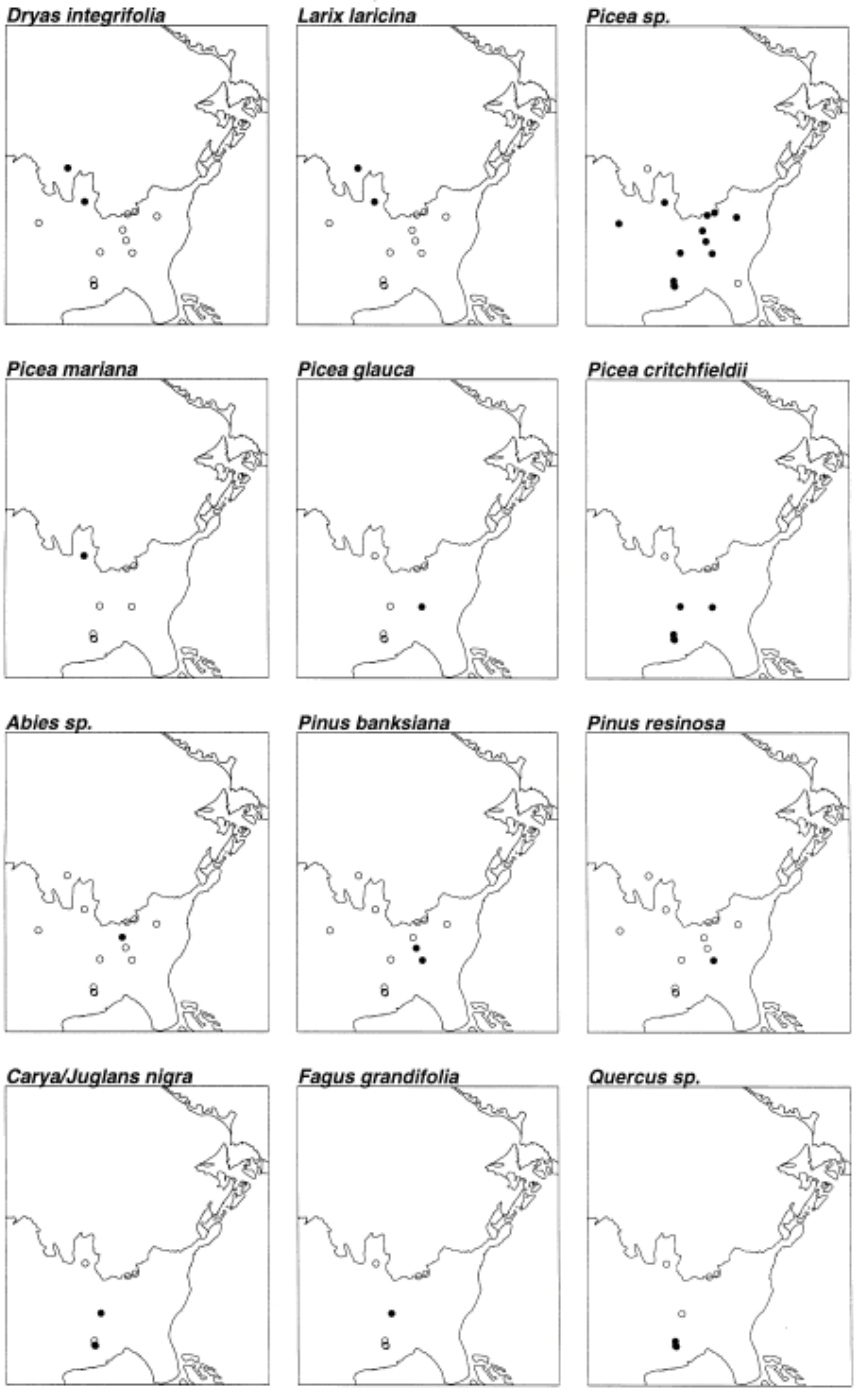

Figure 4.14: Macrofossil data taken from Jackson et al. (2000). Dark circles represent presents of fossils, while circles represent either absence or presence but counted as absent (cf. Jackson et al., 2000). *Pinus critchfeldii* is a now extinct species of Pine that is associated with temperate forests.

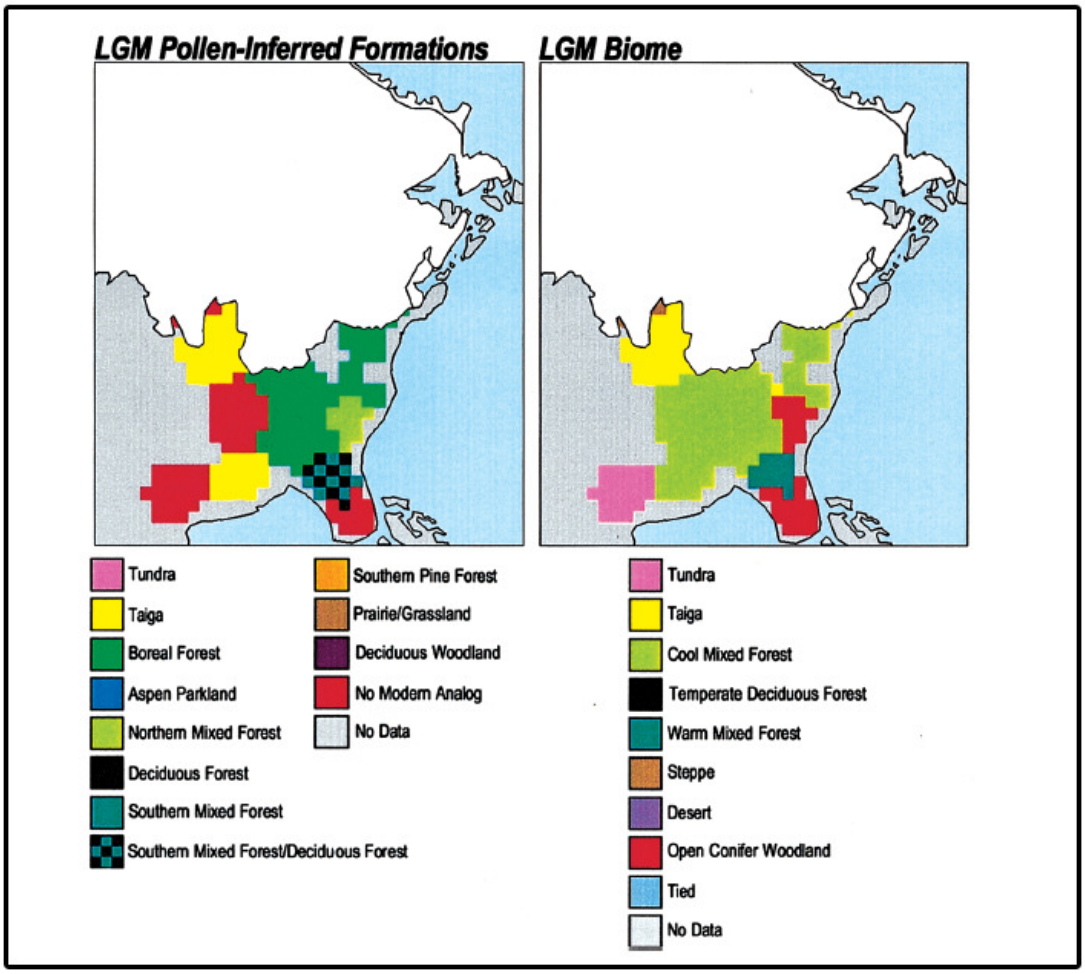

Figure 4.15: Vegetation reconstruction from Jackson et al. (2000).

temperatures than similar counterparts. Furthermore, the presence (or absence; cf. Fig. 4.13) of species such as *Fagus grandifolia*, *Acer* spp., *Quercus* spp, *Juglans nigra, Lirodendron tulipifera, Ulmus Americana,* and *Caprinus carolinana* is unlikely at the inferred cooler temperatures (Jackson et al., 2000). Consequently, accuracy of the reconstruction varies regionally with the areas along the ice-margin and interior highlands being more accurate and comparable to some modern assemblages.

Many pollen reconstructions rely on a threshold percentage to delineate the absence or presence of a population, due to dispersion issue. For American Beech, this threshold is around 0.5% (Mclachlan and Clark, 2004). In Jackson et al. (2000), none of the LGM sites meet this threshold (Although some does exist - see Fig. 4.13, 4.15) for this species in the eastern United States – the LGM reconstruction of which is mostly dominated by various groups of Pine, which produces a copious amount of pollen compared to other species. One site in the Jackson et al. (2000) reconstruction contains Beech macrofossils however (Fig. 4.14), which are less easily dispersed simply due to their greater size and may be indicative of a small local population. These results including the potential for warmer temperatures in this area, the no analogue condition, presence of evidence of thermophilous tree species and the low-variability region first identified in the hourly integration may be interconnected, although further evidence needs to be presented before it can be accepted – the lack of proxies and the far from ideal conditions of preservation in this area makes this difficult.

Other evidence which may lend credence to the regional results lies south of the Laurentide Ice Sheet where large areas were covered with deposits of loess, especially within the Missouri and Mississippi drainage areas (Wells and Stewart, 1987). Although these deposits are not favourable to the preservation of pollen and plant macrofossils (due to the large interstitial pore space), it has preserved large quantities of LGM landsnails. One in particular is the fossil range of the Central Plains pleniglacial land snail, *Discus shimekii* (Wells and Stewart, 1987) which may support the synoptic scale results (and climatological) in this area.

Figure 4.16 shows the current range of *Discus shimekii*, as well as in-situ LGM sites. Currently, the range of the snails resides along the Rocky Mountains in the western United States (shaded area). During the LGM however, the colder conditions contributed to the eastward expanse of the range. Sometime during the deglacial transition therefore, the landsnails began to shift their ranges westward until they became restricted to their current positions of cordilleran-boreal forests in the Rocky Mountains, and Canada. The exact timing of the demise of the landsnails within the

Central Plains is not known. Noticeably however, the eastward limit of the LGM range resides on the north eastern boundary of the low variability core seen in the synoptic scale integration presented in Fig. 4.12 (a, b), and the area where the synoptic *and* climatological surface results show a shift towards more south-westerly flow (Fig. 4.3, 4.6). So, although the hourly results demonstrate the variability pattern for a single season, the more equable environment is manifested in all four-years of the climatological run with the south-westerly shift in surface winds on the eastern flanks of this area. Subsequently, this produces meridional heat fluxes similar to that of the climatological modern run which will be highlighted in the next Chapter – these values are not seen in lower resolution (e.g. T42) CCM3 experiments where the LGM to MOD differences are much more negative in the area (cf. Kim et al., 2008).

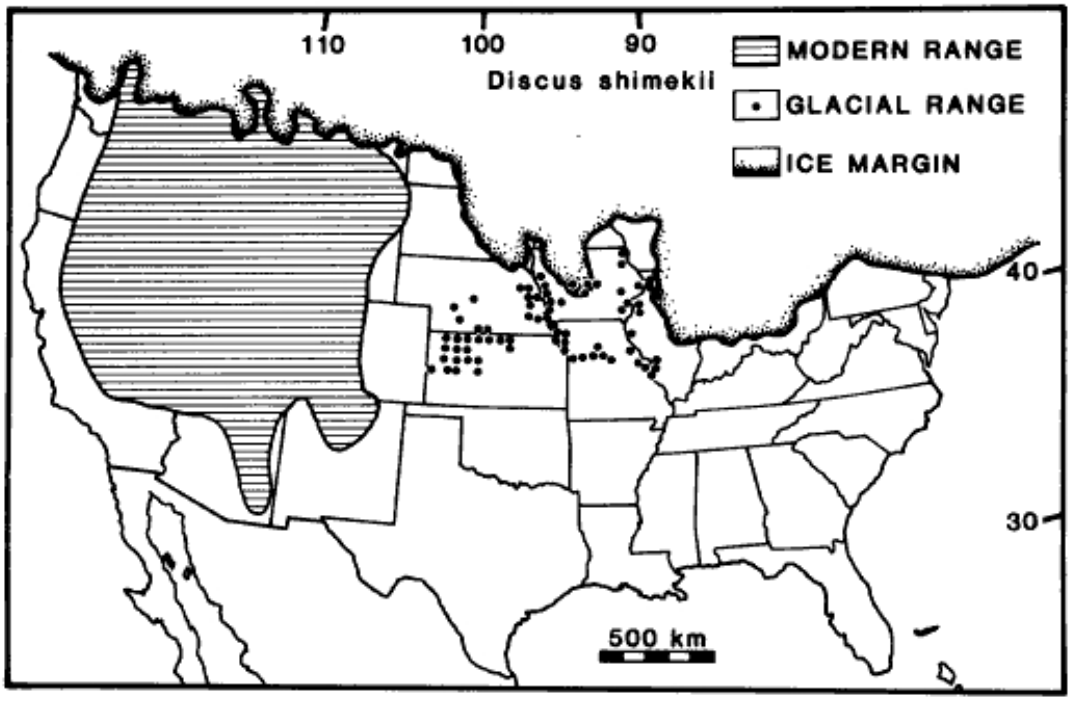

Figure 4.16: Modern and LGM ranges of *Discus shimekii* over the continental United States (taken from Wells and Stewart, 1987).

4.6 Discussion and Summary:

In this chapter surface flow, sea level pressure and sea level pressure variability during the LGM were analyzed and the first comparisons were made between the climatological simulation, other GCM experiments, modern observations and specific geological records. Since the general results compare well with the climatological integration, as well as other recent (longer) modelling studies and geological interpretations which have lent considerable insight into our understanding of the LGM atmosphere (e.g. Charles et al., 1994; Bromwich et al., 2004; Langen and Vinther, 2008; Donohue and Battisti, 2009; and several others) the hourly-scale wintertime must be somewhat typical of an LGM winter (cf. Fig. 1). The synoptic scale simulation presents the opportunity to look at synoptic events, including extreme events which may have a disproportionate impact on proxy records – as opposed to an overall (normal) mean.

Results show that the LGM mid-level northern hemisphere jet is forced into a modified split (cf. Manabe and Broccoli, 1985). The northern branch extends up over Alaska and Canada and subsequently drops southward over the northern margin of the Laurentide Ice Sheet and the Labrador Sea. The southern branch extends southward towards Mexico. Although this represents the mean state of the jet, the jet synoptically fluctuates between transient wave-forms. One wave-form consists of a large southerly dip towards the ITCZ (cf. Figs. 4.9, 4.10), which imbricates and detaches forming a Kona Low system (Moore et al., 2008). At the surface, precipitation is pulled from the tropics towards the North Pacific track. If the LGM moisture sources to Greenland were to shift similar to the hypothesis of Charles et al. (1994) and become entrained into the North Pacific storm track, then this precipitation would modify the $\delta^{18}O$ seen in the Greenland ice cores.

In the climatological run, North Pacific inter-annual variability increased around the Aleutian low by ~25% as compared to the modern reanalysis data. In the North Atlantic, sea level pressure variability decreased by ~35%. This variability is also manifested in terms of changes in cyclogenesis in the synoptic run, which is within 2σ range of variability of the climatology, and will be discussed in Chapter 5.

Geological records lend credence to the low-variability (and relatively warmer) pattern seen just below the ice sheet margin in the synoptic scale simulation. This area, just west of the Appalachian Mountains may represent a no-analogue condition in which the region is bound on three sides by topography with the low variability core in the centre. This area is coincident with a shift towards south-westerly flow in both the synoptic mean surface winds and *each* of the four years within the climatological LGM simulation. The large areas of no-analogue vegetation, and the presence of temperature hardwoods and cool-temperate conifers as far north as 35°N in the Jackson et al. (2000) reconstruction continue to suggest that conditions were not as severe in this region. The presence of *Pinus critchfeldii* and species of Aster (*Asteraceae*) within the low variability core region also lends credence to the synoptic scale integration result. Furthermore, some studies have found trace amounts of in-situ temperature sensitive tree pollen further north, although the small amounts and nature of the proxy make it hard to reconcile (cf. Maclachlan and Clark, 2004). It should also be noted that the reconstructions of Webb et al. (1993, 1998) are even less severe and warmer than the Jackson et al. (2000) reconstruction. Consequently, conditions below the ice sheet margin on the eastern edge of the Great Plains of North America may in fact be less severe and more equable than the surrounding regions. This area produced large quantities of no-analogue vegetation and the western edge of which represents the eastern boundary of pleniglacial landsnails which prefer the modern cooler climates of the Rocky Mountains. If the synoptic results are indeed indicative of such a regional paleo-environment and the relatively low amounts of LGM dated pollen below the margin represent small populations of thermophilous tree species, the current migration rates used in models (see section 4.4) may need to be adjusted (and significantly reduced) to be more comparable to modern measurements of seed dispersal (Clark et al., 2002; Clark per. com.). A synoptic-scale "gust" analysis, similar to that presented briefly here (e.g. Fig. 4.8) and more so in Chapter 6, may help our understanding of paleo-dispersion rates.

Chapter 5

Results: Paleometeorology - Mid-Latitude Northern Hemisphere Cyclogenesis during the LGM

5.0 Introduction and Background:

This chapter primarily focuses on surface and upper level flow during the LGM on the synoptic scale, with specific attention given to the ice age properties of cyclogenesis, storm tracks, and the convective precipitation delivered to specific regions via transient eddies within the hourly-scale simulation. These results are intimately linked to the surface features presented in Chapter 4 and comparisons will be made between them.

High-resolution animations of the ice age have been developed and can be utilized to analyze the "paleometeorological" circulation. They have been compiled for initial model observations of mid-latitude storm processes and other synoptically interesting features (individual events) that may not be described by lower resolved simulations (such as the storm occlusion process which can happen on the order of several hours). The animations are included in the Appendix and will be made available online for interested parties. Further discussion on both animation and model methodologies can be found in Chapters 2 and 3.

***

The synoptic results presented here represent a single LGM winter and therefore bring with it the caveats of such as discussed throughout this thesis. To determine the typicality of the results presented in this chapter to all ice-age winters, comparisons to the in-tandem 4-year climatological run, geological data, and longer-duration recent GCM experiments will be made, in addition to those already mentioned in Chapter 4.

In several cases, results show responses that could help explain the interpretation or lend insight into the debate of specific geological records, and/or may also be extrapolated to the longer glacial time scale. However, the later instances are mentioned only when results are consistent with other models *and* the geological data always recognizing that the field of "paleometeorology" needs to develop further before such conclusions can be fully accepted. In some instances, these cases may be explained by a specific meteorological event having a disproportionate impact on the "mean-state" as recorded in proxy records (e.g. Question 4 below; Bishop et al., 2002) which itself could also then be interpreted to represent longer time-scales (such as Winograd, 1992; Herbert et al., 1998; Herbert et al., 2001; Winograd, 2002). The synoptic results will first be presented alongside some of those of the climatological run and geological data, but a final section will highlight key comparisons.

***

Recently, high spatially-resolved model studies of the LGM have advanced our understanding of circulation responses to massive northern-hemispheric ice sheets (e.g. Toracinta et al., 2004; Kim et al., 2008). Studies are now better able to quantify mesoscale processes such as temperature and precipitation changes over ice sheets and regions of moderate topography (Bromwich et al., 2004; Toracinta et al., 2004; Kim et al., 2008) which are important for the continued inspection of proxy data. Models such as the CCM version 3.6 used here can be run at grid resolutions higher than 1° (latitude/longitude), better resolving geographical and topographical features which impact meteorological results such as the ability to resolve storm intensities

along the full length of a storm lifetime (Blender and Schubert, 2000). Such results can also provide valuable constraints on evaluating the reliability of regional-scale predictions of climate change due to global warming.

Lower resolution studies of the past have investigated LGM and modern storm tracks and precipitation (e.g. Kageyama et al., 1999; Kageyama and Valdes, 2000) and have documented the importance of ice age orography and sea ice on transient eddies. Widely accepted is the Laurentide Ice Sheet's (LIS) capability to impact northern hemispheric flow, both at the surface in regards to storm tracks, and upwards to include the mid-level jet. Storm tracks in these studies have been demonstrated to shift eastward in the North Atlantic away from the North American coast. Many LGM studies find that the mid-level jet develops into a split (cf. Manabe and Broccoli, 1985) or enhanced ridge-trough pattern off the west coast of North America (Bromwich et al., 2004; Toracinta et al., 2004; Kim et al., 2008; and here – Chapter 4). However, the specific nature of LGM storm tracks is still under debate. The intensity and spatial distribution of storm tracks is highly dependant on boundary conditions, resolution and the specific climate model itself (cf. Chapter 2). Consequently, early model studies investigating storm tracks were at variance – the reader is pointed to the multi-model comparison study of Kageyama et al. (1999). Several questions still remain (which are potentially resolvable), in varying degrees of uncertainty, given ice age conditions:

1. In the North Atlantic, was there a change from the modern in storm frequency, lifetimes and magnitude?
2. How were storm tracks spatially perturbed?
3. How could the change in storm tracks affect our understanding of proxy data such as the increased LGM atmospheric dust burden and fluctuations of $\delta^{18}O$ Greenland ice cores?
4. Can individual synoptic events such as large storms have a disproportionate impact on specific geological records?

The hourly outputs obtained in the project presented here, presents the opportunity to further study storm tracks, cyclogenesis (this chapter), air-parcel trajectories (next chapter) and convective precipitation during the LGM, at the synoptic level and to address many of these questions in this Chapter and the next.

Investigating LGM storm intensity, structure, and lifetime requires increased spatial and temporal resolution, which has yet to be fully explored for the majority of paleo-simulations. For example, for modern simulations, it has been shown that "the higher the resolution, the better the storm tracks are modelled" (Kageyama et al. 1999). Bengtsson et al. (2009) also demonstrated that at increased spatial resolutions (approaching T213), extra-tropical cyclones were simulated with greater realism, including a better representation of storm development and growth rates, with the full observed range of intensities which are not picked up by lower resolution runs. A more detailed discussion on resolution impacts on meteorological results can be found in Chapter 2, section 2.2. The analysis of storm intensity variations is included in Unterman et al., (submitted).

***

Abstract of Results:

Results from the North Pacific show high storm intensity during the LGM, whereas the North Atlantic is more quiescent. This result agrees with other simulations of the ice-age winter (e.g. Unterman, 2007; Donohue and Battisti, 2009). Plots of storm tracks indicate (section 5.1) that for the synoptic simulation, all North Pacific storms were steered northward into the Gulf of Alaska, bringing relatively warm air and precipitation into the region (e.g. Fig. 5.1 and 5.2). The strong tendency for Pacific storms to track up the west coast of North America presumably causes/contributes to "early" warming in nearby land areas due to increased poleward heat transport and the subsequent decreased upwelling due to the onshore south-westerly flow. It could be erroneous to interpret such warming as a forcing agent for deglaciation; the response could well disappear as ice sheets melt. Similar "warmings" observed

elsewhere might need to be reassessed in terms of a natural regional response to ice age boundary conditions, rather than as causes of deglaciation. This hypothesis is in agreement with other geological data such as evidence of an Alaskan white spruce refuge (Andersson et al., 2006), Cordilleran glacier records (Young et al., 2011) and expansion of Great Basin Lakes (Benson et al., 1990). The inferred decrease in coastal upwelling along the North American coast is also in agreement with a statement made in Herbert et al. (2001) in regards to the decline of California Sequoia.

Overlay of the hourly wind fields illustrates striking regional features, including atmospheric "boundary currents" along the base of ice sheets, very sharp Intertropical Convergence Zones, a well-defined high pressure system over the eastern Mediterranean, and "strings" of northerly flow from Siberia and Greenland that penetrate into lower latitudes (shown later). For the Pacific case, north-westerly flow turns north-easterly in the Indonesian sector and crosses the equator east of New Guinea. This strong equatorial Pacific westerly flow, which is consistent with the climatological run, may conceivably have had an effect on the west-east hydrostatic head responsible for El Niño oscillations (cf. Chapter 4, Fig. 4.3, 4.5). These features, along with storm systems across both ocean basins (e.g. Fig. 5.1, 5.2), can also be noted in the high-resolution animations. Further investigation of these runs may provide additional insight into features such as wave-wave interactions. These fields have previously been unavailable to the research community for an alternate-Earth climate that has been at least as common as the present one over the last 500,000 years.

5.1 LGM Cyclogenesis – from Birth to Death:

High spatially and temporally resolved climate models can more accurately portray storm tracks and cyclogenic processes responsible for the delivery of warm air and regional convective precipitation (Blender and Schubert, 2000; Bengtsson et al., 2009). Changes in either the background large scale precipitation or transient eddy moisture sources can affect the geological record such as the oxygen isotope ratios

preserved in ice. Fluctuations of past surface temperature are preserved in the $\delta^{18}O$ isotope record of many proxies such as speleothems (cave deposits) and ice cores such as those on Greenland. These proxies have been used to estimate the magnitude of temperature change of past climate events including that of the LGM. However, the extent of surface cooling during this time, and the sources of past Greenland precipitation have been a topic of debate for decades (CLIMAP, 1985; Broecker et al., 1985; Charles et al., 1995; Fawcett et al., 1997; Dahl-Jenson et al., 1998; Langen and Vinther, 2009). One way to analyze this problem is to look at the high resolution storm tracks, to better resolve circulation changes and synoptic scale systems that impact such precipitation delivery to the west coast of North America, the Laurentide Ice Sheet, and subsequently Greenland.

Trajectories are binned based on the maximum intensity along the entire pathway of the storm in Figure 5.3. Storms entering the North Pacific from eastern Siberia and the Northern Japan area migrate eastward until they are driven northward along the coast of North America and middle Alaska and over the Laurentide Ice Sheet. These storms then terminate west of Greenland along the northern edges of Canada or the Labrador sea (cf. 5.4). In the North Atlantic, the storm track is narrowed along the sea ice margin until expanding towards the European sector and Fennoscandian Ice Sheet. The total number of storms tracked entering each basin is 83 for the North Pacific and 61 for the North Atlantic (using MSLP).

In the North Atlantic, storm trajectories are mainly confined to a narrow strip 3-4° south of the southern edge of the sea ice margin and rarely migrate northward of 43°N-44°N, except in the easternmost Atlantic (Fig. 5.3). The offset from the sea ice margin is probably due to the strong northerly winds coming off the ice and forcibly displacing the track southwards (cf. Chapter 4). The band of maximum surface wind convergence corresponds approximately to the northern edge of the Gulf Stream in the western Atlantic during the LGM (Crowley, 1981).

Although the dominant Pacific-Alaskan trajectory (see also Fig. 5.1 and 5.2) might have been influenced by upper-level high pressure over the dome of the North

American ice sheet, inspection of the composite of the hourly mean flow fields for the synoptic run (cf. Chapter 4, Fig. 4) indicates a quasi-permanent surface high pressure system in the eastern North Pacific. The feature is centered on about 30°N, 130°W, and appears to have exerted a significant surface block to the easterly moving North Pacific lows, with the southwesterly flow from the high pressure system effectively steering the North Pacific lows along a southwest-northeast trend from about 25°N, 160°W to 45°N, 140°W. Streamflow convergence in this region may also have affected sub-surface mode-water formation.

Intensity distributions reveal differences between the ocean basins. Both MSLP and vorticity parameters were used in the tracking analysis, following the methodology of Hoskins and Hodges (2002). This is because vorticity is much more sensitive and picks up a wide range of disturbances (Chapter 3). Consequently, although both are shown, MSLP is primarily described in terms of the spatial distribution of the trajectories and vorticity for intensity distributions – to account for the full range of intensities along the length of a storms lifetime including shortly after development and right before termination.

Overall the North Pacific is 14.9% more intense than the North Atlantic during the LGM. Storm counts in the North Atlantic (Fig. 5.5) reveal a broad standard distribution in vorticity intensity during the modern,

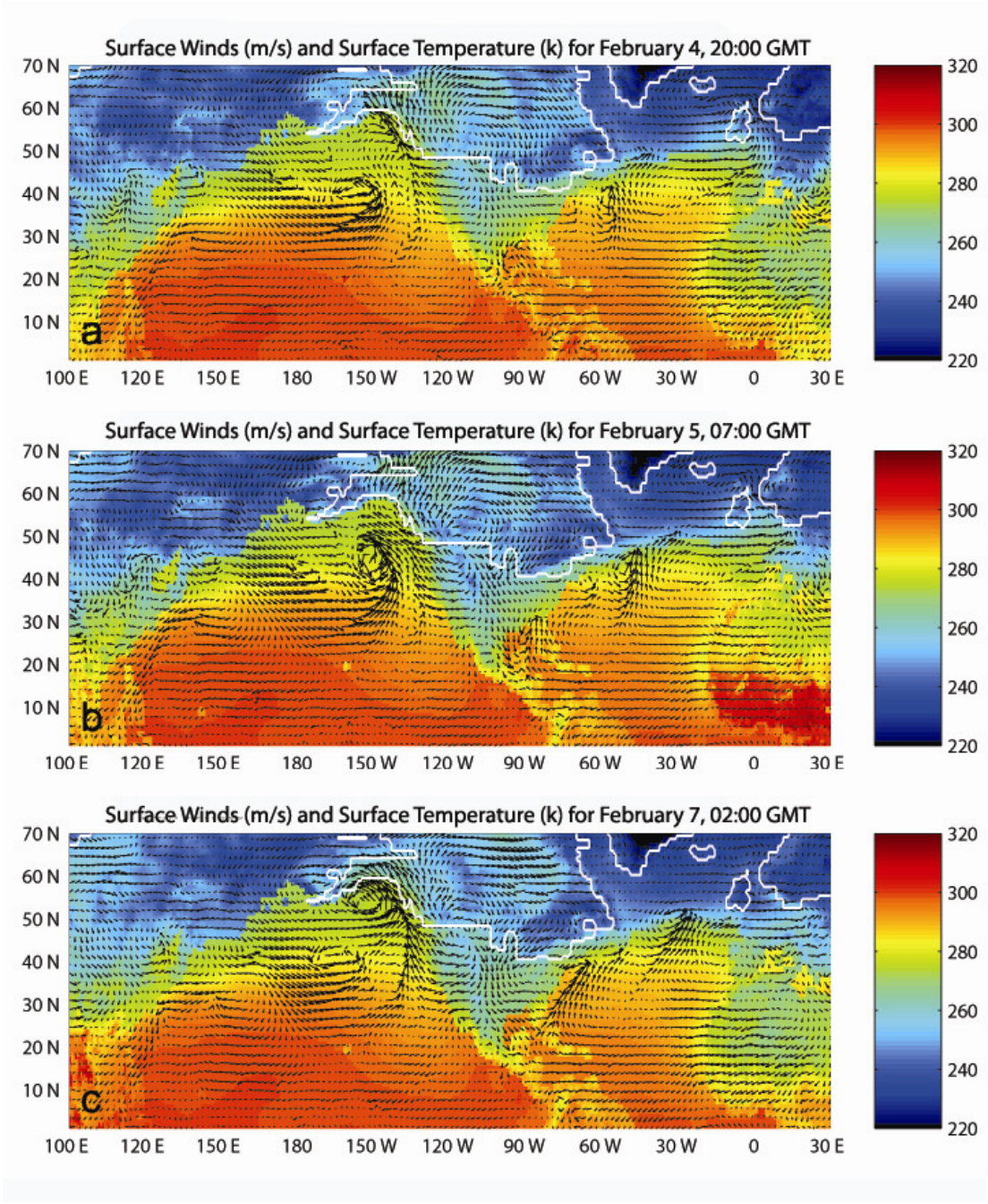

Figure 5.1: A trans-Pacific storm forms off the north east coast of Siberia and eventually is deflected northward along the enhanced ridging towards middle Alaska. It should be noted that this is a relatively large storm with winds exceeding the 45-50 m/s mark after February 5, 07:00 GMT model time.

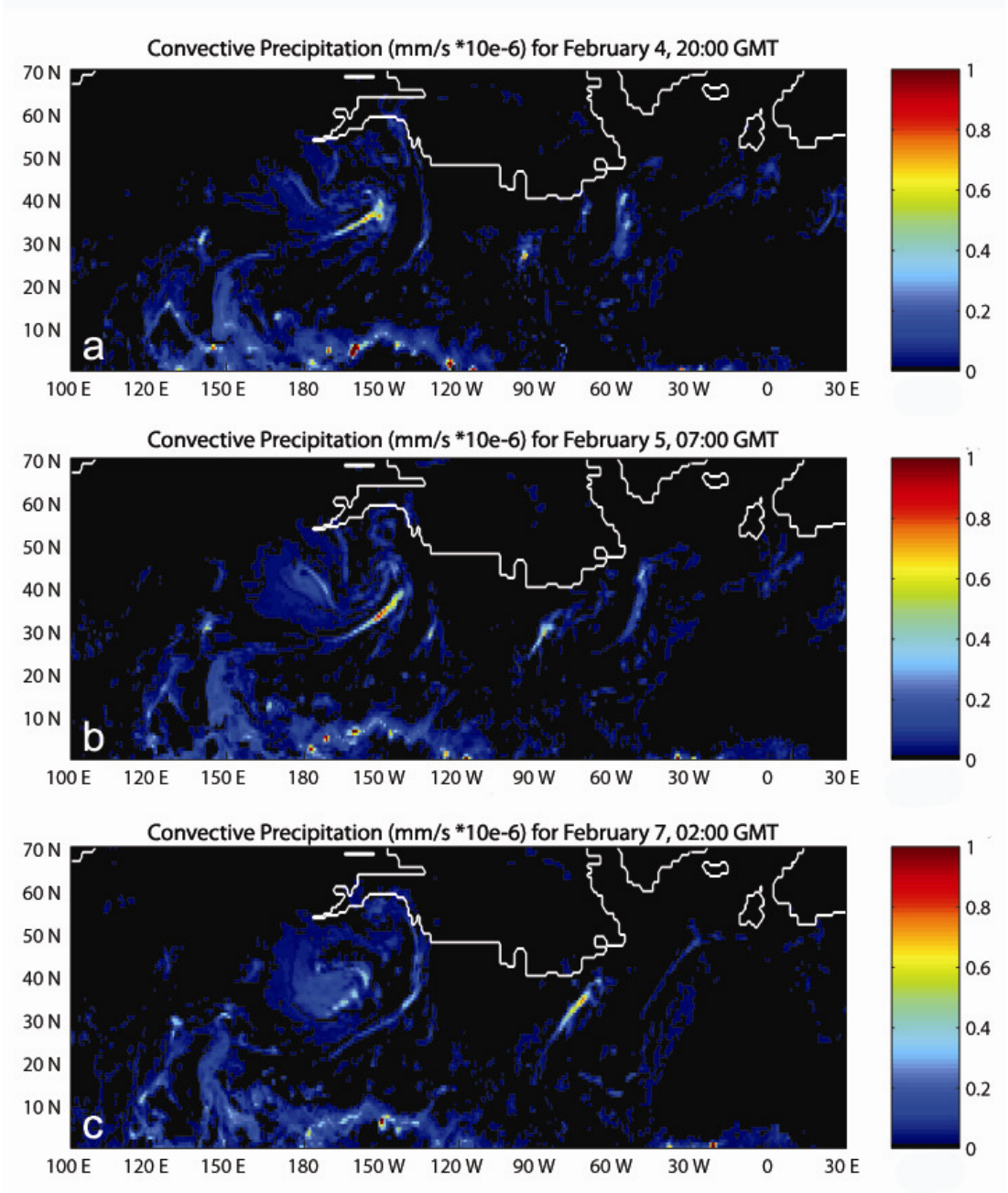

Figure 5.2: Tracking the same large Pacific storm shown in the surface wind fields of Fig. 5.1 but within the convective precipitation parameter. White outline is the margin of the ice sheet. Pacific storms such as this one, which formed off the north east coast of Siberia or northern Japan, bring relatively warmer air to middle Alaska as well as the potential for strong rain or serial rain-out events.

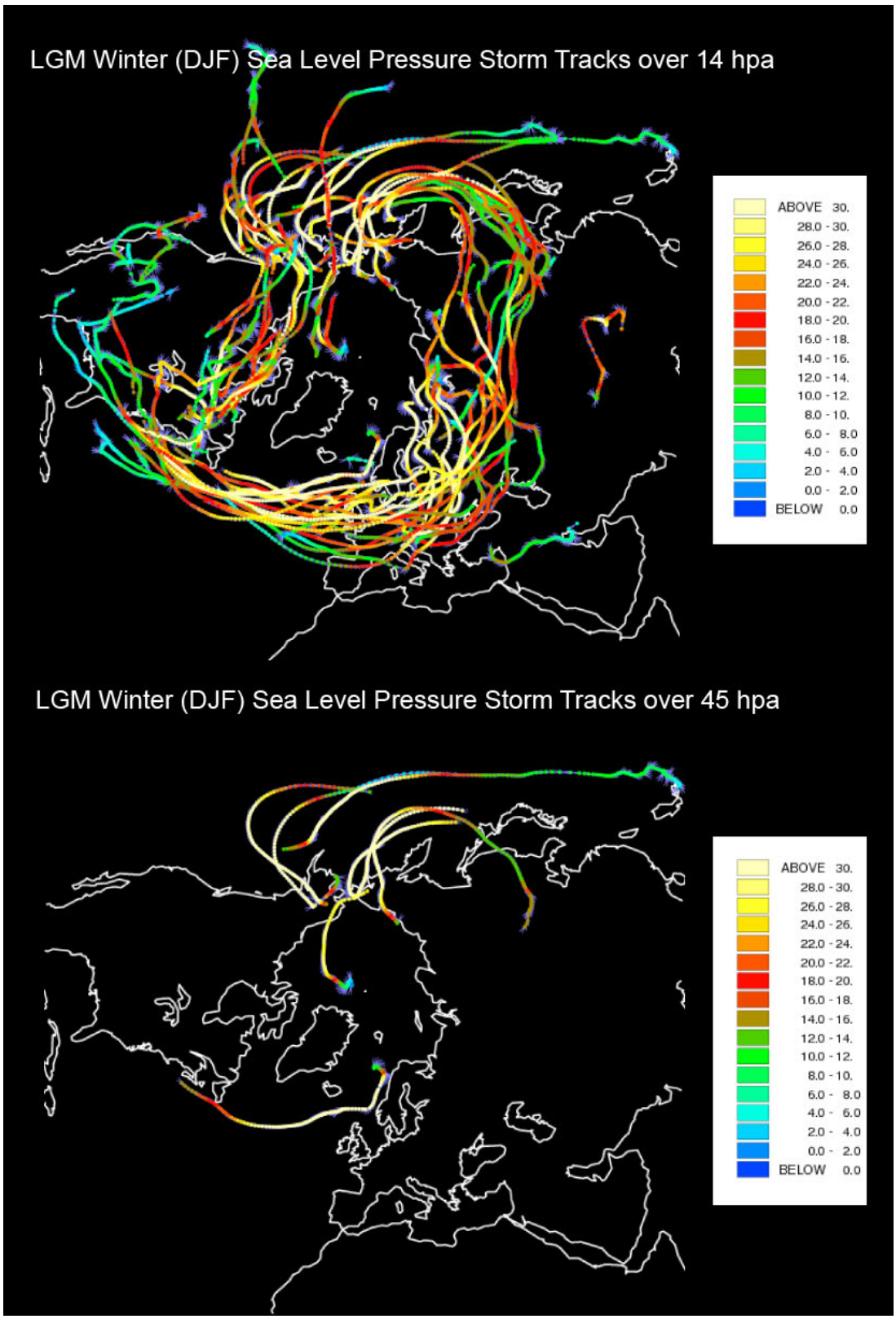

Figure 5.3a: LGM storm tracks in the hourly simulation using MSLP using the methodology of Hoskins and Hodges (2002).

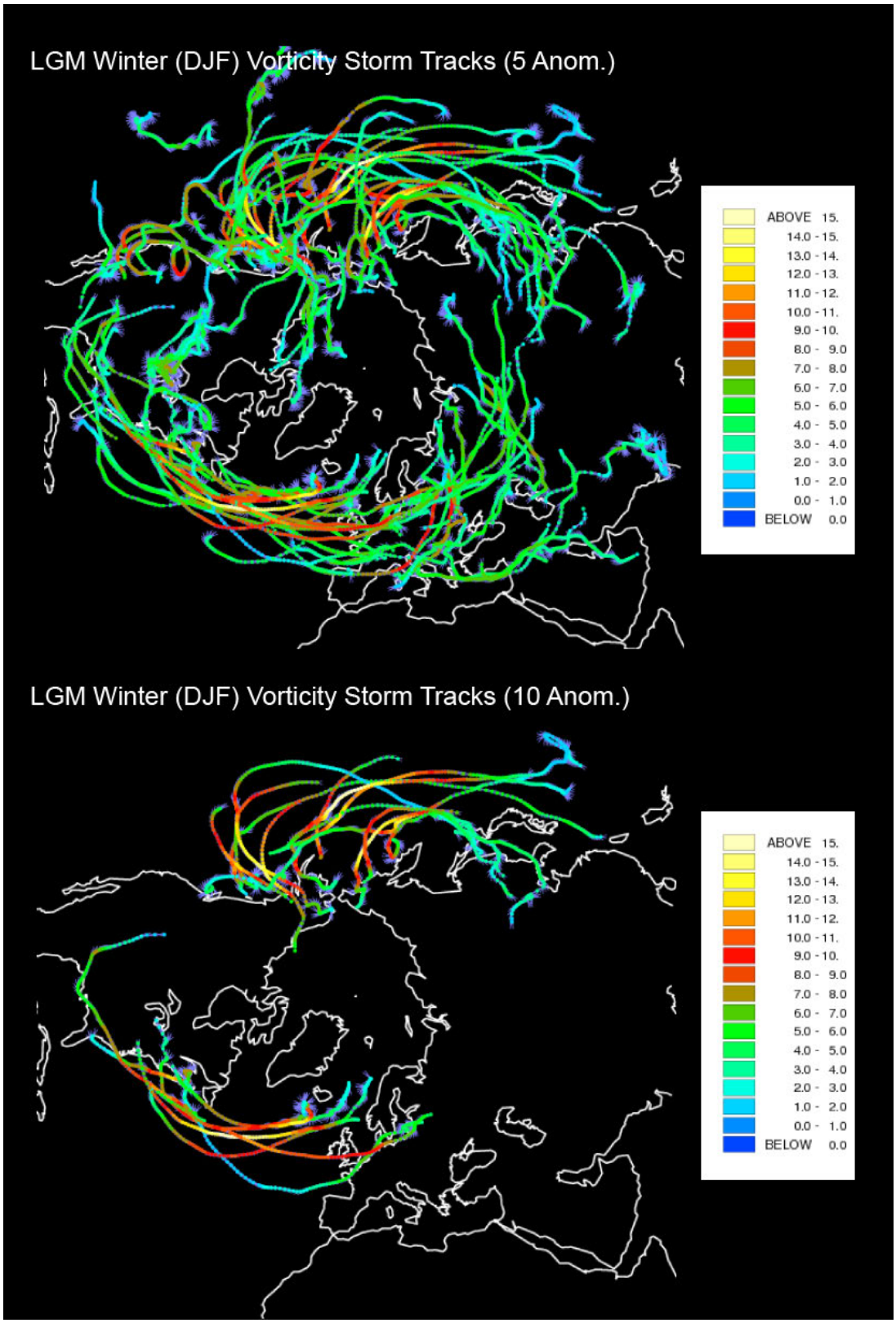

Figure 5.3b: LGM storm tracks in the hourly simulation using vorticity using the methodology of Hoskins and Hodges (2002).

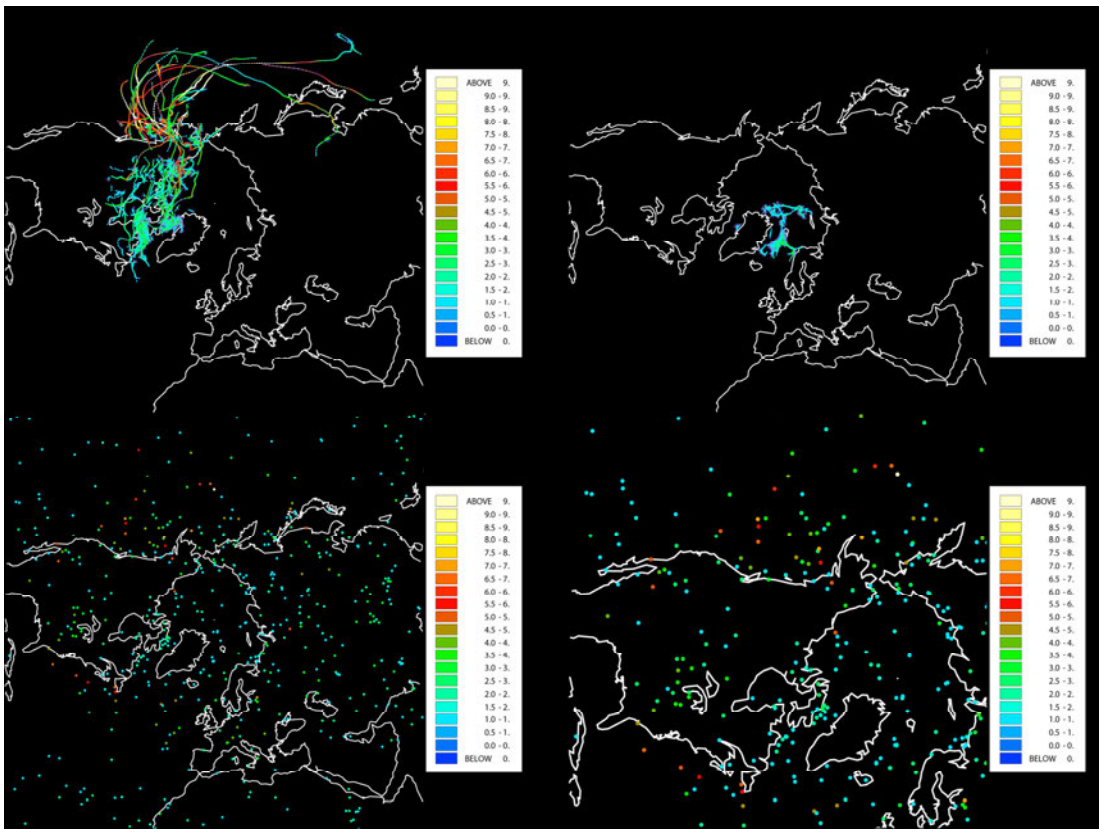

Figure 5.4: North Pacific sourced storms that comprise the lysis points (storm termini) between 50-80N, 90-0W (top-left) and the weak regionally sourced polar disturbances responsible for the lysis points to the northeast bound at 70-90N, 60-15W (top-right). Full unfiltered cyclogenic lysis points for the northern hemisphere derived from the LGM hourly output simulation (bottom-left) and an expanded selection around the North American-Greenland sector (bottom-right). Colour represents magnitude upon death. Hotter colours will therefore represent situations that are interesting synoptically such as merging. Serial storms are observed in the data set, and occur during the northward migration of storms over middle Alaska. Storm death occurs along the exit of the Pacific track, along the Labrador Sea and Davis Strait. The lysis regions north of Iceland and east of Greenland are from local sources.

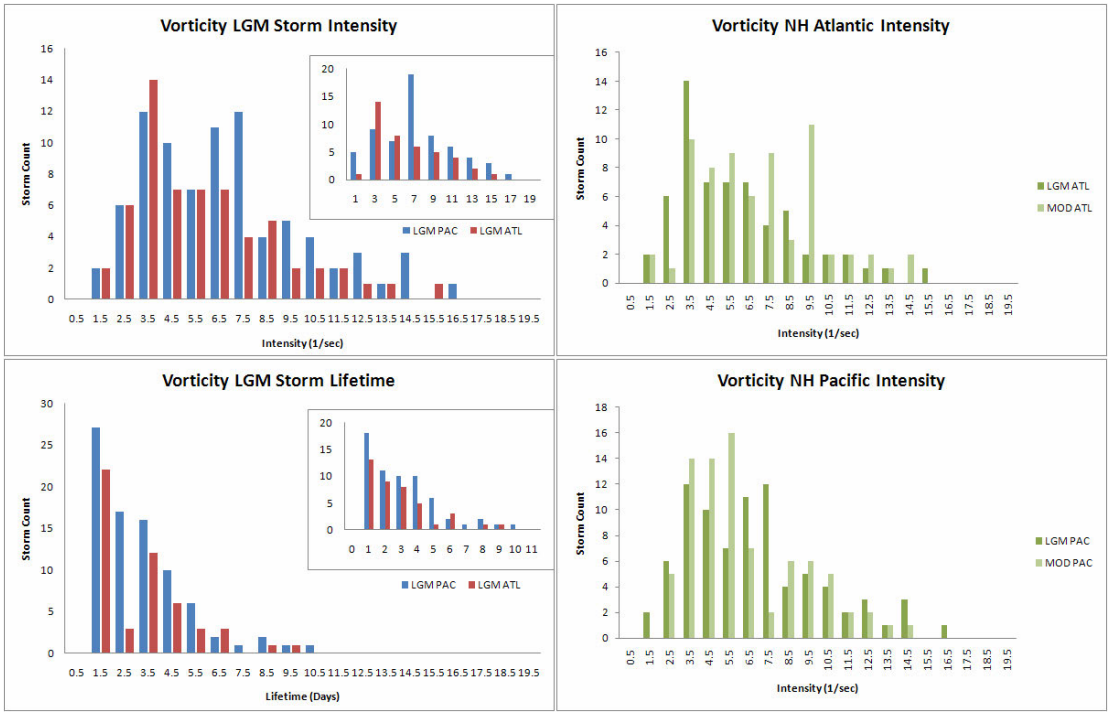

Figure 5.5: (Top left) LGM winter storm intensity between the North Pacific (140°, 230°), (25°, 70°) and North Atlantic (290°, 360°), (25°, 70°) where storms were counted upon entering the region but their maximum could occur anywhere along the storm track. Insets demonstrate those storms that only achieve their maximum intensity within the predefined window. LGM winter storm lifetime between the North Pacific and North Atlantic sectors using the same method as the intensity calculation (bottom left). Right most panels are North Atlantic (top right) and North Pacific (bottom right) storm intensities between the LGM and control run simulations. Note the distribution shift between the two basins.

with the major peaks ranging from 3.5 s^{-1} to 9.5 s^{-1} (cf. Chapter 3). During the LGM the North Atlantic has 15.4% less intense storms compared to the modern, with a reduction of mean intensity in the vorticity parameter of 1.2 s^{-1} (cf. Fig. 5.5). This result (cf. Unterman 2007) is comparable to the recent 17% found in Donohue and Battisti (2009).

In contrast, the North Pacific shows LGM storms to be 7.7% more intense, with major peaks around 3.5 s^{-1} to 7.5 s^{-1}, and a mean intensity increase of 0.48 s^{-1}. Very large storms are also identified in the North Pacific LGM simulation with several storms reaching the 14.5 s^{-1} and even 16.5 s^{-1} levels. The intensity difference

between the LGM North Atlantic and North Pacific is consistent with the interpretation of storm magnitude changes seen in compiled high resolution animations of the LGM hourly outputs (cf. Appendix; cf. Unterman 2007).

Trajectories show nine large-magnitude storms in the Pacific and only one in the North Atlantic (Fig. 5.3). No storms are tracked over Greenland. Analysis of lysis points lend credence to this result, with storm points clustering in the Labrador Sea and Davis Strait (Fig. 5.4). The lysis points northeast of Greenland are derived from locally sourced very weak polar lows (Fig. 5.4 top-right panel).

In modern moisture source experiments (Charles et al., 1994; Langen and Vinther, 2009) Greenland precipitation is derived from a wide range of source locations including local North Atlantic and Greenland sources, a North American source and a North Pacific source. This also includes storms developing off the Canadian Rockies that spin up into systems bound for the North Atlantic known as Clippers. In the LGM however, the mid-latitude general circulation pattern is disrupted by the Laurentide Ice Sheet such that flow is diverted northward over middle Alaska and over the northern edge of Canada. This result is consistent with other GCM experiments as well as geological evidence (Anderson et al., 2006). In the North Atlantic, the storm track is anchored further south over the extended sea ice margin (cf. Manabe and Broccoli, 1985; Kageyama et al., 1999). Delivery to Greenland then would come primarily from the exiting North Pacific eddies under the condition that they migrated far enough to the east. However, trajectories in the synoptic-scale simulation are further west. They are also cut-off from the North Atlantic baroclinic zone, ending further north and consequently contributing to the decreased cyclogenesis in the region (cf. Donohue and Battisti, 2009). The spatial patterns of increased meridional heat flux in the climatological run (Kim et al., 2008 Fig. 4) further support the synoptic-scale trajectories as the large positive anomalies are confined over the LIS, Canada and the Labrador Sea. Consequently, In the synoptic scale LGM simulation, there is a significant reduction in the wintertime Greenland precipitation rate (~1.6 x 10-3 mm/hour) and total accumulation (3.5 mm), with ~25% of the total deposited over a week long event (the peak rate is ~1.0 x 10-2

mm/hour – at hours 628-894). The four climatological winters range from 2 mm to 6 mm total, as compared to 75 mm to 106 mm in the climatological control simulation with similar values in modern observed winters (~90 mm).

As discussed in Kim et al (2008) the shallower North Atlantic lows may also reflect the shift of the jet stream maximum from over North America in winter (present) to over the zone of maximum North Atlantic thermal contrast (central North Atlantic sea ice margin) in the ice age. Thus acceleration and convergence occurs over the western North Atlantic (cf. Fig. 5) – features that suppress uplift resulting from any incipient surface baroclinicity due to strong temperature gradients.

Since the hourly-saved winter run captures many features of the circulation shown in lower-resolution models and even the decrease in Greenland precipitation, trajectories in the Pacific sector are examined in more detail (Fig. 5.3). Particularly notable is the tracking of storm systems along the west coast of North America, which is the region where climatological atmospheric heat transport is greater than the modern simulation by 16 km/s (cf. section 5.2). The strong south-westerly flow for this sector should certainly decrease any wintertime coastal upwelling along the California. Both of these processes would cause/contribute to the warming signal observed in nearby land areas (Winograd et al., 1992; Ludwig et al., 1992; Herbert et al., 2001) and could have significant implications with respect to interpretation of such “early” warming in ice age proxy records.

LGM Cyclogenesis Animation Discussion:

High-resolution animations enable a better appreciation of the storm tracking features. Individual frames indicate a typical low pressure system crossing the Pacific (Fig. 5.1 and 5.2), along with a less-frequent large dip in the upper air jet towards ~15°N at a different time (see Chapter 4). The latter pattern triggers pulses of convective moisture in the ITCZ (cf. Fig. 5.2). In the surface animation (cf. Appendix), the Pacific is characterized by a near-continuous string of strong surface fronts generated from the outflow of air off eastern Siberia. The large cyclonic

systems are steered across the Pacific and northward over Alaska, delivering warmer air and convective precipitation to the region above 57°N.

The animations also illustrate some well-known phenomena of cyclogenesis, such as serial storms (e.g., hours 775 and 805) and Kona Lows (beginning at hour 1148) near the Hawaiian Islands. As discussed by Moore et al. (2008) the latter are subtropical cyclones that form when an upper-level extratropical disturbance detaches from the midlatitude westerly flow. Hour 1177 of the upper level flow animation illustrates such a detachment. Examination of the accompanying convective precipitation field indicates a strong stream of air flowing from the ITCZ "feeding" the Kona Low. Serial storms have been tracked in the animations where a large, trailing parent front causes successive multiple secondary storms to deflect into the mid-Alaska region. For instance, at hour 775 a storm is seen in the eastern Pacific moving towards the Gulf of Alaska. This comes from the same disturbance back at hour 699 off the coast of Japan - probably due to outbreaks from the edge of Northern Siberia. The eddy heads up into the Gulf of Alaska with a long trailing cold front which produces secondary cyclones, becoming the same storm as seen in hour 775. There is then another series of secondary generation along the front of this storm, to the south, from about step 805, which develops and then movies northward. This may be the first description of cyclogenic seriality (and Kona Low development) in a paleometeorological simulation (Figure 5.6 and 5.7).

The large number of low pressure systems coming off Siberia affects not only cyclogenesis but also dominates airflow in the western Pacific all the way into the tropics. Similar to that of the case of south Iceland, there is a strong mid-Pacific flow stream east of the Philippines that cuts across the emerged Indonesian sector, flows along the north coast of New Guinea, and then passes into the equatorial South Pacific in a gap between 140°E-150°E. Backtracking of the wind vectors indicates that this air, though clearly modified, can be linked to the very substantial winter outpouring of Siberian air in the North Pacific.

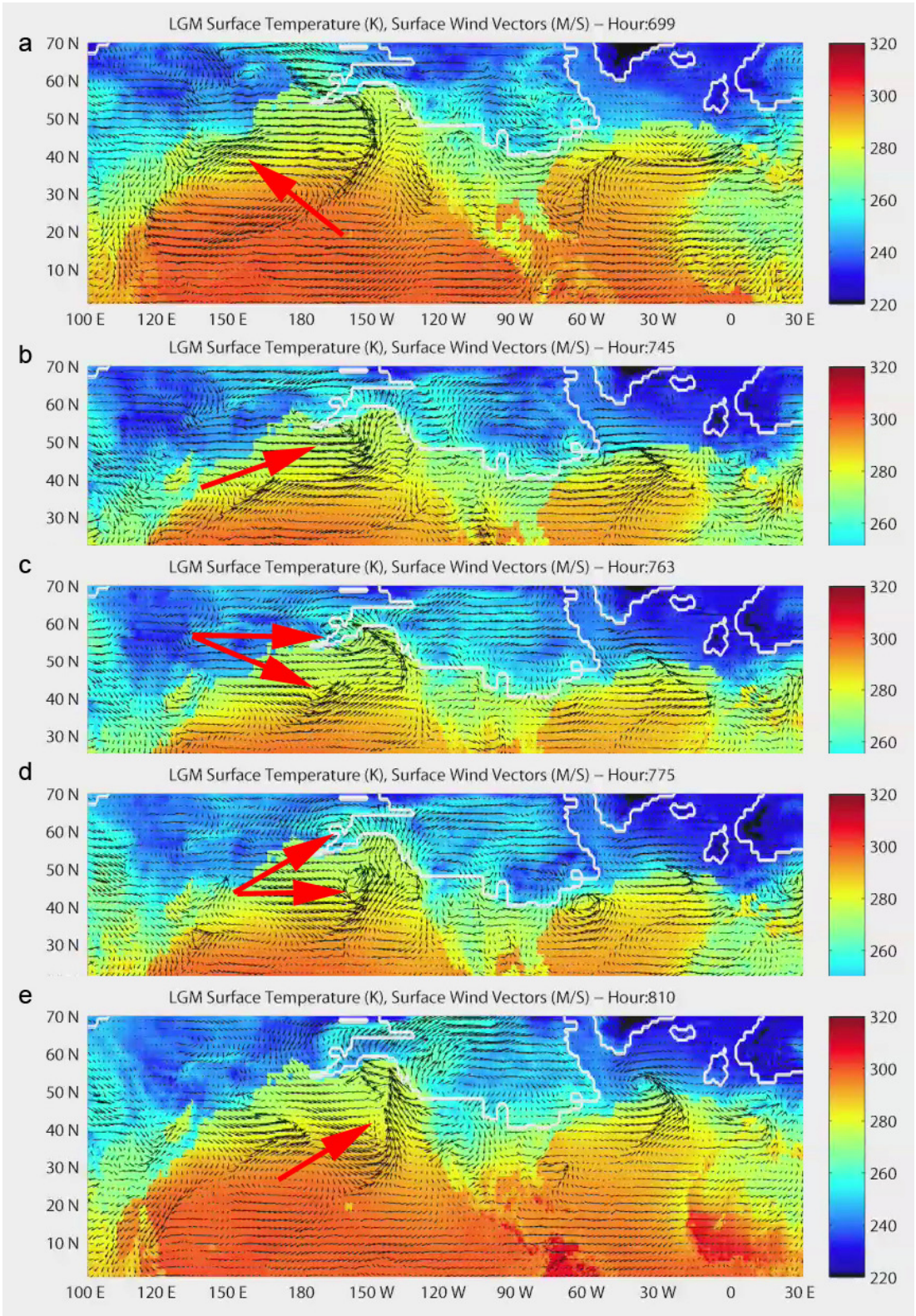

Figure 5.6: Surface winds (m/s) and surface temperature (k) in the synoptic scale simulation for the specified hours noted in the figure sub-titles. Sequence a through e shows the development of serial storms. The initial disturbance (a) forms off the coast of Northern Japan and migrates eastward over

the Pacific before developing into a cyclonic system (b) near Alaska with a large trailing front which subsequently generates secondary storms (c), (d), and (e). The associated convective precipitation panels can be found in the high-resolution animations. White outline denotes ice sheet margins.

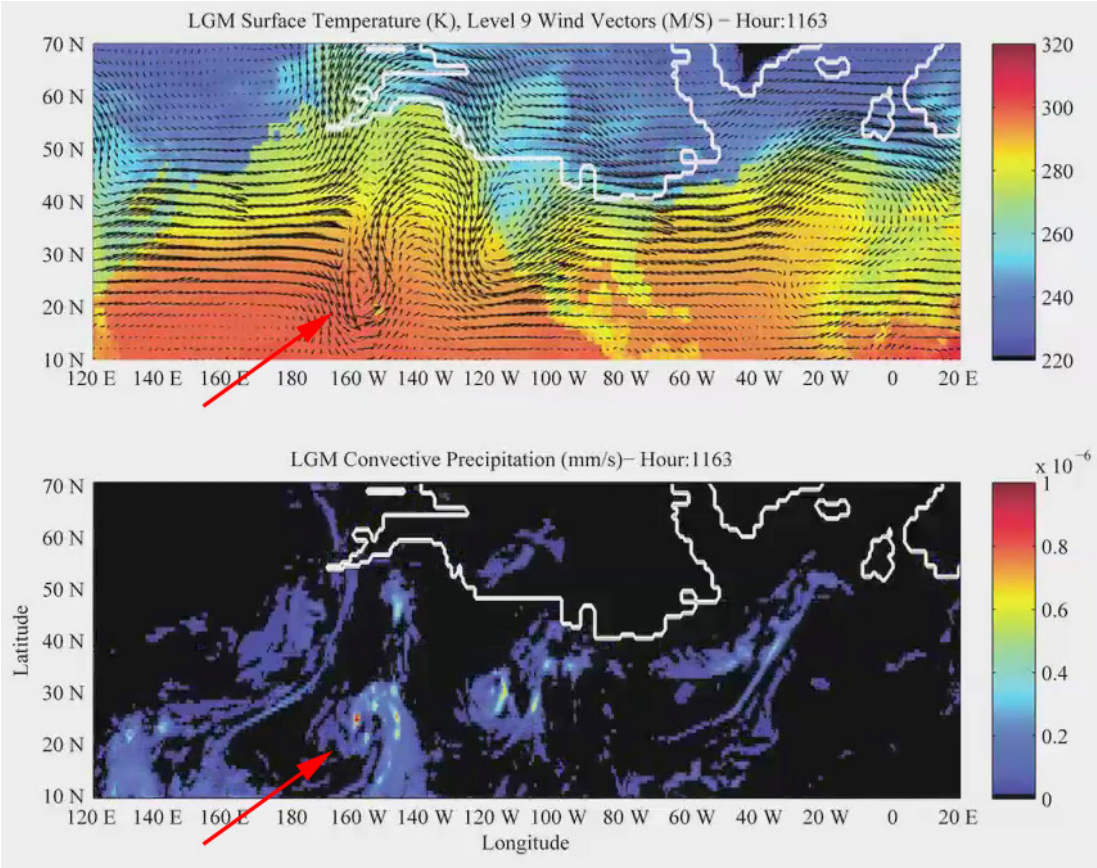

Figure 5.7: A single snapshot of the upper-level winds animation showing an extreme southward dip of the mid-latitude jet which subsequently imbricates (folds in on itself) and detaches into a Kona Low system (Moore et al., 2008). Red arrows denote the beginning of such detachment in both the wind flow (top) and the convective precipitation field (bottom). This may be the first description of Kona Low development in a global paleometeorological simulation. From the perspective of an LGM simulation, such a finding is important with respect to the source of precipitation to the ice sheets. One can clearly see the tropical precipitation (lower panel) being pulled northward into the Pacific storm track. White outline denotes ice sheet margins.

Upper level winds were also compiled in a high resolution to investigate the synoptic properties of the mid-level jet and the impact of convective precipitation at the surface (cf. supplementary material). Results from the climatological run, and the mean of the synoptic integration, indicate a modified split jet with the northern

branch extending up over the LIS and the southern branch dipping towards Mexico (c.f. Chapter 4). Synoptically however, the mid-level jet fluctuates between a modified and fully split jet (e.g. hour 882 in the upper level animation) with two distinct branches similar to that of the mean state. This is further discussed in Chapter 4.

5.2 Key Comparisons to the Climatological Run, GCMs and the Proxy Record:

Several results presented in this Chapter are comparable to both the geological record and previous GCM experiments, and many were presented alongside the synoptic results in the previous sections. This section however, will highlight several key comparisons to the high-resolution simulations, including to specific *interpretations* of geological results.

Some of the primary findings reported in this chapter that are new or appear more clearly at this temporal scale are: (1) the focusing of trans-Pacific storms along the west coast of North America and into the Gulf of Alaska bringing relatively warmer air and convective precipitation to the region; (2) The lack of surface disturbances over Greenland air-space resulting from the westward exit of storms from the North Pacific storm track – and "bowing" over the Laurentide Ice Sheet; (3) Reduction of North Atlantic and increase in North Pacific storm cyclogenesis; (4) Significant reduction in Greenland precipitation during the LGM wintertime compared to the modern simulation(s).

The storm track positioning in the synoptic integration is clearly comparable to the meridional heat transport as seen in the 4-year climatological run (Fig. 5.8), with

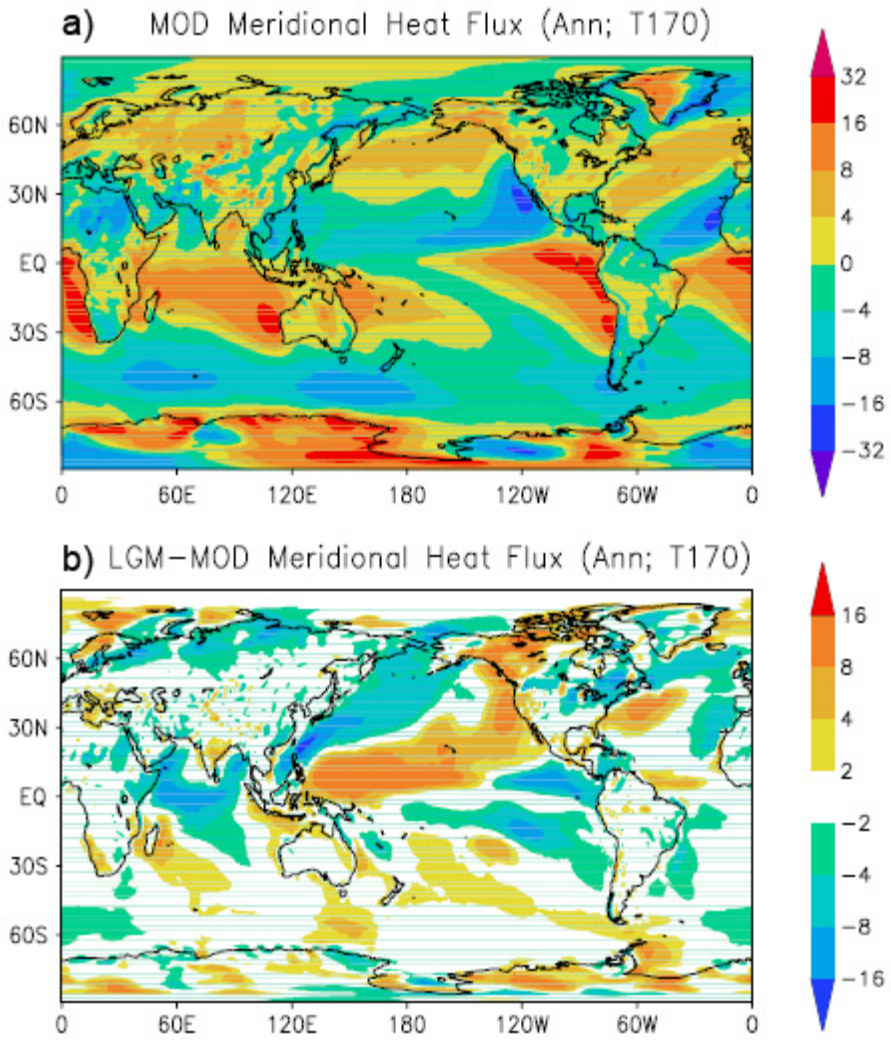

Figure 5.8: 4-year mean annual meridional heat flux from the climatological control and LGM simulations (produced from Kim et al., 2008). Units are in $K*ms^{-1}$. Note the focusing of heat along the length of California, United States and over Alaska. Comparison to the T42 ccm3 integration can be found in Unterman (2007) and Kim et al. (2008). The spatial distribution of the positive anomalies in the climatological mean annual heat transport is what one would expect if the wintertime synoptic integration results were having an effect (and therefore also prevalent) on the longer climatological integration – especially given the marked agreement along the west coast of North America (see also the individual climatological winters in Chapter 4, Fig. 2, 5, Table 1 and Appendix).

large positive anomalies ranging from +2 to +8 km/s (LGM-MOD) along the west coast of North America, the Gulf of Alaska, and areas north of the Laurentide Ice Sheet, and is coincident with the arching of the North Pacific storm track and the delivery of warmer air to the region. There is also a large (+8 km/s) anomaly in the Great Basin area of California which is exactly coincident with the tongue of warm-

air and precipitation seen in the synoptic integration that is delivered from the Pacific. The focusing of storms along the California Coast and the synoptic-scale eddie results are also coincident with all four years of the climatological run's wind stress field (cf. Chapter 4, Fig. 4.7; Appendix) further demonstrating that the wintertime results of the hourly-run is representative of other ice age winters. Interestingly, the increased zonal wind stress in the climatological run is also coincident with focusing of storms exiting the North Atlantic storm track over the United Kingdom and Northern Europe, the increased precipitation of which should have contributed to the maintenance of the Fennoscandian Ice Sheet in this region.

The Pacific storm trajectories and precipitation patterns (cf. Chapter 4 Fig. 4) along the west coast of North America is also the area of the infamous several-decade old geological debate of "early deglaciation" (Winograd et al., 1992; Imbrie et al., 1993; Herbert et al., 1998; Herbert et al., 2001; Winograd, 2002; cf. Thompson and Goldstein, 2006). Here, Winograd et al. (1992) inferred from the overall strong similarity of the Devils Hole calcite vein isotope record to that of the SPECMAP dataset (an average of many open ocean isotopic records; Imbrie et al, 1984; cf. Chapter 2) that Devils Hole offers a global chronology of glacial-interglacial cycles. This was further interpreted (Winograd et al., 1992) to pose a "threat" to the orbital theory of the ice-ages as the early occurrence of heavy $\delta^{18}O$ relative to the SPECMAP chronology (cf. Imbrie et al., 1984; Imbrie et al., 1993; Chapter 2) appeared well before any increase in Northern Hemisphere insolation. However as Herbert et al. (2001) prudently point out, that although the large-scale features between the marine and terrestrial isotopic records generally correlate, as one decreases the total time-scale, regional responses to glacial-interglacial global changes might not occur in lock-step. The area around Devils Hole and the west cost of North America for instance is highly influenced by wintertime precipitation from the Pacific and any modification of such may be reflected in the regional (high resolution) geological record. When the California current system – a marine current system intimately linked to the atmospheric pressure systems in the North Pacific and Western North America (Emery and Hamilton, 1985) – is disrupted, sea surface temperatures increase along the California margin, upwelling diminishes, and rainfall

becomes more frequent on land (Herbert et al., 2001). Herbert et al. (2001) used alkenones (Chapter 2) gathered along the California margin to demonstrate that the California Current collapsed, presumably due to the reorganization of the atmosphere, during the LGM and during all previous glacial maxima. This occurs only during the glacial peaks, implying a set of atmospheric feedbacks relating to a threshold size of the Northern Hemispheric ice sheets. Although this continues to be debated (see citations above) the regional patterns of wind flow, heat flux, precipitation and the North Pacific storm tracks in the synoptic scale integration presented here produce features that are also reflected in the climatology, and that are directly comparable to those hypothesized by Herbert et al. (2001) during the LGM, and suggest that this area may produce a regional "early warming" signal without necessarily having *anything* to do with early global deglaciation. Furthermore, Herbert et al. (2001) take note of a delayed rise in California *Sequoia* as compared to the "early warming" which requires coastal fog to thrive. The south-westerly onshore surface wind flow from the North Pacific onto the California coast (cf. Fig. 4.3, 4.5, 4.6, 5.1, 5.3 and others) as seen in the hourly run (and the climatological) would suppress upwelling and subsequently the coastal fog (see previous section). Herbert et al. (2001) suggests in a passing phrase that the signal, if correct, would require such suppression in upwelling in this region.

There is also no geological evidence of early mountain glacial retreat in the cordilleran region during this time (Young et al., 2011) and it is conceivable that the precipitation delivered from the North Pacific storms would help supply the Pinedale glaciers ("Pinedale" simply refers to the last glaciation in the Rocky Mountains) along the western United States especially if the same pattern persisted in other ice-age winters - the positioning of the precipitation and the heat flux in the climatological run suggests that the synoptic scale systems outlined previously do operate in a similar manner, within the level of the documented interannual variability (cf. Chapter 4, Fig. 2) during other LGM winters. In fact, the vast majority of the Pinedale glaciers do not go into heavy retreat until around ~16 kya including the location at Bishop's Creek in Sierra Nevada (cf. Young et al., 2011 Fig. 1).

The expansion of Great Basin (just east of Sierra Nevada) lakes in western North America continues the line of evidence for the synoptic and climatological results presented in this chapter and Chapter 4. Benson et al. (1990) assigned patterns to lake levels through the past 35 kya including the last glacial. Four of the major lakes (Lake Lahontan, Lake Bonneville, Lake Russell, and Lake Searles) were analyzed and were shown to have lake level oscillations through the glacial until achieving a high stand at around 15 kya, with all four lakes receding through the Younger Dryas. Lake Russel maintained a high level even at the glacial maximum. Benson hypothesized that the lakes "responded to large synoptic-scale changes in climate" creating the observed oscillations in the record including the expansion within the glacial (Benson et al., 1990). The results presented here lend credence to Benson's hypothesis with the delivery of warm air and precipitation to this sector.

In regards to the heat flux over the Laurentide Ice Sheet, above Canada, the LGM heat transport in the climatological run is positive until the area north of Victoria Island and Baffin Island, approaching south west of Ellesmere Island in northernmost Nunavut, Canada, which is west of Greenland and is coincident with the terminus of LGM North Pacific storms (Fig. 5.4) in the hourly integration. The negative anomaly in the North Atlantic is situated along "strike" of the extended sea-ice margin and is also the area of reduced cyclogenesis in the hourly LGM integration. The 15.4% reported here is comparable to the 17% found in Donohue and Battisti (2009). The combination of the reduction in local North Atlantic cyclogenesis, and the spatial modification of the North Pacific track would modify the precipitation source locations onto the Greenland Ice Sheet (see previous section). This and the large reduction in Greenland wintertime precipitation supports the Charles et al. (1994) hypothesis of a shift towards Northern Pacific precipitation sources (and also Fawcett et al., 1997; Langen and Vinther, 2008), and is comparable to the overall geological interpretations of the ice cores (Johnsen et al., 2001) – although the shift in moisture sources to the North Pacific could conceivable bias the geological interpretation in regards to $\delta^{18}O$ shifts, with rare synoptic events bringing distally sourced, lighter, wintertime precipitation (see previous section).

Other Caveats and Discussion:

Although surface geography is better resolved at T170, ice sheet reconstructions vary in elevation profiles which influences the northward steering of eddies and could conceivably affect the robustness of some of the regional results presented here. The Peltier (1994) ICE-4G reconstruction was used here, to maintain consistency with the in-tandem climatological run, which has significantly less ice west of Hudson Bay (500 – 1000 m) than the newer ICE-5G reconstruction (Peltier, 2004). Some caution is therefore needed with respect to some of the results. However, it is probable that a higher elevated ice sheet will not significantly change the results, as the higher elevation ICE-5G ice sheet would further amplify the ridge-trough system over western North America, and the lower relief ICE-4G ice sheet in the in-tandem runs is already steering the low pressures northward. The consistency of the Pacific results with ice-free parts of Alaska and a wave-number one perturbation of the high latitude flow causing cooling over Greenland and Western Europe is further support for the synoptic results (c.f. Kim et al., 2008).

5.3 Summary:

The key findings of this chapter include: (1) The documented high storm activity in the North Pacific compared to the North Atlantic during the LGM (14.9%); (2) The reduction in North Atlantic (15.4%), and increase in North Pacific (7.7%) cyclogenesis compared to the modern; (3) North Pacific storm trajectories are modified by the Laurentide Ice Sheet such that trans-Pacific storms are diverted northward along the western edge of the continental United States into the Gulf of Alaska and subsequently over the northern margin of Canada and the Laurentide Ice Sheet; (4) Storm termini show some clustering in the Labrador sea west of Greenland; (5) The restructuring of the LGM storm tracks brings relatively warmer air and precipitation to the western coast of North America; (6) Storm tracking identifies a wide range of lifetimes and intensities during the LGM with larger storms in the North Pacific; (7) The North Atlantic storm track is shifted eastward and along the extended sea ice margin; (8) Kona Low development and serial storms are

described in the North Pacific for the first time in a high-resolution paleometeorological simulation. However, this is not to imply that other models are incapable of producing such features.

Although the ocean has been suggested to be the primary contributor, a change in atmospheric circulation has also been suggested to affect Greenland's isotopic shifts on timescales shorter than a human lifetime (Charles et al., 1994; Fawcett et al., 1997; Langen and Vinther, 2009). Understanding these shorter, more rapid fluctuations in past temperature is of great importance given the predicted changes in climate over the next century as well as the way we interpret proxy data.

Within the synoptic scale simulation, storms are 15.4% less intense in the North Atlantic and 7.7% more intense in the North Pacific during the LGM. Storms exiting the diverted Pacific track are confined to the Labrador Sea and Davis Strait with lysis points west of Greenland. The absence of Greenland wintertime storms in the synoptic run, and overall significant reduction in precipitation in the area, would affect the $\delta^{18}O$ record through a shift in source location or null deposition during winter – especially if moisture from the tropics becomes injected into the North Pacific storm track via the extreme southward dips of the mid-latitude jet.

The northward tracking of North Pacific storms along the coast of North America is consistent with glacial-maximum warming in nearby land areas, due to increased poleward heat transport in this sector and presumably the subsequent decreased upwelling due to onshore south-westerly flow. The increased precipitation, heat and onshore winds in this sector are entirely comparable to the hypothesis of Herbert et al. (2001) and suggests that this area may produce a regional "early warming" signal at the peak of the last glacial without necessarily having *anything* to do with early global deglaciation (e.g. Winograd et al., 1992; Winograd, 2002; cf. previous section). The onshore flow in this area provides conditions appropriate to decrease coastal upwelling during the LGM winter, which in today's climate is necessary to create the coastal fog needed to maintain California Sequoia (cf. Herbert et al., 2001). The marked delayed in the decline of California Sequoia out of the last glacial

(see previous section) further lends credence to the local results during the LGM as described, rather than an early global synchronous shift into the deglacial. This area is also coincident with the rising levels of the Great Basin Lakes in California during the LGM (Benson et al., 1990) and the stability or expansion, rather than the early melting, of the Pinedale glaciers (Young et al., 2011). Consequently, although it might be tempting to interpret inferred glacial-maximum warming along the west coast of North America as an "early response" of deglaciation, the most appropriate interpretation is that the trend reflects a natural regional response to ice-age physics.

***

In summary, in this Chapter, the synoptic results of cyclogenesis were presented alongside that of the climatological run, other GCM results and several geological data sets. The agreement between the modified storm tracks in the North Pacific and North Atlantic during the LGM in the hourly integration with the heat flux and regional precipitation in the longer 4-year climatological run suggests that the wintertime results, although they would be variable from winter to winter (cf. Chapter 4; Table 1) are not anomalous, and the patterns resulting from the atmospheric re-organization in the LGM are at least persistent in some ice-age winters. These results are further lent credence by coastal marine data during the LGM (Herbet et al., 2001), recorded warming in calcite (cf. Winograd et al., 1992; Herbert et al., 2001; cf. Winograd et al., 2002), delayed declines in California Sequoia, expansion or maintenance of the lake level size in Great Basin Lakes in California during the peak of the last glacial (Benson et al., 1990), expansion or maintenance of Pinedale glaciers (Young et al., 2011) and many other geological data sets such as those also presented in Chapter 4. This permits the (continued) more detailed inspection of individual synoptic events, especially extreme events, that may have a disproportionate impact on the preservation (and consequently interpretation) of geological data (e.g. Benson et al., 1990; Bishop et al., 2001; cf. Mahowald et al., 2006; cf. Geibert et al., 2010; cf. next Chapter).

Chapter 6

Results: Paleometeorology - Wind Gustiness over Dust Source Locations and Synoptic Scale Parcel Trajectories during the LGM

6.0 Introduction and Background:

The hourly outputs obtained here can be used to analyze synoptic scale events that may be responsible for processes such as dust delivery and sea ice transport which have yet to be fully explored in high resolution paleo-modelling studies. Consequently, this chapter focuses on the hourly variability of wind velocities (gustiness) over geologically important locations in the Northern and Southern Hemispheres. Specific areas of focus will include the eastern Pacific sector and areas around Antarctica and the Southern Ocean.

This is a unique use of a traditional global climate model as the focus is not necessarily on the impact of the synoptic features on the climatological mean state, but the possibility of such events given ice age boundary conditions. This is because a single, relatively rare synoptic event can have a large impact on the annual dust delivery to any given region. It has been shown, for instance, that 0.1% of events over a certain threshold velocity can account for over 50% of all dust emissions in a region (cf. Tegen and Rind, 2000). Consequently, understanding the number of

hourly events over a given wind velocity threshold during the LGM can lend valuable insight into the glacial dust burden increase.

***

Mineral dust transport within the atmosphere can have a dramatic effect on the Earth system. Dust can influence climate directly, by influencing the radiative balance of the atmosphere (e.g. Overpeck et al, 1996), and indirectly by modifying cloud properties. The transport of dust to the oceans can also dramatically affect climate through ocean fertilization in areas that are limited in iron and subsequently modulate the uptake of carbon through increased biological productivity and in turn, the atmospheric concentration of CO_2.

According to geological records, mineral dust emissions during the LGM increased by a factor of 2-5 (cf. Havon et al., 1989; Mahowald et al., 1999; Maher et al., 2010; and others), with evidence from some higher-latitude sites even suggesting a factor of 20 or higher (e.g. Cragin et al., 1977; Petit et al., 1981; Dahl-Jensen et al., 1993 suggest a 68:1 ratio, but this was calculated solely from the highest peak in the LGM period). This even holds true for ice cores taken from mountain ice-caps at lower latitudes (e.g. Thomson et al., 1995).

The change in dust is one of the significant glacial-interglacial changes observed in both ice and marine cores. However, the dominant mechanism responsible for such an increase during the LGM is continually under debate, ranging from the expansion of dust source areas due to the reduction of vegetative cover (cf. Mahowald et al., 1999; 2006), exposure of continental shelves, synoptic-scale surface wind velocity changes (McGee et al., 2010) and increased sediment supply from glacial erosion (e.g. Sugden et al., 2009). The fact that high resolution ice cores show rapid fluctuations (temporally) in dust concentrations, sometimes by an order of magnitude, during the LGM (Mahowald et al., 1999) seemingly suggests that atmospheric changes on shorter timescales, as opposed to the long term climatological mean, modify such deposition (cf. McGee et al., 2010).

Normally, the analysis of dust emissions is limited to remote sensing systems such as satellite measurements, large scale field experiments, and fine-scale regional transport models. This is partially because individual synoptic events can have a significant effect on dust related processes, including those within the ocean (Husar et al., 2001; Bishop et al., 2002; Williams, 2008; Sow et al., 2009). The synoptic scale simulation presented here represents a unique opportunity to examine a process "typical" paleo-GCM experiments neglect (or which cannot fully describe), especially with regards to monitoring the hourly variability of surface winds, storminess and source wind location over dust source areas during the LGM.

Precipitation rates during the winter months of the LGM were significantly reduced (Chapter 4 Fig. 4.5; Chapter 5; Johnsen et al., 2001), which suggests that changes in dust fluxes from the atmosphere to the ice cores are smaller than the actual changes in concentration. A complication in the geological record is that reported concentrations cover different time intervals (e.g. Steffensen, 1997; Hansson, 1994) depending on continuous or discontinuous sampling within the cores themselves. Furthermore, marine cores never achieve the temporal resolution represented in the Greenland ice cores and represent average values over periods of several thousand years (Mahowald et al., 1999). Consequently, the proxy and the method of sampling also will determine the dust ratio as described by the geology.

***

Mahowald et al. (1999) used the BIOME3 terrestrial biosphere model to determine the distribution of dust source areas in the modern and during the LGM. They used the climatology derived from an ECHAM3 simulation of the LGM which integrated CLIMAP (non-modified) SST's as a boundary condition. BIOME3 considers the physiological effects of changes in atmospheric conditions, such as reduced CO_2 (the importance of which was first discussed in Chapter 4, section 4.4). Changes in vegetative cover were used to determine variances in dust source locations, determined by a threshold of leaf area index (cf. Mahowald et al., 1999). Dust source

locations increased over the East Asian deserts (including northward), Central America, South America, including the eastern coastal regions of modern day Brazil, and Patagonia, the Altiplano, and Australia in the southern hemisphere. Interestingly, the African regions didn't change significantly as a dust source as they are already a very significant dust source contributor today. There were also indications of potential dust source areas in the high latitudes such as Alaska, contrasting with the very minimal high arctic sources today.

One of the major goals of the Mahowald study (Mahowald et al., 1999) was to simulate the *average* LGM and current climates for comparisons with geological data, rather than to account for extreme values and variability during the glacial. Further to this, the integrated LGM ECHAM3 simulation was made using monthly mean climate anomalies, superimposed on the modern observations. By varying the size of the dust source areas they were able to obtain larger dust deposition values during the LGM. Yet, a more recent study by McGee et al., (2010) presents compelling evidence suggesting dust source areas alone may not be the primary mechanism responsible for the large increase in dustiness during the ice ages. Rather, rapid shifts in wind speed, or gustiness, over the known dust source locations may actually be the driver.

Similarly, in the southern hemisphere, mechanisms including increased aridity and synoptic-winds have been suggested to cause the large increase in dust concentrations (concentrations 20-50 times higher than present in some cores) preserved in the Antarctic record (e.g. Sugden et al., 2009). It remains relatively unclear what specific variable was primarily responsible for such an increase. Isotopic tracers suggest that South America is the dominant source of Antarctic dust during the glacial. Sugden et al., (2009) mention that finer particles typically become entrained over Patagonia at wind velocities ranging from 4-8 m/s and that the Patagonia region experiences strong winds today – with maximum velocities reaching ~22 m/s during some events. There is further sub-daily variability in glacial braided stream systems, which migrate over glacial outwash plains, which produce wide deposits of sediments during high flows each day only to rapidly dry out and

become available for removal some hours later (Sugden et al., 2009). In terms of seasonal variability, there is an increased seasonal load in the southern hemisphere summer due to summertime glacial melting flushing out fresh sediments (cf. Sugden et al., 2009). Yet, until now, no exploratory high-resolution modelling at the synoptic-scale has been used with a focus on: (1) wind parcel trajectories to determine or validate the source of Antarctic glacial dust and (2) the southern hemisphere summertime synoptic-scale surface wind variability over Patagonia and the Altiplano during the glacial.

In the coming sections, synoptic-scale wind gustiness (hourly fluctuations in high velocity surface winds) will be analyzed as a process that may be responsible for the increased dust loading during the LGM - and is a mechanism that only a simulation at the time scale presented here can address. Defined 1°x1° "stations" will be analyzed over several dust source areas and the results will be compared to the recorded dust loading in some proxies (further methodologies can be found in Chapter 3). Although the shortness of the simulation is the primary caveat for both the hourly and climatological run, the duration is similar to (or longer than) other analyses of processes attempting to discern the story of ice age dust (Bishop et al., 2002; Sow et al., 2009; cf. Maher et al., 2010).

6.1 LGM Surface Winds over Dust Source Locations:

As a means to quantitatively assess one of the main suspects for increased glacial dustiness, surface wind gustiness (the hourly changes in wind velocity) is analyzed over published LGM dust source sites, including the Central Loess Plateau, Taklamakan Desert in East Asia and the Patagonia-Altiplano regions in South America (cf. Liu et al., 1985; Mahowald et al., 1999; 2006) using the hourly-scale integration. The former two regions are also areas of interest given the suggested provenance of East Asian mineral dust found on Summit, Greenland (Biscaye et al., 1997), the expanse of nonvegetated land cover in the area (Crowley and Baum, 1997; Mahowald et al., 1997), as well as the potential shift of precipitation sources (and consequently modifying wet deposition) towards the Pacific during this time (e.g.

Charles et al., 1994; Langen and Vinther, 2008; Chapter 5). These results are also further linked to ice age cyclogenesis discussed in Chapter 5.

A one by one degree sampling scheme was adopted over the Central Loess Plateau (CLP) region, encompassing the Badain Jaran Desert and the Tengger Desert (37°N-45°N, 97°E-108°E boxed area with no bias for topography) for both the LGM and modern simulations. Percentages of events over suggested wind thresholds of 16 m/s (Chomette et al., 1999), 8 m/s (Chomette et al., 1999; Sugden et al., 2009; McGee et al., 2010) and 5 m/s (e.g. Sugden et al., 2009) were calculated from the data set in a manner to be consistent with the simple analysis of McGee et al., 2010. Table 6.1 shows a section of the sites with minimum, maximum and average wind velocities over each location in m/s as well as the percentage of events over the specified threshold velocities. Among all sites (cf. Appendix) over the CLP, maximum wind gusts reach 24 m/s for several sites in both the LGM and modern (at 40°N, 98°E for both data sets). However, LGM sites have a 1.75 m/s greater hourly wind velocity, with average maximum gust events 0.40 m/s more intense. Furthermore, 63% of all sites have a higher max gust event during the LGM, with 96% of sites having a higher average velocity. Consequently, more events during the LGM pass wind velocity thresholds that have been previously been cited for thresholds needed to significantly increase the atmospheric dust burden from these sources (Chomette et al., 1999). In particular, there is a ~2x fold increase in the number of events over the 16 m/s and a ~2.5x fold increase in the 8 m/s threshold over the Central Loess Plataeu sampling region during the LGM.

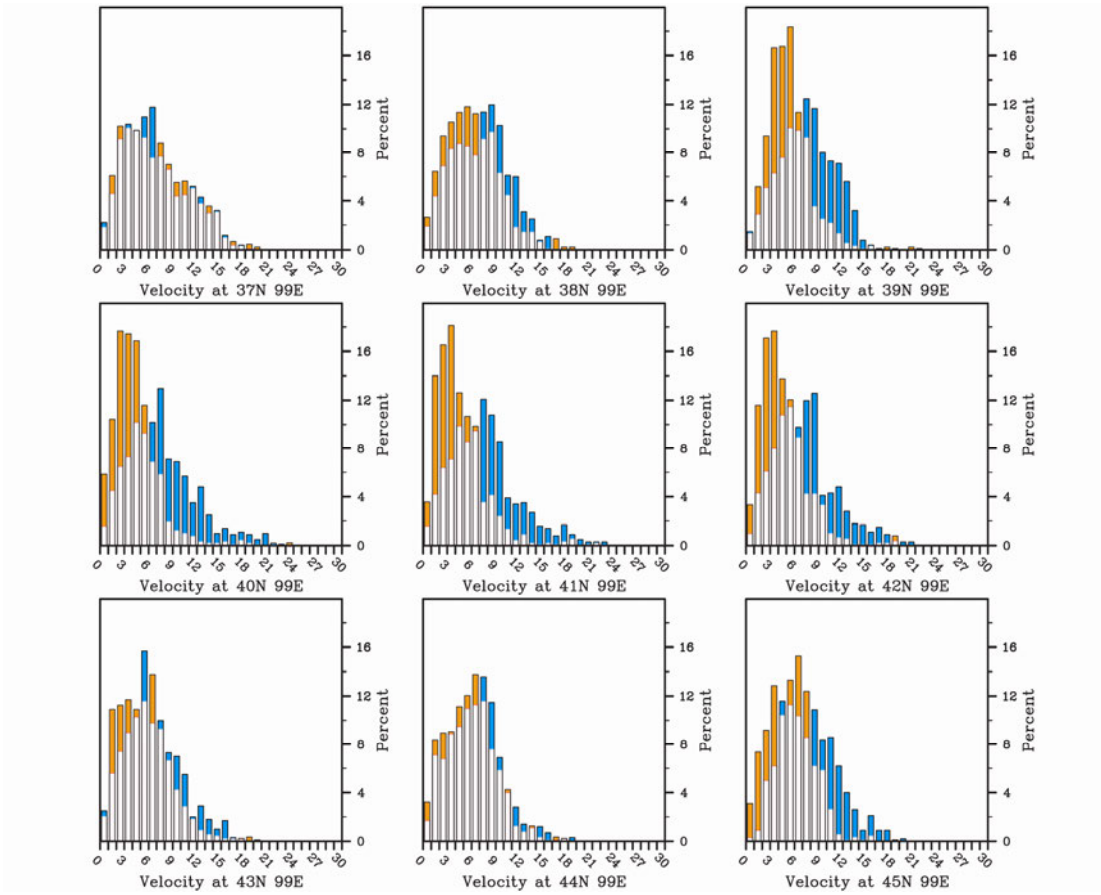

Figure 6.1: Percentage histograms of hourly wind velocity (m/s) over a section of the sampled Central Loess Plateau sector during the modern (orange) and LGM (blue). White area represents velocity overlap. This area includes the recorded LGM dust source areas of the Badain Jaran Desert, Tengger Desert and the Mu Us Desert (cf. McGee et al., 2010; Maher et al., 2010). Further information can be found in Table 6.1 and in the supplementary material.

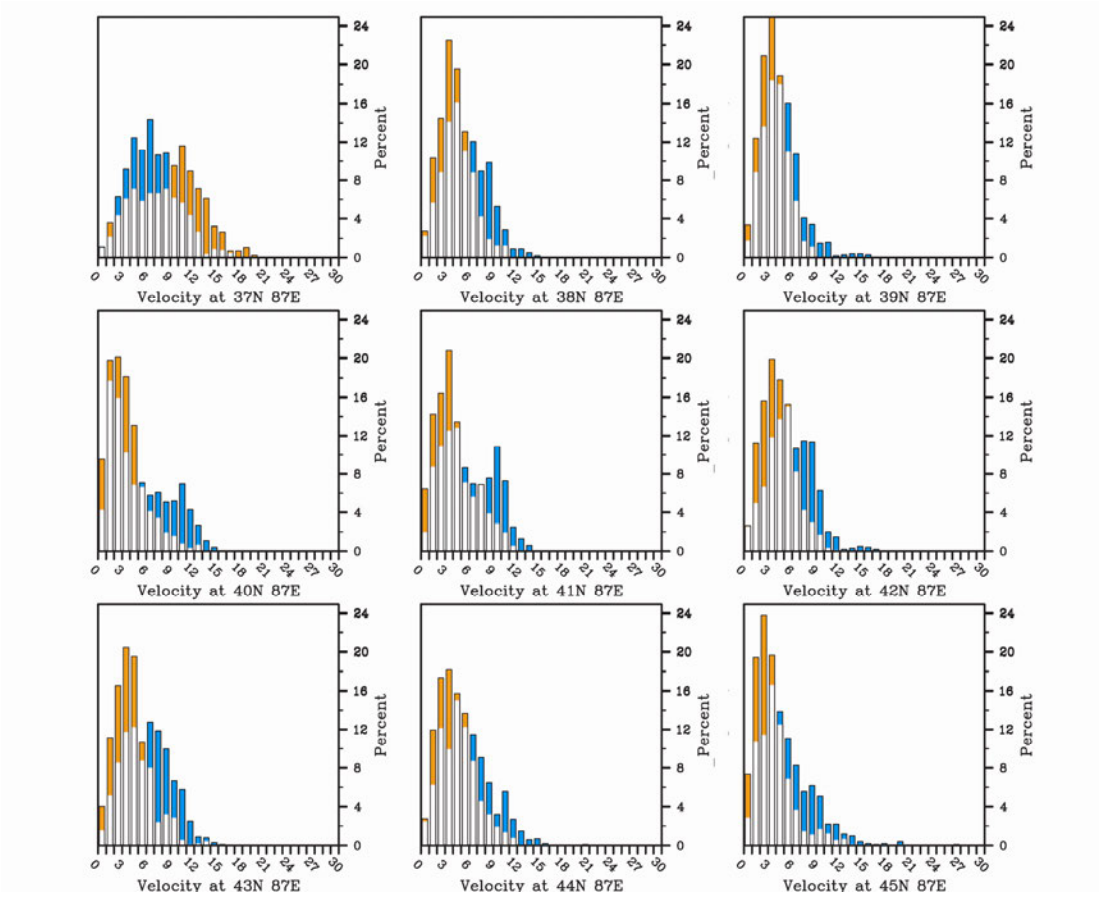

Figure 6.2: Percentage histograms of hourly wind velocity (m/s) over a section of the sampled Taklamakan Desert sector during the modern (orange) and LGM (blue). White area represents velocity overlap. Further information can be found in Table 6.2 and in the supplementary material.

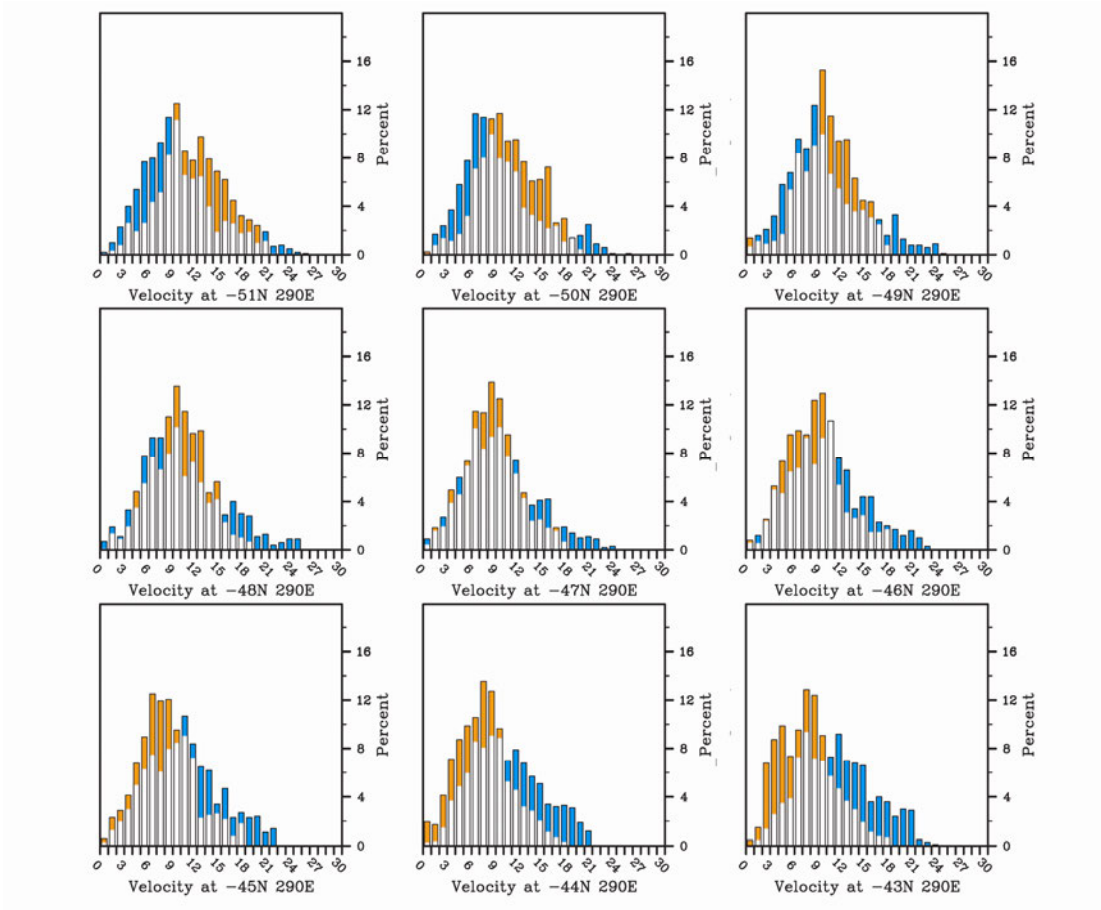

Figure 6.3: Percentage histograms of hourly wind velocity (m/s) over a section of the sampled Patagonia region during the modern (orange) and LGM (blue). White area represents velocity overlap. Further information can be found in Table 6.3 and in the Appendix.

Lat	Lon	MOD AVG	MOD MAX	MOD MIN	LGM AVG	LGM MAX	LGM MIN	L-M MAX	L-M MIN	L-M AVG	MOD 16%	MOD 8%	MOD 5%	LGM 16%	LGM 8%	LGM 5%
37N	103E	4.34	14.83	0.12	5.41	12.29	0.04	-2.55	-0.07	1.07	0.00%	3.11%	34.26%	0.00%	10.29%	57.44%
38N	103E	4.96	20.82	0.10	6.91	16.70	0.13	-4.12	0.03	1.95	1.00%	7.01%	46.27%	0.10%	35.26%	75.52%
39N	103E	4.96	22.34	0.19	7.41	18.95	0.22	-3.40	0.03	2.46	1.11%	10.12%	40.71%	1.00%	39.26%	76.52%
40N	103E	5.11	21.96	0.27	7.22	19.56	0.37	-2.40	0.10	2.11	1.00%	14.79%	42.16%	3.10%	37.86%	68.73%
41N	103E	5.20	21.10	0.13	6.97	20.41	0.11	-0.69	-0.03	1.77	1.11%	14.68%	48.16%	2.10%	35.46%	65.83%
42N	103E	5.60	20.77	0.02	6.65	21.59	0.20	0.82	0.18	1.06	1.11%	17.91%	53.28%	2.40%	33.17%	62.84%
43N	103E	5.45	17.33	0.08	6.38	20.10	0.35	2.77	0.26	0.94	0.67%	17.91%	50.83%	1.20%	27.97%	63.24%
44N	103E	5.39	16.17	0.18	6.67	19.61	0.04	3.44	-0.15	1.28	0.11%	21.25%	47.27%	0.70%	30.47%	69.43%
45N	103E	5.14	14.01	0.10	7.04	17.60	0.15	3.59	0.05	1.90	0.00%	14.24%	46.72%	0.30%	33.87%	77.52%
37N	104E	4.63	19.30	0.10	5.58	20.66	0.12	1.36	0.02	0.95	1.11%	5.23%	37.49%	0.50%	13.19%	56.84%
38N	104E	5.44	19.73	0.33	7.63	21.83	0.67	2.10	0.34	2.18	1.45%	14.24%	46.72%	2.10%	42.46%	73.83%
39N	104E	5.38	21.56	0.18	7.63	20.48	0.26	-1.08	0.08	2.25	1.11%	12.79%	46.94%	2.70%	41.46%	73.43%
40N	104E	5.42	21.31	0.34	7.35	19.18	0.19	-2.13	-0.14	1.93	1.00%	13.68%	48.94%	3.70%	40.06%	69.53%
41N	104E	5.64	21.29	0.25	7.10	21.05	0.21	-0.24	-0.04	1.46	1.33%	15.91%	49.72%	2.70%	37.76%	66.53%
42N	104E	5.76	21.37	0.40	6.79	20.83	0.15	-0.53	-0.24	1.04	1.22%	20.91%	53.95%	1.90%	36.36%	63.94%
43N	104E	5.42	17.11	0.15	7.14	21.25	0.21	4.15	0.06	1.72	0.56%	17.24%	46.05%	1.50%	39.66%	72.83%
44N	104E	5.58	15.40	0.42	7.61	20.90	0.38	5.50	-0.05	2.03	0.00%	19.13%	48.83%	0.90%	45.65%	81.02%
45N	104E	4.66	13.87	0.12	7.81	17.31	0.81	3.45	0.69	3.15	0.00%	11.23%	40.60%	0.20%	44.86%	84.22%
37N	105E	4.94	18.92	0.37	5.85	20.63	0.17	1.71	-0.20	0.91	1.00%	10.46%	41.71%	0.70%	17.78%	60.94%
38N	105E	5.47	19.93	0.04	7.74	22.47	0.14	2.55	0.11	2.27	1.33%	15.80%	46.05%	2.50%	45.45%	73.73%
39N	105E	5.56	20.63	0.16	7.92	19.92	0.45	-0.71	0.30	2.36	1.33%	15.24%	51.39%	3.10%	45.05%	77.52%
40N	105E	5.60	20.22	0.18	7.52	19.82	0.12	-0.40	-0.07	1.92	1.33%	13.79%	50.83%	3.70%	42.56%	70.63%
41N	105E	5.68	21.29	0.20	7.15	20.93	0.24	-0.36	0.04	1.47	1.45%	16.69%	50.17%	2.50%	38.06%	68.93%
42N	105E	5.67	21.27	0.04	6.86	20.04	0.17	-1.23	0.13	1.19	1.33%	20.58%	51.39%	1.60%	36.66%	65.23%
43N	105E	5.35	17.42	0.19	7.33	20.65	0.60	3.23	0.42	1.97	0.44%	17.46%	44.61%	1.20%	39.66%	74.83%
44N	105E	5.55	15.34	0.50	7.77	20.57	0.59	5.23	0.09	2.22	0.00%	17.91%	48.94%	0.70%	46.15%	81.82%
45N	105E	4.54	13.99	0.06	7.67	17.42	0.61	3.43	0.55	3.14	0.00%	10.23%	36.93%	0.40%	43.46%	83.12%

Table 6.1: LGM and modern wind velocity frequencies and threshold events over a single section of the Central Loess Plateau (see text). Full tables can found in the Appendix.

Lat	Lon	MOD AVG	MOD MAX	MOD MIN	LGM AVG	LGM MAX	LGM MIN	L-M MAX	L-M MIN	L-M AVG	MOD 16%	MOD 8%	MOD 5%	LGM 16%	LGM 8%	LGM 5%
38N	81E	3.02	8.41	0.08	3.92	20.89	0.05	12.49	-0.03	0.90	0.00%	0.67%	10.90%	0.40%	4.50%	25.87%
39N	81E	3.08	7.10	0.19	4.28	17.80	0.14	10.70	-0.06	1.20	0.00%	0.00%	11.90%	0.30%	6.09%	35.16%
40N	81E	2.95	8.67	0.20	4.36	13.32	0.14	4.65	-0.07	1.40	0.00%	0.44%	10.68%	0.00%	5.09%	40.06%
41N	81E	3.70	12.88	0.13	5.28	13.41	0.21	0.54	0.08	1.58	0.00%	2.67%	23.14%	0.00%	16.08%	49.75%
38N	82E	3.25	9.70	0.11	4.03	17.66	0.08	7.96	-0.02	0.78	0.00%	1.33%	15.13%	0.40%	5.19%	29.07%
39N	82E	3.39	8.60	0.18	4.24	12.81	0.15	4.21	-0.03	0.85	0.00%	0.22%	15.02%	0.00%	5.59%	34.97%
40N	82E	2.91	9.90	0.05	3.77	9.99	0.10	0.09	0.05	0.86	0.00%	0.89%	9.12%	0.00%	3.50%	28.27%
41N	82E	3.41	11.48	0.12	4.32	12.22	0.08	0.74	-0.04	0.91	0.00%	2.89%	19.35%	0.00%	8.69%	37.46%
38N	83E	3.55	10.10	0.25	4.06	17.68	0.02	7.58	-0.22	0.51	0.00%	1.33%	20.02%	0.50%	4.90%	29.77%
39N	83E	3.42	9.39	0.18	4.10	11.64	0.17	2.25	-0.01	0.68	0.00%	0.22%	16.46%	0.00%	4.60%	31.67%
40N	83E	3.06	9.22	0.11	3.95	10.77	0.01	1.55	-0.10	0.89	0.00%	0.67%	9.57%	0.00%	2.70%	29.57%
41N	83E	3.47	10.55	0.09	4.01	12.97	0.13	2.43	0.04	0.54	0.00%	1.11%	21.25%	0.00%	5.89%	32.97%
38N	84E	3.63	10.31	0.10	3.93	18.29	0.15	7.98	0.05	0.29	0.00%	1.11%	20.36%	0.50%	3.80%	26.47%
39N	84E	3.38	10.79	0.21	3.91	11.84	0.19	1.05	-0.03	0.53	0.00%	0.78%	14.91%	0.00%	4.40%	29.97%
40N	84E	3.00	7.79	0.17	4.02	11.19	0.03	3.40	-0.14	1.01	0.00%	0.00%	8.01%	0.00%	4.30%	28.47%
41N	84E	3.37	9.08	0.12	3.82	14.44	0.02	5.36	-0.10	0.45	0.00%	0.44%	18.80%	0.00%	3.90%	29.17%
38N	85E	3.46	8.33	0.08	4.01	16.87	0.05	8.55	-0.03	0.55	0.00%	0.44%	22.91%	0.20%	5.69%	25.87%
39N	85E	3.67	10.43	0.15	3.84	12.53	0.05	2.10	-0.10	0.16	0.00%	1.45%	21.36%	0.00%	5.09%	25.27%
40N	85E	3.26	8.64	0.04	3.92	10.99	0.06	2.35	0.02	0.66	0.00%	0.44%	14.91%	0.00%	9.39%	29.97%
41N	85E	3.43	8.53	0.06	4.22	10.97	0.04	2.45	-0.02	0.79	0.00%	0.78%	20.02%	0.00%	8.49%	34.27%

Table 6.2: LGM and modern wind velocity frequencies and threshold events over a single non-topographic section of the Taklamakan Desert (see text). Full tables can found in the Appendix.

Lat	Lon	MOD AVG	MOD MAX	MOD MIN	LGM AVG	LGM MAX	L-M MIN	L-M MAX	L-M MIN	L-M AVG	MOD 16%	MOD 8%	MOD 5%	LGM 16%	LGM 8%	LGM 5%
-46	287	6.65	13.77	0.18	9.05	23.22	0.26	9.45	0.08	2.41	0.00%	26.70%	71.97%	3.34%	64.52%	93.99%
-45	287	6.16	13.12	0.03	8.40	20.39	0.13	7.28	0.10	2.23	0.00%	19.91%	67.52%	1.45%	57.29%	94.10%
-44	287	5.73	15.59	0.05	7.38	19.59	0.78	4.01	0.74	1.65	0.00%	16.69%	58.62%	0.67%	45.61%	84.20%
-43	287				6.42	15.78	0.44							0.00%	33.82%	74.19%
-51	288	11.70	20.91	1.46	10.41	23.36	1.46	2.45	-0.01	-1.28	14.57%	80.53%	91.32%	14.68%	70.41%	99.67%
-50	288	11.49	20.57	0.55	10.79	23.46	0.53	2.89	-0.02	-0.70	13.35%	77.98%	91.21%	19.80%	75.64%	99.44%
-49	288	10.26	18.41	0.12	11.16	24.17	0.35	5.76	0.23	0.90	4.00%	73.41%	89.10%	23.47%	73.41%	97.22%
-48	288	9.44	18.40	0.66	11.09	24.32	0.42	5.92	-0.24	1.65	1.89%	67.63%	85.98%	22.47%	74.64%	96.22%
-47	288	8.18	16.93	0.31	10.57	21.94	0.30	5.01	0.00	2.39	1.33%	48.39%	81.54%	19.02%	70.52%	96.33%
-46	288	7.92	16.62	0.53	10.96	23.89	0.35	7.27	-0.18	3.04	1.00%	44.38%	78.64%	21.47%	74.30%	96.89%
-45	288	7.60	15.96	0.18	11.16	23.78	0.84	7.82	0.66	3.56	0.00%	41.49%	73.75%	23.58%	78.09%	97.11%
-44	288	6.76	15.39	0.23	9.91	21.54	1.85	6.16	1.62	3.15	0.00%	30.26%	66.96%	10.12%	67.74%	102.78%
-43	288	6.45	15.19	0.24	9.19	18.58	0.71	3.39	0.47	2.74	0.00%	25.25%	66.30%	4.12%	66.96%	99.33%
-51	289	11.67	21.19	0.90	10.16	25.12	0.54	3.92	-0.36	-1.51	15.24%	80.20%	90.99%	14.02%	71.86%	98.89%
-50	289	10.99	19.94	0.07	10.01	23.94	0.85	4.00	0.78	-0.98	9.90%	76.53%	91.21%	14.13%	70.30%	98.89%
-49	289	9.99	17.61	0.39	10.35	24.65	0.22	7.03	-0.17	0.36	3.23%	72.30%	88.88%	16.57%	71.86%	96.22%
-48	289	9.53	18.28	0.28	10.67	25.35	0.61	7.07	0.33	1.13	2.22%	67.85%	87.10%	19.02%	72.86%	97.55%
-47	289	8.35	17.34	0.20	9.98	23.39	0.31	6.06	0.12	1.63	2.00%	51.50%	83.76%	13.90%	66.74%	95.11%
-46	289	8.20	17.75	0.46	10.59	23.12	0.22	5.37	-0.24	2.39	3.11%	49.17%	80.31%	17.69%	72.30%	98.00%
-45	289	7.94	17.29	0.25	11.07	22.96	0.30	5.67	0.05	3.13	2.11%	42.83%	77.20%	20.47%	76.75%	100.00%
-44	289	7.20	15.79	0.74	10.42	21.21	1.64	5.42	0.90	3.22	0.00%	37.49%	71.86%	14.57%	73.30%	102.45%
-43	289	7.12	16.59	0.58	10.64	20.86	1.26	4.27	0.69	3.51	0.44%	35.37%	70.30%	13.13%	75.53%	105.23%
-51	290	11.51	21.02	0.43	9.80	25.87	0.42	4.85	0.00	-1.71	13.79%	79.64%	91.43%	12.79%	69.19%	97.00%
-50	290	10.65	19.38	0.57	9.45	25.07	0.77	5.69	0.20	-1.20	7.23%	74.19%	91.99%	11.90%	61.74%	96.11%
-49	290	9.95	17.87	0.13	9.79	24.05	0.09	6.18	-0.04	-0.15	3.23%	70.97%	90.99%	13.68%	68.41%	96.44%

Table 6.3: LGM and modern wind velocity frequencies and threshold events over an area over Patagonia (see text). Full tables can found in the Appendix. Shaded area represents ocean-covered regions during the modern that are exposed during the LGM.

A similar one by one degree sampling scheme was adopted over the Taklamakan Desert, which is further inland from the Central Loess Plateau. This area is bound at the south by Tibet, China, and to the Northeast by the Pamir Mountains, Tajikistan. The sampling scheme was for a 37°N-45°N, 80°E-91°E boxed area with no bias for topography. A secondary analysis for this region was creating solely consisting of sites between 38°N-41°N, 81°E-85°E to remove any effect, if any, by foreland topography. Maximum gust events are at 19.89 m/s over 37°N, 87°E for the modern and 26.21 m/s over 45°N, 87°E for the LGM. The later has a 13.06 m/s increase during the LGM - the highest for this sampling region. On average, wind velocities are 1.39 m/s stronger during the LGM, and the average of maximum gust events are 4.49 m/s more intense in this region. 90% of all sites have a higher max gust event during the LGM and 95% of sites have a higher average wind velocity during this time. There is a ~3x fold increase in the percentage of 16 m/s and 8 m/s events in the Taklamakan Desert source area.

With a cubic (or even fourth power) relationship between surface wind velocity and dust flux (e.g. Gillette, 1974; Tegen and Rind, 2000; Maher et al., 2010; and also McGee et al., 2010 Fig. 3), the higher velocity events (up to the top 0.1% of events) can account for 50% or more of cumulative mineral dust emissions (cf. Timmreck and Schulz, 2004; Maher et al., 2010). Both East Asian source locations that were examined have higher hourly gust events during the LGM. The Taklamakan Desert had the highest increase with 4.49 m/s more intense maximum gust velocities, compared to the CLP, and a high average LGM hourly velocity. One site has 9.9% of its hourly frequency above the 16 m/s threshold in the Taklamakan Desert, as compared to maximum site of 6.29% in the CLP during the LGM (see Table 6.1; Appendix). Although these results are concerned with the “extreme” values of gustiness, they are coincident with increased zonal surface stress in all four winters of the climatological run. The higher stress values extend eastward over the North

Pacific from East Asia, Eastern Siberia and over Northern Japan, agreeing with the North Pacific cyclogenesis results discussed in Chapter 5.

The 2-3x fold increase in high velocity events during the LGM over these regions, and an average velocity increase across the distribution (see plots) suggests that the increase in wind gustiness during the glacial can provide a driver for increased glacial dust emissions, with the assumption that aridity isn't necessarily the primary global control. It has been suggested that changes in aridity and dust source sizes play a more regional (as opposed to global) role as evident in lake level records (McGee et al., 2010).

A similar third analysis was done over the Patagonian region in South America within the Southern Hemisphere (SH). This area is of significant importance as our understanding of the mechanisms responsible for dust delivery to the Southern Ocean and Antarctica is still greatly debated and impacts ocean productivity in an area that highly modulates global ocean-atmosphere CO_2 interactions (Mahowald et al., 1999; Sugden et al., 2009; Martinez-Garcia et al., 2009; Giebert et al., 2010; and others). Isotopic tracers have suggested that South America is the primary dust source to the Antarctic ice cores (Petit et al., 1990; Sugden et al., 2009) but the primary mechanisms responsible for the large dust burden increase seen in the Antarctic record remains unclear – and until now, no high-resolution paleo-modelling studies have attempted to explore synoptic-scale events during the LGM over this area. Consequently, another one-by-one degree sampling section was analyzed around 43°S-51°S, 65°W-76°W to cover the Altiplano Plateau-Patagonia area and encompasses the SH glacial dust source areas outlined in both McGee et al., (2010) and Sugden et al., (2009).

Table 6.3 shows a section of this area (cf. Appendix). Here, there is a ~4-5x fold increase (2.30% to 8.96% over all "stations" and 2.30% to 10.97% when *only* taking into account coincident land areas where the modern land mass is not covered by ocean) in the number of events exceeding the 16 m/s threshold during the LGM compared to the modern. The LGM also has an average maximum gust event of 5

m/s greater than the modern station counterparts both over the topography to the west and lowlands to the east. The single highest velocity maximum "station" in the modern in this region is just over 21 m/s (21.19 m/s) and the highest maximum in the LGM integration is ~29 m/s (28.89 m/s). Several corresponding grid points have a ~10 m/s maximum gust event larger than the modern. LGM max gust events are on average 22 m/s, with some stations around the 30 m/s level. Station by station, hourly wind velocities are on average 1.26 m/s greater during the LGM compared to the modern in this area (cf. Tables).

6.2: LGM Air Parcel Trajectories and Source Wind Locations:

Although the initial gust analysis demonstrates that LGM wind gustiness may provide more events over wind velocity thresholds which have been shown to significantly increase dust emissions in the modern, it is also important to determine the source location of air in the synoptic simulation to both ice and marine core locations.

***

Using a version of the three-dimensional Melbourne Parcel Trajectory Software (see Chapter 3) that was modified for this work, a first-look of backward trajectories was compiled for the LGM over several southern and northern hemisphere locations with documented geological sites such as ice and marine cores. A 9-day lifetime was used on each air parcel to simulate pathways within the simulation with a duration analogous to the simulated average lifetimes of atmospheric dust by Mahowald et al., (1999; 2006). Given the large increase in the glacial dust burden in the geological record, understanding the LGM source locations of terrestrial mineral dust to the ice cores is a long sought after issue in the field (cf. Biscay et al., 1997; Martinez-Garcia et al., 2009; Sugden et al., 2009).

The results presented here are synoptic scale trajectories that will change depending on the variability of the winds. Consequently, results demonstrate the potential

existence of such pathways during the LGM given ice age physics, especially when considering the similarities of flow between the synoptic run and the short "climatological" simulation as well as the agreement of the general results with recent studies (e.g. Charles et al., 1994; Bromwich et al., 2004; Langen and Vinther, 2008; Donohue and Battisti, 2009; and several others). They are not to be considered permanent features however. The similarities between the hourly-scale findings and the interpretation of the geological record within these regions is compelling - and enough so that the agreements are reported upon herein.

Antarctic ice cores suggest a massive increase in dust flux during the glacial times with many records indicating concentrations 20-50 times higher than today (Sugden et al., 2009). Some evidence suggests South America (specifically Patagonia and the Altiplano) to be the major contributor to the SH ice cores, especially given the geographical changes in the region under ice age conditions, such as the lowered eustatic sea level exposing more of the continental shelf and thereby introducing longer rivers in the region (cf. Sugden et al., 2009). However, this is still under investigation (e.g. Mahowald et al., 1999) along with the specific driver responsible for the increase.

Dome C, Vostok, Dome F, MGA, and Neumayer (and UK group – see Figure) ice cores, James Ross Island and the marine core site 1090 (cf. Martinez-Garcia et al., 2009; Geibert et al., 2010) are analyzed for parcel source locations using the modified trajectory software (cf. Chapter 3). Source locations were computed every 6-hours within the synoptic scale simulation with a lifetime of 9-days. Target locations were permitted to stack vertically into the atmosphere to ~300 hpa.

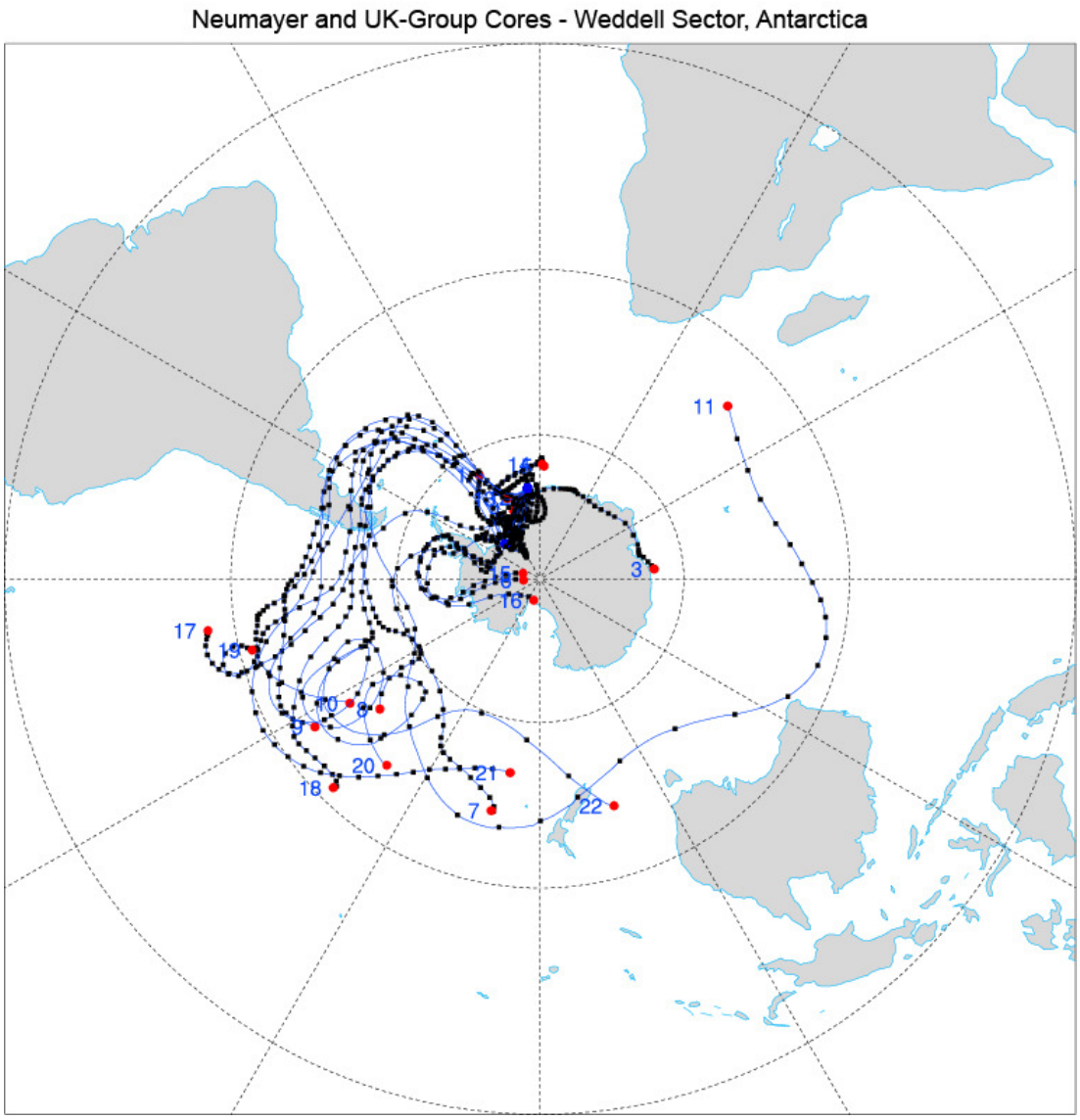

Figure 6.4: Neumayer and UK group ice core locations backward trajectories in a single snapshot. Trajectory lifetime is set at 9-days to be consistent with LGM dust lifetime estimates of Mahowald et al. (1999).

Figure 6.4 shows the backward trajectories during the LGM, over the Weddell Sea sector with target locations set at the Neumayer and UK group ice core locations. This figure represents a single snapshot, with each calculation six hours apart from the previous. The full trajectory compilation for this location, and others, can be found in the Appendix. At this location, 87% of all trajectory instances have pathways that extend over the Patagonia-Altiplano sector and 64% of all trajectory instances have pathways over New Zealand. Noticeably, many trajectories that pass

through the Drake Passage are subsequently diverted southward onto the ice as also evident in Fig. 6.4.

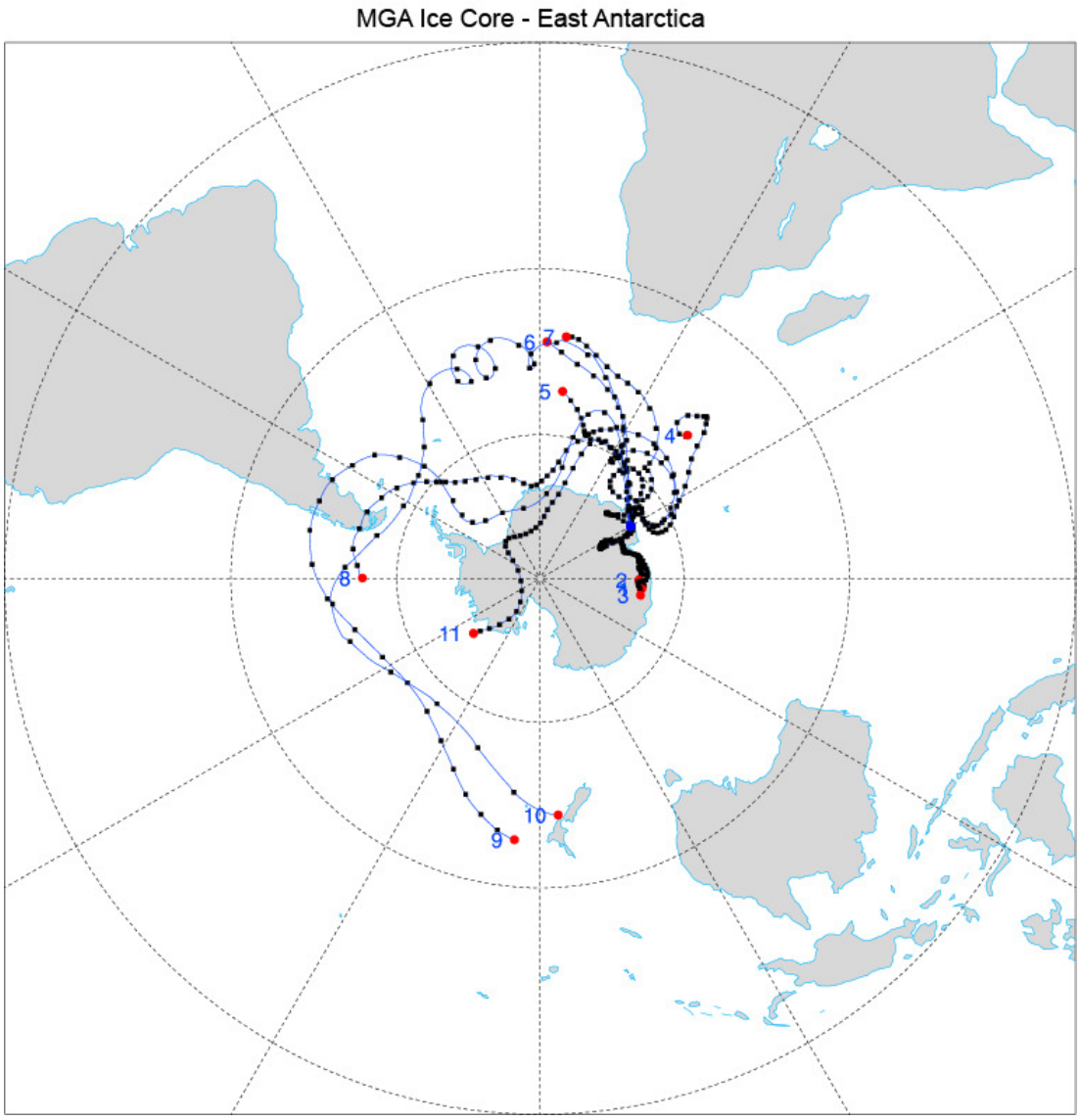

Figure 6.5: MGA ice core location backward trajectories in a single snapshot. Trajectory lifetime is set at 9-days to be consistent with LGM dust lifetime estimates of Mahowald et al. (1999).

Figure 6.5 shows a snapshot of LGM backward trajectories for the eastern Antarctic ice core of MGA. At this location, 57% of the trajectory time-frames have pathways extending over the Patagonia-Altiplano area. Interestingly, there are numerous instances of trajectories being confined to an eastern Antarctic boundary current along the coastline, sometimes emanating all the way from the Ross Sea (a smaller

version of this is visible in Fig. 6.5 along the eastern coast by Princess Elizabeth Land). Trajectories at this location are also seen sourcing from over the South Atlantic, and are clearly reacting to synoptic events along the South Atlantic Convergence Zone, as well as eddies funnelling through the Drake Passage. There are moments when trajectories are just off the coast of South Africa, but are never sourced directly over land.

Figure 6.6 shows a snapshot of the LGM trajectories to Dome C and Vostok core locations. These, like the Neumayer location, were grouped together due to their relative proximity compared to other locations. Although they are much further inland compared to the last few compilations, 24% of trajectory moments have trajectories sourcing from over the Patagonia-Altiplano sector, and 4% are derived from locations over land in South Africa – although there are numerous instances when parcels source from just off the coast (as evident in Fig. 6.6). Many trajectories are sourced from over New Zealand. Trajectories at this location synoptically transition (on the order of a few days) from confined local sources, to being more extended (northward) into the South Atlantic and South America.

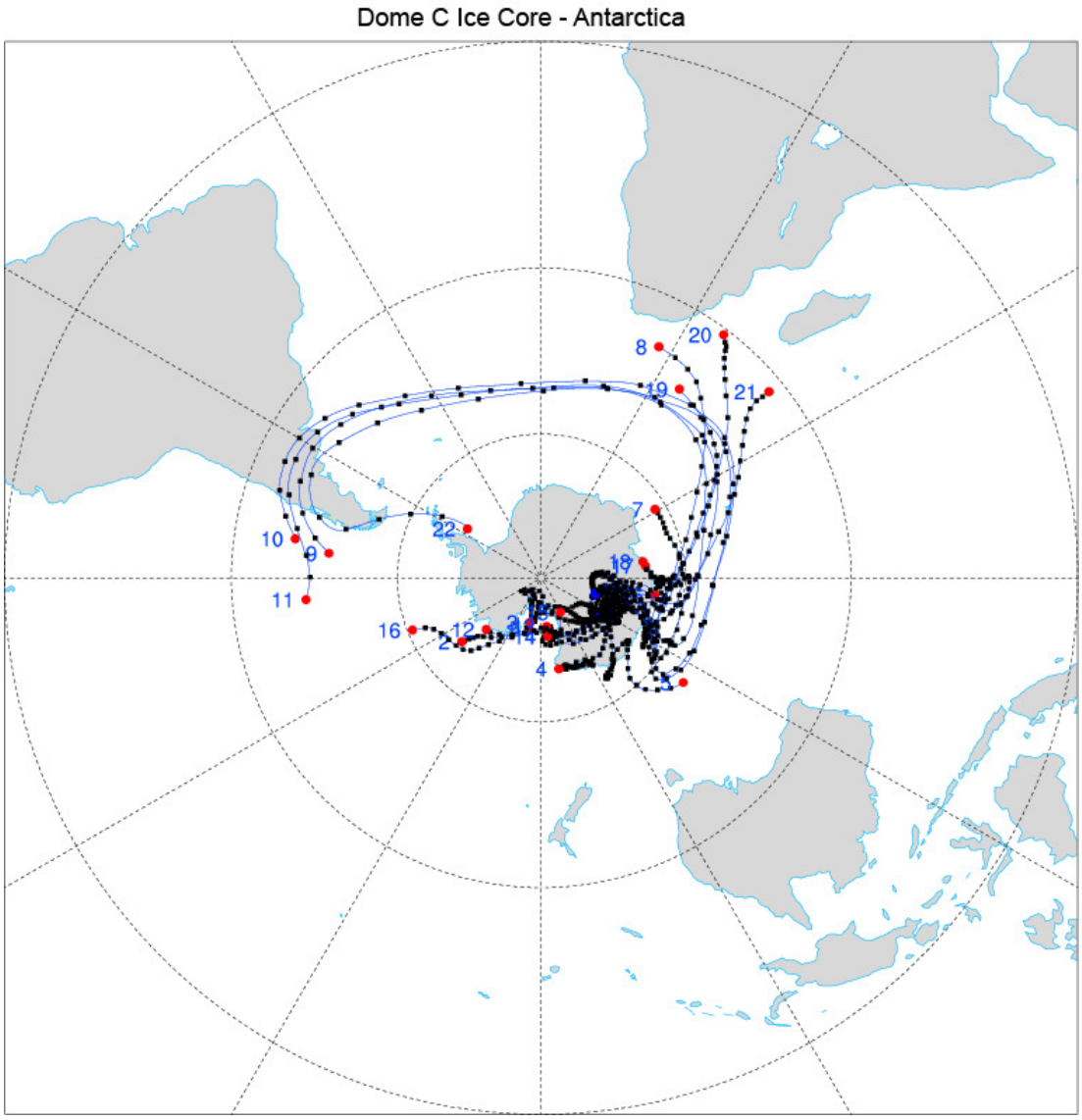

Figure 6.6: Backward trajectories from the Dome C and Vostok ice core locations in a single snapshot. Trajectory lifetime is set at 9-days to be consistent with LGM dust lifetime estimates of Mahowald et al. (1999).

An instance of backwards LGM trajectories for Dome F in Queen Maud Land is shown in Figure 6.7. Like the MGA ice core location, Dome F has many trajectories that are derived from a boundary current along the Eastern Antarctic coastline (not actually captured in this snapshot – see Appendix). A large percentage of instances have pathways extending into the South Atlantic and are clearly reacting to synoptic events near the South Atlantic Convergence Zone. Overall, 12% of the trajectory snapshots capture parcels that are derived from trajectories passing over the

Patagonia-Altiplano region. This is a relatively large decrease compared to the percentages in the Neumayer core to the west, and MGA core to the east that originate from (or passing over) the South American dust source. Although no trajectories at this location cross over land in South Africa, there are several instances that are just off the coast.

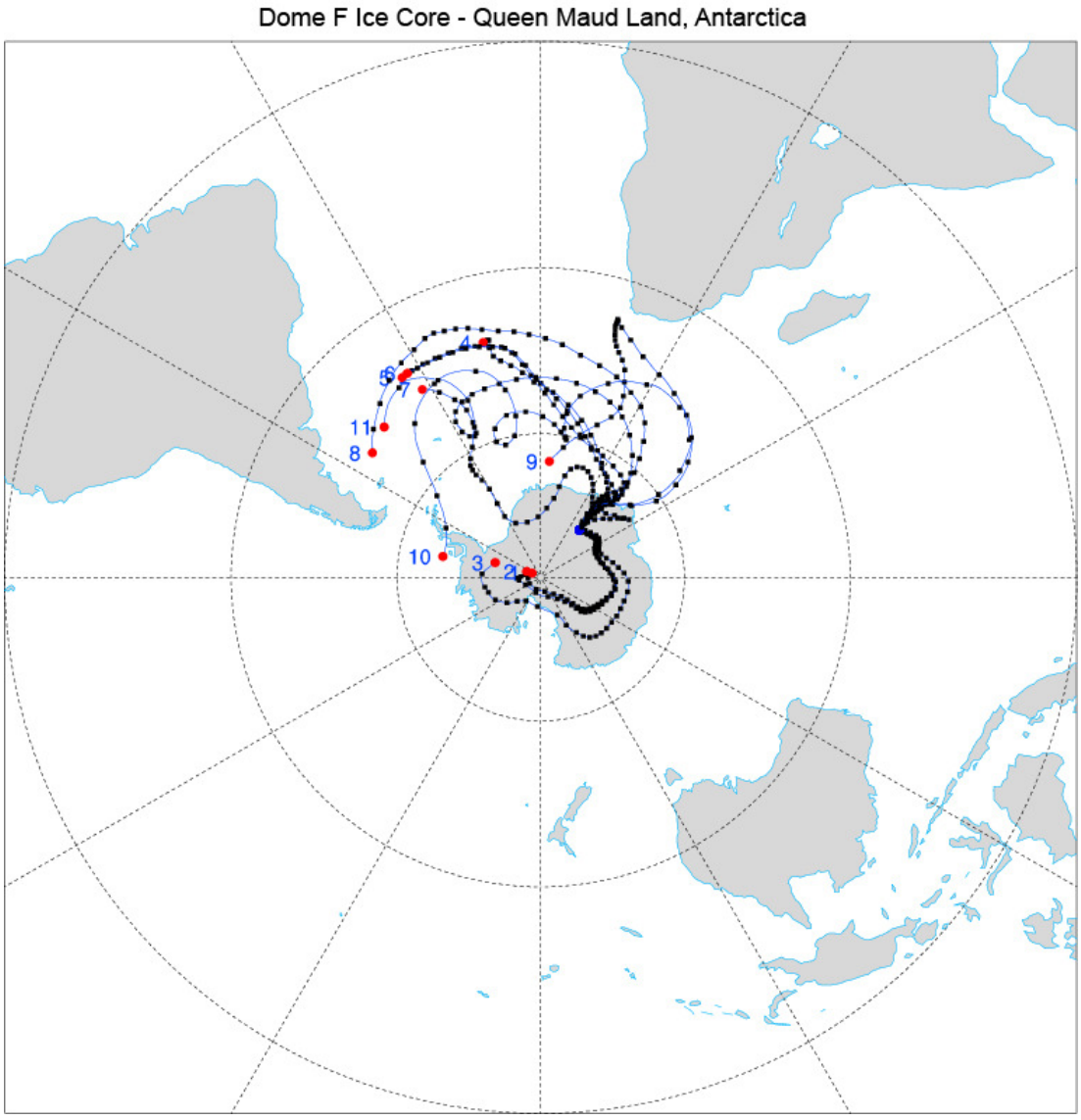

Figure 6.7: Same as Fig. 6.6 but for the Dome F ice core.

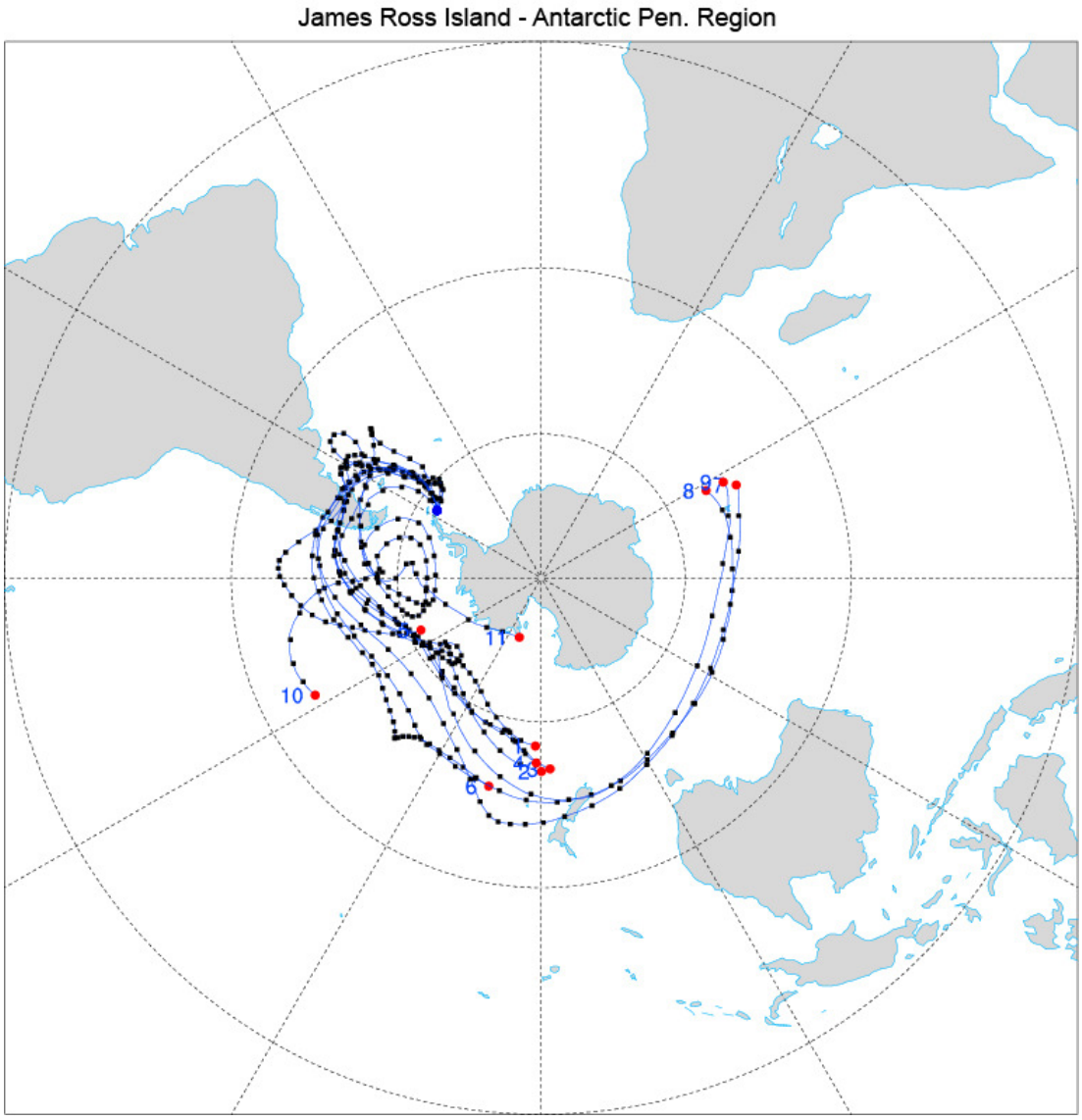

Figure 6.8: Same as Fig. 6.7 but for the James Ross Island location.

The same analysis was done over James Ross Island along the Antarctic Peninsula (Fig. 6.8). Here, the majority of 6-hourly calculations have trajectories that pass over the Patagonia-Altiplano source area. Numerous parcels also pass over New Zealand and southern Australia, while 3% contain trajectories that pass over land in South Africa (with a higher percentage right off the coast in this region). Many trajectories are forced by transient eddies passing through the Drake Passage (see Figure 6.8) which, given the 9-day lifetime, pass too and from the source area to over the

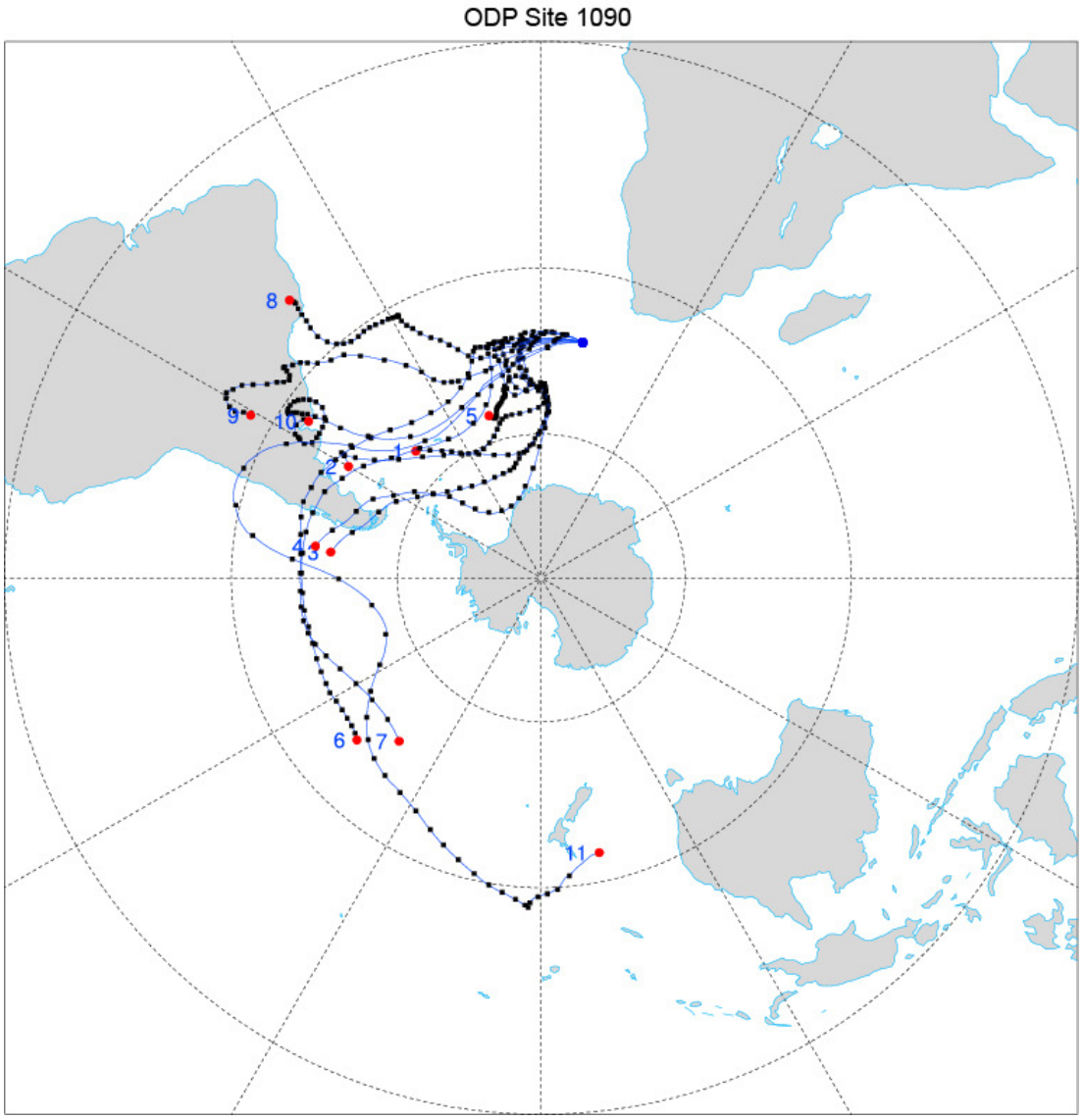

Figure 6.9: Same as Fig. 6.8 but for the ODP 1090 marine core (cf. Martinez-Garcia et al., 2009).

peninsula more than once in a given track (see figure). The majority of tracks are sourced from the west, while there are a few 6-hourly composites that are derived far from the east including from parcels tightly bound to the coast of Antarctica.

Also examined are the three-dimensional trajectories from the marine core ODP site 1090 south of South Africa. This core records the typical glacial-interglacial changes in dust but the sources to this location have been suggested to have emanated from South America or South Africa (cf. Martinez-Garcia et al., 2009). A snapshot of the

trajectories for this location is shown in Figure 6.9. The vast majority (95%) of the 6-hourly composites contain pathways extending over South America including Patagonia, the Altiplano and even into Brazil and the interior. The trajectories extending into Brazil follow the northwest-southeast orientation typical of the South Atlantic Convergence Zone. In contrast, about 9% source from South Africa. Pathways to this location also originate from the south over Antarctica and the Weddell Sea.

6.3 Discussion and Summary:

One of the primary objectives of the paleoclimatological community is to use the dust record preserved in ice cores and ocean sediments, coupled with our knowledge of current Earth system processes, to improve our understanding of these linkages in the current climate state and consequently our interpretation of past climate regimes (Maher et al., 2010).

McGee et al. (2010) proposed multiple lines of compelling arguments that suggest gustiness as a first-order control on glacial dust levels. During glacial times, reduced vegetation and aridity expanded dust source areas and eustatic sea level dropped exposing shelf sediments, but gustiness may provide the best available mechanism for explaining such dust flux changes seen in the ice cores. McGee et al. (2010) concluded that although paleo-records demonstrate strong links between high-latitude temperatures, seasonality and dust fluxes, high-resolution modelling is needed over dust source areas. The hourly-simulation here provides a first-look into LGM gustiness with modelling on a level similar to large-scale field experiments.

Results show, over the Central Loess Plateau in East Asia there is a two fold increase in the percentage of number of events over the 16 m/s and a ~2.5x fold increase in the 8 m/s threshold during the LGM hourly simulation compared to the modern simulation. There is also an average of 1.75 m/s greater hourly wind velocity with average maximum gust events, over all stations, 0.40 m/s more intense during the LGM over the region. Over the Taklamakan Desert, there is a ~3x fold increase in

the percentage of 16 m/s and 8 m/s threshold events. Average hourly wind velocities are 1.39 m/s stronger during the LGM and maximum gust events are 4.49 m/s more intense in this region as well. Over the Patagonia dust source location (see text), there is an up to 5x fold increase in the number of gust events over the 16 m/s velocity threshold. Maximum gust velocities are also 5 m/s greater in this region during the LGM compared to the modern simulation.

Over several Antarctic ice core locations, a three-dimensional backward trajectory analysis (cf. Chapter 3) finds that most sites source air in varying amounts from the Patagonia-Altiplano region, coinciding with the dust source area analyzed in section 6.1. The Neumayer (87% of the time sampling had pathways over the Patagonia-Altiplano region), MGA (57%), Dome C (24%), Vostok (24%) and James Ross Island (65%) ice cores were analyzed along with ODP site 1090 (95%) south of South Africa. Dome C and ODP Site 1090 have some trajectories (4% and 3% respectively) sourcing from over land in South Africa. Several of the locations also have trajectories crossing over New Zealand and Southern Australia (cf. Appendix).

The gust analysis and backwards trajectories are supported by recent studies and the geological record (Petit et al., 1990; Sugden et al., 2009; Geibert et al., 2010; McGee et al., 2010). The 2-5x fold increase in maximum hourly wind velocities over dust source locations lend credence to the hypothesis of McGee et al. (2010) that gustiness is a driver for the increased dust burden during the LGM.

Sugden et al. (2009) note that modern wind velocities over Patagonia reach 22 m/s (reaching higher speeds along the coast further south out of the analyzed area) and state that dust entrainment in this area should have been greater during the glacial given enhanced atmospheric vigour - which is indeed the case in the hourly integration. Further to this, the trajectories demonstrate that a large percentage of pathways extend over Patagonia, supporting isotopic tracer evidence which suggest South America to be a dominate source for Antarctic glacial dust (Petit et al., 1990).

This chapter is primarily concerned with the "extreme" wind events over published velocity thresholds estimated to cause the majority of dust entrainment (e.g. Chomette et al., 1999; Mahowald et al., 1999; Sugden et al., 2009; McGee et al., 2010), results are expected to be blurred in the climatological mean values. Nonetheless, results are coincident with high surface stress along eastern boundaries of the CLP and Taklamakan Desert region in all four winters of the climatological run (cf. Chapter 4; Appendix). The increased surface stress extends into the North Pacific, including from Eastern Siberia and over Northern Japan, linking these results with the cyclogenesis findings presented in Chapter 5.

Chapter 7

Final Statements & Conclusions:

7.0 Summary:

An exploration into high-resolution "paleometeorology" during the Last Glacial Maximum has been presented, using what may be the highest spatial and temporal resolution in-tandem global simulations of the LGM.

The simulations were used to analyze specific synoptic-scale events that may have occurred during the LGM given ice age boundary conditions and to determine the differences in northern hemispheric flow and cyclogenesis. Furthermore, the paleometeorological results were used to address: (1) whether examination of higher resolution simulations, on both spatial and temporal scales, can enhance paleometeorological inferences based previously on monthly statistics of model output and in turn examine (2) whether certain synoptic-scale events, which may have only a modest impact on seasonal statistics, might have exerted a disproportional impact on the preservation of geological climate records such as the large increase in glacial dust emissions.

From a climatological viewpoint, the duration of both the synoptic and climatological integrations (cf. Kim et al., 2008) might seem limited. However, from the meteorological perspective, the duration of the "record" is comparable (or longer in duration) to large-scale field experiments and experiments concerned with analyzing impacts of synoptic systems such as those responsible for aerosol dust emissions (e.g. Bishop et al., 2002; Sow et al., 2009).

In previous chapters, comparisons were made between the synoptic scale results to the climatological simulation first presented in Kim et al. (2008), other GCM experiments and several geological records. The summary of the novel results of the simulations are presented in this final chapter.

***

A widely known geological interpretation has controversially suggested that evidence along the west coast of North America poses a threat to the orbital theory of the ice ages and an earlier global deglaciation (Winograd et al., 1992; Winograd, 2002). This has been scrutinized using alkenone data off the coast of California (Herbert et al., 2001), suggesting that the changes seen in the Devils Hole Calcite may actually reflect a change in the California Current System, which is heavily effected by pressure systems in the North Pacific, rather than a global lock-step change out of the glacial. The modelling results presented here, which better our understanding of such interpretations show: (1) A ~15% decrease in storm intensity of the North Atlantic; (2) An ~8% increase in North Pacific storm intensity; (3) A shift in the LGM North Pacific storm track ("sickle" shaped) with trans-Pacific storm systems being focused along the west coast of North America, into the Gulf of Alaska and subsequently north of Canada and north of the Laurentide Ice Sheet; (4) Wintertime precipitation is significantly decreased over Greenland; (5) The North Atlantic storm track is confined to a narrow band along the extended sea ice margin. Storms exiting the North Atlantic are focused along the western edge of Northern Europe and the United Kingdom, the increased precipitation of which may help the expansion (or stability) of the ice sheet in this region.

The hourly-scale findings in the North Pacific show an increase in convective precipitation and relatively warmer air along the California coast and south-westerly onshore flow during winter. These results are lent credence by the in-tandem climatological run, with all years showing a tongue of increased precipitation in the region and increased (relative) meridional heat flux. This is further compounded by geological evidence *not* showing Cordilleran glacial retreat (cf. Young et al., 2010;

Chapter 5) and rising lake levels in the Great Basin (Benson et al., 1990; Chapters 4, 5) during the LGM. The balance of evidence therefore suggests that although it might be tempting to interpret inferred glacial-maximum warming along the west coast of North America as an "early response" of deglaciation, the most appropriate interpretation is that the trend reflects a natural regional response to ice-age warming - and has nothing to do with subsequent deglaciation.

The arching of the Pacific track over Canada and the Laurentide Ice Sheet subsequently results in a significant reduction in the wintertime Greenland precipitation rate (~1.6 x 10^{-3} mm/hour) and total accumulation (3.5 mm), with ~25% of the total deposited over a week long event (the peak rate is ~1.0 x 10^{-2} mm/hour – at hours 628-894). The four climatological winters range from 2 mm to 6 mm total, as compared to 75 mm to 106 mm in the climatological control simulation. The majority of storms terminate west of Greenland in the Labrador Sea. This is also north of the North Atlantic baroclinic zone which has recently been suggested to cause reduced cyclogenic seeding in the region - resulting in a more quiescent North Atlantic. The 15% decrease found here is comparable to the 17% found in Donohue and Battisti (2009; Chapter 5). The decrease in the simulated precipitation over Greenland is coincident with geological data in the ice cores (Johnson et al., 2001; Chapter 5) supporting the results of the simulations which give a better understanding of the mechanisms responsible for Greenland moisture delivery.

Below the ice sheet margin, the hourly integration shows a pan-handle of low variability bound by the Appalachian Mountains to the east, the Laurentide Ice Sheet to the north and the Colorado Plateau/Rocky Mountains to the west – the western edge becomes more variable around the Mississippi River (cf. Chapter 4, Fig. 4.12). This area is manifested in all four years of the climatological integration (and synoptic mean) with a turn to south-westerly flow in the area. Conditions are appropriate to explain a more equable climate in this region which encompasses approximately 8250 km^2 east of the Mississippi River and extending southward. Geological evidence in the form of vegetation reconstructions shows that biomes below the ice sheet margin may support this finding with evidence of thermophilous

tree species around the Ohio area including some macro fossil evidence of American Beech (*Fagus grandifolia*). Furthermore, in-situ land snail (*Discus shimekii*) data demonstrates that the eastward migration of this species halted along the eastern edge of the low variability pan-handle (cf. Chapter 4). These findings may help with the effort in reconciling the paleo-migration rates which have been suggested to be an order of magnitude too rapid (Mclachlan and Clark, 2004) given the assumption that LGM tree species were primarily confined to southern refugia.

The hourly outputs also allow inspection of fine scale events such as gustiness. McGee et al., (2010) made a compelling argument for gustiness being a major driver for the increased dust burden during the LGM. In regards to this, individual storms over such areas have been shown to double ocean productivity in Fe limited regions (Bishop et al., 2002; Sow et al., 2009; cf. Maher et al., 2010). The synoptic scale integration allows at least for the first inspection of such processes during the LGM and these findings support the hypotheses of McGee et al., (2010). In the hourly-simulation, over the Central Loess Plateau in East Asia, there is a ~2x fold increase in the number of events over the 16 m/s and a ~2.5x fold increase in the 8 m/s threshold during the LGM compared to the modern simulation (cf. Chomette et al., 1999). There is also an average of 1.75 m/s greater hourly wind velocity, with average maximum gust events 0.40 m/s more intense during the LGM over this dust source location. Over the Taklamakan Desert, there is a ~3x fold increase in the percentage of 16 m/s and 8 m/s events. Average hourly wind velocities are ~1.4 m/s stronger during the LGM and maximum gust events are ~4.5 m/s more intense in this region as well. Over the Patagonia dust source location (see Chapter 6), there is up to a 5x fold increase in the number of gust events over the 16 m/s velocity threshold. Maximum gust velocities are also 5 m/s greater in this region during the LGM compared to the modern simulation. With such gust events, the top 0.1% of synoptic scale wind events may account for over 50% of the total atmospheric dust burden (cf. McGee et al., 2000).

***

The primary caveat for this project is that the synoptic integration is a single ice age wintertime and the Kim et al., (2008) experiment is short in terms of "climatology". Nonetheless, it is important to point out specific findings that are similar to the presented results and can be explained by either specific synoptic events having a disproportionate impact on the mean-state, geological record, or which may explain the interpretation of some proxies if future paleometeorological integrations confirm the typicality of these results. The general results in the synoptic integration compare well with the four winters of the climatological simulation of Kim et al., (2008) but also several other GCM and geological experiments which have had a large impact of our understanding of the LGM (Charles et al., 1994; Kageyama et al., 1999; Herbert et al., 2001; Langen and Vinther, 2009; Donohue and Battisti, 2009; McGee et al., 2010; and others). This includes the modified split jet over North America, the shifting of the storm track in this region, the suggested decrease in North Atlantic cyclogenesis, increased gustiness over dust source areas and the interpretation of the south-westerly flow along the west coast of North America (which was suggested in a statement in Herbert et al., 2001 in regards to the decline in Californian Sequoia). Consequently, many of the synoptic scale results may be considered typical, suggesting that recent interpretations of GCM and geological evidence may simply be a natural regional result given ice age boundary conditions rather than a response due to a global "climatological" modification. For instance a shift in the delivery of precipitation from local sources to the North Pacific during the LGM could conceivably contribute to rapid seasonal fluctuations in ^{18}O in the Greenland ice cores (cf. Charles et al., 1994; Fawcett et al., 1999; Langen and Vinther, 2009). These results continue to stack evidence in terms of the atmosphere playing a critical role in effecting the ice core record and not just the ocean.

Overall, results demonstrate that high temporally and spatially resolved simulations can provide valuable insight to add to the cornucopia of information already available from lower-resolution runs. They can also adjust our interpretation of geological records which may have been previously assumed to solely record longer time-scale, climatological mean-states, ignoring any extreme synoptic events which may actually have had a disproportionate impact on their preservation. It is therefore

important, in light of this investigation, to continue to explore paleometeorology with higher resolution runs in an attempt to address some of the problems which have plagued both the paleoclimate and geological communities for decades. Consequently, future work will involve running a multi-decadal synoptic-scale paleometeorological simulation using a stable build of the high-resolution version of the CAM3 model at Oak Ridge National Labs using their new generation of supercomputers.

References:

Adams, J.M., Faure, H., Faure-Denard, L., McGlade, J.M., and Woodward, F.I.: Increases in terrestrial carbon storage from the last glacial maximum to the present. Nature 348, 711-714, 1990.

Agassiz, L.: Études Sur Les Glaciers; Ouvrage Accompagné d'un Atlas de 32 Planches. Neuchâtel, Jent et Gassmann, 1840.

Anderson, D.M., Prell, W.L., and Barratt, N.J.: Estimates of sea surface temperature in the Coral Sea at the last glacial maximum. Paleoceanog., 4, 615-627, 1989.

Anderson, L.L., Sheng Hu, F., Nelson, D.M., Petit, R.J. and Paige, K.N.: Ice-age endurance: DNA evidence of a white spruce refugium in Alaska. Proc. Nat. Acad. Sci., 103, 33, 12447-12450, 2006.

Anderson, R. F., S. Ali, L. I. Bradtmiller, S. H. H. Nielsen, M. Q. Fleisher, B. E. Anderson, and Burckle, L. H.: Wind-Driven Upwelling in the Southern Ocean and the Deglacial Rise in Atmospheric CO2. Science, 323(5920), 1443-1448, 2009.

Ballantyne, A.P., Lavine, M., Crowley, T.J., Liu, J., and Baker P.B.: Meta-analysis of tropical surface temperatures during the Last Glacial Maximum. Geophys. Res. Letters, 32, L05712, 2005.

Bartlein, P.J., Anderson, K.H., Anderson, P.M., Edwards, M.E., Mock, C.J., Thompson, R.S., Webb, R.S., Webb III, T., and Whitlock, C.: Paleoclimate simulations for North America over the past 21,000 years: features of the simulated climate and comparisons with paleoenvironmental data. Quat. Sci. Rev. 17, 535-548, 1998.

Beck, J.W., Edwards, R.L., Ito, E., Taylor, F.W., Recy, J., Rougerie, F., Joannot, P., and Henin, C.: Sea surface temperature from skeletal Sr/Ca ratios. Science, 257, 644-647, 1992.

Beck, J.W., Récy, J., Taylor, F., Edwards, R.L., and Gabioch, G.: Abrupt changes in early Holocene tropical sea surface temperature derived from coral records. Nature, 385, 705-707, 1997.

Bengtsson, L., Hodges, K.I., and Keenlyside, N.: Will extra-tropical storms intensify in a warmer climate? J. Clim., 22, 2276–2301, 2009.

Benson, L.V., et al.: Chronology of expansion and contraction of 4 Great Basin lake systems during the past 35,000 years. Palaeogeog., Palaeoclim., Palaeoecol., 78, 241-286, 1990.

Berger, A.: Long-term variations of caloric insolation resulting from earth's orbital elements. Quat. Res., 9, 2, 139-167, 1978.

Betts, A.K., and Ridgway, W.: Tropical boundary layer equilibrium in the last ice age. J. Geophys. Res., 97, 2529-2534, 1992.

Biscaye, P.E., Grousset, F.E., Revel, M., Van der Gaast, S., Zielinksi, G.A., Vaars, A., and Kukla, G.: Asian provenance of glacial dust (stage 2) in the Greenland Ice Sheet Project 2 Ice Core, Summit, Greenland. J. Geophys. Res., 102, 26,765-26,781, 1997.

Bishop, J.K.B., Davis, R.E., and Sherman, J.T.: Robotic observations of dust storm enhancement of carbon biomass in the North Pacific. Science 298 (5594), 817–821, 2002.

Blender, R., and Schubert, M.: Cyclone tracking in different spatial and temporal resolutions. Mon. Weath. Rev., 128, 377-383, 2000.

Bonan, G.B: The land surface climatology of the NCAR Land Surface Model (LSM 1.0) coupled to the NCAR Community Climate Model (CCM3). J. Climate, 11, 1307–1326, 1998.

Boville B. A., and Gent, P.R.: The NCAR Climate System Model, version 1. J. Clim., 11, 1115–1130, 1998.

Broecker, W.S., Peteet, D.M., and Rind, D.: Does the ocean-atmosphere system have more than one stable mode of operation? Nature, 315, 21-26, 1985.

Broecker, W.S.: Mountain glaciers: recorders of atmospheric water vapor content? Global Biogeochem. Cycles, 11, 589-597, 1997.

Bromwich, D.H., Toracinta, E.R., Wei, H., Oglesby, R.J., Fastook, J.L., and Hughes, T.J.: Polar MM5 simulations of the winter climate of the Laurentide Ice Sheet at the LGM, J. Climate, 17, 3415-3433, 2004.

Bromwhich, D.H., Fogt, R.L., Hodges, K.I., and Walsh, J.E.: A tropospheric assessment of the ERA-40, NCEP, and JRA-25 global reanalyses in the polar regions. J. Geophys. Res., 112, D10111, doi:10.1029/2006JD007859, 2007.

Charles, C.D., Rind, D., Jouzel, J., Koster, R.D., and Fairbanks, R.G.: Glacial-interglacial changes in moisture sources for Greenland: Influences on the ice core record of climate. Science, 263, 508-511, 1994.

Clark, P.U and Mix, A..: Ice sheets and sea level of the last glacial maximum. Quat. Sci. Rev., 21, 1, 1-7, 2002.

Clark, J.S., Beckage, B., Hille Ris Lambers, J., Ibanez, I., Ladeau, S., McLachlan, J., Mohan, J., and Rocca, M.: Plant dispersal and migration. In: Mooney, H.A.,

Canadell, J.G. (Eds.), Encyclopedia of Global Environmental Change. Wiley, Chichester, pp. 81–93, 2002.

CLIMAP: The surface of the ice age Earth. Science, 191: 1131-1136, 1976.

CLIMAP: Seasonal reconstructions of the Earth's surface at the Last Glacial Maximum. Geol. Soc. Amer. Map Chart Ser., MC36, 1981.

COHMAP Members: Climatic changes of the last 18,000 years: observations and model simulations. Science, 241, 1043-1052, 1998.

Collins, W. D., Cecilia, M.B., et. al.: The Community Climate System Model version 3 (CCSM3). J. Clim., 19, 2122–2143, 2006a.

Cox, S.K., Griffith, K.T.: Estimates, of radiative divergence during Phase III of the GARP Atlantic Tropical Experiment: Part 1. methodology. J. Atmo. Sci., 36, 576-585, 1979.

Cox, S.K., Griffith, K.T.: Estimates of radiative divergence during Phase III of the GARP Atlantic Tropical Experiment: Part II. analysis of phase III results. J. Atmo. Sci., 36, 586-601, 1979.

Crowley, T.J.: Temperature and circulation changes in the eastern North Atlantic during the last 150,000 years: Evidence from the planktonic foraminiferal record. Mar. Micro., 6, 97-129, 1981.

Crowley, T.J.: Ice age terrestrial carbon changes revisited. Glob. Biogeo. Cycle, 9, 3, 377-389, 1995;

Crowley, T.J.: CLIMAP SSTs revisited, Clim. Dyn., 16, 241-255, 2000.

Crowley, T.J., Baum, S.K.: Effect of vegetation on an ice-age climate model simulation. J. Geophys. Res., 102, 16463, 1997.

Crowley, T.J., and North, G.R.: Paleoclimatology. Oxford University Press, 1991.

Crowley, T.J., and Hakkinen, S.: A new mechanism for decreasing North Atlantic Deep Water production rates in the Pleistocene. Paleoceanog., 3, 249-258, 1988.

Crowley, T.J., and Matthews, R.K.: Isotope-plankton comparisons in a late Quaternary core with a stable temperature history. Geology, 11, 275-278, 1983.

Curray, J.R.: The Quaternary of the United States, Princeton Univ. Press, Princeton, N.J., 723-735, 1965.

Dahl-Jensen, D., Mosegaard, K., Clow, G.D., Johnsen, S.J., Hansen, A.W., and Balling, N.: Past temperatures directly from the Greenland Ice Sheet. Science, 282, 268-271, 1998.

Denton, G.H., and Hughes, T.J.: The Last Great Ice Sheets. John Wiley & Sons, 1981.

Donohue, A., and Battisti, D.S.: Causes of reduced North Atlantic storm activity in a CAM3 simulation of the Last Glacial Maximum. Journ. Clim., 22, 4793–4808, 2009.

Dong, B., and Valdes, P.J.: Simulations of the Last Glacial Maximum climates using a general circulation mode: prescribed versus computed sea surface temperatures. Clim. Dyn., 14, 571-591, 1998.

Duffy., P.B., Govindasamy, B., Iorio, J.P., Milovich, J., Sperber, K.R., Taylor, K.E., Wehner, M.F., and Thompson, S.L.: High-resolution simulations of global climate, part 1: present climate. Clim. Dyn., 21, 371-390, 2003.

Emiliani, C.: The amplitude of Pleistocene climatic cycles at low latitudes and isotopic composition of glacial ice. Turekian KK, The Late Cenozoic Glacial Ages, Yale University Press, 183-197, 1971.

Emiliani, C.: Isotopic paleotemperatures and shell morphology of Globigerinoides rubra in the type section for the Pliocene-Pleistocene boundary. Micropaleo., 17, 2, 233-238, 1971.

Fairbanks, R.G.: A 17 000-year glacio-eustatic sea level record: influence of glacial melting rates on Younger Dryas eventand deep-ocean circulation. Nature, 342, 637-642, 1989.

Fawcett, P., Agustsdottir, A.M., Alley, R.B., and Shuman, C.A.: The Younger Dryas termination and North Atlantic Deep Water formation: Insights from climate model simulations and Greenland ice cores. Paleooceanography, 12, 23-38, 1997.

Gates, W.L.: The numerical simulation of ice-age climate with a global general circulation model. J. Atmos. Sci., 33, 1844-1876, 1976.

Gates, W.L.: Modeling the ice-age climate. Science, 191, 1138-1144, 1976.

Geibert, W., Assmy, P., Bakker, D.C.E., Hanfland, C., Hoppema, M., Pichevin, L., Shroder, M., Schwarz, N., Stimac, I., Usbeck, R., and Webb, A.: High productivity in an ice melting hotspot at the eastern boundary of the Weddell Gyre.: Glob. Biogeo. Cycles, 24, GB3007., doi:10.1029/2009GB003657, 2010.

Gillette, D.A., Blifford, I.H, and Fryrear, D.W.: The influence of wind velocity on the size distributions of aerosols generated by the wind erosion of soils. J. Geophys. Res., 79, 27,4068-4075, 1974.

Guilderson, T.P., Fairbanks, R.G., and Rubenstone, J.L.: Tropical temperature variations since 20,000 years ago: modulating interhemispheric climate change. Science, 263, 663-665, 1994.

Hack, J.J.: Parameterization of moist convection in the National Center for Atmospheric Research Community Climate Model (CCM2). J. Geophys. Res., 99, 55551-5568, 1994.

Hack, J.J.: Sensitivity of the simulated climate to a diagnostic formulation for cloud liquid water. J. Climate, 1998a.

Hakkinen : A coupled dynamic-thermodynamic model of an ice-ocean system in the marginal ice zone. J. Geophys. Res., 92(C9), 9469–9478, doi:10.1029/JC092iC09p09469, 1987.

Hanebuth, T., Statteger, K., and Grootes, P.M.: Rapid flooding of the Sunda Shelf: a late glacial sea level record. Science, 288, 1033–1035, 2000.

Herbert, T.D, Schuffert, J.D., Thomas, D., Lange, C., Weinheimer, A., Paleo-Alampay, A., Herguera, J.-C.: Depth and seasonality of alkenone production along the California Margin inferred from a core top transect. Paleoocean., 13, 3, 263-271, 1998.

Herbert, T.D., et al. : Collapse of the California Current during glacial maxima linked to climate change on land. Science, 293, 5527, 71-76, 2001.

Hoskins, B.J., and Hodges, K.I.: New perspectives on the northern hemisphere winter storm tracks. J. Atmos. Sci., 59, 1041-1061, 2002.

Hostetler, S.W., and Clark, P.U.: Tropical climate at the Last Glacial Maximum inferred from glacier mass-balance modelling. Science, 290, 1747-1750, 2000.

Hurrell, J.W., Hack, J.J., Boville, B.A., Williamson, and D.L., Kiehl, J.T.: The dynamical simulation of the NCAR Community Climate Model version 3 (CCM3), J. Clim., 11, 1207-1236, 1998.

Imbrie, J., and Kipp, N.G.: A new micropaleontological method for quantitative paleoclimatology: Application to a late Pleistocene Caribbean core. In: The Late Cenozoic Glacial Ages. K.K. Turekian (Ed.), Yale Univ. Press, New Haven, Conn., 71-179, 1971.

Imbrie, J., Hays, J. D., Martinson, D. G., McIntyre, A., Mix, A. C., Morley, J. J., Pisias, N. G., Prell, W. L., and Shackleton, N. J.: The orbital theory of Pleistocene climate : support from a revised chronology of the marine δ18 O record. Milankovitch and Climate: Understanding the Response to Astronomical Forcing, Proceedings of the NATO Advanced Research Workshop, D. Reidel Publishing, 269, 1984.

Imbrie, J., Mix, A.C., and Martinson, D.G.: Milankovitch theory viewed from Devils Hole. Nature, 363, 531-533, 1993.

Jackson, S.T., Webb, R.S., Anderson, K.H., Overpeck, J.T., Webb, T., Williams, J.W., and Hansen, B.C.S: Vegetation and environment in Eastern North America during the Last Glacial Maximum. Quat. Sci. Rev., 19, 489-508, 2000.

Johnsen, S.J., et al.: Oxygen isotope and palaeotemperature records from six Greenland ice-core stations: Camp Century, Dye-3, GRIP, GISP2, Renland and NorthGRIP. J. Quat. Sci., 16, 299-307, 2001.

Joussaume, S. and Taylor, K. E.: Status of the Paleoclimate Modeling Intercomparison Project (PMIP), in: Proceedings of the first international AMIP scientific conference, WCRP Report, 425–430, 1552, 1995.

Kageyama, M., Valdes, P.J., Ramstein, G., Hewitt, C., and Wyputta, U.: Northern hemisphere storm tracks in present day and Last Glacial Maximum climate simulations: A comparison of the European PMIP models. J. Clim., 12, 742-760, 1999.

Kageyama, M., and Valdes, P.J.: Impact of North American ice-sheet orography on Last Glacial Maximum eddies and snowfall. Geophys. Res. Let., 27, 1515-1518, 2000.

Kim, S., Crowley, T.J., Erickson, D.J., Govindasamy, B., Duffy, P.B., and Lee, B.Y.: High-resolution climate simulation of the last glacial maximum. Clim. Dyn., 31, 1-16, 2008.

Kiehl, J. T.: Sensitivity of a GCM climate simulation to differences in continental versus maritime cloud drop size. J. Geophys.Res., 99, 23 107–23 115, 1994.

Kutzbach, J.E., and Guetter, P.E.: The influence of changing orbital parameters and surface boundary conditions on climate simulations for the past 18,000 years. J. Atmos. Sci., 16, 1726-1759, 1986.

Kutzbach, J.E., and Wright, Jr., H.E.: Simulation of the climate of 18,000 yr BP: Results for the North American/North Atlantic/European sector. Quat. Sci. Rev., 4, 147-187, 1985.

Kutzbach, J.E., Guetter, P.J., Behling, P.J., and Selin, R.: Simulated climatic changes: results of the COHMAP climate-model experiments. In: Wright Jr., H.E., Kutzbach, J.E., Webb, T.III, Ruddiman, W.F., Street-Perrott, F.A., Bartlein, P.J. (Eds.), Global Climates Since the Last Glacial Maximum. University of Minnesota Press, Minneapolis, pp. 24-93, 1993.

Kutzbach, J.E., Gallimore, R., Harrison, S., Behling, P., Selin, R., and Laarif, F.:Climate and biome simulations for the past 21,000 years. Quat. Sci. Rev. 17, 473-506, 1998.

Langen, P.L., and Vinther, B.M.: Response in atmospheric circulation and sources of Greenland precipitation to glacial boundary conditions. Clim. Dyn., 32, 1035-1054, 2009.

Lee, K.E., and Slowey, N.C.: Cool surface waters of the subtropical North Pacific Ocean during the last glacial. Nature, 397, 512-514, 1999.

Li, C. and Battisti, D.S.: Reduced Atlantic storminess during Last Glacial Maximum: Evidence from a coupled climate model. J. Climate, 21, 3561-3579, 2008.

Ludwig, K.R., et al.: Mass-Spectrometric ^{230}Th-^{234}U-^{238}U dating of the Devils Hole calcite vein. Science, 258, 5080, 284-287, 1992.

Maher, B.A., Prospero, J.M., Mackie, D., Gaiero, D., Hesse, P.P., and Balkanski, Y.: Global connections between aeolian dust, climate and ocean biogeochemistry at the present day and at the last glacial maximum. Earth Sci. Rev., 99, 61-97, 2010.

Mahowald, N., Kohfeld, k., Hansson, m., Balkanski, Y., Harrison, S., Prentice, C., Schulz, and Rodhe., H.: Dust sources and deposition during the last glacial maximum and current climate: A comparison of model results with paleodata from ice cores and marine sediments, J. Geophys. Res., 104, 15,895–15,916, 1999.

Mahowald, N.M., Muhs, D.R., Levis, S., Rasch, P.J., Yoshioka, M., Zender, C.S., and Luo, C.: Change in atmospheric mineral aerosols in response to climate: Last glacial period, preindustrial, modern, and doubled carbon dioxide climates. J. Geophys. Res., 111, D10202, doi:10.1029/2005JD006653, 2006.

Manabe, S., and Broccoli A.J.: The influence of continental ice sheets on the climate of an ice age. J. Geophys. Res. Letters, 90, 2167-2190, 1985.

MARGO Project Members: Constraints on the magnitude and patterns of ocean cooling at the Last Glacial Maximum, Nature Geo., 2, 127-132, 2009.

McGee, D., Broecker, W.S., and Winckler, G.: Gustiness: The driver of glacial dustiness? Quat. Sci. Rev., 17-18, 2340-2350, 2010.

McIntyre, A., Kipp, N. G., Be, A.W.H., Crowley, T., Kellogg, T., Gardner, J. V., Prell, W. and Ruddiman, W.F.: Glacial north Atlantic 18,000 years ago: A CLIMAP reconstruction. Geol. Soc. Am., Memoir 145, 43-76, 1976.

McLachlan, J.S. and Clark, J.S.: Reconstructing historical ranges with fossil data at continental scales. Forest Eco. and Management, 197, 139-147, 2004.

Mikolajewicz, U, Crowley, T.J., Schiller, A., and Voss, R.: Modelling teleconnections between the North Atlantic and North Pacific during the Younger Dryas. Nature 387, 384 - 387, doi:10.1038/387384a0, 1997.

Moore, G.W.K. and Renfrew, I.A.: Tip jets and barrier winds: A QuickSCAT climatology of high wind speed events around Greenland. J. Climate, 18, 3713-3725, 2005.

Moore, R.W., Martius, O., and Davies, H.C.: Downstream development and Kona Low genesis. Geophys. Res. Letters, 35, L20814, doi:10.1029/2008GL035502, 2008.

Peltier, W.R.: Ice Age paleotopography. Science, 265, 195-201, 1994.

Peltier, W.R.: Global glacial isostatic adjustment: palaeogeodetic and space-geodetic tests of the ICE-4G (VM2) model. J. Quat. Sci., 17(5-6), 491-510, 2002.

Peltier, W.R.: Global glacial isostasy and the surface of the ice-age earth: the ICE-5G (VM2) model and GRACE. Annu. Rev. Earth Planet. Sci., 32, 111-149, 2004.

Petit, J.R., Jouzel, J. et al.: Climate and atmospheric history of the past 420,000 years from the Vostok ice core, Antarctica. Nature, 399, 429-436, 1999.

Rea, D. K.: The Paleoclimatic record provided by eolian deposition in the deep sea. The geologic history of wind, Rev. Geophys., 32, 159–195, 1994.

Rind, D., and Peteet, D.: Terrestrial conditions at the last glacial maximum and CLIMAP sea-surface temperature estimates: are they consistent? Quat. Res. 24, 1-22, 1985.

SethuRaman, S., Riordan, A.J., Holt, T., Stunder, M., and Hinman, J: Observations of the marine boundary layer thermal structure over the Gulf Stream during a cold air outbreak. J. Clim. Appl. Meteor. 25:14-21, 1986.

Shea, D.J., Trenberth, K.E. and Reynolds, R.W.: A global monthly sea surface temperature climatology. NCAR Tech. Note NCAR/TN-345+STR, 167 pp, 1990.

Shin, K.-S., G. R. North, Y.-S. Ahn, and P. A. Arkin: Time scales and variability of area-averaged tropical oceanic rainfall, Mon. Wea. Rev., 118, 1507-1516, 1990.

Stute, M., Schlosser, P., Clark, J.F., and Broecker, W.S.:Paleotemperatures in the southwestern United States derived from noble gas measurements in groundwater. Science, 256, 1000-1003, 1992.

Stute, M., Forster, M., Frischkom, H., Serejo, A., Clark, J.F., Schlosser, P., Broecker, W.S., and Bonani, G.: Cooling of tropical Brazil (5C) during the last glacial maximum. Science, 269, 379-383, 1995.

Stute, M., Khoi, L.-V., Schlosser, P., Tobin, M., and Higgins, S.: Glacial paleotemperature records for the tropics derived from noble gases dissolved in groundwater. Eos Trans. Am. Geophy. Union, 78, F44, 1997.

Sugden, D.E., McCulloch, R.D., Bory, A.J.-M., and Hein, A.S.: Influence of Patagonia glaciers on Antarctic dust deposition during the last glacial period. Nature Geo., 282-285, doi: 10.1038/NGEO474, 2009.

Sugimoto, S., and K. Hanawa: Impact of Aleutian Low activity on the STMW formation in the Kuroshio recirculation gyre region. Geophys. Res. Lett., 37, L03606, doi:10.1029/2009GL041795, 2010.

Toracinta, E.R., Oglesby, R.J., and Bromwich, D.H.: Atmospheric response to modified CLIMAP ocean boundary conditions during the Last Glacial Maximum. J. Clim., 17, 504–522, 2004.

Unterman, M.B.: High resolution simulations of synoptic scale meteorology for the Last Glacial Maximum, Duke University Archives, M.S. U61H 2007, 2007.

Webb, T.III., Bartlein, P.J., Harrison, S., and Anderson, K.H.,: Vegetation, lake levels, and climate in eastern North America for the past 18,000 years. In: Wright Jr., H.E., Kutzbach, J.E., Webb, T.III., Ruddiman, W.F., Street-Perrott, F.A., Bartlein, P.J. (Eds.), Global Climates Since the Last Glacial Maximum. University of Minnesota Press, Minneapolis, pp. 415-467, 1993.

Webb III, T., Anderson, K.H., Bartlein, P.J., and Webb, R.S.: Late Quaternary climate change in eastern North America: a comparison of pollen-derived estimates with climate model results. Quaternary Science Reviews 17, 587-606, 1998.

Webster, P. J., and R. Lukas: TOGA COARE: The coupled Ocean-Atmosphere Response Experiment. Bull. Amer. Meteor. Soc, 73, 1377-1416, 1992

Wells, G.L.: Late-glacial circulation over central North America revelead by Aeolian features. In: Variations in the global water budget. A. Street-Perrot et al. (Eds.). D. Reidel, Dordrecht, Netherlands, pp. 317-330, 1983.

Wells, P.V., and Stewart, J.D.: Cordilleran-boreal taiga and fauna on the central Great Plains of North America, 14,000-18,000 years ago. American Midland Naturalist 118, 94-106, 1987.

Werner, M., Mikolajewicz, U., Heimann, M., and Hoffmann, G.: Borehole versus isotope temperatures on Greenland: Seasonality does matter. Geophy. Res. Let., 27, 5, 723-726, 2000.

Williams, J., Barry, R.G., and Washington, W.M.: Simulation of the atmospheric circulation using the NCAR Global Circulation Model with ice age boundary conditions. J. App. Met., 13, 305-317, 1974.

Williamson, D.L.: Description of NCAR Community Climate Model (CCM0B). NCAR Tech. Note NCAR/TN-210+STR, 88, 1983.

Williamson, D.L.: CCM2 datasets and circulation statistics. NCAR Tech. Note NCAR/TN-391+STR, 85, 1993.

Williamson, D.L, and Olson, J.G.: Climate simulations with a semi-Lagrangian version of the NCAR Community Climate Model. Mon. Wea. Rev., 122, 1594-1610, 1994.

Winograd, I.J., et al: Continuous 500,000-Year climate record from vein calcite in Devils Hole, Nevada. Science, 258, 255-260, 1992.

Winograd, I.J.: The California Current, Devils Hole, and Pleistocene Climate. Science, 296, 7, 2002.

Wu, P., Peltier, W.R.: Pleistocene deglaciation and the Earth's rotation: a new analysis. Geophys. J. R. Astron. Soc., 76, 202–242, 1984.

Yokoyama, Y., Lambeck, K., de Dekhar, P., Johnston, P., and Fifield, L.K.: Timing of the last glacial maximum from observed sea level minima. Nature, 406, 713–716, 2000, Correction: Nature, 412-499, 2001.

Young, N.E., et al., Assessing climatic and nonclimatic forcing of Pinedale glaciation and deglaciation in the western United States. Geology, 39, 171-174, 2011.

Appendix A:

Additional Figures:

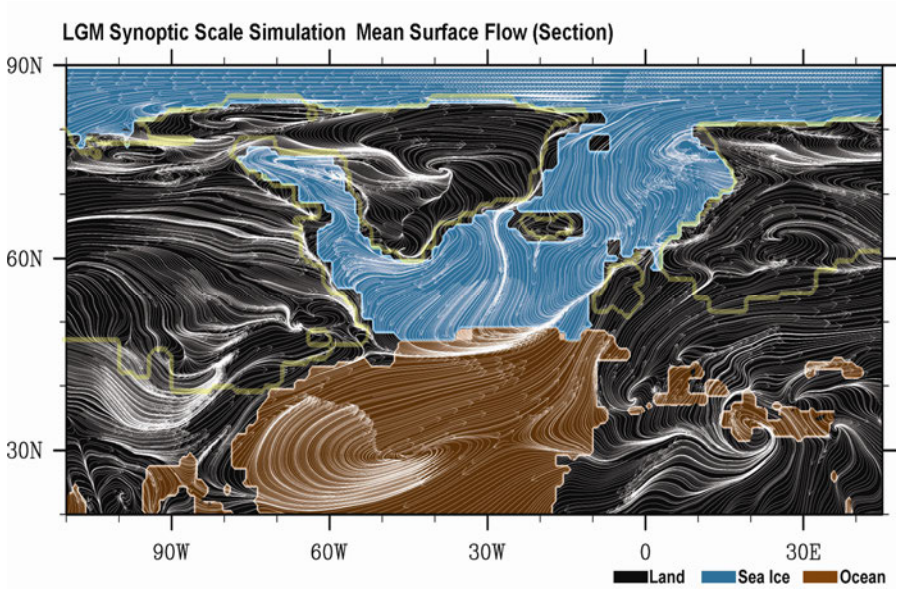

Figure S1: LGM synoptic scale simulation wintertime mean surface flow over a sectioned area in the North Atlantic showing the land mask – modified from Fig. in Chapter 4. Yellow outlines represent the margin of the LGM ice sheets in the region using the ICE4G reconstruction (cf. Peltier, 1994).

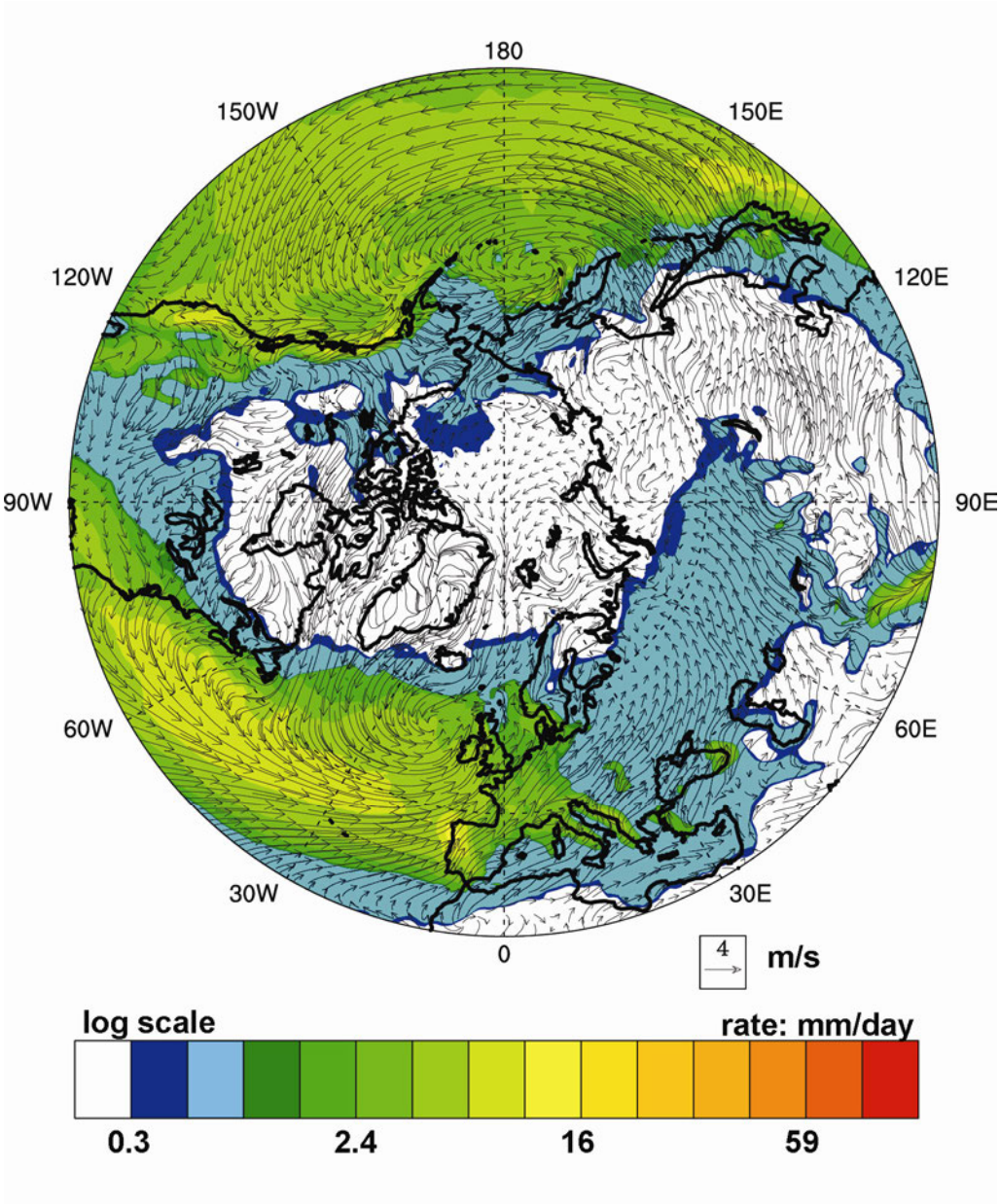

Figure S2a: Climatological four-year mean DJF surface flow and total precipitation in the Northern Hemisphere. Single panel re-plotted from Chapter 4. Note the increased precipitation along the west coast of North American and into the Great Basin region. Precipitation is also focused along the United Kingdom and northern Europe. Individual panel of the hourly-scale run can be found in Chapter 4.

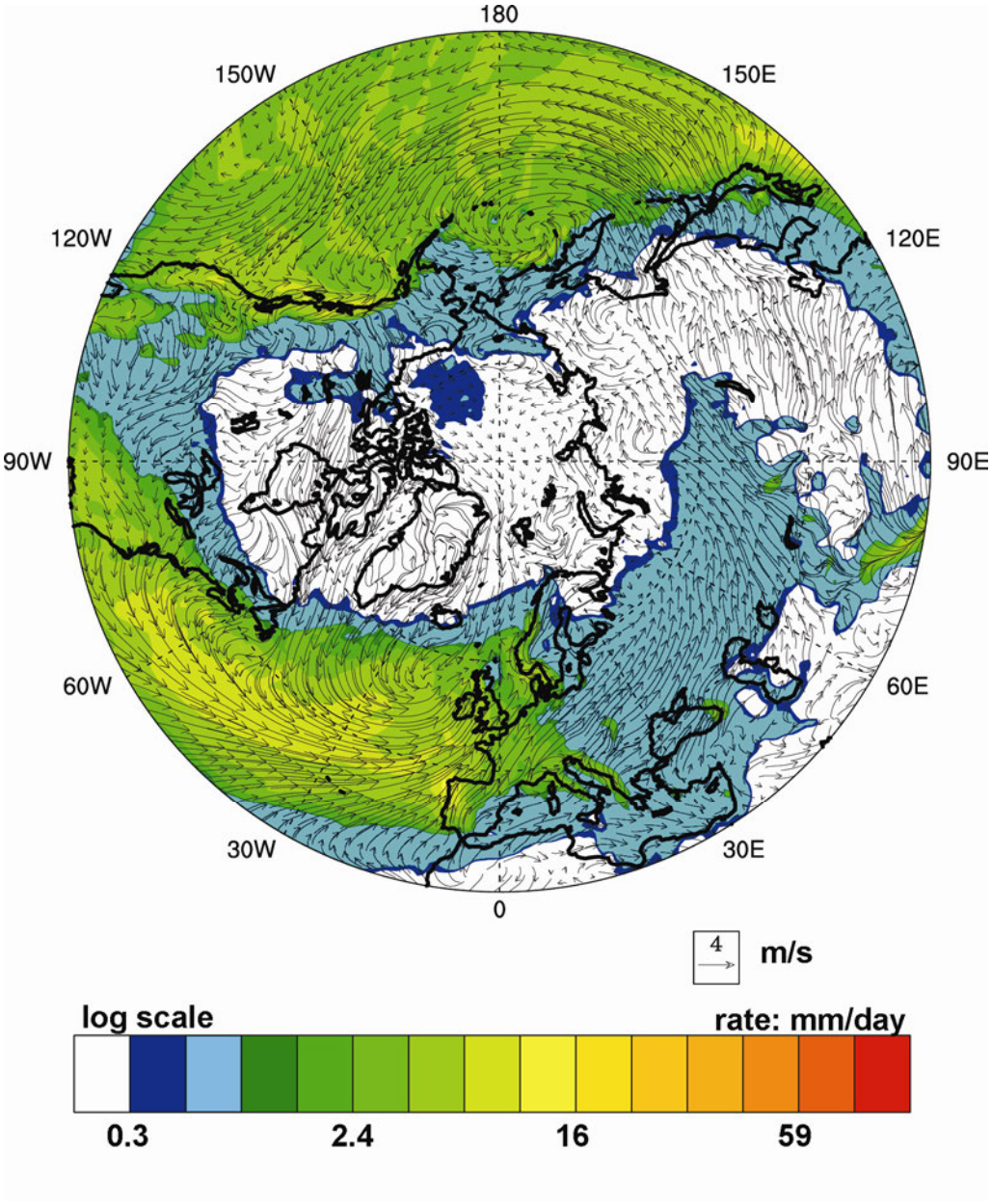

Figure S2b: Year 3 DJF climatological simulation mean surface flow and total precipitation in the Northern Hemisphere. Single panel re-plotted from Chapter 4.

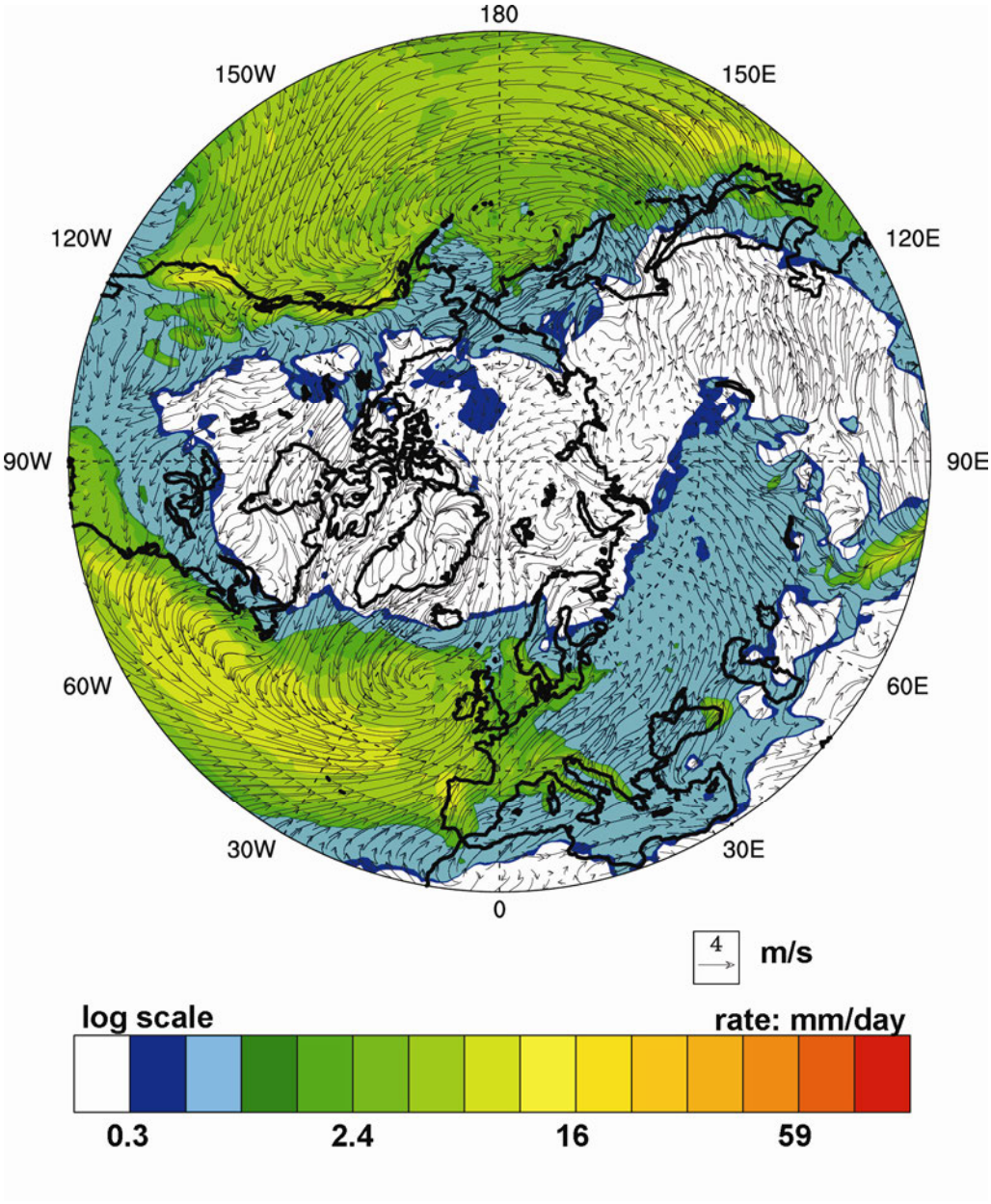

Figure S2c: Year 4 DJF climatological simulation mean surface flow and total precipitation in the Northern Hemisphere. Single panel re-plotted from Chapter 4.

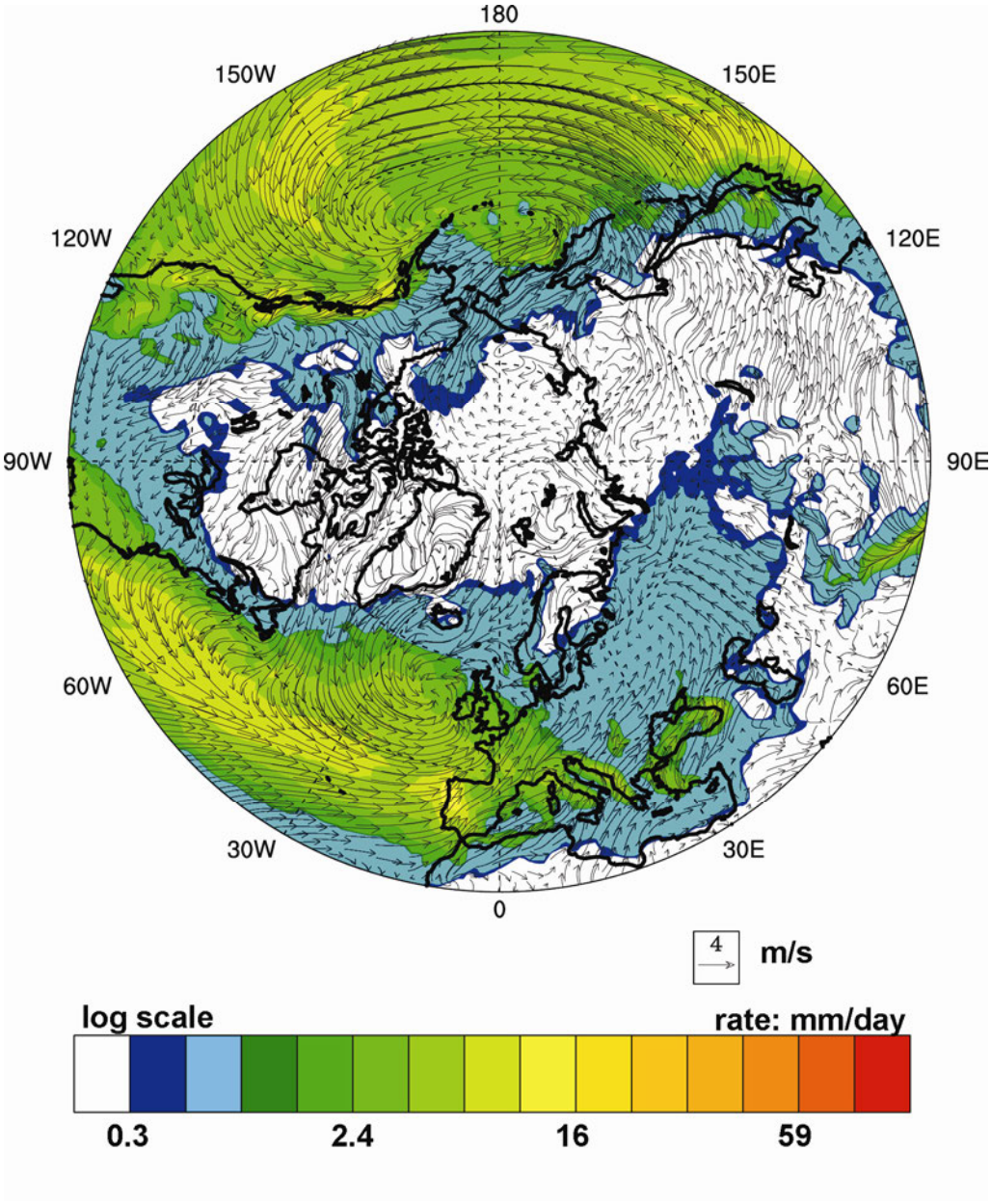

Figure S2d: Year 5 DJF climatological simulation mean surface flow and total precipitation in the Northern Hemisphere. Single panel re-plotted from Chapter 4.

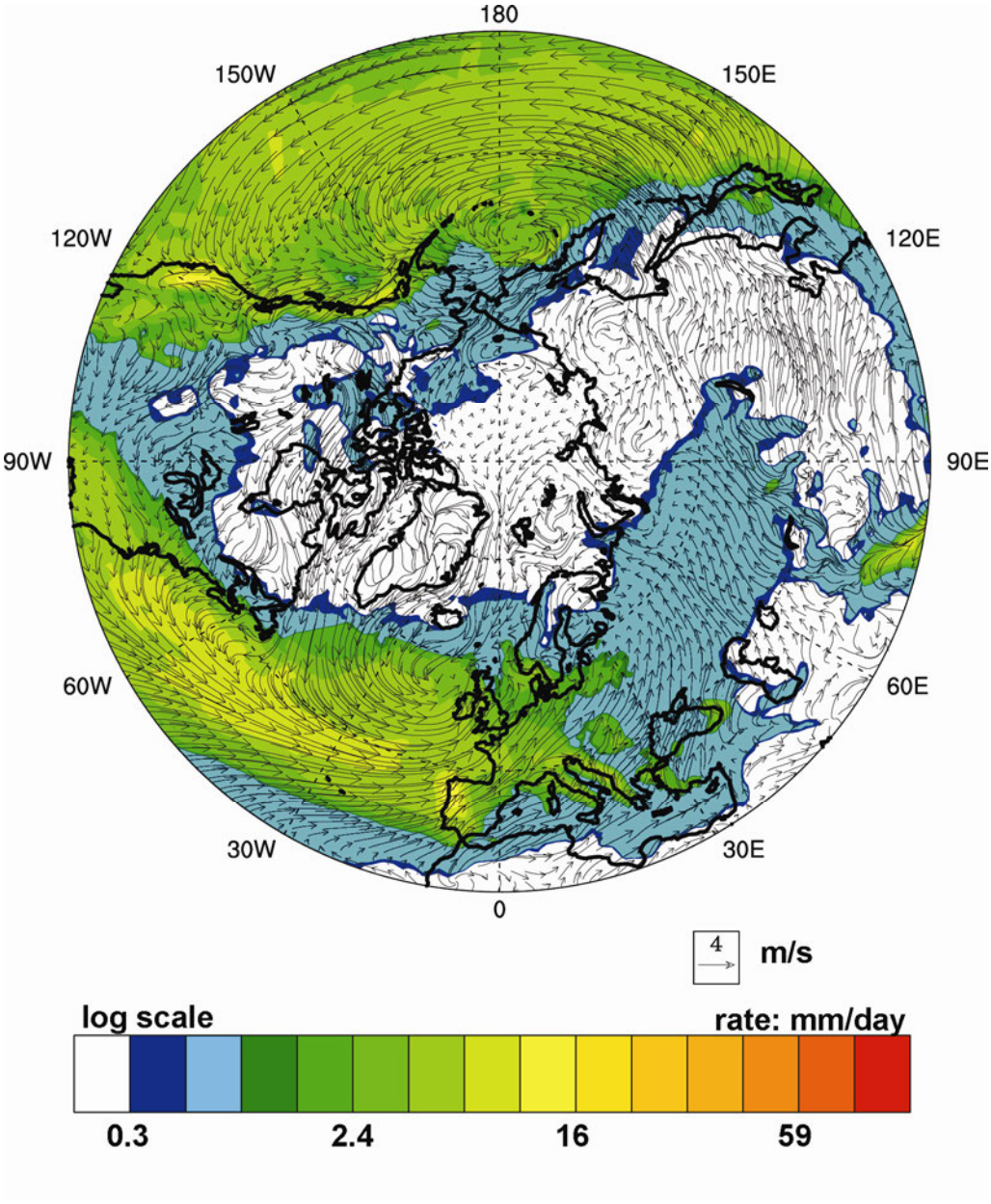

Figure S2e: Year 6 DJF climatological simulation mean surface flow and total precipitation in the Northern Hemisphere. Single panel re-plotted from Chapter 4.

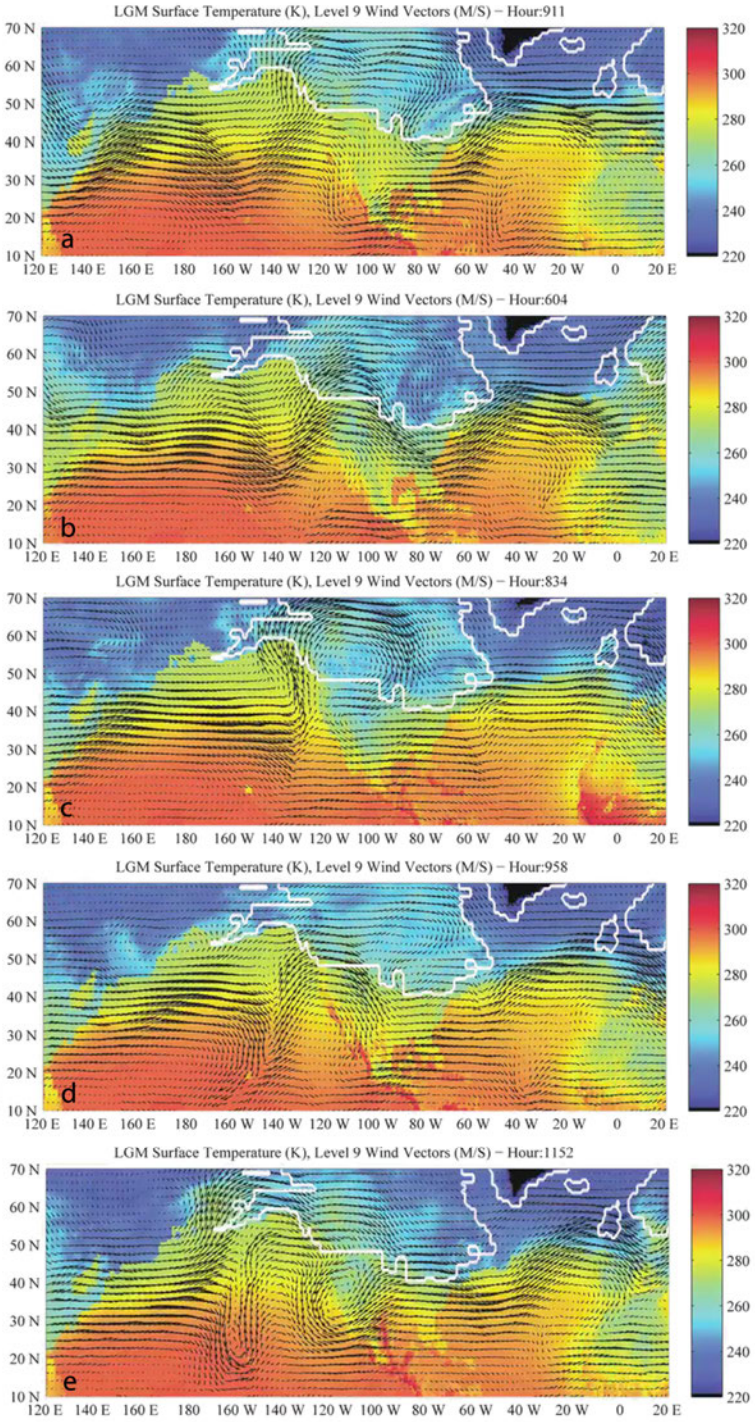

Figure S3a: Different model moments of the mid-latitude jet wave pattern, similar to that presented in Chapter 4, but with surface temperature in the background. Panel (a) represents a similar pattern to the mean state with a modified split jet. Panels (b) and (c) are variations of the jet with the later forced into a large ridge-trough pattern. Panels (d) and (e) are instances where the jet dips southward, with (e) becoming the start of a Kona Low with an imbricated mid-latitude jet around 160°W.

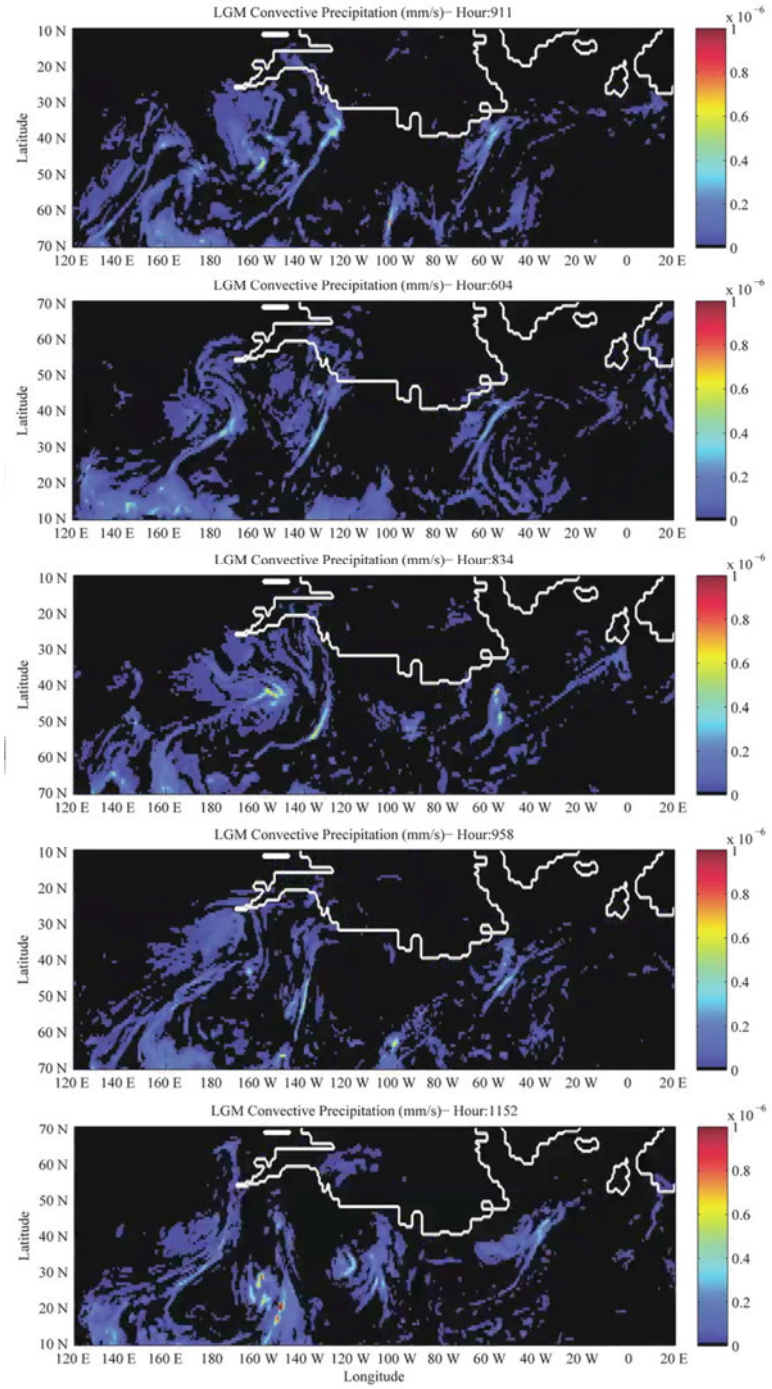

Figure S3b: The surface convective precipitation at the same hours as the mid-level jet slides in Figure S3a.

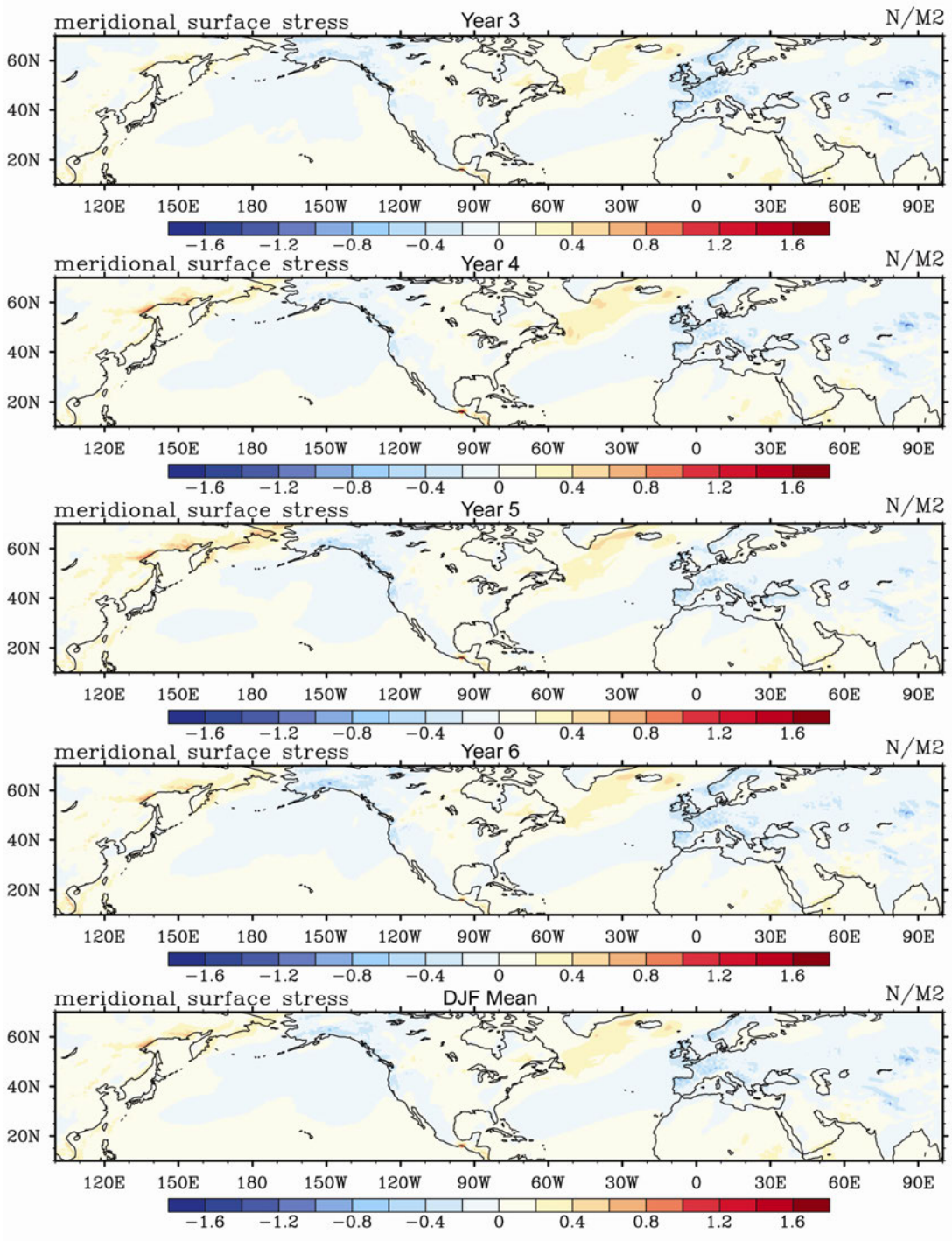

Figure S4: LGM DFJ meridional surface stress similar to the zonal stress figure shown in Chapter 4. All four winters of the climatological simulation are shown, along with the four-year wintertime mean. Note the differences in signs along a north-south transect in the North Atlantic. Winds in this region converge along the sea ice margin as seen in the synoptic integration – the area around the North Atlantic storm track.

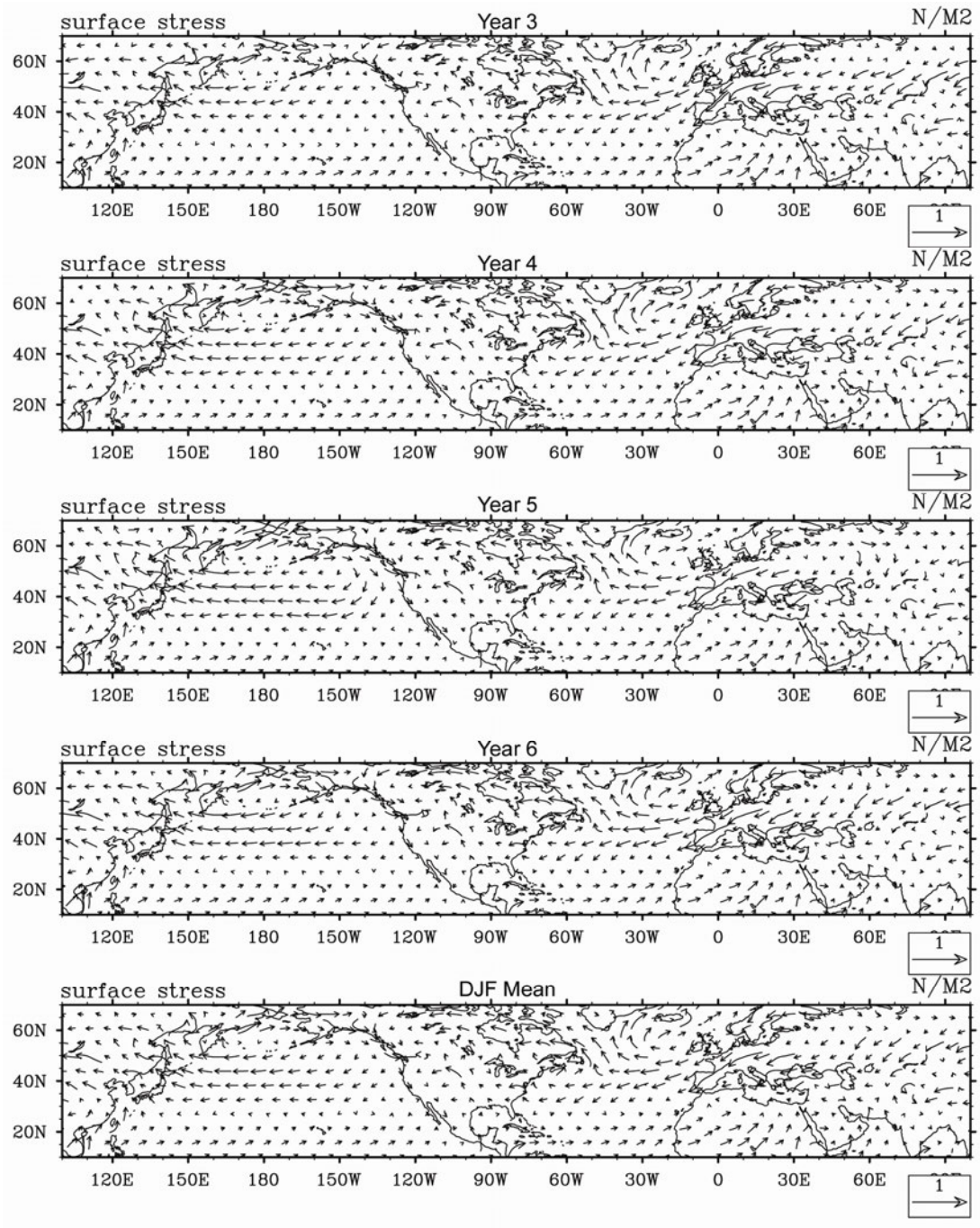

Figure S5: LGM DJF surface stress in all four years (and mean) of the climatological simulation. High values are seen in eastern Asia, the eastern North Pacific, along the northern edge of Canada and the Laurentide Ice Sheet, the North Atlantic around Greenland north of the extended sea ice margin and along it's edge and over the Fennoscandian Ice Sheet sector in Northern Europe and the United Kingdom.

Appendix B:

Additional Gust Analysis Data:

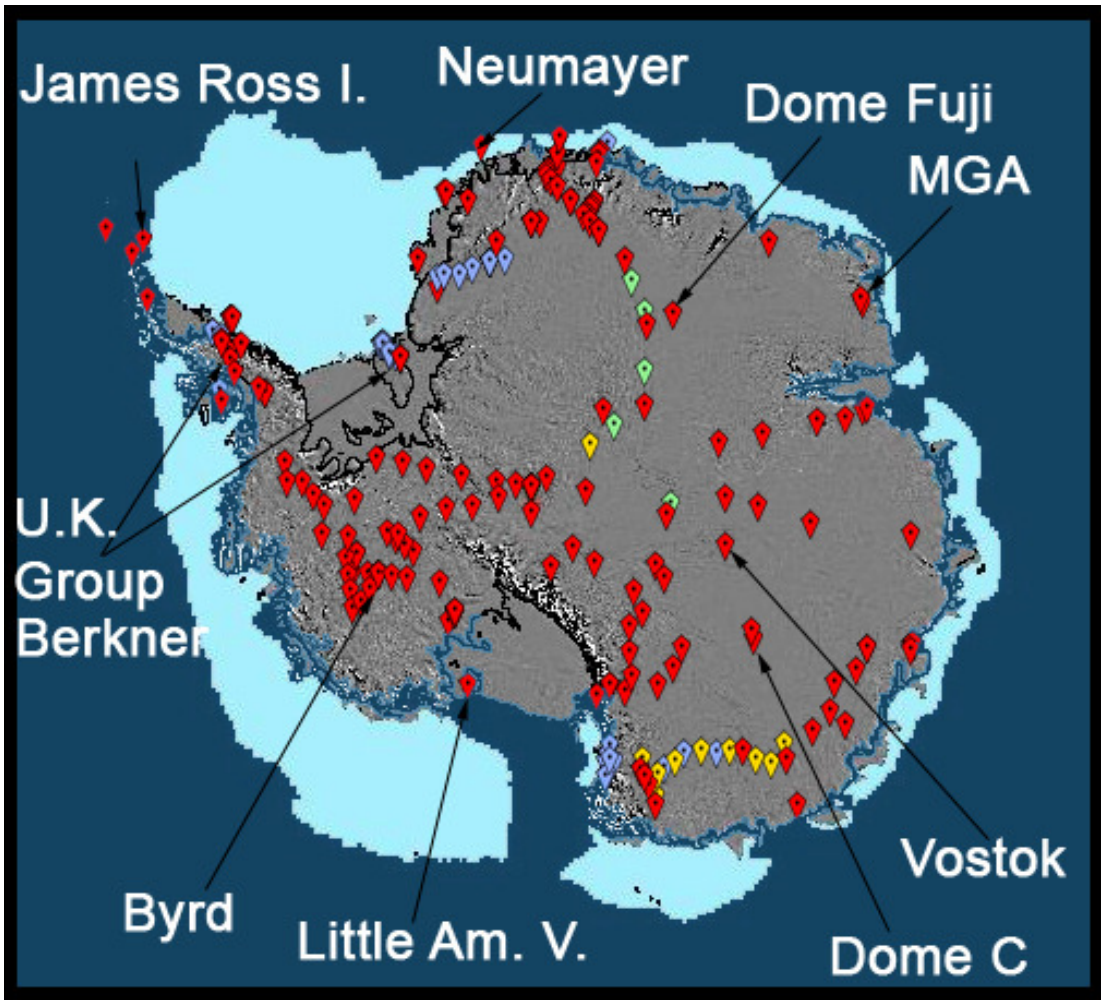

Figure S6: Location of Antarctic ice cores - plotted from data obtained from the National Snow and Ice Data Center.

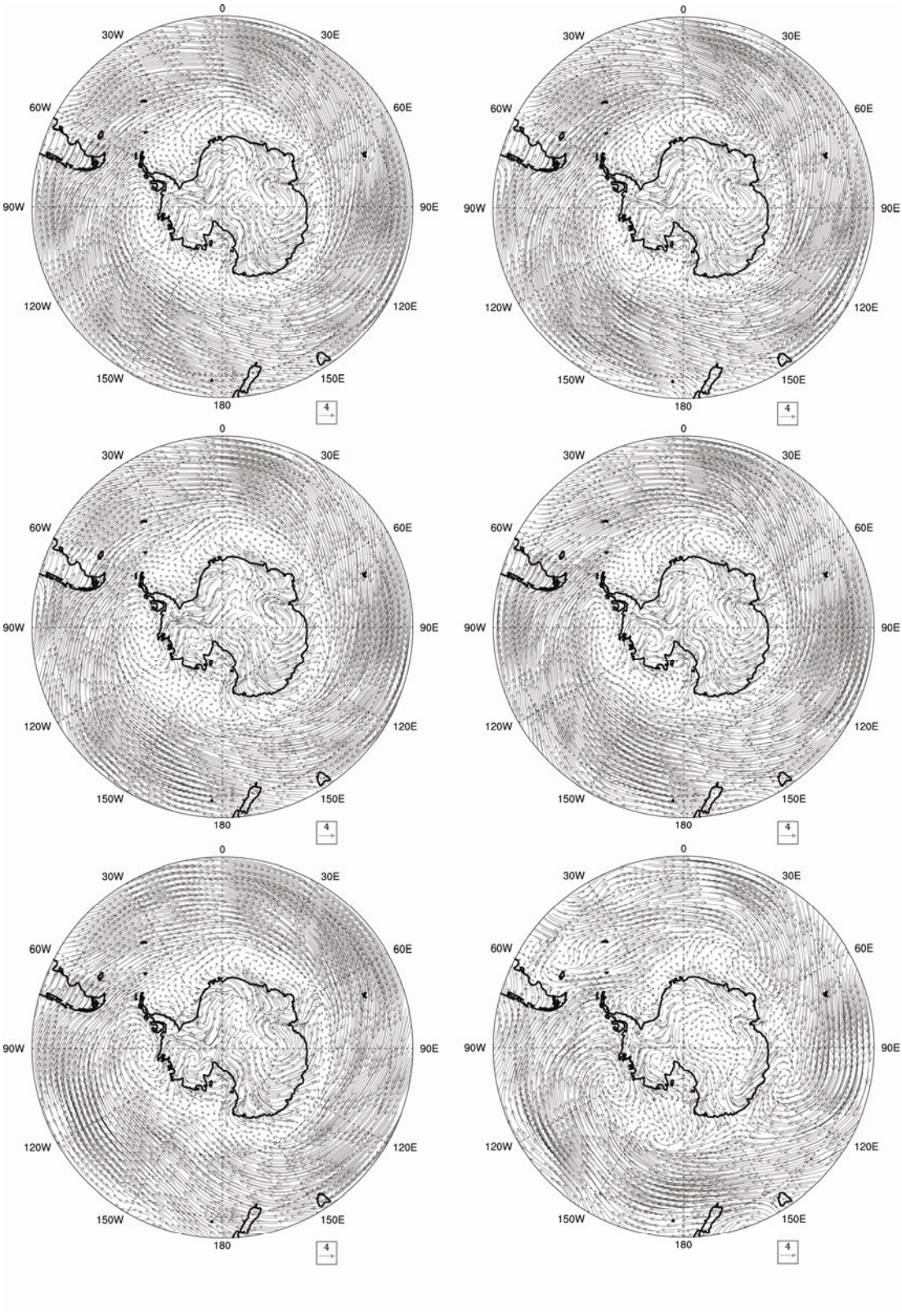

Figure S6: LGM DJF Surface flow in the Southern Hemisphere, S.O. sector, for the climatological DJF mean (top-left), Year 3 (top-right), Year 4 (middle-left), Year 5 (middle-right), Year 6 (bottom-left) and synoptic integration (bottom-right).

Lat	Lon	MOD AVG	MOD MAX	MOD MIN	LGM AVG	LGM MAX	LGM MIN	L-M MAX	L-M MIN	L-M AVG	MOD 16%	MOD 8%	MOD 5%	LGM 16%	LGM 8%	LGM 5%
37N	97E	4.71	14.98	0.06	4.50	13.04	0.15	-1.94	0.10	-0.21	0.00%	11.12%	39.71%	0.00%	11.29%	36.46%
38N	97E	6.96	21.60	0.13	6.45	16.03	0.22	-5.57	0.09	-0.51	2.45%	37.15%	59.51%	0.10%	30.47%	60.64%
39N	97E	7.90	22.50	0.36	8.76	18.97	0.23	-3.53	-0.14	0.85	3.56%	42.49%	68.63%	3.30%	58.84%	79.02%
40N	97E	5.97	22.86	0.24	8.17	22.98	0.34	0.12	0.10	2.20	1.67%	23.25%	56.28%	4.00%	51.25%	78.82%
41N	97E	5.63	19.78	0.07	7.20	22.03	0.19	2.25	0.12	1.57	1.11%	20.91%	52.06%	2.00%	37.06%	68.53%
42N	97E	5.53	18.85	0.14	7.35	17.66	0.14	-1.19	0.00	1.82	1.11%	17.46%	46.72%	2.00%	37.26%	71.23%
43N	97E	5.23	18.03	0.21	6.67	17.05	0.07	-0.98	-0.15	1.44	0.78%	15.80%	47.94%	0.10%	36.46%	64.54%
44N	97E	5.42	17.25	0.19	6.60	18.41	0.47	1.17	0.28	1.19	0.56%	18.91%	48.05%	0.50%	33.87%	64.24%
45N	97E	5.55	16.57	0.28	7.15	16.97	0.47	0.40	0.19	1.60	0.11%	13.90%	53.50%	1.00%	36.06%	75.02%
37N	98E	5.14	16.69	0.25	4.92	13.24	0.20	-3.45	-0.05	-0.22	0.44%	16.13%	45.49%	0.00%	17.68%	41.56%
38N	98E	7.45	21.98	0.10	7.16	16.93	0.19	-5.06	0.10	-0.29	4.12%	38.82%	63.96%	0.80%	40.56%	65.83%
39N	98E	7.33	23.67	0.25	9.45	20.09	0.25	-3.59	0.01	2.12	2.56%	38.93%	64.29%	6.29%	63.04%	82.02%
40N	98E	5.48	24.32	0.20	8.47	24.03	0.33	-0.29	0.12	2.98	1.89%	17.35%	47.05%	5.79%	51.45%	75.82%
41N	98E	5.30	21.56	0.04	7.80	23.05	0.13	1.49	0.09	2.50	1.45%	14.35%	46.27%	4.10%	42.06%	73.43%
42N	98E	5.06	19.05	0.24	7.65	19.71	0.22	0.66	-0.02	2.60	1.11%	15.13%	40.93%	1.80%	42.16%	74.23%
43N	98E	5.56	18.83	0.00	6.81	17.52	0.32	-1.31	0.32	1.25	0.89%	16.35%	52.50%	0.30%	36.86%	65.53%
44N	98E	5.96	17.74	0.17	6.72	18.76	0.30	1.02	0.14	0.76	0.56%	22.36%	57.62%	0.60%	34.07%	66.73%
45N	98E	5.92	17.21	0.19	7.63	18.07	0.30	0.86	0.11	1.71	0.33%	16.91%	59.29%	2.20%	43.86%	78.22%
37N	99E	6.97	19.10	0.08	6.84	18.01	0.21	-1.09	0.13	-0.13	1.67%	35.26%	60.18%	0.90%	33.27%	63.74%
38N	99E	6.14	18.99	0.08	7.10	15.90	0.22	-3.09	0.15	0.95	1.33%	26.70%	57.95%	0.00%	41.86%	69.63%
39N	99E	5.37	21.19	0.29	7.53	16.15	0.16	-5.04	-0.13	2.17	0.78%	11.46%	49.28%	0.10%	44.16%	76.62%
40N	99E	4.44	23.19	0.13	7.51	21.93	0.27	-1.26	0.14	3.07	1.33%	7.34%	30.92%	4.60%	37.46%	69.93%
41N	99E	4.57	21.97	0.21	7.59	22.80	0.17	0.83	-0.04	3.02	1.33%	10.90%	34.26%	4.80%	40.66%	70.83%
42N	99E	4.62	18.60	0.19	7.22	20.58	0.13	1.98	-0.06	2.61	1.22%	11.12%	35.60%	3.40%	36.56%	69.83%
43N	99E	5.50	19.16	0.10	6.52	19.20	0.10	0.04	0.00	1.02	0.89%	18.13%	51.72%	0.60%	29.77%	65.23%
44N	99E	5.84	17.19	0.34	6.47	18.71	0.26	1.53	-0.07	0.63	0.56%	21.36%	57.62%	0.60%	30.17%	66.03%
45N	99E	5.48	15.90	0.19	7.82	19.21	0.69	3.31	0.49	2.34	0.00%	15.80%	55.51%	2.10%	45.75%	76.02%

Table S.1: LGM and modern Central Loess Plateau surface wind flow, max gust events and percentages of events over threshold velocities.

Lat	Lon	MOD AVG	MOD MAX	MOD MIN	LGM AVG	LGM MAX	LGM MIN	L-M MAX	L-M MIN	L-M AVG	MOD 16%	MOD 8%	MOD 5%	LGM 16%	LGM 8%	LGM 5%
37N	100E	6.76	19.24	0.18	7.52	18.47	0.12	-0.77	-0.07	0.76	1.67%	33.82%	59.73%	2.10%	41.26%	69.73%
38N	100E	5.76	18.85	0.28	7.06	15.14	0.42	-3.71	0.14	1.30	0.78%	16.80%	56.95%	0.00%	39.36%	72.83%
39N	100E	5.01	20.95	0.07	7.03	15.04	0.48	-5.90	0.40	2.02	0.67%	10.68%	42.16%	0.00%	37.16%	72.53%
40N	100E	4.26	22.03	0.13	6.82	19.87	0.11	-2.16	-0.02	2.57	1.22%	7.34%	28.70%	3.50%	31.17%	65.73%
41N	100E	4.59	20.86	0.21	7.07	21.43	0.21	0.57	0.00	2.47	1.22%	10.90%	34.82%	3.90%	33.57%	66.13%
42N	100E	4.82	19.00	0.27	6.99	20.96	0.09	1.96	-0.18	2.18	1.22%	13.13%	36.71%	3.60%	34.47%	64.14%
43N	100E	5.39	18.84	0.15	6.31	20.04	0.16	1.20	0.01	0.92	0.89%	18.46%	47.94%	0.90%	27.47%	62.64%
44N	100E	5.51	16.66	0.11	6.36	18.80	0.26	2.14	0.15	0.85	0.33%	18.46%	53.95%	0.70%	28.27%	65.33%
45N	100E	5.14	15.21	0.13	7.29	17.74	0.38	2.54	0.25	2.15	0.00%	11.35%	50.17%	1.00%	38.66%	76.12%
37N	101E	5.22	12.46	0.47	6.42	14.43	0.08	1.97	-0.39	1.20	0.00%	16.02%	46.61%	0.00%	28.97%	66.43%
38N	101E	5.20	21.10	0.21	6.80	14.46	0.45	-6.64	0.25	1.60	0.67%	10.34%	49.72%	0.00%	33.57%	74.63%
39N	101E	4.74	22.01	0.29	7.05	15.40	0.25	-6.60	-0.05	2.31	1.11%	6.45%	39.60%	0.00%	38.16%	73.93%
40N	101E	4.83	20.62	0.34	6.83	19.98	0.24	-0.64	-0.11	2.00	1.11%	12.90%	36.48%	1.90%	31.17%	68.03%
41N	101E	4.85	19.96	0.12	6.83	19.36	0.23	-0.60	0.11	1.97	1.11%	14.68%	37.82%	2.20%	32.37%	64.24%
42N	101E	5.25	19.83	0.13	6.77	20.46	0.12	0.63	-0.01	1.52	1.11%	14.79%	47.72%	2.60%	33.47%	65.53%
43N	101E	5.48	18.27	0.18	6.13	20.17	0.27	1.91	0.09	0.64	0.89%	19.35%	48.72%	1.20%	25.27%	60.14%
44N	101E	5.24	16.55	0.12	6.19	18.64	0.08	2.10	-0.04	0.95	0.22%	17.80%	48.05%	0.70%	24.48%	61.74%
45N	101E	4.97	15.31	0.01	6.34	17.03	0.16	1.73	0.15	1.37	0.00%	10.34%	45.38%	0.20%	26.67%	65.63%
37N	102E	4.74	13.08	0.21	5.65	12.89	0.17	-0.19	-0.04	0.91	0.00%	9.01%	41.71%	0.00%	17.48%	59.94%
38N	102E	4.91	21.42	0.26	6.72	13.52	0.22	-7.90	-0.05	1.81	0.89%	5.90%	46.83%	0.00%	32.17%	75.22%
39N	102E	4.82	22.32	0.01	7.28	17.69	0.27	-4.63	0.26	2.46	1.11%	7.79%	38.82%	0.50%	39.16%	76.02%
40N	102E	5.05	21.10	0.17	7.17	19.90	0.08	-1.20	-0.09	2.13	1.00%	14.68%	39.60%	2.10%	36.36%	70.43%
41N	102E	4.98	20.39	0.13	6.93	19.64	0.04	-0.75	-0.09	1.95	1.00%	14.57%	42.27%	2.20%	34.37%	66.03%
42N	102E	5.42	20.28	0.14	6.70	21.11	0.20	0.83	0.06	1.28	1.11%	15.35%	50.83%	2.60%	32.17%	64.44%
43N	102E	5.45	17.92	0.14	6.16	19.68	0.09	1.76	-0.05	0.71	1.00%	18.13%	50.50%	1.30%	26.17%	60.64%
44N	102E	5.26	16.38	0.12	6.30	18.87	0.14	2.49	0.02	1.04	0.22%	20.02%	46.16%	0.70%	25.37%	64.24%
45N	102E	5.09	15.11	0.34	6.49	17.28	0.16	2.17	-0.18	1.40	0.00%	13.35%	47.39%	0.30%	27.27%	69.33%

Table S.1: Continued from previous table section. LGM and modern surface wind velocities over the CLP.

Lat	Lon	MOD AVG	MOD MAX	MOD MIN	LGM AVG	LGM MAX	LGM MIN	L-M MAX	L-M MIN	L-M AVG	MOD 16%	MOD 8%	MOD 5%	LGM 16%	LGM 8%	LGM 5%
37N	103E	4.34	14.83	0.12	5.41	12.29	0.04	-2.55	-0.07	1.07	0.00%	3.11%	34.26%	0.00%	10.29%	57.44%
38N	103E	4.96	20.82	0.10	6.91	16.70	0.13	-4.12	0.03	1.95	1.00%	7.01%	46.27%	0.10%	35.26%	75.52%
39N	103E	4.96	22.34	0.19	7.41	18.95	0.22	-3.40	0.03	2.46	1.11%	10.12%	40.71%	1.00%	39.26%	76.52%
40N	103E	5.11	21.96	0.27	7.22	19.56	0.37	-2.40	0.10	2.11	1.00%	14.79%	42.16%	3.10%	37.86%	68.73%
41N	103E	5.20	21.10	0.13	6.97	20.41	0.11	-0.69	-0.03	1.77	1.11%	14.68%	48.16%	2.10%	35.46%	65.83%
42N	103E	5.60	20.77	0.02	6.65	21.59	0.20	0.82	0.18	1.06	1.11%	17.91%	53.28%	2.40%	33.17%	62.84%
43N	103E	5.45	17.33	0.08	6.38	20.10	0.35	2.77	0.26	0.94	0.67%	17.91%	50.83%	1.20%	27.97%	63.24%
44N	103E	5.39	16.17	0.18	6.67	19.61	0.04	3.44	-0.15	1.28	0.11%	21.25%	47.27%	0.70%	30.47%	69.43%
45N	103E	5.14	14.01	0.10	7.04	17.60	0.15	3.59	0.05	1.90	0.00%	14.24%	46.72%	0.30%	33.87%	77.52%
37N	104E	4.63	19.30	0.10	5.58	20.66	0.12	1.36	0.02	0.95	1.11%	5.23%	37.49%	0.50%	13.19%	56.84%
38N	104E	5.44	19.73	0.33	7.63	21.83	0.67	2.10	0.34	2.18	1.45%	14.24%	46.72%	2.10%	42.46%	73.83%
39N	104E	5.38	21.56	0.18	7.63	20.48	0.26	-1.08	0.08	2.25	1.11%	12.79%	46.94%	2.70%	41.46%	73.43%
40N	104E	5.42	21.31	0.34	7.35	19.18	0.19	-2.13	-0.14	1.93	1.00%	13.68%	48.94%	3.70%	40.06%	69.53%
41N	104E	5.64	21.29	0.25	7.10	21.05	0.21	-0.24	-0.04	1.46	1.33%	15.91%	49.72%	2.70%	37.76%	66.53%
42N	104E	5.76	21.37	0.40	6.79	20.83	0.15	-0.53	-0.24	1.04	1.22%	20.91%	53.95%	1.90%	36.36%	63.94%
43N	104E	5.42	17.11	0.15	7.14	21.25	0.21	4.15	0.06	1.72	0.56%	17.24%	46.05%	1.50%	39.66%	72.83%
44N	104E	5.58	15.40	0.42	7.61	20.90	0.38	5.50	-0.05	2.03	0.00%	19.13%	48.83%	0.90%	45.65%	81.02%
45N	104E	4.66	13.87	0.12	7.81	17.31	0.81	3.45	0.69	3.15	0.00%	11.23%	40.60%	0.20%	44.86%	84.22%
37N	105E	4.94	18.92	0.37	5.85	20.63	0.17	1.71	-0.20	0.91	1.00%	10.46%	41.71%	0.70%	17.78%	60.94%
38N	105E	5.47	19.93	0.04	7.74	22.47	0.14	2.55	0.11	2.27	1.33%	15.80%	46.05%	2.50%	45.45%	73.73%
39N	105E	5.56	20.63	0.16	7.92	19.92	0.45	-0.71	0.30	2.36	1.33%	15.24%	51.39%	3.10%	45.05%	77.52%
40N	105E	5.60	20.22	0.18	7.52	19.82	0.12	-0.40	-0.07	1.92	1.33%	13.79%	50.83%	3.70%	42.56%	70.63%
41N	105E	5.68	21.29	0.20	7.15	20.93	0.24	-0.36	0.04	1.47	1.45%	16.69%	50.17%	2.50%	38.06%	68.93%
42N	105E	5.67	21.27	0.04	6.86	20.04	0.17	-1.23	0.13	1.19	1.33%	20.58%	51.39%	1.60%	36.66%	65.23%
43N	105E	5.35	17.42	0.19	7.33	20.65	0.60	3.23	0.42	1.97	0.44%	17.46%	44.61%	1.20%	39.66%	74.83%
44N	105E	5.55	15.34	0.50	7.77	20.57	0.59	5.23	0.09	2.22	0.00%	17.91%	48.94%	0.70%	46.15%	81.82%
45N	105E	4.54	13.99	0.06	7.67	17.42	0.61	3.43	0.55	3.14	0.00%	10.23%	36.93%	0.40%	43.46%	83.12%

Table S.1: Continued from previous table section. LGM and modern surface wind velocities over the CLP.

Lat	Lon	MOD AVG	MOD MAX	MOD MIN	LGM AVG	LGM MAX	LGM MIN	L-M MAX	L-M MIN	L-M AVG	MOD 16%	MOD 8%	MOD 5%	LGM 16%	LGM 8%	LGM 5%
37N	106E	5.38	20.06	0.12	6.70	17.49	0.11	-2.56	-0.01	1.33	0.78%	12.12%	49.72%	0.90%	35.26%	65.73%
38N	106E	5.48	18.60	0.11	7.74	20.06	0.54	1.46	0.43	2.26	1.22%	15.35%	50.17%	2.40%	45.55%	73.23%
39N	106E	5.65	19.23	0.24	8.07	20.90	0.52	1.67	0.27	2.42	1.33%	15.57%	51.50%	4.00%	49.35%	75.72%
40N	106E	5.76	19.78	0.13	7.64	20.89	0.10	1.11	-0.03	1.88	1.22%	16.02%	56.73%	3.30%	44.06%	72.13%
41N	106E	5.83	19.82	0.37	7.31	20.74	0.42	0.92	0.05	1.48	1.45%	17.80%	55.95%	2.30%	40.06%	69.73%
42N	106E	5.69	19.17	0.33	7.12	19.61	0.09	0.44	-0.24	1.44	1.33%	20.02%	50.72%	1.50%	37.16%	68.23%
43N	106E	5.30	16.92	0.60	7.53	19.59	0.46	2.67	-0.13	2.23	0.33%	16.02%	47.72%	1.00%	41.56%	78.42%
44N	106E	5.49	14.53	0.71	7.84	19.31	0.10	4.78	-0.61	2.35	0.00%	15.57%	51.95%	0.80%	44.46%	84.62%
45N	106E	5.07	13.75	0.26	7.52	17.41	0.31	3.66	0.05	2.45	0.00%	9.01%	48.16%	0.80%	39.06%	83.12%
37N	107E	5.34	18.65	0.23	6.94	17.41	0.18	-1.24	-0.05	1.61	1.22%	9.90%	49.28%	0.80%	38.96%	66.63%
38N	107E	5.54	18.36	0.20	7.94	21.33	0.27	2.97	0.07	2.40	1.11%	13.46%	51.95%	2.80%	48.05%	75.02%
39N	107E	5.59	18.07	0.06	8.16	21.61	0.32	3.54	0.25	2.57	1.11%	14.24%	52.73%	3.90%	50.25%	76.52%
40N	107E	5.85	19.44	0.07	7.71	20.76	0.27	1.32	0.21	1.85	1.11%	16.69%	58.18%	3.00%	43.76%	73.33%
41N	107E	5.91	20.21	0.25	7.46	20.41	0.29	0.20	0.03	1.55	1.33%	19.47%	55.28%	2.10%	40.66%	71.83%
42N	107E	5.68	19.23	0.15	7.38	19.84	0.02	0.61	-0.12	1.69	1.22%	19.47%	48.72%	1.70%	37.76%	72.03%
43N	107E	5.25	15.64	0.11	7.69	19.22	0.34	3.58	0.22	2.44	0.00%	15.68%	46.61%	1.20%	42.56%	81.92%
44N	107E	5.50	13.62	0.53	7.96	19.16	0.65	5.54	0.13	2.47	0.00%	15.57%	54.17%	1.20%	44.96%	87.11%
45N	107E	5.39	14.30	0.30	7.75	17.89	0.19	3.59	-0.10	2.36	0.00%	10.90%	53.28%	0.70%	41.86%	85.91%
37N	108E	5.20	18.82	0.15	7.62	19.57	0.76	0.75	0.61	2.42	1.89%	9.01%	45.94%	0.90%	41.36%	76.42%
38N	108E	5.72	19.38	0.17	8.53	22.80	0.66	3.42	0.49	2.82	1.11%	12.35%	55.62%	4.10%	52.35%	82.62%
39N	108E	5.83	19.30	0.23	8.54	22.30	0.43	2.99	0.20	2.71	1.11%	13.79%	59.96%	4.30%	52.75%	81.72%
40N	108E	5.92	18.52	0.13	7.92	20.19	0.55	1.67	0.42	2.01	1.33%	18.46%	58.84%	2.80%	45.15%	77.52%
41N	108E	5.71	18.51	0.17	7.59	18.77	0.17	0.26	0.00	1.87	1.11%	18.24%	54.84%	1.90%	41.66%	75.12%
42N	108E	5.55	17.61	0.41	7.59	18.52	1.01	0.92	0.60	2.04	0.44%	18.13%	49.72%	1.30%	40.56%	78.92%
43N	108E	5.33	13.19	0.10	7.91	18.51	0.94	5.33	0.84	2.57	0.00%	16.80%	47.16%	1.30%	43.06%	87.31%
44N	108E	5.48	12.87	0.45	8.16	18.54	0.31	5.66	-0.15	2.69	0.00%	15.24%	53.39%	2.00%	47.55%	89.81%
45N	108E	5.80	14.86	0.16	8.24	18.67	0.30	3.81	0.14	2.44	0.00%	15.80%	60.96%	1.30%	50.25%	90.31%
Average		5.43	18.67		7.18	19.07		0.40	0.08	1.75	0.91%	16.09%	48.78%	1.70%	37.59%	71.19%

Table S.1: Continued from previous table section, and the final section from the Central Loess Plateau region. Total site averages for average and maximum gust events shown at the bottom, with average percentages of events over the specified wind velocity thresholds.

Lat	Lon	MOD AVG	MOD MAX	MOD MIN	LGM AVG	LGM MAX	LGM MIN	L-M MAX	L-M MIN	L-M AVG	MOD 16%	MOD 8%	MOD 5%	LGM 16%	LGM 8%	LGM 5%
37N	80E	3.97	11.84	0.13	4.92	13.08	0.13	1.23	0.00	0.95	0.00%	3.00%	30.70%	0.00%	11.79%	45.15%
38N	80E	3.29	8.87	0.21	4.06	19.90	0.22	11.03	0.01	0.76	0.00%	0.78%	16.80%	0.40%	6.19%	27.57%
39N	80E	3.13	6.97	0.15	3.99	19.97	0.10	13.00	-0.05	0.85	0.00%	0.00%	10.46%	0.40%	4.60%	30.07%
40N	80E	3.43	9.01	0.08	4.71	13.44	0.25	4.43	0.18	1.28	0.00%	0.67%	19.69%	0.00%	7.49%	42.86%
41N	80E	4.26	12.58	0.08	5.65	14.16	0.22	1.59	0.14	1.40	0.00%	3.78%	29.48%	0.00%	20.58%	54.55%
42N	80E	4.73	12.56	0.17	6.83	23.70	0.16	11.13	-0.01	2.10	0.00%	9.12%	41.94%	1.60%	31.37%	69.93%
43N	80E	4.82	11.72	0.28	7.25	17.41	0.46	5.69	0.19	2.43	0.00%	8.68%	44.38%	1.00%	37.46%	73.13%
44N	80E	4.16	11.22	0.03	7.53	17.49	0.25	6.27	0.23	3.36	0.00%	4.34%	29.81%	0.60%	45.15%	79.52%
45N	80E	5.40	13.55	0.29	7.91	19.34	0.48	5.79	0.20	2.50	0.00%	13.68%	53.17%	1.10%	49.25%	79.12%
37N	81E	3.88	10.83	0.07	4.47	12.49	0.07	1.66	0.00	0.59	0.00%	4.67%	28.03%	0.00%	8.49%	40.06%
38N	81E	3.02	8.41	0.08	3.92	20.89	0.05	12.49	-0.03	0.90	0.00%	0.67%	10.90%	0.40%	4.50%	25.87%
39N	81E	3.08	7.10	0.19	4.28	17.80	0.14	10.70	-0.06	1.20	0.00%	0.00%	11.90%	0.30%	6.09%	35.16%
40N	81E	2.95	8.67	0.20	4.36	13.32	0.14	4.65	-0.07	1.40	0.00%	0.44%	10.68%	0.00%	5.09%	40.06%
41N	81E	3.70	12.88	0.13	5.28	13.41	0.21	0.54	0.08	1.58	0.00%	2.67%	23.14%	0.00%	16.08%	49.75%
42N	81E	4.21	14.12	0.21	6.12	18.43	0.23	4.31	0.02	1.91	0.00%	6.79%	33.59%	0.80%	23.28%	58.34%
43N	81E	4.88	12.03	0.08	7.37	20.40	0.28	8.37	0.20	2.49	0.00%	8.45%	44.72%	1.70%	39.26%	78.42%
44N	81E	4.00	12.65	0.11	7.33	19.42	0.44	6.77	0.32	3.33	0.00%	4.45%	25.03%	2.10%	38.76%	76.72%
45N	81E	5.27	14.90	0.43	8.54	20.10	0.27	5.21	-0.15	3.27	0.00%	9.45%	51.61%	1.40%	58.04%	81.12%
37N	82E	3.55	10.62	0.10	4.31	12.45	0.09	1.83	-0.01	0.77	0.00%	3.00%	23.03%	0.00%	4.70%	38.76%
38N	82E	3.25	9.70	0.11	4.03	17.66	0.08	7.96	-0.02	0.78	0.00%	1.33%	15.13%	0.40%	5.19%	29.07%
39N	82E	3.39	8.60	0.18	4.24	12.81	0.15	4.21	-0.03	0.85	0.00%	0.22%	15.02%	0.00%	5.59%	34.97%
40N	82E	2.91	9.90	0.05	3.77	9.99	0.10	0.09	0.05	0.86	0.00%	0.89%	9.12%	0.00%	3.50%	28.27%
41N	82E	3.41	11.48	0.12	4.32	12.22	0.08	0.74	-0.04	0.91	0.00%	2.89%	19.35%	0.00%	8.69%	37.46%
42N	82E	3.70	14.78	0.21	5.39	17.29	0.24	2.51	0.03	1.69	0.00%	4.89%	21.02%	0.30%	16.08%	53.95%
43N	82E	5.12	13.87	0.19	6.89	14.06	0.40	0.18	0.21	1.77	0.00%	11.01%	46.72%	0.00%	31.07%	72.83%
44N	82E	4.63	13.55	0.23	6.63	18.75	0.16	5.20	-0.07	2.00	0.00%	6.56%	37.60%	1.20%	27.27%	70.63%
45N	82E	4.72	13.26	0.12	8.70	24.22	0.49	10.96	0.36	3.98	0.00%	9.90%	40.38%	4.60%	56.54%	82.22%

Table S.2: LGM and modern Taklamakan Desert surface wind flow, max gust events and percentages of events over threshold velocities.

Lat	Lon	MOD AVG	MOD MAX	MOD MIN	LGM AVG	LGM MAX	LGM MIN	L-M MAX	L-M MIN	L-M AVG	MOD 16%	MOD 8%	MOD 5%	LGM 16%	LGM 8%	LGM 5%
37N	83E	3.66	10.43	0.12	4.57	13.06	0.07	2.63	-0.06	0.91	0.00%	3.56%	24.81%	0.00%	6.09%	41.66%
38N	83E	3.55	10.10	0.25	4.06	17.68	0.02	7.58	-0.22	0.51	0.00%	1.33%	20.02%	0.50%	4.90%	29.77%
39N	83E	3.42	9.39	0.18	4.10	11.64	0.17	2.25	-0.01	0.68	0.00%	0.22%	16.46%	0.00%	4.60%	31.67%
40N	83E	3.06	9.22	0.11	3.95	10.77	0.01	1.55	-0.10	0.89	0.00%	0.67%	9.57%	0.00%	2.70%	29.57%
41N	83E	3.47	10.55	0.09	4.01	12.97	0.13	2.43	0.04	0.54	0.00%	1.11%	21.25%	0.00%	5.89%	32.97%
42N	83E	3.71	13.17	0.08	4.82	15.49	0.15	2.32	0.08	1.11	0.00%	4.23%	19.24%	0.00%	12.69%	41.16%
43N	83E	5.54	15.20	0.31	6.89	15.70	0.29	0.50	-0.02	1.35	0.00%	14.57%	50.28%	0.00%	34.27%	68.23%
44N	83E	5.46	14.88	0.40	6.62	15.57	0.22	0.69	-0.18	1.16	0.00%	13.57%	51.72%	0.00%	30.27%	65.63%
45N	83E	4.37	11.55	0.12	7.02	24.42	0.13	12.86	0.01	2.66	0.00%	7.68%	32.37%	2.30%	35.26%	70.13%
37N	84E	3.74	10.44	0.05	4.89	13.77	0.10	3.33	0.06	1.15	0.00%	3.89%	25.36%	0.00%	11.39%	44.86%
38N	84E	3.63	10.31	0.10	3.93	18.29	0.15	7.98	0.05	0.29	0.00%	1.11%	20.36%	0.50%	3.80%	26.47%
39N	84E	3.38	10.79	0.21	3.91	11.84	0.19	1.05	-0.03	0.53	0.00%	0.78%	14.91%	0.00%	4.40%	29.97%
40N	84E	3.00	7.79	0.17	4.02	11.19	0.03	3.40	-0.14	1.01	0.00%	0.00%	8.01%	0.00%	4.30%	28.47%
41N	84E	3.37	9.08	0.12	3.82	14.44	0.02	5.36	-0.10	0.45	0.00%	0.44%	18.80%	0.00%	3.90%	29.17%
42N	84E	3.82	11.79	0.08	4.29	17.54	0.11	5.75	0.03	0.48	0.00%	2.56%	20.47%	0.20%	8.19%	32.27%
43N	84E	5.70	14.69	0.31	7.85	17.28	0.41	2.59	0.10	2.14	0.00%	16.24%	52.95%	1.50%	43.66%	69.73%
44N	84E	6.05	16.88	0.34	7.77	18.96	0.36	2.08	0.02	1.72	0.67%	22.02%	57.40%	6.29%	40.46%	72.03%
45N	84E	4.16	11.40	0.26	5.60	23.76	0.21	12.35	-0.05	1.45	0.00%	8.01%	32.59%	0.90%	19.38%	52.15%
37N	85E	4.86	14.16	0.09	5.06	12.67	0.19	-1.48	0.11	0.19	0.00%	14.35%	41.27%	0.00%	14.59%	45.35%
38N	85E	3.46	8.33	0.08	4.01	16.87	0.05	8.55	-0.03	0.55	0.00%	0.44%	22.91%	0.20%	5.69%	25.87%
39N	85E	3.67	10.43	0.15	3.84	12.53	0.05	2.10	-0.10	0.16	0.00%	1.45%	21.36%	0.00%	5.09%	25.27%
40N	85E	3.26	8.64	0.04	3.92	10.99	0.06	2.35	0.02	0.66	0.00%	0.44%	14.91%	0.00%	9.39%	29.97%
41N	85E	3.43	8.53	0.06	4.22	10.97	0.04	2.45	-0.02	0.79	0.00%	0.78%	20.02%	0.00%	8.49%	34.27%
42N	85E	3.87	10.76	0.10	5.01	14.04	0.08	3.28	-0.02	1.14	0.00%	3.11%	24.47%	0.00%	11.99%	45.25%
43N	85E	5.35	18.46	0.28	7.57	17.91	0.01	-0.55	-0.26	2.22	0.67%	15.35%	48.16%	0.60%	44.26%	74.23%
44N	85E	5.81	18.46	0.14	8.65	21.27	0.14	2.80	0.00	2.83	0.33%	21.13%	52.73%	9.99%	48.45%	75.12%
45N	85E	4.32	12.80	0.19	5.34	23.59	0.09	10.79	-0.10	1.01	0.00%	6.56%	34.15%	0.70%	19.08%	47.55%

Table S.2: Continued from previous table section. Shown are the LGM and modern wind velocity frequencies over the Taklamakan Desert.

Lat	Lon	MOD AVG	MOD MAX	MOD MIN	LGM AVG	LGM MAX	LGM MIN	L-M MAX	L-M MIN	L-M AVG	MOD 16%	MOD 8%	MOD 5%	LGM 16%	LGM 8%	LGM 5%
37N	86E	6.09	17.30	0.17	5.30	13.63	0.21	-3.67	0.04	-0.79	0.44%	27.81%	55.84%	0.00%	17.58%	48.95%
38N	86E	3.54	8.98	0.09	4.28	15.33	0.09	6.35	0.00	0.74	0.00%	1.00%	23.25%	0.00%	6.19%	35.26%
39N	86E	3.71	9.97	0.09	4.00	13.14	0.08	3.17	-0.01	0.29	0.00%	1.56%	25.25%	0.00%	6.29%	25.47%
40N	86E	3.27	9.88	0.07	4.20	11.87	0.05	1.99	-0.02	0.93	0.00%	1.89%	16.02%	0.00%	14.69%	33.57%
41N	86E	3.58	9.05	0.14	4.81	11.53	0.17	2.48	0.02	1.23	0.00%	3.67%	22.58%	0.00%	15.88%	41.06%
42N	86E	3.94	10.30	0.23	5.37	13.78	0.21	3.48	-0.02	1.43	0.00%	2.67%	27.25%	0.00%	15.38%	53.85%
43N	86E	4.90	18.46	0.29	7.12	17.11	0.12	-1.35	-0.18	2.23	0.67%	12.24%	40.71%	0.30%	41.36%	72.13%
44N	86E	5.21	17.00	0.32	7.76	19.37	0.10	2.37	-0.21	2.55	0.22%	15.68%	46.50%	3.70%	42.06%	69.43%
45N	86E	4.20	13.89	0.15	5.34	23.35	0.10	9.47	-0.04	1.14	0.00%	4.78%	29.81%	0.70%	19.28%	48.15%
37N	87E	8.76	19.89	0.34	6.76	16.90	0.28	-2.99	-0.06	-2.01	2.56%	57.06%	75.64%	0.50%	32.47%	68.73%
38N	87E	4.21	10.66	0.23	5.57	14.66	0.08	4.01	-0.15	1.36	0.00%	4.34%	29.70%	0.00%	20.58%	52.75%
39N	87E	3.68	8.51	0.31	4.65	15.67	0.23	7.16	-0.08	0.96	0.00%	1.11%	19.13%	0.00%	8.09%	39.06%
40N	87E	3.48	12.56	0.03	5.30	14.34	0.15	1.78	0.12	1.82	0.00%	5.23%	19.02%	0.00%	25.77%	44.76%
41N	87E	4.13	11.82	0.13	5.87	13.60	0.28	1.78	0.15	1.74	0.00%	9.01%	28.03%	0.00%	30.17%	52.75%
42N	87E	4.23	12.16	0.30	5.86	16.10	0.20	3.93	-0.09	1.62	0.00%	5.12%	32.04%	0.20%	22.78%	60.04%
43N	87E	4.17	13.65	0.24	6.13	15.77	0.07	2.13	-0.16	1.96	0.00%	7.23%	27.70%	0.00%	27.07%	60.54%
44N	87E	4.31	11.41	0.26	5.71	20.04	0.19	8.63	-0.07	1.40	0.00%	7.12%	33.26%	0.10%	21.08%	53.95%
45N	87E	3.46	13.15	0.08	5.27	26.21	0.19	13.06	0.12	1.81	0.00%	5.34%	17.02%	0.80%	19.28%	44.26%
37N	88E	9.33	19.68	0.44	7.90	18.33	0.62	-1.35	0.18	-1.43	4.56%	60.07%	80.09%	1.20%	45.85%	83.02%
38N	88E	4.92	12.66	0.16	6.53	15.66	0.29	3.00	0.13	1.61	0.00%	9.34%	44.61%	0.00%	30.47%	65.63%
39N	88E	3.82	7.96	0.29	5.11	16.47	0.34	8.51	0.05	1.29	0.00%	0.00%	20.36%	0.10%	7.79%	47.05%
40N	88E	3.70	13.15	0.02	5.66	15.00	0.02	1.85	0.00	1.96	0.00%	7.23%	22.80%	0.00%	30.27%	47.45%
41N	88E	4.37	11.84	0.10	6.15	13.27	0.30	1.43	0.21	1.78	0.00%	11.46%	31.70%	0.00%	31.87%	60.04%
42N	88E	4.41	12.91	0.25	6.21	16.13	0.12	3.22	-0.13	1.80	0.00%	5.56%	34.37%	0.10%	25.97%	65.63%
43N	88E	4.23	11.24	0.15	6.07	16.47	0.21	5.22	0.06	1.84	0.00%	5.34%	32.70%	0.20%	27.07%	60.44%
44N	88E	4.26	11.13	0.18	5.73	19.27	0.12	8.14	-0.07	1.48	0.00%	6.56%	30.81%	0.30%	23.18%	53.55%
45N	88E	3.83	14.68	0.08	5.14	22.58	0.28	7.91	0.20	1.31	0.00%	5.78%	23.25%	1.00%	19.58%	41.76%

Table S.2: Continued from previous table section. Shown are the LGM and modern wind velocity frequencies over the Taklamakan Desert.

Lat	Lon	MOD AVG	MOD MAX	MOD MIN	LGM AVG	LGM MAX	LGM MIN	L-M MAX	L-M MIN	L-M AVG	MOD 16%	MOD 8%	MOD 5%	LGM 16%	LGM 8%	LGM 5%
37N	89E	9.08	19.37	0.17	8.71	17.52	0.48	-1.85	0.31	-0.36	5.56%	57.06%	79.31%	1.80%	58.84%	86.11%
38N	89E	5.63	15.94	0.29	7.36	20.24	0.10	4.31	-0.19	1.73	0.00%	19.13%	53.17%	1.70%	39.86%	71.83%
39N	89E	4.50	12.37	0.22	5.52	18.81	0.04	6.44	-0.18	1.02	0.00%	3.89%	36.15%	0.90%	15.38%	53.15%
40N	89E	3.85	11.79	0.05	5.37	14.11	0.27	2.33	0.22	1.53	0.00%	6.67%	25.58%	0.00%	24.08%	50.85%
41N	89E	4.29	13.87	0.12	6.02	14.50	0.36	0.62	0.23	1.74	0.00%	7.90%	32.48%	0.00%	25.17%	62.04%
42N	89E	4.08	12.04	0.10	6.09	15.88	0.39	3.84	0.29	2.01	0.00%	3.89%	31.81%	0.00%	21.68%	64.64%
43N	89E	4.13	10.61	0.12	6.72	20.84	0.19	10.22	0.07	2.59	0.00%	6.90%	32.15%	2.00%	33.57%	67.43%
44N	89E	4.89	12.42	0.21	7.39	22.29	0.24	9.87	0.02	2.50	0.00%	13.01%	41.94%	1.70%	41.66%	64.04%
45N	89E	5.26	15.26	0.09	6.91	23.24	0.26	7.98	0.16	1.65	0.00%	19.91%	39.38%	1.60%	36.66%	63.54%
37N	90E	8.82	19.43	0.72	8.07	18.01	0.17	-1.42	-0.55	-0.75	5.67%	54.84%	77.31%	0.80%	50.25%	82.92%
38N	90E	5.54	17.47	0.42	6.96	18.88	0.37	1.41	-0.04	1.42	0.33%	17.91%	51.61%	1.00%	34.47%	69.13%
39N	90E	4.59	13.50	0.13	5.57	18.83	0.08	5.33	-0.05	0.98	0.00%	6.34%	37.71%	0.70%	16.58%	54.05%
40N	90E	3.81	11.91	0.10	5.07	13.34	0.10	1.44	-0.01	1.26	0.00%	4.56%	23.92%	0.00%	18.58%	48.25%
41N	90E	4.09	13.52	0.09	5.82	15.93	0.52	2.41	0.43	1.73	0.00%	6.45%	30.26%	0.00%	21.08%	59.44%
42N	90E	3.87	10.43	0.12	5.69	16.00	0.13	5.57	0.02	1.81	0.00%	2.00%	28.70%	0.00%	14.49%	58.94%
43N	90E	3.87	11.83	0.22	6.60	21.92	0.12	10.10	-0.11	2.73	0.00%	5.12%	26.59%	3.50%	28.77%	63.84%
44N	90E	4.83	12.40	0.13	7.83	22.38	0.20	9.97	0.07	3.00	0.00%	10.90%	41.16%	3.40%	48.45%	69.93%
45N	90E	5.08	13.79	0.14	7.56	22.52	0.13	8.72	-0.01	2.48	0.00%	20.13%	37.26%	1.60%	43.86%	67.03%
37N	91E	8.09	18.19	0.48	7.44	18.04	0.29	-0.15	-0.18	-0.65	2.56%	47.83%	73.97%	0.40%	42.06%	76.02%
38N	91E	5.24	18.43	0.27	6.43	16.59	0.18	-1.84	-0.10	1.19	0.44%	12.24%	49.05%	0.50%	26.47%	67.33%
39N	91E	4.46	14.10	0.04	5.47	17.79	0.08	3.69	0.04	1.01	0.00%	5.90%	36.60%	0.50%	15.78%	52.45%
40N	91E	3.76	11.97	0.13	4.89	11.02	0.12	-0.94	-0.01	1.13	0.00%	4.56%	24.36%	0.00%	14.69%	47.15%
41N	91E	3.91	12.85	0.22	5.56	15.76	0.13	2.91	-0.09	1.65	0.00%	5.67%	27.59%	0.00%	19.28%	57.44%
42N	91E	3.74	9.08	0.04	5.32	16.12	0.22	7.04	0.18	1.59	0.00%	1.67%	22.91%	0.10%	14.39%	51.45%
43N	91E	3.82	10.96	0.05	6.29	20.93	0.19	9.97	0.14	2.47	0.00%	2.22%	26.25%	3.50%	25.37%	58.14%
44N	91E	4.57	10.81	0.13	7.71	22.94	0.16	12.14	0.04	3.14	0.00%	9.79%	36.93%	3.00%	47.05%	71.83%
45N	91E	4.92	13.40	0.13	7.57	21.36	0.78	7.96	0.64	2.66	0.00%	17.69%	36.82%	1.20%	45.75%	67.33%
Average		4.37	12.37		5.76	16.86		4.49		1.39	0.23%	8.76%	32.13%	0.75%	22.85%	53.43%

Table S.2: Continued from previous table section, and the final section from the Taklamakan Desert region. Total site averages for average and maximum gust events shown at the bottom, with average percentages of events over the specified wind velocity thresholds.

Lat	Lon	MOD AVG	MOD MAX	MOD MIN	LGM AVG	LGM MAX	L-M MIN	L-M MAX	L-M MIN	L-M AVG	MOD 16%	MOD 8%	MOD 5%	LGM 16%	LGM 8%	LGM 5%
-51	284	9.21	17.42	0.44	9.71	28.53	0.46	11.11	0.02	0.51	0.56%	67.19%	83.98%	13.57%	63.96%	90.43%
-50	284	8.39	18.43	0.18	9.36	28.84	0.67	10.41	0.49	0.97	0.44%	57.73%	82.54%	12.12%	60.18%	89.77%
-49	284	7.03	16.72	0.40	9.25	26.14	0.10	9.42	-0.30	2.22	0.11%	33.37%	77.31%	10.23%	61.18%	91.88%
-48	284	6.76	17.48	0.27	9.15	27.92	0.52	10.44	0.25	2.39	0.33%	30.59%	68.97%	9.12%	63.18%	91.32%
-47	284	6.89	20.24	0.25	9.21	26.11	0.23	5.86	-0.02	2.32	1.22%	33.70%	66.52%	6.45%	67.19%	95.22%
-46	284				9.57	26.63	0.26							7.79%	73.75%	97.00%
-51	285				8.19	24.52	0.20							5.90%	48.50%	84.09%
-50	285				7.93	22.89	0.47							4.89%	47.05%	83.09%
-49	285				8.02	23.38	0.25							3.23%	47.27%	86.54%
-48	285				7.92	23.32	0.35							2.67%	47.83%	88.32%
-47	285				7.88	23.32	0.32							2.67%	50.17%	88.99%
-46	285				8.12	22.31	0.54							2.78%	55.17%	90.88%
-51	286	8.68	15.41	0.33	8.26	19.41	0.93	4.00	0.59	-0.43	0.00%	60.85%	85.87%	3.45%	50.17%	87.65%
-50	286	8.84	18.98	0.65	8.96	19.64	0.61	0.66	-0.04	0.12	0.22%	62.29%	87.10%	7.12%	59.07%	91.10%
-49	286	8.11	14.53	0.02	9.57	22.47	0.70	7.94	0.67	1.46	0.00%	51.50%	85.09%	9.12%	63.96%	92.44%
-48	286	7.27	15.15	0.25	9.18	21.39	1.04	6.25	0.80	1.91	0.00%	38.26%	77.98%	6.12%	62.07%	95.55%
-47	286	6.45	15.10	0.42	8.51	20.49	0.22	5.40	-0.19	2.06	0.00%	25.36%	66.52%	2.78%	59.29%	94.22%
-46	286	6.06	14.10	0.39	7.77	21.20	0.48	7.10	0.09	1.71	0.00%	18.58%	64.63%	1.67%	48.83%	89.88%
-45	286	5.78	14.04	0.31	7.40	20.70	0.17	6.66	-0.14	1.62	0.00%	15.24%	63.18%	1.33%	41.60%	88.10%
-44	286	5.96	16.84	0.12	7.12	19.51	0.39	2.67	0.27	1.17	0.44%	18.24%	62.85%	0.89%	41.16%	81.87%
-43	286	5.99	16.87	0.23	6.43	16.41	0.21	-0.46	-0.03	0.44	0.44%	18.69%	64.29%	0.22%	31.26%	74.08%
-51	287	9.92	18.03	1.49	9.37	19.53	0.46	1.50	-1.03	-0.55	1.11%	71.30%	88.88%	10.90%	61.85%	95.77%
-50	287	10.44	20.45	0.49	10.44	21.19	0.42	0.74	-0.08	0.00	2.78%	74.08%	90.10%	18.02%	71.75%	95.55%
-49	287	9.56	16.38	0.23	11.04	23.15	0.59	6.76	0.36	1.48	0.56%	68.74%	87.88%	24.81%	74.75%	96.66%
-48	287	8.39	15.91	0.33	10.48	22.62	0.94	6.71	0.61	2.09	0.00%	54.62%	86.10%	18.24%	71.30%	95.11%
-47	287	7.10	14.15	0.18	9.77	22.00	0.49	7.85	0.31	2.67	0.00%	33.93%	76.31%	7.56%	69.86%	94.99%

Table S.3: LGM and modern surface wind flow, max gust events and percentages of events over threshold velocities over Patagonia.

Lat	Lon	MOD AVG	MOD MAX	MOD MIN	LGM AVG	LGM MAX	L-M MIN	L-M MAX	L-M MIN	L-M AVG	MOD 16%	MOD 8%	MOD 5%	LGM 16%	LGM 8%	LGM 5%
-46	287	6.65	13.77	0.18	9.05	23.22	0.26	9.45	0.08	2.41	0.00%	26.70%	71.97%	3.34%	64.52%	93.99%
-45	287	6.16	13.12	0.03	8.40	20.39	0.13	7.28	0.10	2.23	0.00%	19.91%	67.52%	1.45%	57.29%	94.10%
-44	287	5.73	15.59	0.05	7.38	19.59	0.78	4.01	0.74	1.65	0.00%	16.69%	58.62%	0.67%	45.61%	84.20%
-43	287				6.42	15.78	0.44							0.00%	33.82%	74.19%
-51	288	11.70	20.91	1.46	10.41	23.36	1.46	2.45	-0.01	-1.28	14.57%	80.53%	91.32%	14.68%	70.41%	99.67%
-50	288	11.49	20.57	0.55	10.79	23.46	0.53	2.89	-0.02	-0.70	13.35%	77.98%	91.21%	19.80%	75.64%	99.44%
-49	288	10.26	18.41	0.12	11.16	24.17	0.35	5.76	0.23	0.90	4.00%	73.41%	89.10%	23.47%	73.41%	97.22%
-48	288	9.44	18.40	0.66	11.09	24.32	0.42	5.92	-0.24	1.65	1.89%	67.63%	85.98%	22.47%	74.64%	96.22%
-47	288	8.18	16.93	0.31	10.57	21.94	0.30	5.01	0.00	2.39	1.33%	48.39%	81.54%	19.02%	70.52%	96.33%
-46	288	7.92	16.62	0.53	10.96	23.89	0.35	7.27	-0.18	3.04	1.00%	44.38%	78.64%	21.47%	74.30%	96.89%
-45	288	7.60	15.96	0.18	11.16	23.78	0.84	7.82	0.66	3.56	0.00%	41.49%	73.75%	23.58%	78.09%	97.11%
-44	288	6.76	15.39	0.23	9.91	21.54	1.85	6.16	1.62	3.15	0.00%	30.26%	66.96%	10.12%	67.74%	100.00%
-43	288	6.45	15.19	0.24	9.19	18.58	0.71	3.39	0.47	2.74	0.00%	25.25%	66.30%	4.12%	66.96%	99.33%
-51	289	11.67	21.19	0.90	10.16	25.12	0.54	3.92	-0.36	-1.51	15.24%	80.20%	90.99%	14.02%	71.86%	98.89%
-50	289	10.99	19.94	0.07	10.01	23.94	0.85	4.00	0.78	-0.98	9.90%	76.53%	91.21%	14.13%	70.30%	98.89%
-49	289	9.99	17.61	0.39	10.35	24.65	0.22	7.03	-0.17	0.36	3.23%	72.30%	88.88%	16.57%	71.86%	96.22%
-48	289	9.53	18.28	0.28	10.67	25.35	0.61	7.07	0.33	1.13	2.22%	67.85%	87.10%	19.02%	72.86%	97.55%
-47	289	8.35	17.34	0.20	9.98	23.39	0.31	6.06	0.12	1.63	2.00%	51.50%	83.76%	13.90%	66.74%	95.11%
-46	289	8.20	17.75	0.46	10.59	23.12	0.22	5.37	-0.24	2.39	3.11%	49.17%	80.31%	17.69%	72.30%	98.00%
-45	289	7.94	17.29	0.25	11.07	22.96	0.30	5.67	0.05	3.13	2.11%	42.83%	77.20%	20.47%	76.75%	100.00%
-44	289	7.20	15.79	0.74	10.42	21.21	1.64	5.42	0.90	3.22	0.00%	37.49%	71.86%	14.57%	73.30%	100.00%
-43	289	7.12	16.59	0.58	10.64	20.86	1.26	4.27	0.69	3.51	0.44%	35.37%	70.30%	13.13%	75.53%	100.00%
-51	290	11.51	21.02	0.43	9.80	25.87	0.42	4.85	0.00	-1.71	13.79%	79.64%	91.43%	12.79%	69.19%	97.00%
-50	290	10.65	19.38	0.57	9.45	25.07	0.77	5.69	0.20	-1.20	7.23%	74.19%	91.99%	11.90%	61.74%	96.11%
-49	290	9.95	17.87	0.13	9.79	24.05	0.09	6.18	-0.04	-0.15	3.23%	70.97%	90.99%	13.68%	68.41%	96.44%

Table S.3: Continued from previous table section. LGM and modern wind velocity frequencies over the Patagonia area.

Lat	Lon	MOD AVG	MOD MAX	MOD MIN	LGM AVG	LGM MAX	L-M MIN	L-M MAX	L-M MIN	L-M AVG	MOD 16%	MOD 8%	MOD 5%	LGM 16%	LGM 8%	LGM 5%
-48	290	9.71	18.38	0.91	10.30	24.84	0.16	6.47	-0.75	0.59	2.89%	68.97%	88.21%	16.69%	70.30%	99.67%
-47	290	8.52	17.60	0.71	9.48	23.38	0.22	5.78	-0.49	0.95	2.45%	54.51%	83.76%	9.34%	66.18%	94.55%
-46	290	8.43	17.91	0.22	9.93	22.42	0.38	4.51	0.16	1.51	3.11%	53.06%	81.09%	11.23%	70.75%	95.88%
-45	290	8.24	17.78	0.40	10.40	21.76	0.56	3.98	0.16	2.16	2.56%	48.61%	80.98%	13.57%	76.31%	98.44%
-44	290	7.53	17.37	0.18	10.32	20.43	0.87	3.07	0.69	2.79	1.00%	41.27%	74.19%	14.13%	74.08%	99.33%
-43	290	7.55	17.60	0.59	11.21	23.21	1.24	5.61	0.65	3.66	1.45%	41.82%	70.63%	18.69%	79.53%	102.45%
-51	291				9.12	22.65	0.08							7.23%	63.40%	92.44%
-50	291	10.64	19.10	1.37	9.25	23.44	0.14	4.34	-1.23	-1.38	5.90%	73.75%	92.66%	8.23%	63.29%	93.77%
-49	291	9.87	18.79	1.01	9.70	23.79	0.23	5.00	-0.78	-0.17	4.00%	70.19%	90.88%	9.12%	70.75%	98.78%
-48	291	9.56	18.85	0.65	9.97	23.08	1.05	4.23	0.40	0.42	2.45%	65.52%	89.54%	9.90%	71.30%	99.00%
-47	291	8.73	17.48	0.92	9.55	21.65	0.49	4.17	-0.44	0.82	1.78%	56.17%	82.76%	7.90%	69.97%	95.22%
-46	291	8.71	18.39	0.56	9.68	21.04	0.25	2.65	-0.31	0.98	2.56%	56.40%	82.87%	8.34%	71.19%	95.22%
-45	291	8.58	18.72	0.48	9.87	21.46	0.77	2.75	0.29	1.30	2.78%	55.51%	81.09%	8.68%	75.53%	97.11%
-44	291	8.14	18.21	0.24	9.84	19.65	0.67	1.45	0.42	1.70	1.11%	52.28%	76.42%	9.34%	75.75%	98.44%
-43	291	7.89	17.42	0.74	10.23	21.85	0.91	4.43	0.17	2.34	1.00%	45.83%	76.64%	11.23%	79.76%	99.00%
-51	292				8.84	22.93	0.58							5.12%	60.85%	93.55%
-50	292	10.50	19.29	1.37	9.22	23.17	0.92	3.88	-0.45	-1.29	7.68%	71.30%	90.77%	6.56%	66.52%	95.55%
-49	292	9.56	18.63	0.49	9.73	23.19	0.15	4.55	-0.34	0.17	3.56%	66.30%	89.32%	8.34%	72.97%	99.22%
-48	292	9.16	18.70	1.20	9.83	21.87	0.85	3.17	-0.35	0.67	2.11%	62.18%	87.43%	8.45%	73.86%	99.22%
-47	292	8.46	17.28	0.33	9.72	20.19	0.33	2.92	0.00	1.26	1.22%	54.84%	81.98%	6.90%	73.53%	97.11%
-46	292	8.41	18.47	0.19	9.72	20.41	0.39	1.93	0.20	1.30	1.67%	54.51%	78.87%	9.01%	72.97%	95.33%
-45	292	8.33	18.79	0.55	9.87	20.94	0.06	2.15	-0.49	1.54	2.22%	55.06%	78.31%	10.01%	74.86%	98.11%
-44	292	8.11	17.21	0.49	9.72	19.95	0.68	2.75	0.19	1.60	0.89%	52.50%	78.64%	8.34%	75.19%	99.11%
-43	292	7.95	17.04	0.16	9.66	20.08	0.36	3.04	0.20	1.72	0.89%	48.05%	77.64%	9.23%	72.97%	99.56%

Table S.3: Continued from previous table section. LGM and modern wind velocity frequencies over the Patagonia area.

Lat	Lon	MOD AVG	MOD MAX	MOD MIN	LGM AVG	LGM MAX	L-M MIN	L-M MAX	L-M MIN	L-M AVG	MOD 16%	MOD 8%	MOD 5%	LGM 16%	LGM 8%	LGM 5%
-51	293				8.72	22.72	0.22							4.23%	61.18%	92.44%
-50	293				8.79	22.65	0.54							4.34%	63.85%	94.77%
-49	293				9.37	22.70	0.39							6.67%	71.41%	93.55%
-48	293	8.55	18.13	0.85	9.63	22.85	0.64	4.72	-0.21	1.08	2.00%	53.62%	80.76%	7.45%	73.53%	98.11%
-47	293				9.42	20.02	0.44							4.45%	70.97%	98.22%
-46	293				9.27	19.02	0.18							4.67%	68.85%	96.22%
-45	293	8.16	17.14	0.20	9.55	19.47	0.35	2.33	0.15	1.40	0.56%	47.72%	77.20%	8.01%	70.86%	97.66%
-44	293	7.76	14.97	0.54	9.65	22.00	0.34	7.03	-0.20	1.88	0.00%	47.83%	74.75%	9.90%	70.41%	95.44%
-43	293	7.74	15.35	0.10	9.45	21.23	0.41	5.88	0.31	1.71	0.00%	49.83%	73.53%	9.01%	71.41%	94.99%
-51	294				9.12	24.98	0.13							5.78%	65.52%	92.44%
-50	294				8.60	22.40	0.47							4.34%	61.29%	91.77%
-49	294				9.19	21.66	0.37							5.90%	70.63%	91.77%
-48	294	8.62	19.19	0.63	9.50	21.86	0.17	2.68	-0.46	0.88	3.11%	53.73%	80.76%	5.67%	70.41%	97.44%
-47	294				9.15	18.91	0.55							2.67%	68.41%	97.11%
-46	294				9.07	18.27	0.28							2.22%	70.19%	96.89%
-45	294				9.47	18.49	0.43							6.34%	70.75%	98.55%
-44	294	7.65	14.39	0.16	9.53	20.95	0.30	6.56	0.13	1.88	0.00%	45.27%	74.86%	9.23%	69.19%	96.66%
-43	294	7.63	14.31	0.41	9.34	21.55	0.34	7.24	-0.07	1.71	0.00%	47.83%	74.97%	7.56%	68.41%	95.44%
-50	295				9.37	24.43	0.83							6.12%	65.96%	100.22%
-49	295				8.76	19.94	0.44							4.00%	63.96%	92.66%
-48	295				8.79	18.03	0.17							3.45%	63.74%	94.66%
-47	295				8.70	16.72	0.31							0.44%	64.63%	95.66%
-46	295				8.74	17.43	0.02							0.78%	64.29%	95.33%
-45	295				8.90	17.49	0.70							0.78%	65.85%	95.44%
-44	295				8.92	18.86	0.37							2.34%	63.85%	94.88%
-43	295	8.03	16.10	0.57	8.97	19.56	0.61	3.46	0.04	0.94	0.11%	48.05%	80.53%	3.45%	64.29%	94.33%
Average		8.42	17.34		9.42	22.03		5.02		1.26	2.30%	51.61%	79.96%	8.96%	66.06%	94.88%

Table S.3: Continued from previous table section, and the final section from the Patagonia region. Total site averages for average and maximum gust events shown at the bottom, with average percentages of events over the specified wind velocity thresholds.

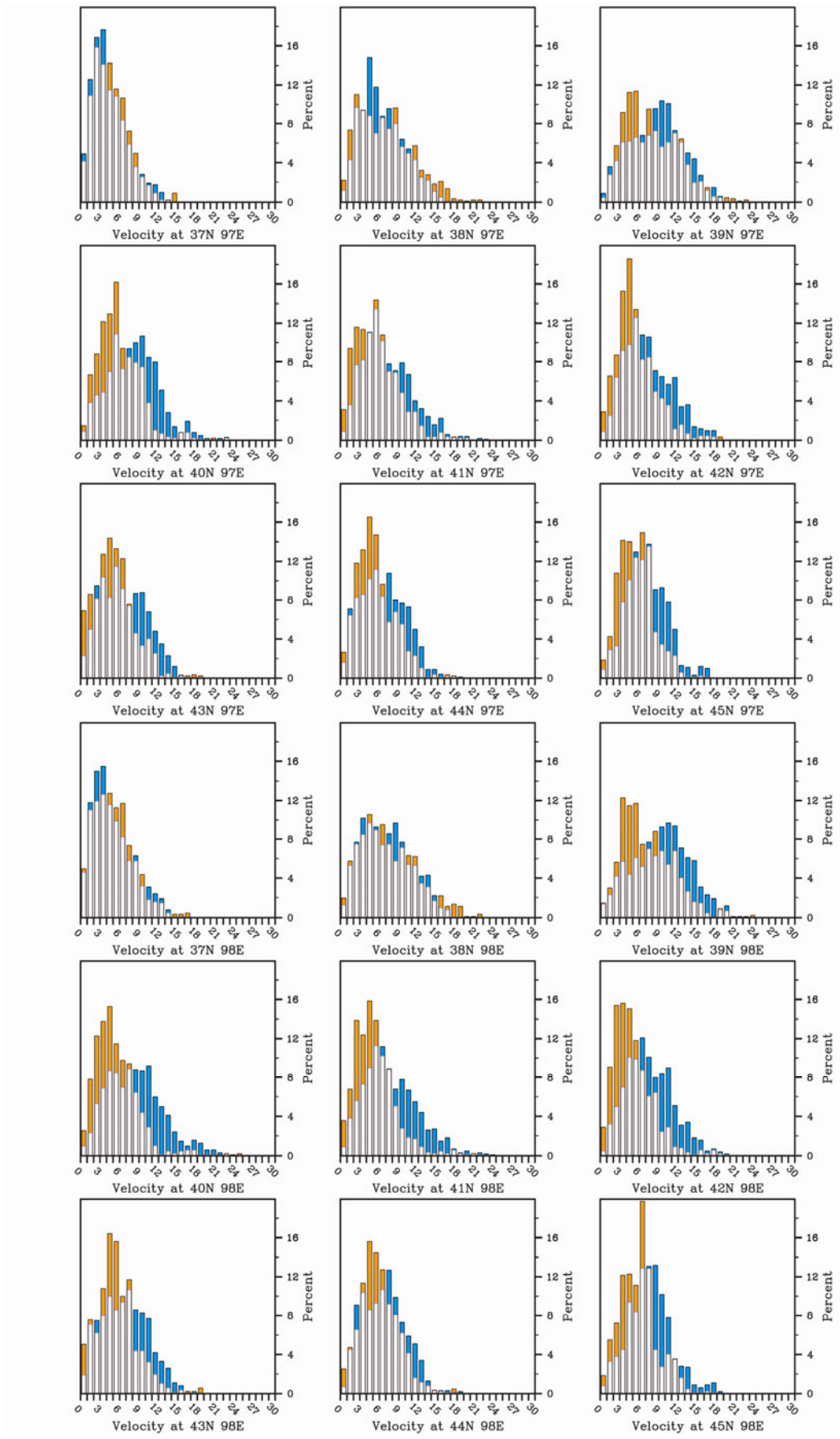
Velocity at 37N 97E
Velocity at 38N 97E
Velocity at 39N 97E
Velocity at 40N 97E
Velocity at 41N 97E
Velocity at 42N 97E
Velocity at 43N 97E
Velocity at 44N 97E
Velocity at 45N 97E
Velocity at 37N 98E
Velocity at 38N 98E
Velocity at 39N 98E
Velocity at 40N 98E
Velocity at 41N 98E
Velocity at 42N 98E
Velocity at 43N 98E
Velocity at 44N 98E
Velocity at 45N 98E
Percent
0 4 8 12 16
0 3 6 9 12 15 18 21 24 27 30

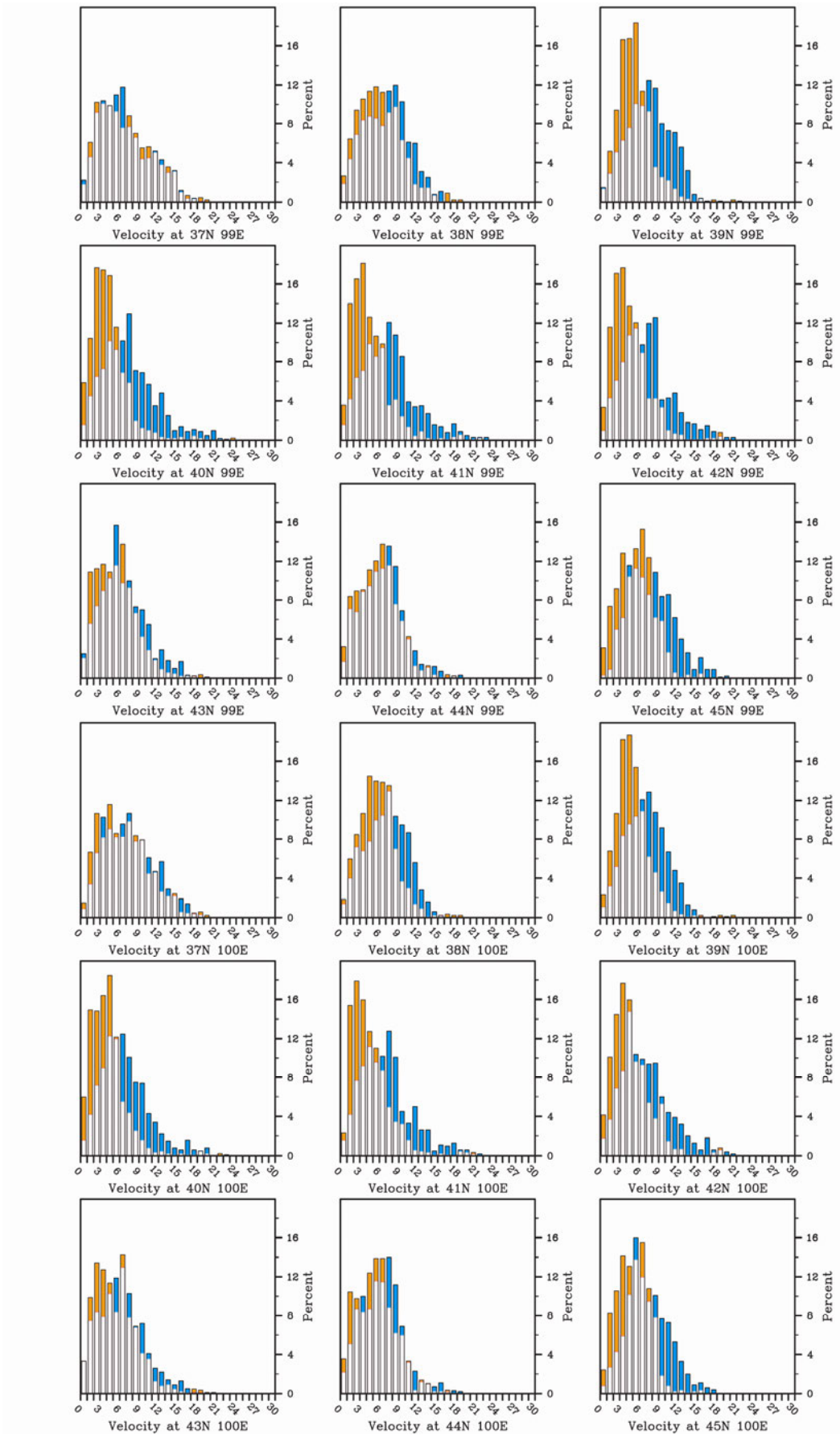
Velocity at 37N 99E
Velocity at 38N 99E
Velocity at 39N 99E
Velocity at 40N 99E
Velocity at 41N 99E
Velocity at 42N 99E
Velocity at 43N 99E
Velocity at 44N 99E
Velocity at 45N 99E
Velocity at 37N 100E
Velocity at 38N 100E
Velocity at 39N 100E
Velocity at 40N 100E
Velocity at 41N 100E
Velocity at 42N 100E
Velocity at 43N 100E
Velocity at 44N 100E
Velocity at 45N 100E
Percent
0 3 6 9 12 15 18 21 24 27 30
0 4 8 12 16

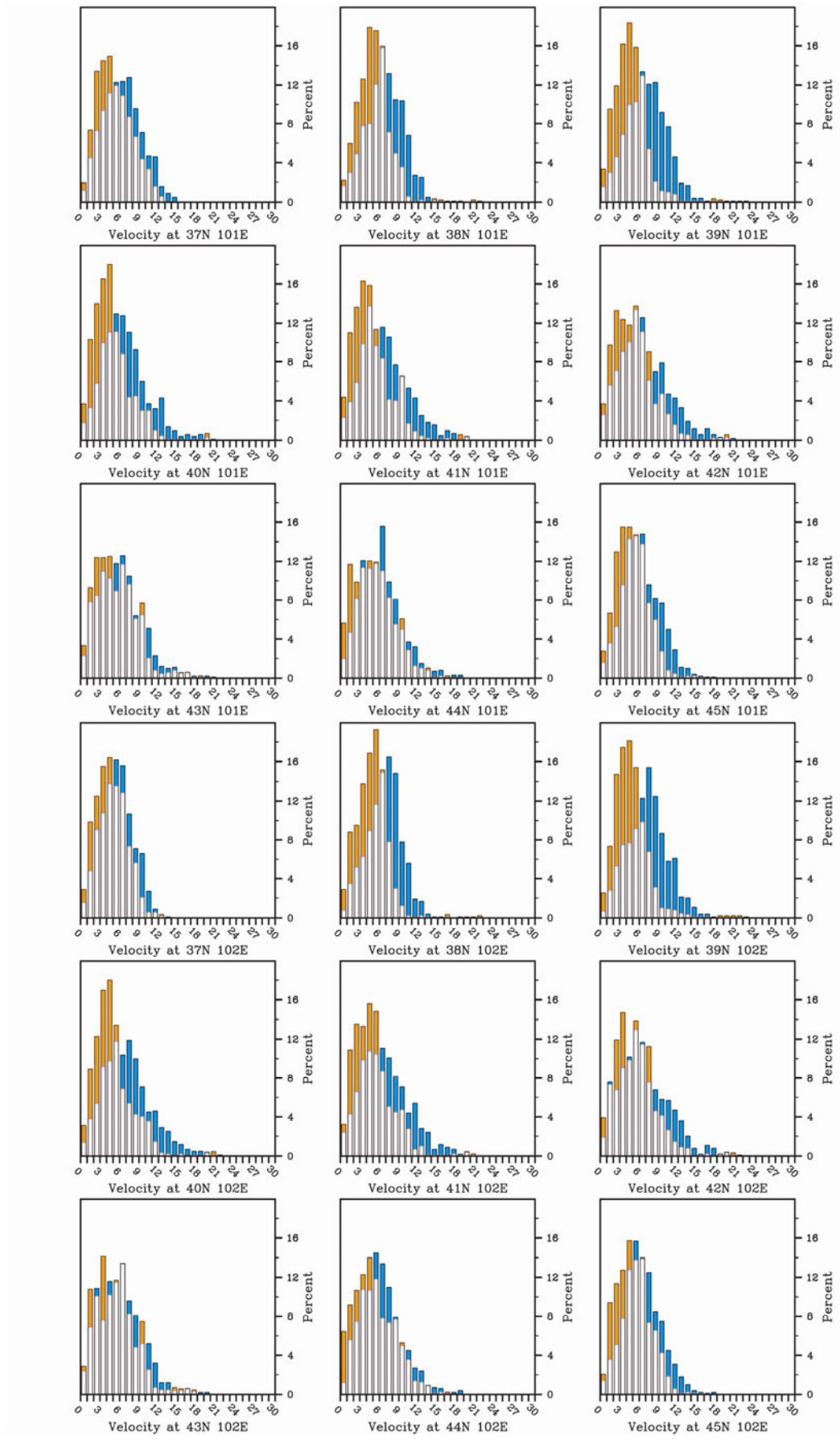
Velocity at 37N 101E
Velocity at 38N 101E
Velocity at 39N 101E
Velocity at 40N 101E
Velocity at 41N 101E
Velocity at 42N 101E
Velocity at 43N 101E
Velocity at 44N 101E
Velocity at 45N 101E
Velocity at 37N 102E
Velocity at 38N 102E
Velocity at 39N 102E
Velocity at 40N 102E
Velocity at 41N 102E
Velocity at 42N 102E
Velocity at 43N 102E
Velocity at 44N 102E
Velocity at 45N 102E
Percent
0 4 8 12 16
0 3 6 9 12 15 18 21 24 27 30

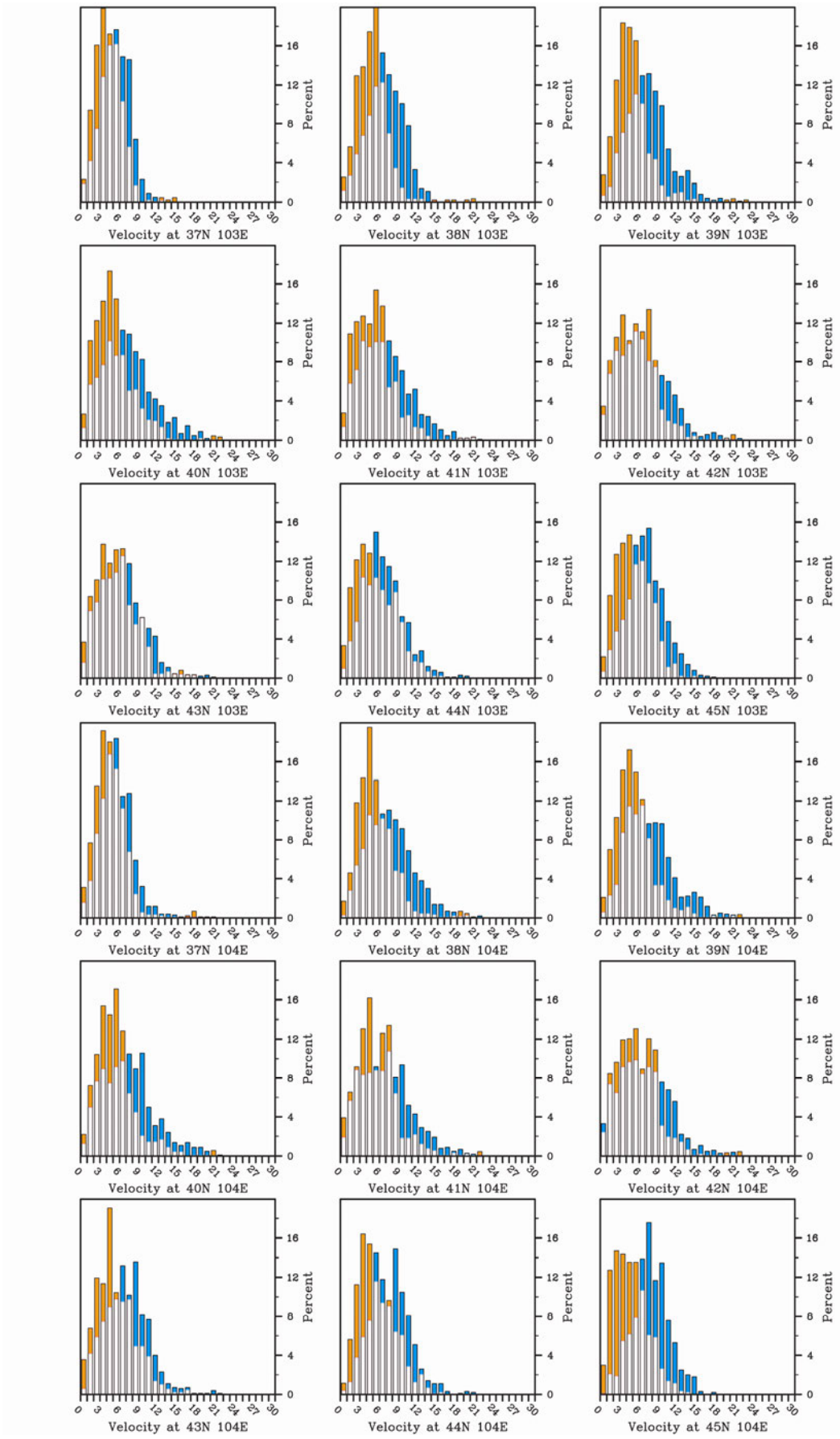
Velocity at 37N 103E
Velocity at 38N 103E
Velocity at 39N 103E
Velocity at 40N 103E
Velocity at 41N 103E
Velocity at 42N 103E
Velocity at 43N 103E
Velocity at 44N 103E
Velocity at 45N 103E
Velocity at 37N 104E
Velocity at 38N 104E
Velocity at 39N 104E
Velocity at 40N 104E
Velocity at 41N 104E
Velocity at 42N 104E
Velocity at 43N 104E
Velocity at 44N 104E
Velocity at 45N 104E
Percent
0 4 8 12 16
0 3 6 9 12 15 18 21 24 27 30

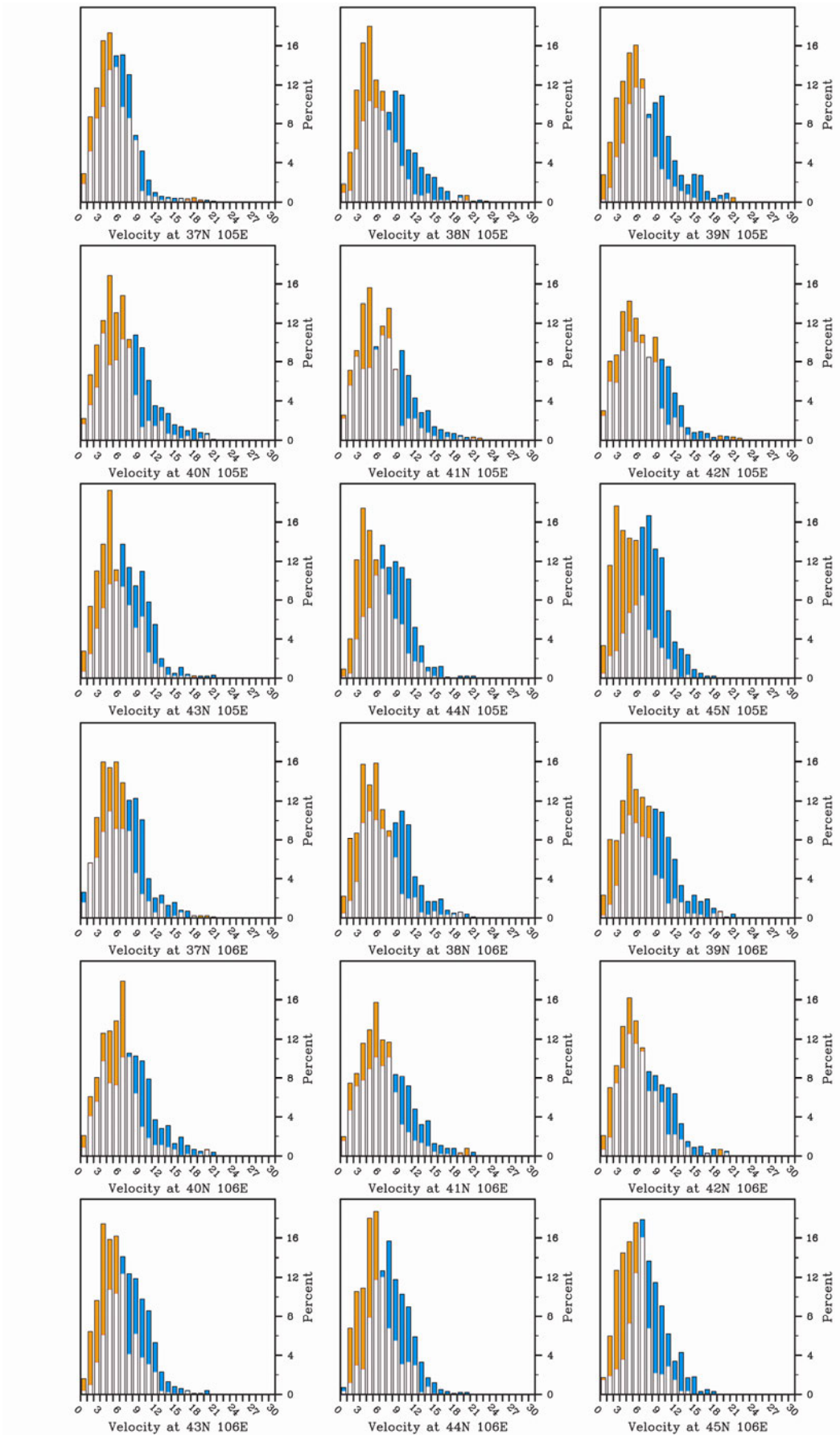
Velocity at 37N 105E
Velocity at 38N 105E
Velocity at 39N 105E
Velocity at 40N 105E
Velocity at 41N 105E
Velocity at 42N 105E
Velocity at 43N 105E
Velocity at 44N 105E
Velocity at 45N 105E
Velocity at 37N 106E
Velocity at 38N 106E
Velocity at 39N 106E
Velocity at 40N 106E
Velocity at 41N 106E
Velocity at 42N 106E
Velocity at 43N 106E
Velocity at 44N 106E
Velocity at 45N 106E
Percent
0 4 8 12 16
0 3 6 9 12 15 18 21 24 27 30

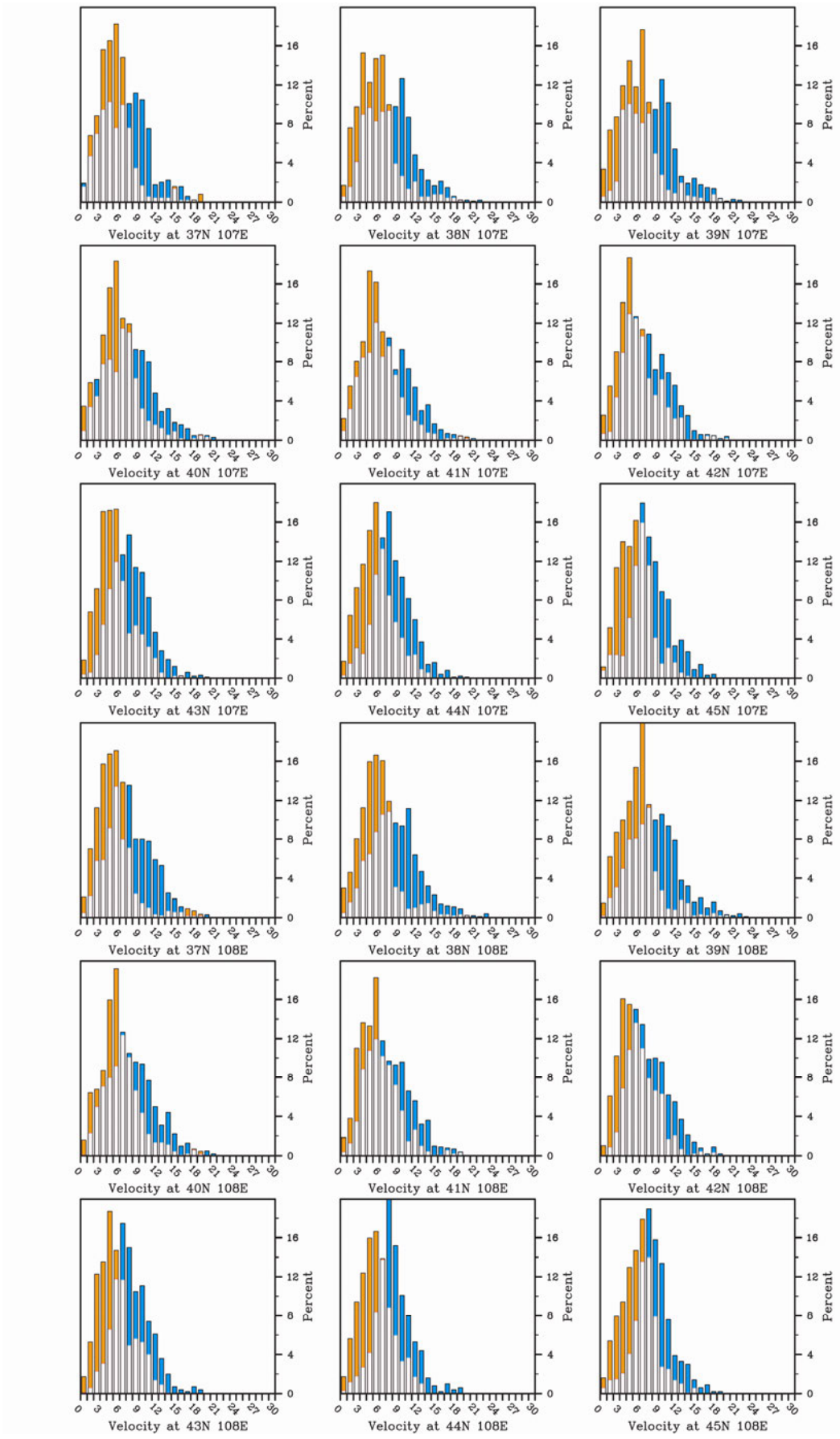
Velocity at 37N 107E
Velocity at 38N 107E
Velocity at 39N 107E
Velocity at 40N 107E
Velocity at 41N 107E
Velocity at 42N 107E
Velocity at 43N 107E
Velocity at 44N 107E
Velocity at 45N 107E
Velocity at 37N 108E
Velocity at 38N 108E
Velocity at 39N 108E
Velocity at 40N 108E
Velocity at 41N 108E
Velocity at 42N 108E
Velocity at 43N 108E
Velocity at 44N 108E
Velocity at 45N 108E
Percent
0 4 8 12 16
0 3 6 9 12 15 18 21 24 27 30

Figure S8: Percentage histograms of hourly wind velocity over the entire one-by-one degree sampling region over the Central Loess Plateau in East Asia (cf. Chapter 6).

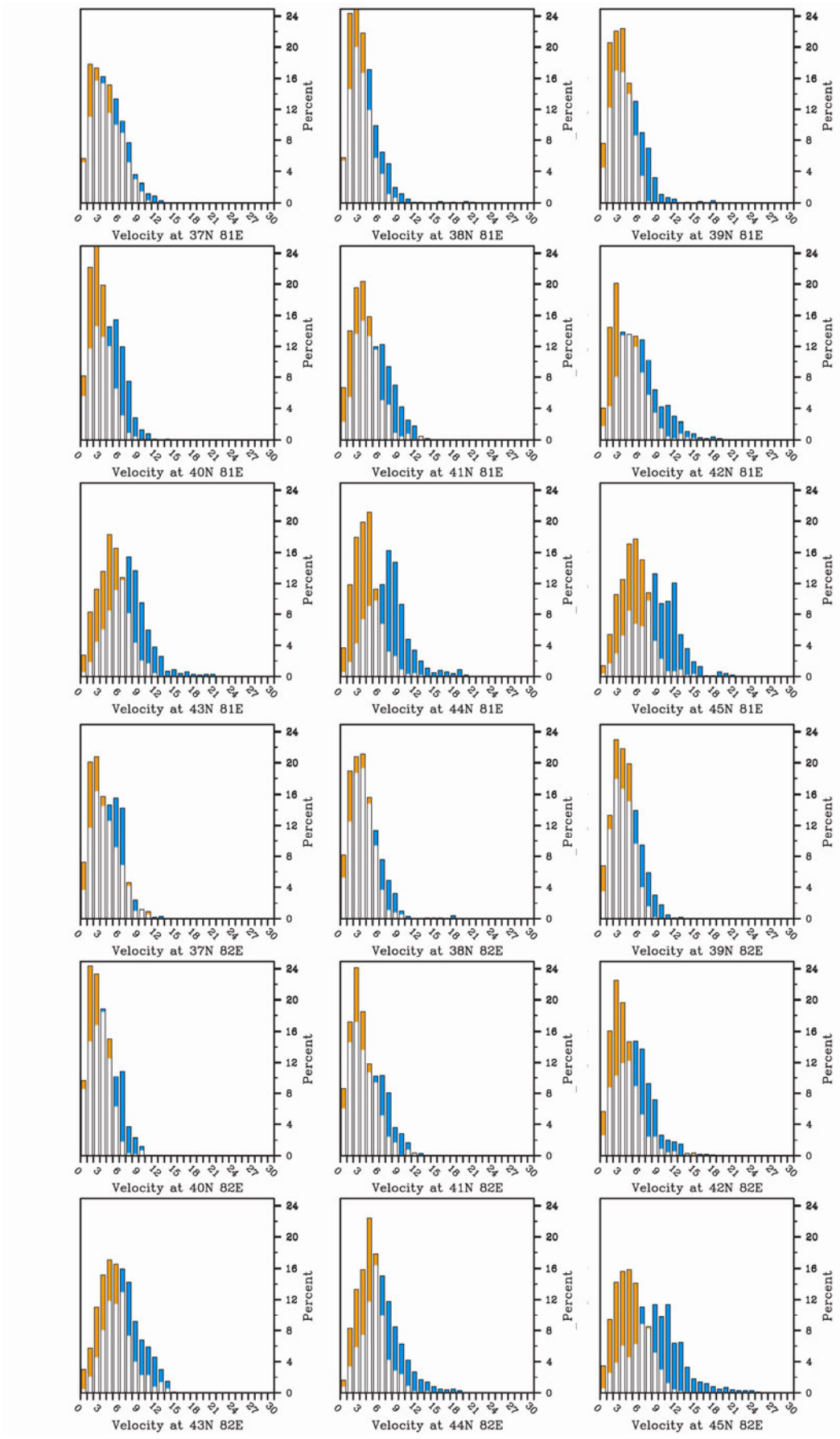
Velocity at 37N 81E
Velocity at 38N 81E
Velocity at 39N 81E
Velocity at 40N 81E
Velocity at 41N 81E
Velocity at 42N 81E
Velocity at 43N 81E
Velocity at 44N 81E
Velocity at 45N 81E
Velocity at 37N 82E
Velocity at 38N 82E
Velocity at 39N 82E
Velocity at 40N 82E
Velocity at 41N 82E
Velocity at 42N 82E
Velocity at 43N 82E
Velocity at 44N 82E
Velocity at 45N 82E
Percent

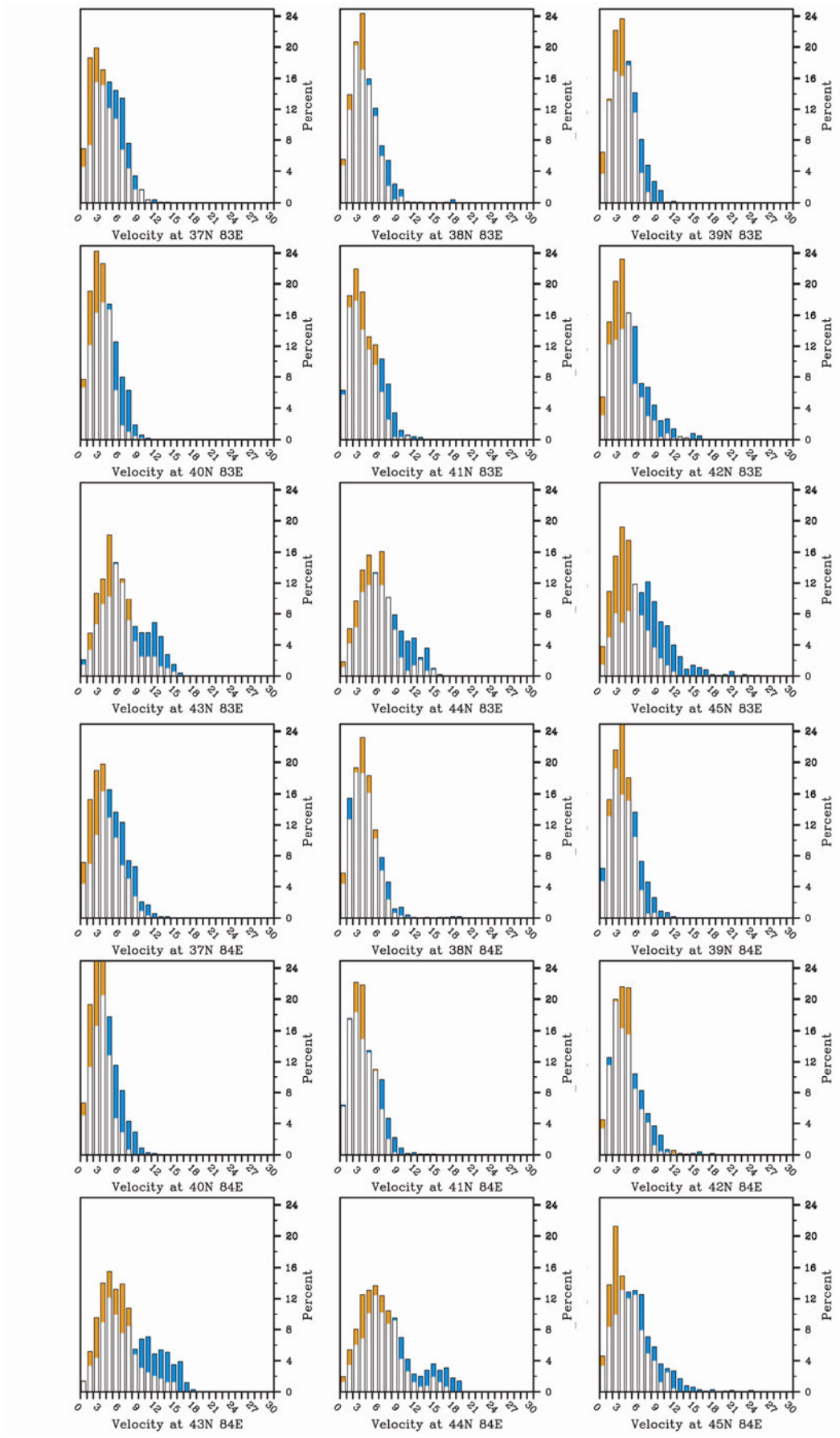
Velocity at 37N 83E
Velocity at 38N 83E
Velocity at 39N 83E
Velocity at 40N 83E
Velocity at 41N 83E
Velocity at 42N 83E
Velocity at 43N 83E
Velocity at 44N 83E
Velocity at 45N 83E
Velocity at 37N 84E
Velocity at 38N 84E
Velocity at 39N 84E
Velocity at 40N 84E
Velocity at 41N 84E
Velocity at 42N 84E
Velocity at 43N 84E
Velocity at 44N 84E
Velocity at 45N 84E
Percent

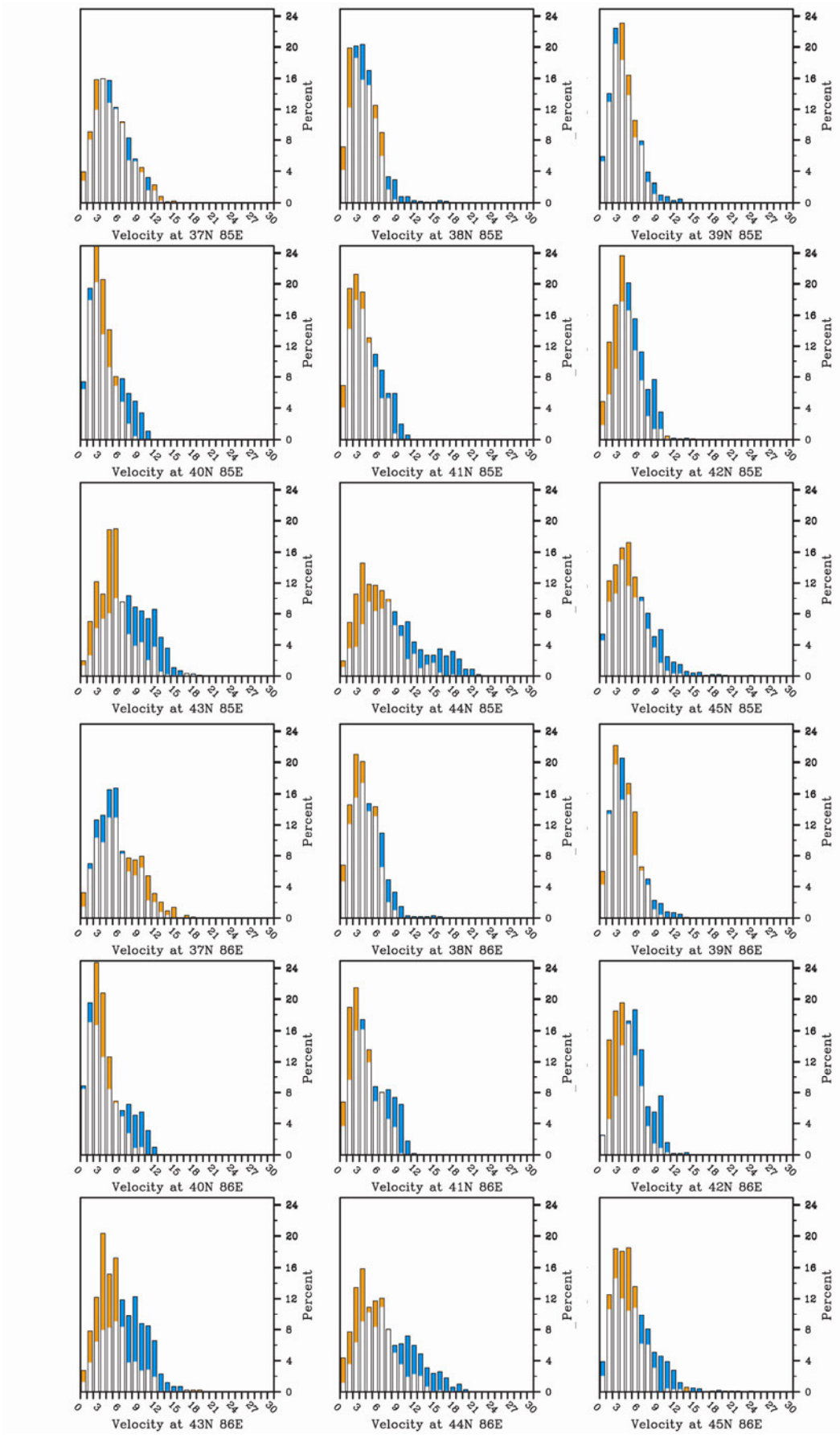
Velocity at 37N 85E
Velocity at 38N 85E
Velocity at 39N 85E
Velocity at 40N 85E
Velocity at 41N 85E
Velocity at 42N 85E
Velocity at 43N 85E
Velocity at 44N 85E
Velocity at 45N 85E
Velocity at 37N 86E
Velocity at 38N 86E
Velocity at 39N 86E
Velocity at 40N 86E
Velocity at 41N 86E
Velocity at 42N 86E
Velocity at 43N 86E
Velocity at 44N 86E
Velocity at 45N 86E
Percent

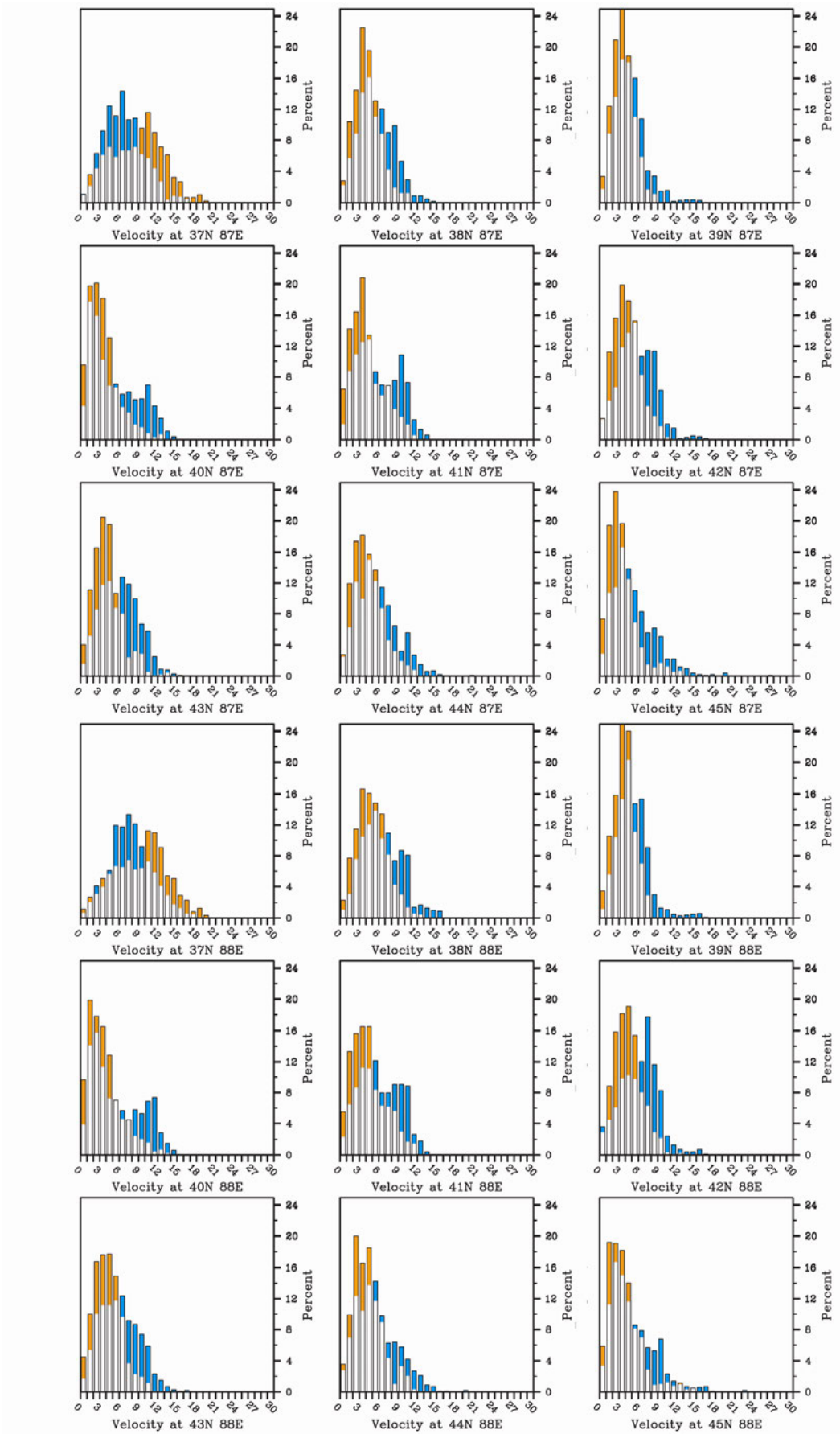
Velocity at 37N 87E
Velocity at 38N 87E
Velocity at 39N 87E
Velocity at 40N 87E
Velocity at 41N 87E
Velocity at 42N 87E
Velocity at 43N 87E
Velocity at 44N 87E
Velocity at 45N 87E
Velocity at 37N 88E
Velocity at 38N 88E
Velocity at 39N 88E
Velocity at 40N 88E
Velocity at 41N 88E
Velocity at 42N 88E
Velocity at 43N 88E
Velocity at 44N 88E
Velocity at 45N 88E
Percent

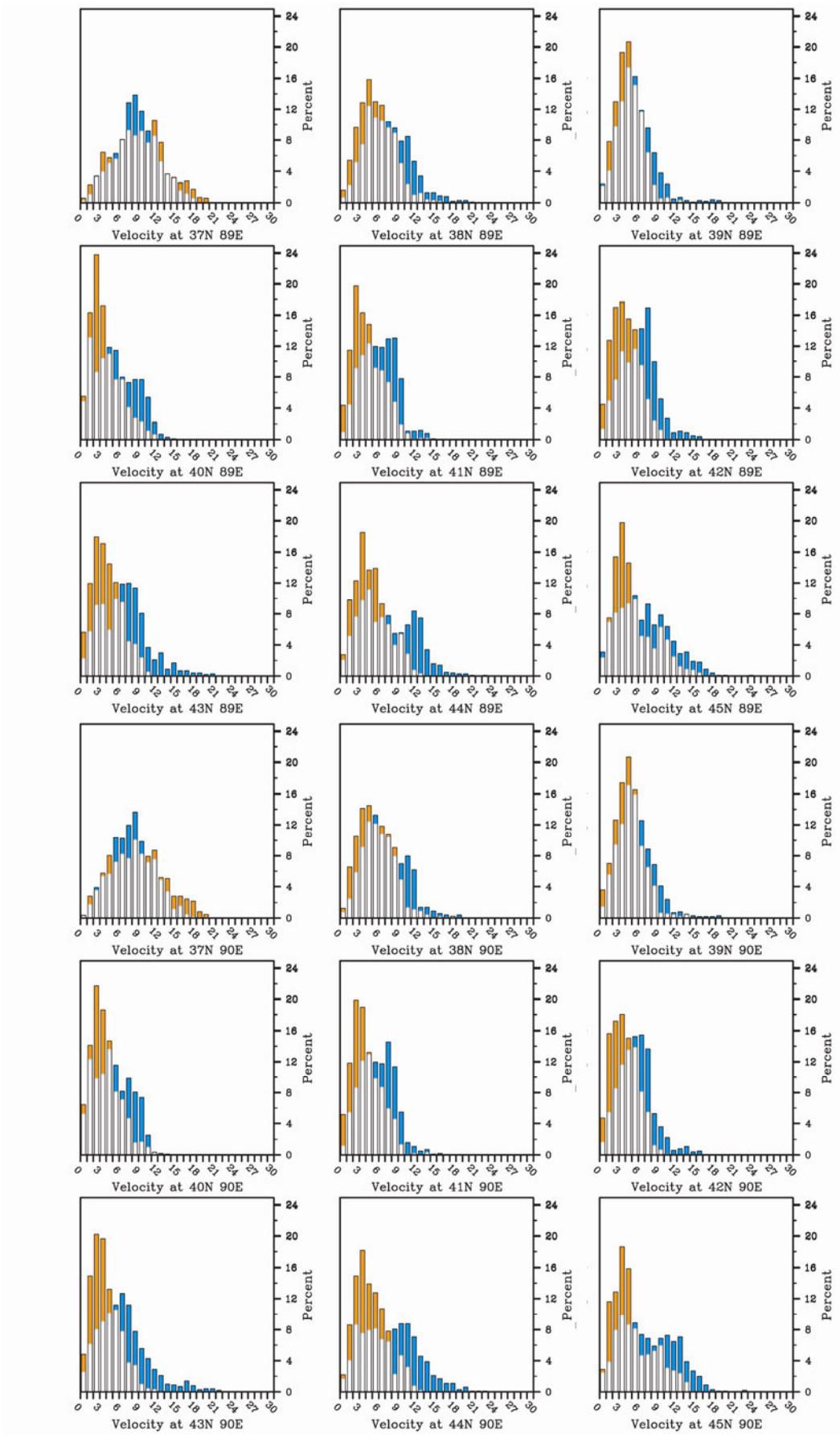
Velocity at 37N 89E
Velocity at 38N 89E
Velocity at 39N 89E
Velocity at 40N 89E
Velocity at 41N 89E
Velocity at 42N 89E
Velocity at 43N 89E
Velocity at 44N 89E
Velocity at 45N 89E
Velocity at 37N 90E
Velocity at 38N 90E
Velocity at 39N 90E
Velocity at 40N 90E
Velocity at 41N 90E
Velocity at 42N 90E
Velocity at 43N 90E
Velocity at 44N 90E
Velocity at 45N 90E
Percent

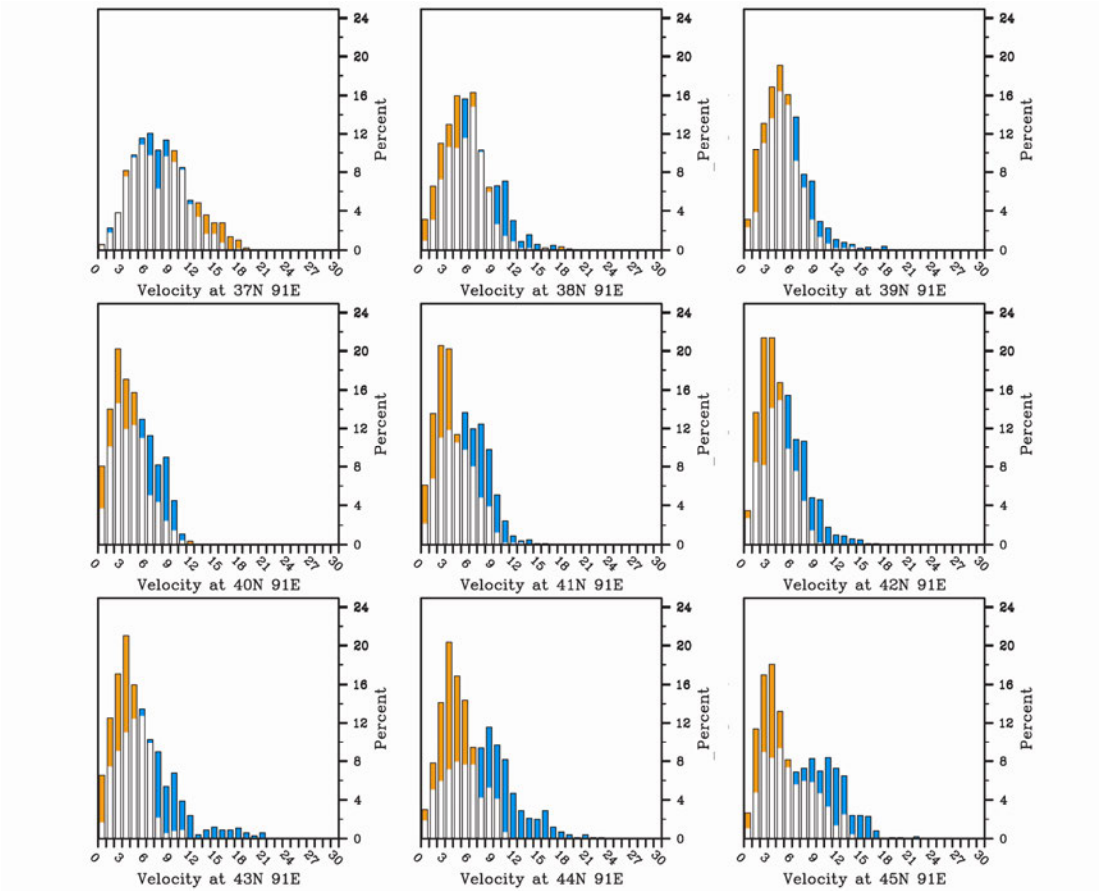

Figure S9: Percentage histograms of hourly wind velocity over the entire one-by-one degree sampling region over the Taklamakan Desert in East Asia (cf. Chapter 6).

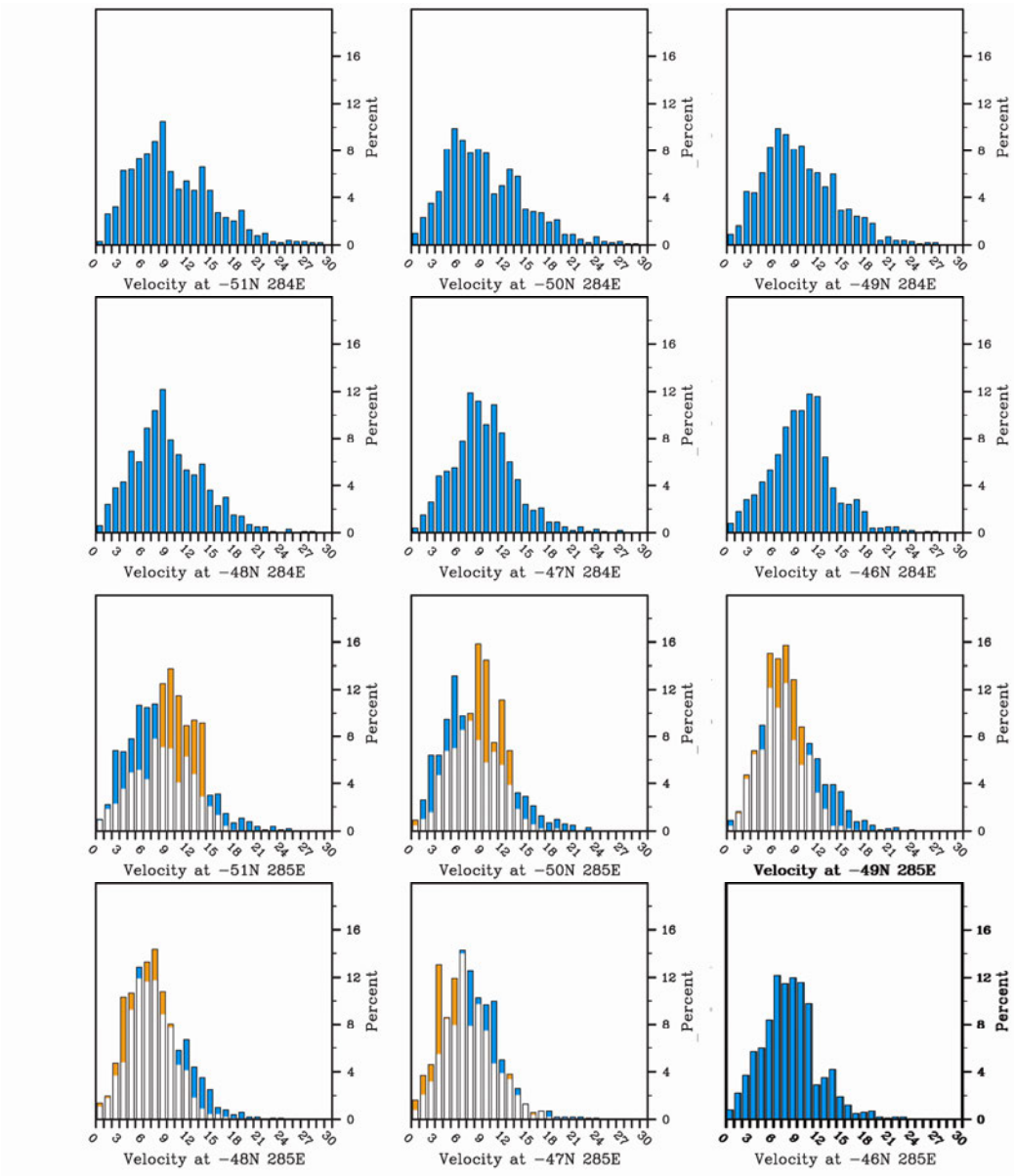
Velocity at −51N 284E
Velocity at −50N 284E
Velocity at −49N 284E
Velocity at −48N 284E
Velocity at −47N 284E
Velocity at −46N 284E
Velocity at −51N 285E
Velocity at −50N 285E
Velocity at −49N 285E
Velocity at −48N 285E
Velocity at −47N 285E
Velocity at −46N 285E
Percent

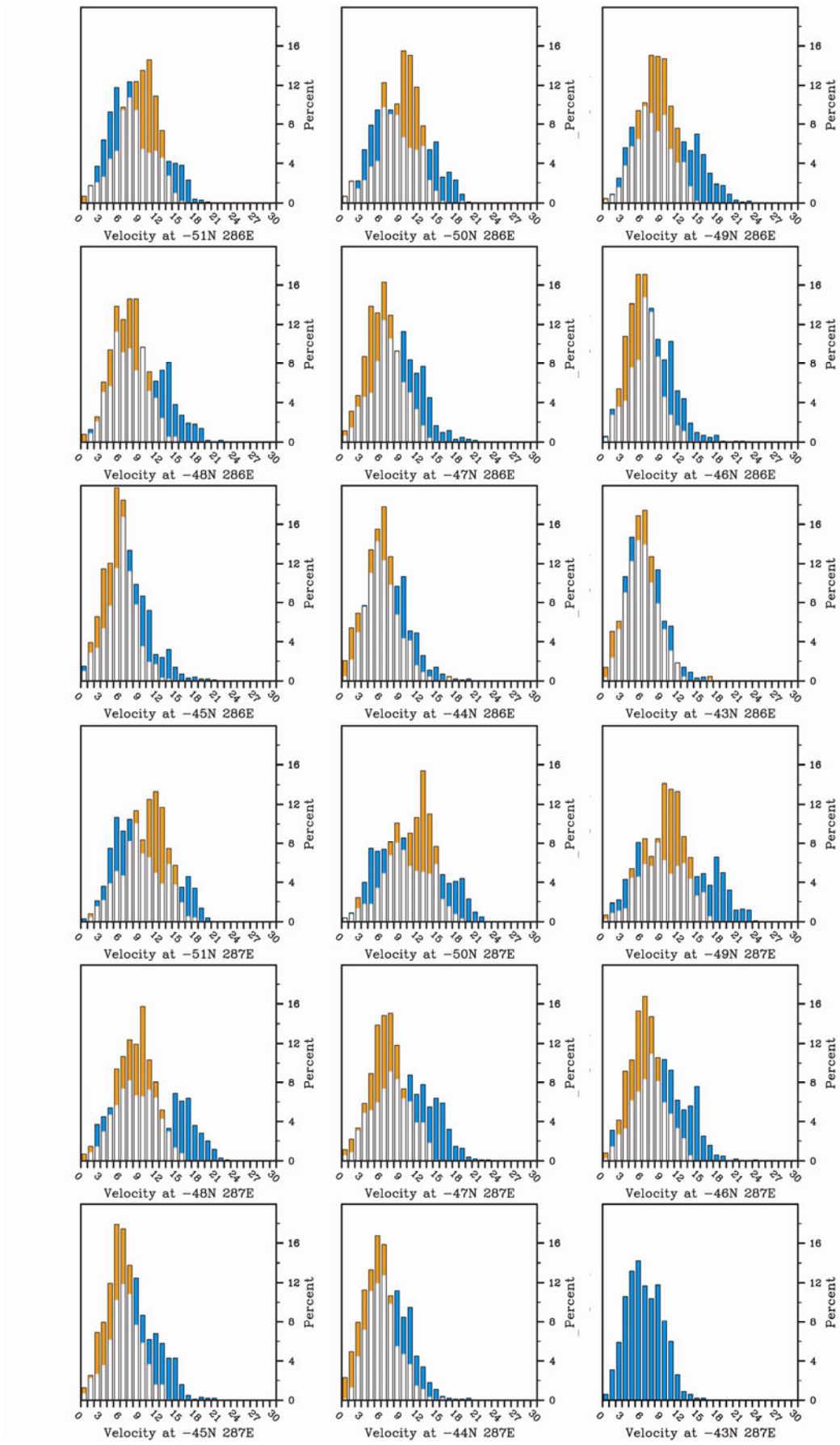
Velocity at −51N 286E
Velocity at −50N 286E
Velocity at −49N 286E
Velocity at −48N 286E
Velocity at −47N 286E
Velocity at −46N 286E
Velocity at −45N 286E
Velocity at −44N 286E
Velocity at −43N 286E
Velocity at −51N 287E
Velocity at −50N 287E
Velocity at −49N 287E
Velocity at −48N 287E
Velocity at −47N 287E
Velocity at −46N 287E
Velocity at −45N 287E
Velocity at −44N 287E
Velocity at −43N 287E
Percent
0 3 6 9 12 15 18 21 24 27 30
0 4 8 12 16

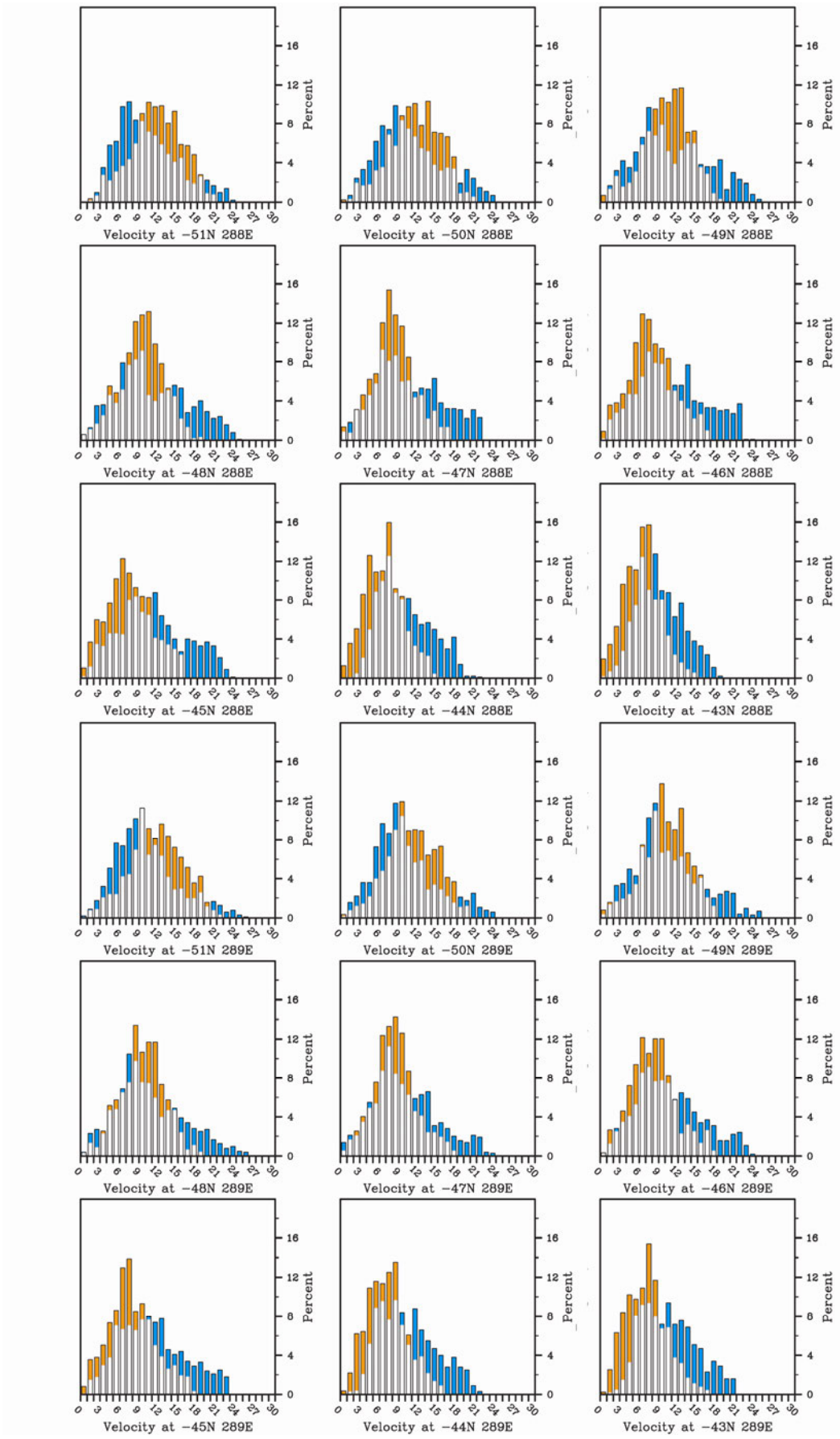
Velocity at −51N 288E
Velocity at −50N 288E
Velocity at −49N 288E
Velocity at −48N 288E
Velocity at −47N 288E
Velocity at −46N 288E
Velocity at −45N 288E
Velocity at −44N 288E
Velocity at −43N 288E
Velocity at −51N 289E
Velocity at −50N 289E
Velocity at −49N 289E
Velocity at −48N 289E
Velocity at −47N 289E
Velocity at −46N 289E
Velocity at −45N 289E
Velocity at −44N 289E
Velocity at −43N 289E
Percent
0 3 6 9 12 15 18 21 24 27 30
0 4 8 12 16

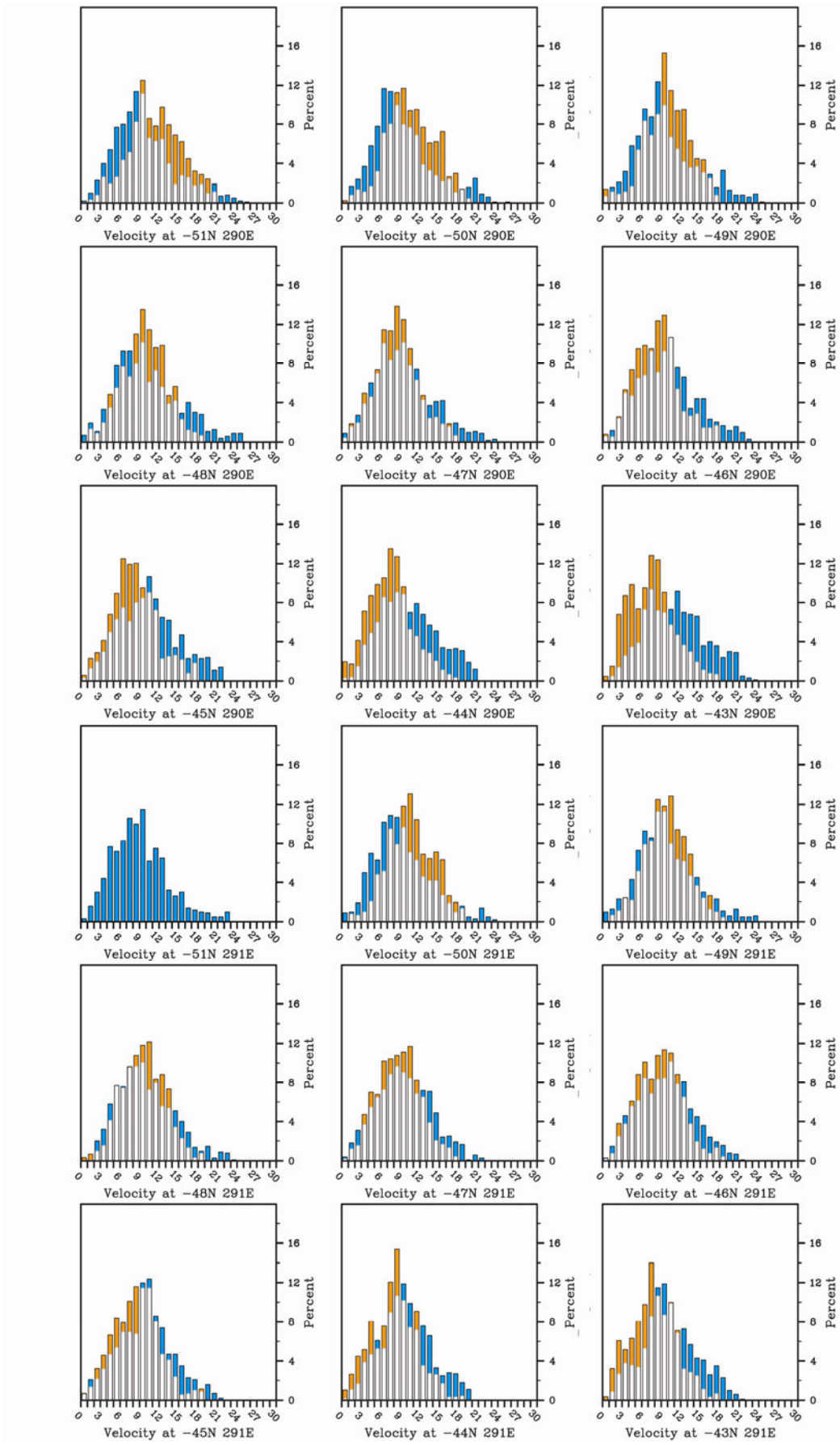
Velocity at −51N 290E
Velocity at −50N 290E
Velocity at −49N 290E
Velocity at −48N 290E
Velocity at −47N 290E
Velocity at −46N 290E
Velocity at −45N 290E
Velocity at −44N 290E
Velocity at −43N 290E
Velocity at −51N 291E
Velocity at −50N 291E
Velocity at −49N 291E
Velocity at −48N 291E
Velocity at −47N 291E
Velocity at −46N 291E
Velocity at −45N 291E
Velocity at −44N 291E
Velocity at −43N 291E
Percent
0 3 6 9 12 15 18 21 24 27 30
0 4 8 12 16

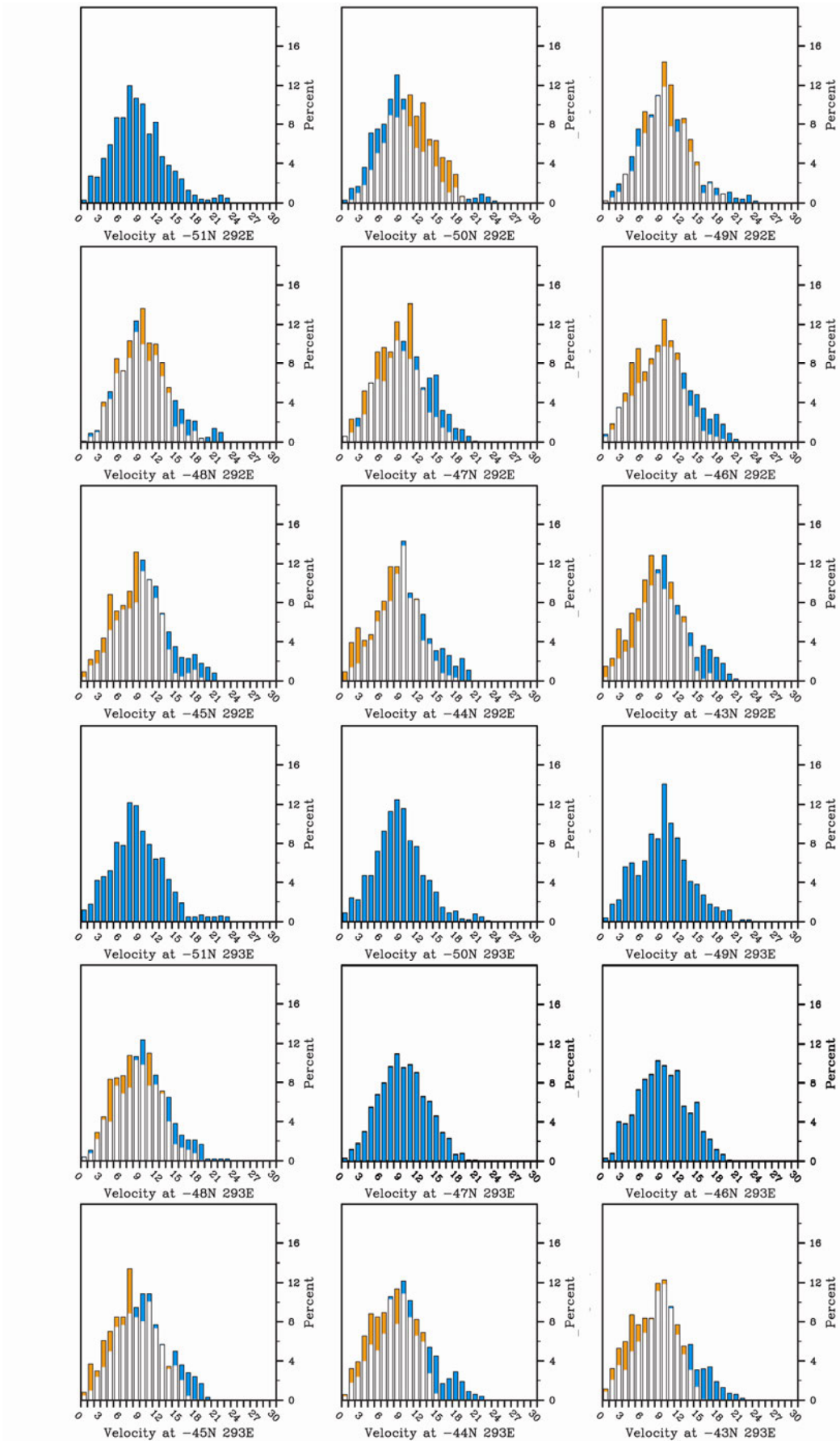
Velocity at −51N 292E
Velocity at −50N 292E
Velocity at −49N 292E
Velocity at −48N 292E
Velocity at −47N 292E
Velocity at −46N 292E
Velocity at −45N 292E
Velocity at −44N 292E
Velocity at −43N 292E
Velocity at −51N 293E
Velocity at −50N 293E
Velocity at −49N 293E
Velocity at −48N 293E
Velocity at −47N 293E
Velocity at −46N 293E
Velocity at −45N 293E
Velocity at −44N 293E
Velocity at −43N 293E
Percent

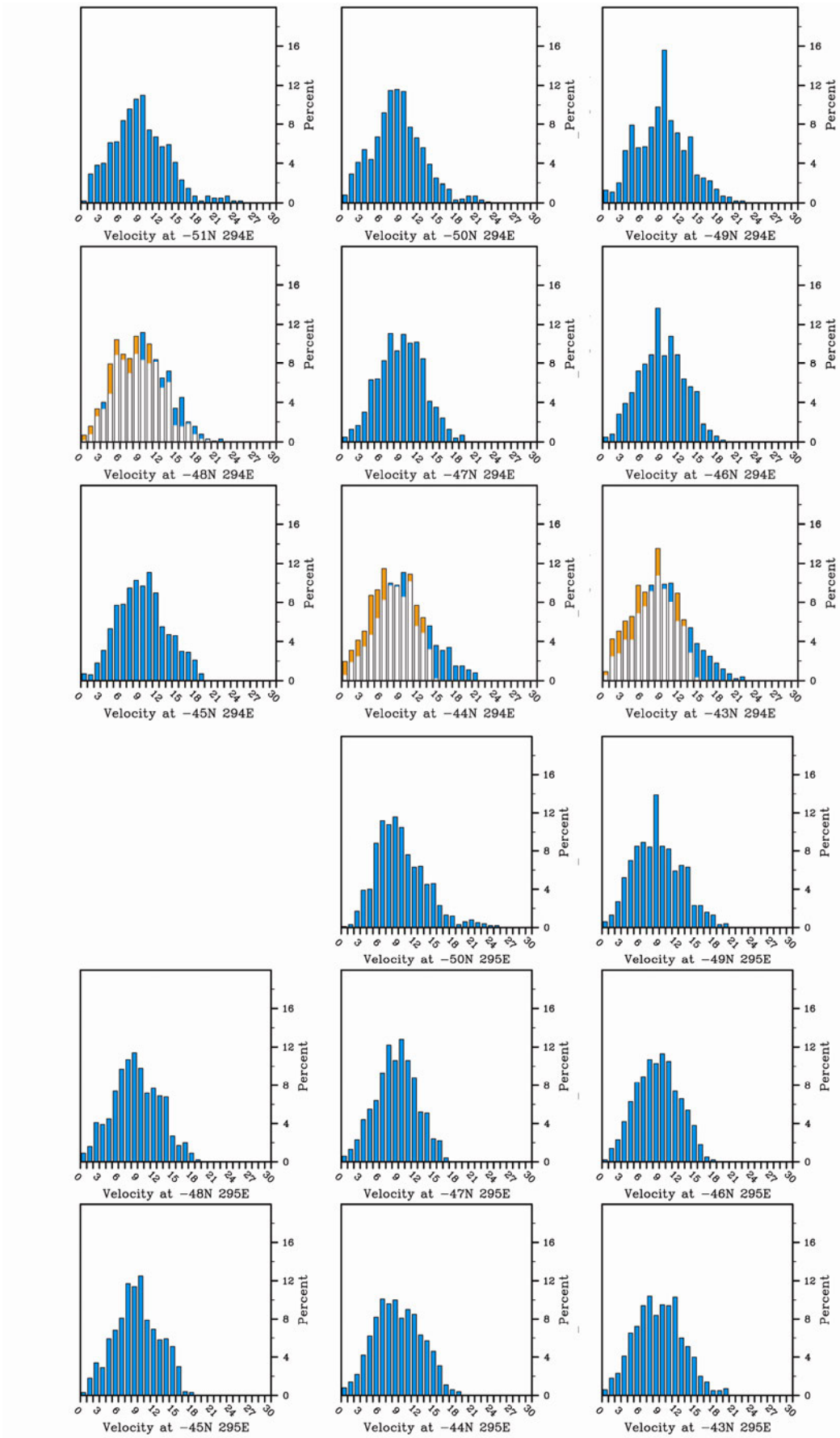
Velocity at −51N 294E
Velocity at −50N 294E
Velocity at −49N 294E
Velocity at −48N 294E
Velocity at −47N 294E
Velocity at −46N 294E
Velocity at −45N 294E
Velocity at −44N 294E
Velocity at −43N 294E
Velocity at −50N 295E
Velocity at −49N 295E
Velocity at −48N 295E
Velocity at −47N 295E
Velocity at −46N 295E
Velocity at −45N 295E
Velocity at −44N 295E
Velocity at −43N 295E
Percent

Figure S10: Percentage histograms of hourly wind velocity over the Patagonia dust source sector (cf. Chapter 6). “Missing” histograms are areas covered by ocean in both the LGM and modern. Several sites (blue only) are exposed only during the LGM due to the eustatic drop in sea level. These are not counted in the comparative statistics presented in Chapter 6.